Doctoral Dissertation
Doctoral Program in Electrical, Electronics and Telecommunications Engineering
(XXXIV cycle)

Parameterized macromodeling of passive and active dynamical systems

...

Tommaso Bradde
* * * * * *

Supervisors
Prof. Giuseppe Carlo Calafiore, Prof. Stefano Grivet-Talocia

Doctoral Examination Committee:
Prof. Tom Dhaene, Referee, Ghent University
Prof. Michel Nakhla, Referee, Carleton University
Prof. Carlo Novara, Politecnico di Torino
Prof. Wil Schilders, Eindhoven University of Technology
Prof. Igor Simone Stievano, Politecnico di Torino

Politecnico di Torino
July 18, 2022

I hereby declare that the contents and organisation of this dissertation constitute my own original work and does not compromise in any way the rights of third parties, including those relating to the security of personal data.

. . . . . .

Tommaso Bradde
Turin, July 18, 2022

List of Figures

List of Tables

List of Acronyms

AWG: Additive White Gaussian
BMI: Bilinear Matrix Inequality
BR: Bounded Real
BRL: Bounded Real Lemma
CAD: Computer Aided Design
CB: Circuit Block
EDA: Electronic Design Automation
FD: Frequency Domain
GSK: Generalized Sanathanan-Koerner
KYP: Kalman-Yakubovich-Popov
LDO: LowDropOut regulator
LMI: Linear Matrix Inequality
LNA: Low Noise Amplifier
LPV: Linear Parameter Varying
LTI: Linear Time Invariant
MOR: Model Order Reduction
OPA: Operational Amplifier
LMI: Linear Matrix Inequality
PCB: Printed Circuit Board
PDN: Power Distribution Network
PMU: Phasor Measurement Unit
PR: Positive Real
PRL: Positive Real Lemma
PSK: Parameterized Sanathanan-Koerner
RF: Radio Frequency
RMS: Root Mean Square
RTVF: Real Time Vector Fitting
SDP: SemiDefinite Program
SER: Signal to Error Ratio
SNR: Signal to Noise Ratio
SK: Sanathanan-Koerner
TD: Time Domain

TDVF: Time Domain Vector Fitting
TVE: Total Vector Error
VF: Vector Fitting

Contents

Notation

In the following, we denote with $\mathbb{N}$, $\mathbb{R}$, and $\mathbb{C}$ the fields of natural, real and complex numbers, respectively. The symbol s is reserved for the Laplace variable, and $j = \sqrt{-1}$ is the imaginary unit. Scalars are denoted with a plain lowercase font x, while uppercase fonts denote matrices X, whose size is specified if not clear from the context. The i, j-th element of a matrix X is denoted either as $X_{i,j}$ or as $X^{i,j}$, depending on the context. Given a complex number z, the notation z^* denotes the conjugate of z. Matrix transpose and Hermitian transpose are denoted with $X^\top$ and $X^\star$, respectively. The set of symmetric matrices of size n is denoted as $\mathbb{S}^n$; accordingly, $\mathbb{S}^n_-$ (resp. $\mathbb{S}^n_{--}$) denotes the set of negative semi-definite (resp. negative definite) matrices of size n; positive definite and semi-definite sets will be denoted with the same notations using the subscript $+$ instead of $-$. A given rational function of the complex variable s is denoted as $\mathsf{H}(s)$, and $\mathbb{I}_\mathrm{P}$ is reserved for the identity matrix of size P. The symbol $\otimes$ is the Kronecker product.

The dependency of a (vector or matrix) function $f(\cdot)$ on its arguments will be omitted whenever it does not introduce ambiguity; the notation $\dot{x}(t)$ will be used to denote the time derivative of the function $x(t)$.

We define a multi-index as a d-dimensional collection of indices $\boldsymbol{i} = (i_1, \ldots, i_d) \in \mathbb{N}^d$. Given two multi-indices $\boldsymbol{j}$ and $\boldsymbol{k}$, we write $\boldsymbol{j} \leq \boldsymbol{k}$ meaning $j_1 \leq k_1, \ldots, j_d \leq k_d$. The sum operation $\boldsymbol{j} + \boldsymbol{k}$ between two multi-indices returns a multi-index $\boldsymbol{i} = (j_1 + k_1, \ldots, j_d + k_d)$. The $\max(\boldsymbol{j}, \boldsymbol{k})$ [resp. $\min(\boldsymbol{j}, \boldsymbol{k})$] function returns the component-wise maximum (resp. minimum) for each entry of its arguments.

Summary

The increasing trends of device integration and miniaturization, combined with the ubiquity of high frequency components and low power applications, pose major challenges in robust design of electronic systems. First-pass designs are only possible through extensive and repeated simulation-driven verification at any stage of product development, aimed at validating both the functional and electrical performance of the system at different levels of granularity. Therefore, Electronic Design Automation (EDA) tools have rightly become one of the pillars that sustain semiconductor industries against the pressing challenges imposed by technological and economic requirements.

A direct approach for system-level verification based on numerical simulations of physics-based descriptions is not realistic. Especially in high-frequency and high-speed applications, the interplay between complex electromagnetic interactions and device/transistor-level descriptions may drive complexity to levels that cannot be handled even with powerful computing hardware. Some model simplification or approximation is in order to enable fast numerical simulations.

Behavioral macromodels provide one of the most effective solutions to this problem. Such models are intended to replace highly complex descriptions through simplified reduced-order equivalents, given an acceptable level of approximation. A macromodel is constructed to accurately mimic the input-output response of a given reference system based on a minimal set of descriptive equations, which (desirably) can be cast as an equivalent reduced-order circuit. Beyond accuracy, the equivalents must reflect fundamental structural properties of the reference devices, such as stability and passivity. Numerical simulations based on certified stable and passive macromodels provide a major speedup and are now regarded as the method of choice in practically all commercial EDA tools.

Parameterized macromodels further extend the potential of this approach by explicitly incorporating the dependence of the target structure response on a number of physical or design parameters. This allows the user to explore different device configurations to perform fast optimization, what-if analyses and statistical assessments.

The generation of guaranteed stable and passive parameterized macromodels is still an open research field. This problem has been addressed in the literature in

two main directions. One approach imposes a model structure that is inherently stable and passive by construction; alternatively, an initial unconstrained model is constructed and is successively perturbed to correct any stability or passivity violations. Both approaches have pros and cons. The former is extremely robust at the price of reduced accuracy due to the conservativity of the constrained model structure. The latter enables better accuracy but may be unreliable due to lack of convergence in the perturbation process.

The first technical contribution of this dissertation fills the gap between these two competing approaches. A general model structure for linear parameterized passive structures is introduced, based on a rational multivariate Bernstein polynomial expansion. Then, a set of numerically tractable conditions on the model coefficients is derived. These are imposed as convex constraints during model extraction, leading to guaranteed stable and passive models for any combination of the parameters, without need of any post-processing. Further, the particular form of these constraints enables a user-defined trade off between identification time and accuracy, a highly desirable feature for designers.

The above convex formulation is exploited to support a second set of technical contributions, aimed at constructing reduced-order models of nonlinear analog circuit blocks. A first extension involves mildly nonlinear devices designed to operate under small-signal assumptions given a predefined bias level, such as integrated voltage regulators. We show that bias-dependent small-signal models with guaranteed stability can be derived in case of programmable, uncertain, and even time-varying bias conditions. The key enabling factors include an affine linear time-varying model structure for which we are able to prove strong quadratic stability. This implies unconditional asymptotic stability under any possible time-varying bias trajectory. The most notable impact of this results is a dramatic speedup in transient simulations, which can reach up to three orders of magnitude on realistic test cases.

The last contribution of this thesis further extends the macromodeling framework to approximate or identify local dynamics of systems for which data samples are available only via real-time monitoring. The result is always a small-signal bias-dependent reduced-order model, whose identification is performed in time domain using samples that possibly include the contribution of non-vanishing (and unknown) initial conditions. The resulting algorithm that we denote as Real-Time Vector Fitting (RTVF) is demonstrated on two applications belonging to power system modeling and even to haemodynamic modeling of the human cardiovascular system, by exploiting the analogy between electric and fluid dynamics variables.

In summary, this dissertation provides a unifying framework and a set of numerical algorithms for the data-driven reduced-order modeling of some wide classes of dynamical systems. Improvement of the state of the art is demonstrated both under theoretical standpoints thanks to the stability and -if required- passivity conditions, and under the practical standpoint through extension in scope and applicability.

Chapter 1

Introduction

This thesis presents novel technical solutions for the generation of macromodels of complex linear and nonlinear dynamical systems. The presented techniques return reduced order descriptions that are at the same time accurate, compact, and coherent with the fundamental physical principles governing the underlying systems. These three features make the models suitable to be exploited in computer aided design tools, enabling fast simulation and optimization of large scale systems of engineering interest, that would be otherwise computationally intractable. This chapter discusses the context and the motivations for this research and provides an overview of the organization of this thesis

1.1 Motivations

Mathematical models and simulations are a cornerstone for modern technological development and industrial manufacturing. The possibility of accurately predicting the behavior of a given design allows engineers to perform preliminary testing and verification stages without relying on the construction of physical prototypes, which is highly consuming in terms of strategical assets. The industrial interest for mathematical models is therefore motivated not only by their effectiveness in predicting physical phenomena, but also by their potential for saving resources in terms of manpower and time-to-market.

In this context, reduced order models, also called *macromodels* or *surrogate models*, gained an increasing importance in the field of Computer Aided Design (CAD). The rationale behind such models is to predict the behavior of a given system with minimal computational efforts, by accurately reproducing those physical quantities that are of interest within a specific simulation [117, 27, 98] . The intrinsic complexity of the first-principle physical laws (e.g. Maxwell's equations) can be reduced to a small set of explanatory instrumental variables, that are sufficient to predict the input-output relationship of interest. This motivated an enormous

amount of research efforts by both academia and private companies (CAD tool vendors mainly) towards the development of model order reduction tools and algorithms. A comprehensive review of the state of the art is available in the recent series of monographs [12, 11, 10].

The broad field of electronics is probably the application area that exploited model order reduction tools and methods to the largest extent, fostering several key developments during the last few decades. In fact, the verification of electrical performance of a complete electronic system requires extensive system-level simulations, in which all relevant system parts are characterized and represented by mathematical models. The presence of thousands or millions of elementary components and structures in close proximity calls for an accurate representation of all electromagnetic interactions. The latter are often neglected in the early design (concept) stages, yet they may have an enormous impact on the compliance of signal and power supply levels with design specifications. A direct electromagnetic simulation of all such effects on the complete system is not feasible. Hence the need of representing all interactions through simpler and compact representations.

Behavioral models enable system-level simulations by drastically reducing their overwhelming complexity, providing also the possibility to perform design optimization, what-if and worst-case analyses, based on global performance assessment. Generation of behavioral models involves a first characterization step, in which a detailed (circuit or electromagnetic) analysis at the component level is carried out. The results of this characterization are then used to build a behavioral model that retains only the dominant features of interest, disregarding or approximating the fine details that are not relevant.

The applications considered in this thesis will mostly fit in the Electronic Design Automation (EDA) domain. Two main classes of structures are considered as targets for proposed algorithms, namely passive components described by Linear and Time Invariant (LTI) differential equations, and analog circuit blocks generally described by nonlinear large-scale differential equations. Under proper conditions, we will see that both classes can be represented by compact macromodels having a similar structure, for which a unifying framework is proposed in this work. A further description of these structures follows, emphasizing the advantages of reduced order macromodels through some practical examples.

1.1.1 Passive components

Passive components are prominent in every electrical and electronic system. To this class belong all the standard electrical components, such as discrete or integrated capacitors, inductors, transformers and antennas. Any electrical interconnects such as Printed Circuit Boards (PCBs), Power Distribution Networks (PDNs), circuit packaging and layouts, or individual transmission lines, are passive components.

Accurate characterizations of passive components are often based on systematic electromagnetic analyses, requiring the numerical solution of the full-wave or quasi-static Maxwell's equations. Electromagnetic field solvers can be employed to perform such analyses, via differential (e.g. finite elements [64, 108]) or integral methods (e.g. method of moments [45]), which perform space discretization via suitable meshes in order to describe the continuous time (or frequency) domain evolution of the electromagnetic field. Although very accurate, these analyses may require extremely expensive computations to be performed.

As an example, Fig. 1.1 shows the voltage distribution on a PCB power distribution network (segmented power planes) excited by harmonic sources operating at frequencies 800 MHz (left panel) and 3 GHz (right panel), obtained by means of a full-wave simulation. For such complex geometry, solving the full-wave problem requires handling an extremely large number of unknowns. Even for simple structures, this number easily grows beyond millions [100]. Nonetheless, the frequency response of this structure depicted in Fig. 1.2 can be represented by a model described by much less degrees of freedom. For this particular example, two rational functions having order 80 are sufficient to fit and represent the behavior of the original structure at the considered ports with excellent accuracy. This example shows that first-principle descriptions based on (discretized) field equations include a large extent of unnecessary details and complexity, which can be safely removed without compromising accuracy.

1.1.2 Analog circuit blocks

Analog circuit blocks can be classified as those functional units including electronic components (i.e. generally speaking, semiconductors) involving continuously varying signals. They implement a variety of functionalities including signal amplification [RF amplifiers of Low Noise Amplifiers (LNA), for instance] and generation (oscillators), voltage regulation [Low DropOut (LDO) regulators], and control (phase-locked loops, feedback networks). They are essential in modern electronics, and, in particular, in mixed Digital-Analog RF systems.

The detailed description of analog circuit blocks require transistor models [111, 96] catching nonlinear solid-state electronic phenomena. Such models are available at different levels of detail, depending on the required trade-off between description compactness and reliability. Additionally, the influence of the actual device layout and packaging (i.e. the passive interconnects entering the design) must be taken into account by means of circuit extraction procedures. These procedures translate the physical topology of the system into an equivalent circuit, in which parasitic electrical phenomena such as unwanted capacitive or inductive couplings are described in terms of suitable lumped elements [7, 1].

Equivalent circuits are usually made available in the form of SPICE [80] netlists, that represent the standard description format for any circuit simulation software.

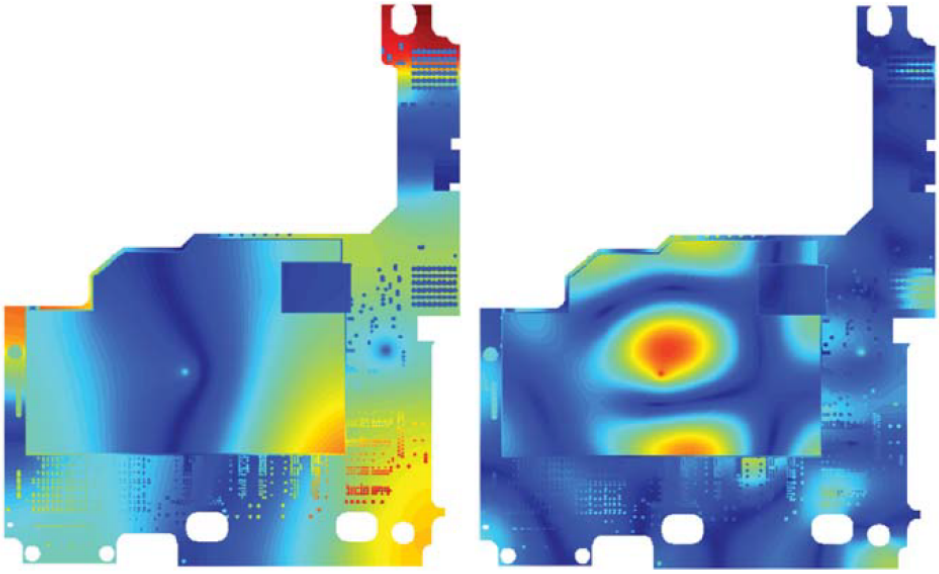

Figure 1.1: Voltage distribution on a PCB power distribution network, when excited by unitary harmonic sources. Left panel: 800 MHz excitation. Right panel: 3 GHz excitation. (courtesy: Prof. M. Swaminathan, Georgia Institute of Technology, Atlanta GA, USA, reproduced with permission from [51])

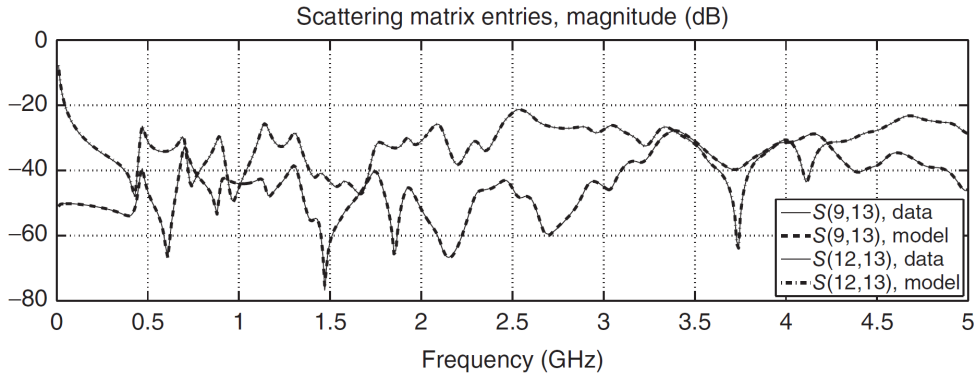

Figure 1.2: Frequency response of the PDN structure depicted in Fig. 1.1 at two reference ports (solid lines). Dashed lines depict the responses of two behavioral models with only 80 poles. Reproduced with permission from [51].

As the number of lumped elements required to describe non-ideal parasitic effects is large, the size of these equivalent circuits can be very large. This is particularly true when the circuits are integrated in a single System-on-a-chip (SoC), in which many components interact together at high frequencies in a miniaturized space.

As an example, Fig. 1.3 depicts the realization of an LDO circuit, that will

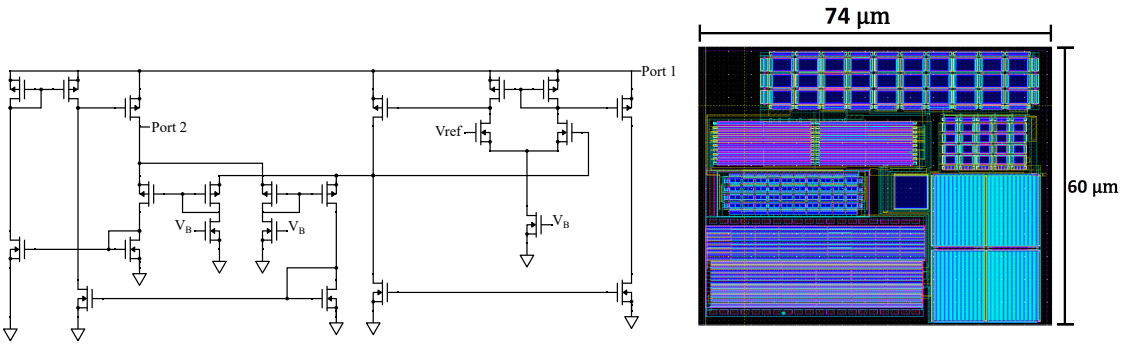

Figure 1.3: A low dropout voltage regulator. left panel: transistor level schematic. right panel: actual circuit implementation including layout, described in terms of a 30 MB equivalent netlist. Reproduced from [18] © 2019 IEEE.

be further analyzed in chapter 5. The left panel shows a schematic description including only transistor models, while the right panel represents the post-layout circuit implementation. The equivalent netlist including all the parasitics from a layout extraction has a size of more then 30 MB. This netlist complexity translates into high computational requirements during any successive simulation stage for power integrity analysis. One of the topics covered in this thesis is the derivation of more compact circuit block representations, with the objective of reducing this complexity. For this specific example, a speedup in transient simulation of almost 3 orders of magnitude was achieved, see below for details.

1.1.3 A reference system example

The following example provides a more complete picture of an entire system where multiple components and subsystems coexist in close proximity, and for which availability of compact macromodels can dramatically boost efficiency in design verification. Consider the structure depicted in Fig. 1.4, representing a Power Distribution Network (PDN) including distributed on-chip Low DropOut voltage regulators (LDOs). The system transfers the supply power from the outer environment to a set of functional circuits embedded within their packages. After the external DC voltage level is transformed to the value required by each load circuit via switching voltage regulator modules (not shown in the picture), it must be kept as constant as possible by the LDOs circuitry, that mitigate voltage drops and fluctuations arising from the parasitic electromagnetic interaction between the load circuits, the on- and off-chip power distribution networks, and the chip packages.

Designers need to carry out a number of transient simulations of the complete system, making sure that all physical phenomena having an effect on voltage and current signals in all system locations are correctly represented. Moreover, the presence of nonlinear components such as the LDOs may trigger instabilities not

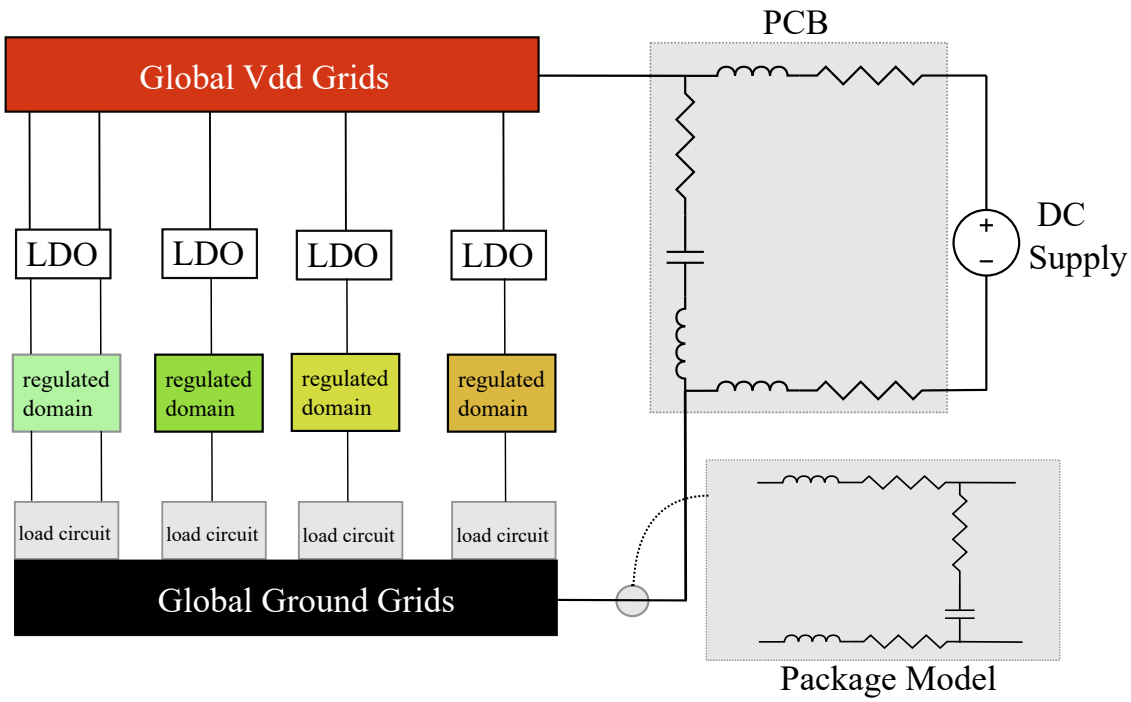

Figure 1.4: A power distribution network system with distributed low dropout voltage regulators.

only in the numerical simulations, but also on the real hardware. It is therefore mandatory to assess system stability by capturing in the models any factor that has an influence.

The system can be decomposed into a number of functional blocks interacting only through well-defined ports. We recognize passive structures (all electrical interconnects, power planes and grids at chip, package and board level), decoupling capacitors (not shown in the picture), and localized LDO regulators (active circuit blocks). A direct simulation of the entire system using first-principle models would require a (transient) multiscale electromagnetic solver coupled with a transistor-level circuit solver. Although feasible in principle, this approach would require enormous computational resources. A better alternative is offered by a macromodel-based system-level approach, which

- characterized each individual component or subsystems using first-principle descriptions;
- uses such descriptions to derive low-complexity reduced-order models;
- connects all reduced-order models in a global simulation deck, which is then solved in reduced time.

1.2 Surrogate modeling and model order reduction

Several and possibly very different approaches are available for constructing low complexity models for large-scale dynamical systems. These approaches can be generally classified in two main classes, denoted in the following as "classical" Model Order Reduction (MOR) and surrogate (behavioral) modeling or *macromodeling*. Note that usage of these terms is not always consistent in the literature.

Although the two approaches share the same goal, they perform the simplification process in different ways when dealing with dynamical systems. Classical MOR schemes perform the simplification by relying on the availability of a reference device mathematical description, provided in the form of a set of differential equations (either partial or ordinary). This initial system is processed by an approximation or truncation algorithm to remove the unnecessary variables or states. For this reason, these methods are said to be *intrusive*, since they need a full detail description as a starting point. The interested reader is referred to [12, 11, 10] for a comprehensive overview of MOR techniques and applications.

On the other hand, macromodeling approaches perform complexity reduction indirectly, by means of *non-intrusive* techniques. In the macromodeling framework the behavior of the target system is reconstructed starting from data samples of the input-output responses (time or frequency domain), obtained through high fidelity simulations or measurements. This approach allows to construct reduced order models of reference systems for which a closed form description is not available, either due to lack of information, or due to industrial secrets. For this reason, macromodeling techniques are commonly referred to also as "data-driven model order reduction methods". A reference macromodeling flow is reported in Fig. 1.5.

Surrogate models are most commonly provided in form of equivalent netlists of small complexity, compatible with SPICE circuit simulation environments. These netlists allow electrical and electronic engineers to assemble large system interconnections, composed of functional black-box units interacting with the environment by means of prescribed electrical ports. Behavioral models will be the main subject of all the following discussions.

1.2.1 Requirements on macromodels

In order to be reliable for general use by designers, macromodels must fulfill a number of mandatory requirements, discussed below.

- *Model compactness.* Effective macromodels should be able to catch the required level of information to reproduce the input-output behavior by keeping at minimum the complexity of the model representation. Figure 1.6 shows how a compact behavioral model represented by 9 linear ordinary differential equations can replace the post-layout circuit of Fig 1.3 in a transient simulation, guaranteeing a speed-up factor of almost three orders of magnitude in

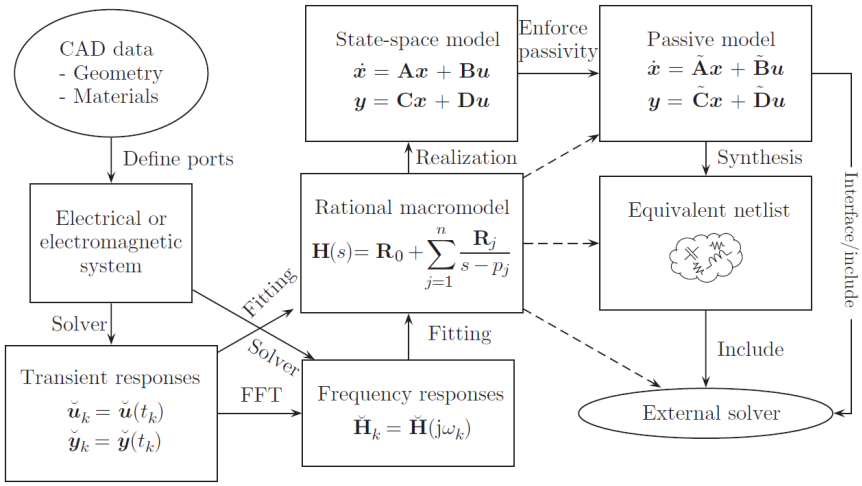

Figure 1.5: A standard data-driven macromodeling flow for passive components. Reproduced from [51] with permission.

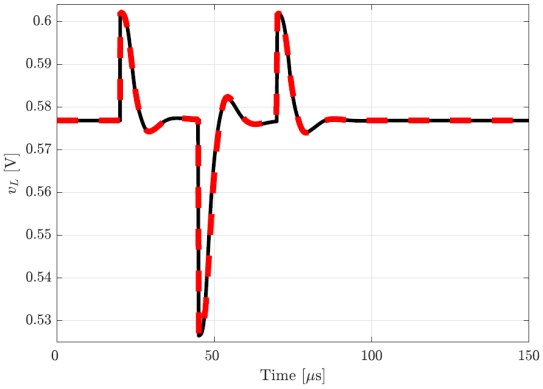

Figure 1.6: Black solid line: the regulated voltage of the post-layout LDO depicted in Fig. 1.3 when the circuit is subject to a sequence of voltage pulses at Port 1. Red dashed line: the corresponding output of a behavioral model derived by means of the techniques presented in chapter 5. When the native 30 MB circuit netlist is replaced by the behavioral model, the speed-up factor amounts at 675×, see [18]. Reproduced from [18] © 2019 IEEE.

transient simulation.

- *Physical consistency.* When behavioral models are used to represent dynamical systems, they must be compliant with their fundamental physical properties. The main structural property that the surrogate must retain is the stability of the dynamics. This requirement is crucial, since any unstable model will potentially lead to totally unreliable simulation results, in which

all the involved numerical quantities undergo divergence or unexpected behaviors.

Closely related to stability, passivity is another structural property that must be reflected by surrogate models of physically passive components, which are unable to generate energy on their own. The importance of this property stems from the fact that the interconnection of passive systems always results in stable dynamics. When behavioral models that violate this property are used in a larger system simulation, they may compromise the validity of the results, by introducing spurious instabilities. In the worst case scenario, the root cause of the instability may not be immediately identified in the model inconsistency, and may lead engineers to draw wrong conclusions about the quality of an actually correct design.

- *Automated generation.* An attractive macromodeling flow should be carried out in an automated way in all of its stages, in order to be exploitable by non-expert users.

- *Parameterization.* Advanced macromodeling schemes also provide surrogates that embed in a compact representation the dependency on a set of external physical or design parameters. Using parameterized macromodels in place of their standard counterparts may dramatically improve the efficiency of the design flow, by avoiding the need to interpose modeling stages with additional simulations when a parameter is modified to obtain some kind of performance. This enables the possibility to exploit macromodels in statistical assessments and automated optimizations. In Fig. 1.7 a practical design application of parameterized macromodels is reported. A high speed PCB interconnection is represented by a parameterized macromodel, and the eye diagram resulting from the transmission of a pseudo-random bit-sequence is derived for two different design parameter configurations. The simulation is easily performed via parameterized transient analysis on a freeware SPICE engine.

  In order to be fully reliable and effective, parameterized macromodels must retain all the features of their univariate counterparts (including compactness of the representation and reflection of the underlying system physical property) for all of the considered parameters configurations.

Whereas in the last decades surrogates of passive components have become well-established in several applications, a number of open issues remain. The technical results proposed in this thesis extend applicability of macromodels, focusing on novel techniques for passive parameterized macromodeling and for the generation of surrogates of nonlinear systems. All these developments are enabled by a unified framework, that is cast in different formulations depending on the class of systems under modeling.

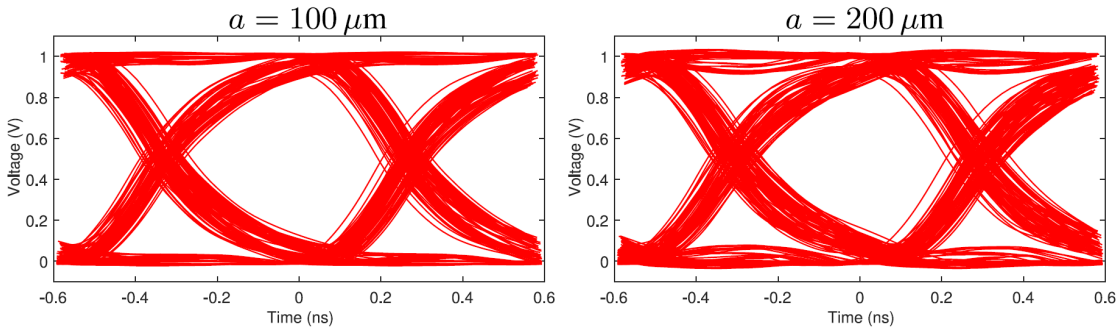

Figure 1.7: The eye-diagram resulting from the transmission of a pseudo-random bit-sequence through a high-speed interconnect. The simulation is performed in a SPICE engine by replacing the native system description with a parameterized macromodel, which allows to perform the transient simulations for different values of the design parameter a (i.e. the interconnect via radius, see Sec. 4.6.3). Reproduced with permission from [53] © 2017 IEEE.

1.3 Technical contributions

The technical contributions of this dissertation are organized and presented as follows. Chapter 2 recalls the background topics that are necessary to derive the novel technical results presented in this work. The concepts of convex optimization, state space models, transfer functions, electrical multiport representations, systems stability and passivity are briefly summarized.

Chapter 3 introduces rational fitting and its extension to the multivariate case. Three rational fitting algorithms, constituting the core of the proposed modeling framework, namely the Generalized Sanathanan-Koerner, the Parameterized Sanathanan-Koerner and the Vector Fitting iterations, are described. Most of this material should be considered as background, although the presented material includes some novel technical solutions to increase the efficiency of the fitting process when dealing with rational matrix functions of large size.

Chapter 4 presents our novel contributions for the generation of parameterized macromodels of passive devices. The presented results improve the state-of-the-art by allowing for the first time the synthesis of parameterized macromodels that are concurrently

1. theoretically guaranteed to be stable and passive by construction, for all of the prescribed parameters configurations,

2. generated via deterministic convex optimization approaches,

3. of minimal complexity and generated automatically by setting a desired trade-off between accuracy and training time.

The performance of proposed algorithms is thoroughly analyzed experimentally in Sec. 4.6, using a set of representative test cases belonging mainly to the domain of passive integrated components and interconnects.

Chapter 5 presents new research findings in the context of behavioral modeling of nonlinear systems. By inheriting model structures and algorithms from chapter 4, a new approach for generating surrogates of analog circuit blocks is discussed. The resulting models can seamlessly replace the underlying circuits in system-level small-signal analyses and

1. can be used under constant (Sec. 5.1.2) or non-stationary (Sec. 5.2) operating conditions, guaranteeing the stability of the dynamics in both cases;

2. are generated via robust and automated multivariate rational fitting algorithms;

3. are characterized by a compact model structure that can be represented either as a set of linear differential equations with time-varying coefficients or as an equivalent SPICE netlist.

Thanks to the above features, the proposed models are expected to be reliable and robust in any system-level simulation. Our results document up to 100× speed-up in the runtime of complex simulations characterized by time-varying operating conditions. This performance is documented in Sec. 5.3.

Keeping the focus on the approximation nonlinear systems local dynamics, Chapter 6 introduces a novel macromodeling scheme specifically designed to perform real-time data-driven model order reduction. The proposed approach allows to generate macromodels based on time domain input-output data obtained via real-time monitoring. The considered modeling setting proves to be useful for applications in which the underlying system can be observed but not directly controlled. This situation occurs in a number of scenarios of practical interest, belonging e.g. to the domains of of power systems modeling and even computational haemodynamics. These applications will be discussed in Sec. 6.2.

Finally, Chapter 7 draws the conclusions and discusses some of the open problems and challenges that may drive future research efforts.

Chapter 2

Background

This chapter provides a summary of the main theoretical background that supports the developments in this thesis. First, the basic definitions of the convex optimization problems involved in the macromodeling procedures presented in Chapters 4, 5 are presented. Then, a brief overview of the mathematical representations used to describe the dynamical systems of interest is given, together with a characterization of stability and passivity. Additionally, a discussion about the immittance and scattering representations for electrical multiports is provided.

All the statements and the definitions provided in this Chapter are classical and well-established in the fields of systems theory, optimization, and macromodeling. The presentation will thus include a minimum level of details, and all results will be stated without proofs.

2.1 Elements of convex optimization problems and LMIs

This section provides some concepts related to mathematical optimization, that are needed for successive derivations. A prototype optimization problem is introduced in a general setting; then the focus is moved to convex programs and, in particular, to the classes of convex programs that are of interest for the presented research, namely least-squares problems and semi-definite programs. An extensive presentation of these topics is available in [16], [26]

2.1.1 Optimization problems and convex programs

Consider a generic optimization problem with decision variables $x \in \mathbb{R}^n$, objective function $f_0(x) : \mathcal{D} \subseteq \mathbb{R}^n \to \mathbb{R}$ and feasible set $\mathcal{X} \subseteq \mathcal{D}$

$$\min_{x \in \mathcal{X}} f_0(x); \tag{2.1}$$

The problem is said to be *feasible* if $\mathcal{X}$ is non-empty, *infeasible* otherwise. The optimal value $p^\star$ for problem (2.1) is defined as

$$p^\star = \inf\{f_0(x),\ x \in \mathcal{X}\}. \tag{2.2}$$

When a point $x^\star$ is feasible and $f_0(x^\star) = p^\star$, then $x^\star$ is an optimal point, which solves problem (2.1). Optimal points may be non-unique; the set of all the optimal points is the *optimal set*

$$X_{\text{opt}} = \{x : x \in \mathcal{X},\ f_0(x) = p^\star\}. \tag{2.3}$$

A feasible point x is *locally optimal* if there exists $R > 0$ such that

$$f_0(x) = \inf\{f_0(z) : z \in \mathcal{X},\ ||z - x||_2 < R\}. \tag{2.4}$$

Problem (2.1) is a *convex optimization problem* whenever $f_0(x)$ is a convex function and $\mathcal{X}$ is a convex set, according to the following definitions.

Definition 2.1. *A set $\mathcal{X}$ is convex if for any z,y $\in \mathcal{X}$ and any $0 \leq \alpha \leq 1$ it holds*

$$\alpha z + (1 - \alpha)y \in \mathcal{X}. \tag{2.5}$$

Definition 2.2. *A function $f : \mathcal{D} \to \mathbb{R}$ is convex if $\mathcal{D}$ is a convex set and $\forall\, z,\ y \in \mathcal{D}$, $0 \leq \alpha \leq 1$ it holds*

$$f(\alpha z + (1 - \alpha)y) \leq \alpha f(z) + (1 - \alpha)f(y). \tag{2.6}$$

In this dissertation, we will consider only convex sets with elements belonging to finite dimensional vector-spaces.

In most applications, the feasible set $\mathcal{X}$ can be expressed in terms of explicit constraints, leading to the standard form of a convex optimization problem

$$\begin{aligned} &\min_x f_0(x), \\ &\quad \text{subject to} \\ &\quad f_i(x) \leq 0, \quad i = 1,2,\ldots,m \\ &\quad w_j^\top x = b_j \quad j = 1,2,\ldots,p \end{aligned} \tag{2.7}$$

where all the functions f_i are convex and the equality constraints are affine in the decision variables. The interest for convex optimization problems stems from two facts; first, every locally optimal point for problem (2.7) is also globally optimal. Second, efficient numerical methods are available to determine a globally optimal solution of a convex optimization problem in polynomial time. See [16] for an overview. Thus, once a problem is formulated in a convex fashion, it can be considered as numerically solvable. The same desirable properties do not hold for problems like (2.1) in which either $f_0(x)$ or $\mathcal{X}$ are not convex.

The techniques developed in this dissertation are based on the solution of convex optimization problems in which the cost function is quadratic and the feasible set is described in terms of Linear Matrix Inequalities (LMI). In this case, the convex optimization problem can be cast into a *semi-definite program* (SDP); the following sections recall the basic notions that are necessary to define the problem of interest.

2.1.2 Least-squares and quadratic programs

The *least-squares* problem is an unconstrained optimization problem with objective function defined as:

$$f_0(x) = ||Ax - b||_2^2 = \sum_{i=1}^{k} (a_i^\top x - b_i)^2, \tag{2.8}$$

being each a_i a row of the matrix $A \in \mathbb{R}^{k \times n}$ with $k \geq n$, and b_i one element of the vector $b \in \mathbb{R}^n$. We assume in the following that A is full column rank.

The (unique) optimal point of the least-squares problem can in principle be found analytically as by means of the pseudo-inverse matrix; the numerical solution of a least-squares problem exhibits in general a time complexity proportional to $n^2 k$. However, it is customary to apply ad-hoc problem transformations or simplifications based on the sparsity pattern of the matrix A in order to reduce such complexity in case the dimensions of the problem are huge. An example of this kind will be given in Sec 3.2.1.

A particular case occurs when $b = 0$, so that

$$f_0(x) = ||Ax||_2^2. \tag{2.9}$$

In this case the least-squares is said to be *homogeneous* and it must be usually solved by ruling out the trivial solution $x = 0$. For instance, this can be done by introducing the (non-convex) constraint $||x||_2 = 1$. The solution of the homogeneous least-square subject to this constraints can be obtained based on the singular value decomposition

$$A = U \Sigma V^\top. \tag{2.10}$$

The optimal solution is $x^\star = v_n$, being v_n the last column of V, i.e. the right singular vector associated with the least singular value of A.

Least-squares problems are special instances of the more general class of convex programs involving quadratic cost functions; this can be verified by recalling that

$$f_0(x) = x^\top P x + q^\top x + r \tag{2.11}$$

with $P \in \mathcal{S}_+^n$ is a convex quadratic function and that

$$||Ax - b||_2^2 = x^\top A^\top A x - 2 b^\top A x + b^\top b \tag{2.12}$$

belongs to this class of functions, as $A^\top A \in \mathcal{S}^n_+$.

When the least-squares problem is subject to some constraints on the decision variables, then no closed-form solutions are available, and the problem must be solved numerically. According to definition (2.7), when each $f_i(x)$ is an affine function of the decision variables, the convex optimization problem is called *quadratic program*. When instead the functions $f_i(x)$ are all convex quadratic like (2.11), then the problem falls into the class of the *quadratically constrained quadratic programs*.

2.1.3 Linear matrix inequalities and semidefinite programs

Consider an affine matrix function $F : \mathbb{R}^n \to \mathcal{S}^k$ of the form

$$F(x) = F_0 + \sum_{i=1}^{n} x_i F_i \tag{2.13}$$

with symmetric matrix coefficients, $F_i \in \mathcal{S}^k$, $i = 0,1,\ldots,n$. A *linear matrix inequality* in standard form is a constraint on the variables $x \in \mathbb{R}^n$ which enforces the following condition

$$F_0 + \sum_{i=1}^{n} x_i F_i \succeq 0. \tag{2.14}$$

This constraint requires that $F(x)$ is a positive semi-definite matrix, with nonnegative eigenvalues. The set of all the admissible values

$$\mathcal{X} = \{x \in \mathbb{R}^n : F(x) \succeq 0\} \tag{2.15}$$

is a convex set. Indeed, $F(x)$ is positive semi-definite if and only if $y^\top F(x) y \geq 0$, $\forall y \in \mathbb{R}^k$; by expanding this condition one obtains

$$y^\top F(x) y = y^\top F_0 y + x_i \sum_{i=1}^{n} y^\top F_i y = b(y) + a(y)^\top x \geq 0; \tag{2.16}$$

for a given vector y, the above condition reduces to an affine inequality, which describes an half-space in $\mathbb{R}^n$. As the half-space is parameterized by y, the set (2.15) can be interpreted as the intersection of an infinity of half-spaces, which is convex. The feasible set $\mathcal{X}$ of an LMI is also referred to as *spectrahedron*.

Another description of the feasible set $\mathcal{X}$ can be given explicitly in terms of polynomial inequalities. It is known that $F(x)$ is positive semi-definite if and only if all the associated principal minors are non-negative. As each principal minor of order j is a polynomial $g_j(x)$ of order j, the spectrahedron can be equivalently rewritten as

$$\mathcal{X} = \{x \in \mathbb{R}^n : g_j(x) \geq 0,\ j = 1,\ldots,k\}. \tag{2.17}$$

The above description shows that, in terms of the standard convex problem formulation (2.7), enforcing a LMI condition means that the functions $f_i(x),\ i = 1,2,\dots,m$ involved in the constraints definition are polynomials of degree at most k.

Of course, even if the standard form of a LMI requires the positive semidefiniteness of $F(x)$, the condition $F(x) \preceq 0$ is still an LMI, obtained from the standard form by simply inverting the sign of all the involved matrix coefficients. Additionally, enforcing two linear matrix inequalities at the same time is equivalent to enforcing one single LMI of larger size. For two affine matrix functions of arbitrary dimensions, $F_1(x),\ F_2(x)$ the following relation holds

$$F_1(x) \succeq 0,\ F_2(x) \succeq 0 \iff \begin{bmatrix} F_1(x) & 0 \\ 0 & F_2(x) \end{bmatrix} \succeq 0, \tag{2.18}$$

as the eigenvalues of a block-diagonal matrix are the union of the eigenvalues of the diagonal blocks. This fact can be extended to handle an arbitrary number of LMIs.

It is customary to express an LMI in terms of matrix variables in place of the vector variables x. Consider the following condition enforced on the unknown matrix $P \in \mathcal{S}^n$, being $A \in \mathbb{R}^{k\times k}$ a known coefficient matrix

$$G(P) = A^\top P + PA + \mathbb{I}_k \succeq 0. \tag{2.19}$$

Defining $e_i \in \mathbb{R}^k$ as the i-th component of the canonical basis, P is rewritten as

$$P = \sum_{i=1}^{k}\sum_{j=1}^{k} p_{i,j} e_i e_j^\top, \quad p_{i,j} = p_{j,i} \tag{2.20}$$

Plugging the above into (2.19) shows that the matrix inequality can be expressed in standard form with scalar variables $p_{i,j}$ and matrix coefficients $A^\top(e_ie_j^\top)+(e_ie_j^\top)^\top A$, $i,j = 1,\dots,k$.

We will make use of the following result, which is a consequence of the *Schur complement*. Consider the symmetric block matrix

$$X = \begin{bmatrix} A & B \\ B^\top & C \end{bmatrix}, \tag{2.21}$$

then if $C \prec 0$ the following implication holds

$$X \preceq 0 \iff A - BC^{-1}B^\top \preceq 0. \tag{2.22}$$

A *semidefinite program* (SDP) in standard form is a convex optimization problem with variables $x \in \mathbb{R}^n$, linear objective function and LMI constraint

$$\begin{aligned} &\min_x c^\top x \\ &\text{subject to} \\ &F(x) \succeq 0. \end{aligned} \tag{2.23}$$

It can be shown that affine inequalities and (convex) quadratic inequalities, admit an equivalent representation in terms of suitable LMIs, so that this kind of constraints represent a very general way to describe convex feasible sets. Imposing the linearity of the cost function does not represent a limitation for the class of problems that can be represented as a SDP in standard form. For instance, consider the convex optimization problem

$$\begin{aligned} &\min_{x} ||Ax - b||_2 \\ &\text{subject to} \\ &F(x) \succeq 0, \end{aligned} \tag{2.24}$$

The problem can be rewritten in the following equivalent *epigraph* form by introducing the auxiliary variable $t \in \mathbb{R}$

$$\begin{aligned} &\min_{x,t} t \\ &\text{subject to} \\ &||Ax - b||_2 \leq t \\ &F(x) \succeq 0, \end{aligned} \tag{2.25}$$

where the new objective is linear and a *second order cone* constraint is introduced. This latter admits a LMI representation[1], since

$$||Ax - b||_2 \leq t \iff \begin{bmatrix} t\mathrm{I} & Ax - b \\ (Ax - b)^\top & t \end{bmatrix} \succeq 0. \tag{2.26}$$

Semidefinite programs can be solved in polynomial time by means of suitable interior point algorithms [3], that are nowadays implemented in most off-the-shelf convex optimization solvers.

2.2 Dynamical system representations

This section recalls the notions of state space representations for the classes of dynamical systems that are of interest for this dissertation. The definition of equilibrium points and system linearization are outlined. For linear time invariant systems, the concepts of transfer function and impulse response are revised with the required level of detail. For further discussions the reader is referred to [65], [9], [51], [24]

[1]From a practical perspective, translating a second order cone constraint into a LMI is often computationally inconvenient. This transformation is reported only to show how the reference problem admits the standard SDP formulation

2.2.1 Non-linear systems

The state space representation is a powerful tool that allows to describe mathematically a dynamical system governed by ordinary differential equations. When the state space model is employed to explain the time domain evolution of a dynamical system, it is assumed that the relevant quantities that determine the system evolution can be grouped in 3 sets that retain qualitatively different interpretations, namely the system input, output, and internal state.

In its most general formulation, a state space representation for a system of dynamical order (i.e. number of involved differential equations) N is

$$\begin{aligned} \dot{x}(t) &= F(x(t), u(t), t), \\ y(t) &= G(x(t), u(t), t); \end{aligned} \tag{2.27}$$

where $x(t) \in \mathbb{R}^{\mathrm{N}}$ is the state vector, $u(t) \in \mathbb{R}^{\mathrm{Q}}$ is the input vector (also referred to as control) and $y(t) \in \mathbb{R}^{\mathrm{P}}$ is the output vector. F and G are generic non-linear maps, that in the context of this dissertation will be assumed to be C^1 differentiable.

In (2.27), it is assumed that the maps F and G are time-dependent, so that the above state space formulation is suitable to represent any *non-linear, time-varying* dynamical system that evolves according to a N-th order system of differential equations.

When the mapping induced by F and G does not change in time, then the underlying dynamical system is *time-invariant*; in such a case, the state space simplifies to

$$\begin{aligned} \dot{x}(t) &= F(x(t), u(t)), \\ y(t) &= G(x(t), u(t)). \end{aligned} \tag{2.28}$$

According to the state space representation (2.28), at each time instant, the evolution of both the system internal states and output variables, are univocally determined by the instantaneous values of the internal states $x(t)$ and of the input $u(t)$, through the mappings induced by F and G respectively.

The explicit dependency of the system behavior on the state vector allows to model its time domain evolution by explicitly taking into account arbitrary initial conditions, which must be specified in order to derive a well-defined and unique solution for (2.27), (2.28). However, computing in such solutions is generally not possible, and the task must be tackled by means of numerical techniques. Nonetheless, qualitative properties of the involved differential equations can be studied by means of classical system theory approaches. In this thesis, the discussion about qualitative properties concerning non-linear systems will be limited to the concept of equilibrium points and passivity; the first is introduced in the following, while the second is treated in Sec. 2.3.2.

Equilibrium points and stability

Consider system (2.28) with constant control $u(t) = U_0$ for $t \geq 0$ and initial state $x(0) = X_e$. The dynamic equations in this case read

$$\dot{x}(t) = F(x(t), U_0), \quad x(0) = X_e. \tag{2.29}$$

An equilibrium point is defined as follows.

Definition 2.3. *The state X_e is an equilibrium point for (2.29) if $x(t) = X_e \, \forall t > 0$, or equivalently, if $F(X_e, U_0) = 0$.*

It is of interest to study the effects induced on the system evolution by small perturbations of the equilibrium configuration. This leads to the following characterization of equilibrium points, that is due to Lyapunov.

Definition 2.4. *An equilibrium point X_e is stable if*

$$\forall \epsilon, \, \exists \delta(\epsilon) : ||X_e - x(0)|| < \delta(\epsilon) \Rightarrow ||X_e - x(t)|| \leq \epsilon, \, \forall t > 0, \tag{2.30}$$

being $|| \cdot ||$ any norm in $\mathbb{R}^{\mathrm{N}}$.

In words, the equilibrium point is stable if it is possible to bound the trajectory of the states $x(t)$ arbitrarily close to X_e by choosing a suitably close perturbed initial condition. An equilibrium point is unstable if it is not stable.

Stable equilibrium points may be further characterized by the following asymptotic stability property

Definition 2.5. *A stable equilibrium point X_e is asymptotically stable if it holds that*

$$\exists \delta_a : ||X_e - x(0)|| < \delta_a \Rightarrow \lim_{t \to \infty} ||X_e - x(t)|| = 0 \tag{2.31}$$

Asymptotic stability guarantees that all the state trajectories starting from a prescribed neighborhood of X_e will converge to this equilibrium point given a sufficient time horizon.

When the convergence to the equilibrium is exponential, we have the following particular definition

Definition 2.6. *An equilibrium point X_e is exponentially stable if there exist positive scalars α, λ, c such that:*

$$||x(t) - X_e|| \leq \alpha ||x(0) - X_e|| e^{-\lambda t}, \qquad \forall t > 0, \, \forall ||x(0) - X_e|| < c \tag{2.32}$$

Stability, asymptotic stability and exponential stability are all *local* properties, as they are defined upon a given neighborhood of X_e inside which the attraction to the equilibrium takes place. Such neighborhood is commonly referred to as *domain of attraction*. When the domain of attraction of an asymptotically (exponentially) stable equilibrium point is the whole space $\mathbb{R}^{\mathrm{N}}$, then this point is additionally qualified as *globally* asymptotically (exponentially) stable equilibrium point. If an equilibrium point is global, then it must be the only equilibrium point for system (2.28)

2.2.2 Linear-time-invariant systems

A special case occurs when the maps F and G in (2.28) are linear in both the state and input vector; in such a case, the dynamical system under study is classified as Linear Time-Invariant (LTI) and the state space equations read

$$\begin{aligned} \dot{x}(t) &= Ax(t) + Bu(t), \quad x(0) = x_0 \\ y(t) &= Cx(t) + Du(t). \end{aligned} \tag{2.33}$$

When the initial conditions are not of interest, the above state space will be represented by the following compact notation

$$\Sigma = \left(\begin{array}{c|c} A & B \\ \hline C & D \end{array} \right). \tag{2.34}$$

Systems like (2.33) are of paramount importance and represent the starting point for most of the topics treated in this dissertation. In what follows, some properties of interest concerning linear state space systems are given.

As opposed to (2.28), a closed form expression is available to compute the solution of (2.33); at a given time $t \geq 0$, the state configuration $x(t)$ can be obtained by means of the formula

$$x(t) = \Phi(t,0)x(0) + \int_0^t \Phi(t,\tau)Bu(\tau)d\tau, \quad \Phi(t,\tau) = e^{A(t-\tau)}. \tag{2.35}$$

In the above, the first term of the sum is called *zero-input response* and represents the free evolution that the system would exhibit due to non-vanishing initial conditions, in absence of external control; the second term is the *zero-state response*, and takes into account the effect of the input on the system dynamics.

For a given LTI system there exist infinitely many state space realizations that are equivalent from an input-output standpoint. To see this, consider the change of variables $\hat{x}(t) = Tx(t)$, being T an invertible linear transformation. Then, simple algebraic manipulations show that the input-output relation induced by state Σ is preserved under the following change of representation of the state space matrices

$$\Sigma \simeq \hat{\Sigma} = \left(\begin{array}{c|c} TAT^{-1} & TB \\ \hline CT^{-1} & D \end{array} \right); \tag{2.36}$$

Additionally, all the structural properties of (2.33) are preserved under this change of representation, which is called *similarity transformation*.

Under the assumption of invertibility of the matrix D, a state space Σ_2 obtained from Σ_1 by exchanging the roles of input and output, i.e. by setting $y_2(t) = u(t)$ and $u_2(t) = y(t)$, is commonly referred to as *inverse* state space, and is defined as

$$\Sigma_2 = \left(\begin{array}{c|c} A - BD^{-1}C & -BD^{-1} \\ \hline D^{-1}C & D^{-1} \end{array} \right). \tag{2.37}$$

For LTI systems, all the information required to characterize the equilibrium points can be inferred from the matrix A, or equivalently, by the properties of the zero-input response. Consider the dynamic equations entering (2.33) and a generic equilibrium point X_e associated with the constant input $u(t) = U_0$. Recalling the definition of stable equilibrium point, we have that X_e is stable if

$$\forall \epsilon, \exists \delta(\epsilon) : ||X_e - x_0|| < \delta(\epsilon) \Rightarrow ||X_e - x(t)|| \leq \epsilon, \forall t > 0, \quad x_0 = x(0), \tag{2.38}$$

Where x_0 is a perturbed initial condition. By defining

$$\delta x(t) = x(t) - X_e, \quad \delta x_0 = x_0 - X_e \tag{2.39}$$

condition (2.38) is rewritten as:

$$\forall \epsilon, \exists \delta(\epsilon) : \delta x_0 < \delta(\epsilon) \Rightarrow ||\delta x(t)|| \leq \epsilon, \forall t > 0. \tag{2.40}$$

Consider then the dynamic equations of (2.33) with the two different initial conditions

$$\dot{x}_e(t) = Ax_e(t) + BU_0, \quad x(0) = X_e \tag{2.41}$$
$$\dot{x}(t) = Ax(t) + BU_0, \quad x(0) = x_0 \tag{2.42}$$

Due to the definition of equilibrium, in (2.41) it holds $\dot{x}_e(t) = 0$, $x_e(t) = X_e \, \forall t \geq 0$; by subtracting (2.42) from (2.41), the following is obtained

$$\dot{\delta x}(t) = A\delta x(t), \quad \delta x(0) = \delta x_0. \tag{2.43}$$

The above shows that the evolution of the deviation from the equilibrium, $\delta x(t)$, is uniquely determined by the zero-input response of the autonomous system (2.43), through the matrix A. By studying the properties of the zero-input response, one can derive conclusions about the properties of the equilibrium point. Neither the choice of the input nor the matrix B play any role in assessing the stability of a LTI system. The following theorems are of interest

Theorem 2.1. *If system* (2.43) *admits multiple equilibrium points, all of them are either stable or unstable.*

Theorem 2.2. *For system* (2.43) *only the state configuration* $\delta x = 0$ *can be asymptotically stable, and only when other equilibrium points do not exist. Additionally, if* $\delta x = 0$ *is asymptotically stable, then it is also globally exponentially stable.*

The above theorems allow to state that stability of (2.33) is not a property of a specific state configuration, but of the whole system, which can be defined as stable, exponentially stable, or unstable. The stability assessment is based solely on the study of the algebraic properties of the matrix A. Different practical approaches are

available to perform this assessment; those that are of interest for the derivations of this thesis will be reported in Sec. 2.3.1.

Beyond stability, the structural properties of observability and controllability of (2.33) will be needed. The pair (A, C) is said to be *observable* if for any time $t_1 > t_0$ the value of the state $x(t_0)$ can be determined from the knowledge of the input $u(t)$ and of the output $y(t)$ in the time interval $[t_0, t_1]$. It is proved that (A, C) is observable if and only if the observability matrix

$$\mathcal{O} = \begin{bmatrix} C \\ CA \\ CA^2 \\ \dots \\ CA^{\mathrm{N}-1} \end{bmatrix} \tag{2.44}$$

is full column rank, i.e. $\mathrm{Rank}(\mathcal{O}) = \mathrm{N}$.

Analogously the pair (A, B) is said to be *controllable* if for any initial state $x(t_0)$, time instant $t_1 > t_0$, and target state x_T, there exists an input signal $u(t)$ such that $x(t_1) = x_T$. Also in this case, it is proved that (A, B) is controllable if and only if the controllability matrix

$$\mathcal{C} = \begin{bmatrix} B & BA & BA^2 & \dots & BA^{\mathrm{N}-1} \end{bmatrix} \tag{2.45}$$

is full row rank, i.e. $\mathrm{Rank}(\mathcal{C}^\top) = \mathrm{N}$.

When the pairs (A, C) and (A, B) are respectively observable and controllable, then the state space (2.33) is *minimal*, in the sense that the number of states N is the least possible to recover the input-output relation of the dynamical system.

The concept of linear state space can be generalized to the case in which some of the state variables are constrained by algebraic equations; in such a case, the LTI dynamical system can be described by a set of *differential algebraic equations* (DAE), by means of the following *descriptor* system

$$\begin{aligned} E\dot{x}(t) &= Ax(t) + Bu(t) \quad x(0) = x_0 \\ y(t) &= Cx(t) + Du(t). \end{aligned} \tag{2.46}$$

Whenever $\mathrm{Rank}(E) = \mathrm{N}$, the descriptor system (2.46) is equivalent to the standard state space (2.33); conversely, when E is singular the actual state variables involved in the dynamics of (2.46) are less then N, and the vector $x(t)$ represents a set of *generalized state variables*.

2.2.3 Linearization

Consider the nonlinear system (2.28) and an equilibrium point defined by the state vector X_0 and the constant input vector U_0. The corresponding system output

is constant and equal to $Y_0 = G(X_0, U_0)$. When one is interested at describing the evolution of the state and output vectors of the nonlinear system in proximity of this equilibrium, a first order approximation of the maps F, G, can be derived to obtain a *local* description of the system behavior.

The local behavior can be characterized by defining two perturbation signals $\tilde{x}(t)$, $\tilde{u}(t)$ as follows

$$\tilde{x}(t) = x(t) - X_0, \quad \tilde{u}(t) = u(t) - U_0; \tag{2.47}$$

these two signals represent the instantaneous deviations of the state and input vectors from the constant equilibrium point configuration (X_0, U_0). Accordingly, the system output can be expressed as

$$y(t) = Y_0 + \tilde{y}(t), \tag{2.48}$$

where $\tilde{y}(t)$ represents the output perturbation induced by $\tilde{u}(t)$.

Adopting these signal representations, the dynamic equations of (2.28) read

$$\dot{\tilde{x}}(t) = F(\tilde{x}(t) + X_0, \tilde{u}(t) + U_0). \tag{2.49}$$

A first-order approximation of the above (exact) expression can be performed around the equilibrium point. By expressing (2.49) in terms of a first-order Taylor expansion we obtain

$$\dot{\tilde{x}}(t) \approx F(X_0, U_0) + \frac{\partial F}{\partial x}\Big|_{\substack{x=X_0 \\ u=U_0}} \tilde{x}(t) + \frac{\partial F}{\partial u}\Big|_{\substack{x=X_0 \\ u=U_0}} \tilde{u}(t), \tag{2.50}$$

where by definition we have $F(X_0, U_0) = 0$. By defining the matrices of partial derivatives as

$$A = \frac{\partial F}{\partial x}\Big|_{\substack{x=X_0 \\ u=U_0}}, \quad B = \frac{\partial F}{\partial u}\Big|_{\substack{x=X_0 \\ u=U_0}} \tag{2.51}$$

one obtains the linear system

$$\dot{\tilde{x}}(t) \approx A\tilde{x}(t) + B\tilde{u}(t) \tag{2.52}$$

which represents the *Jacobian Linearization* of (2.28) around the equilibrium (X_0, U_0). For sufficiently small deviations from this equilibrium, equations (2.52) approximate the relationship between the deviation variables $\tilde{x}(t)$, $\tilde{u}(t)$.

Applying the same approximation procedure to the output equation leads to the state space that explains the relation between the signals $\tilde{x}(t)$, $\tilde{u}(t)$ and $\tilde{y}(t)$

$$\begin{aligned} \dot{\tilde{x}}(t) &\approx A\tilde{x}(t) + B\tilde{u}(t) \\ \tilde{y}(t) &\approx C\tilde{x}(t) + D\tilde{u}(t), \end{aligned} \tag{2.53}$$

where the matrices C and D are defined as

$$C = \frac{\partial G}{\partial x}\Big|_{\substack{x=X_0\\u=U_0}}, \quad D = \frac{\partial G}{\partial u}\Big|_{\substack{x=X_0\\u=U_0}}. \tag{2.54}$$

As state space (2.53) represents an approximation for the dynamics of (2.28), which is valid for small deviations around the equilibrium, it is commonly referred to as *small signal* model for the reference system in correspondence of the operating point defined by the triplet (X_0, U_0, Y_0).

2.2.4 Uncertain and parameter varying linear systems

When the linear state space equations (2.33) depend on a set of external physical or mathematical parameters, whose value is constant in time but unknown apriori, the resulting LTI system is said to be *uncertain*. Consider a vector of parameters $\boldsymbol{\vartheta} \in \mathbb{R}^d$; in the following it is assumed that $\boldsymbol{\vartheta}$ can attain values within the compact set

$$\Theta = [\underline{\vartheta}_1, \overline{\vartheta}_1,] \times \ldots \times [\underline{\vartheta}_d, \overline{\vartheta}_d], \tag{2.55}$$

where $\underline{\vartheta}_i$ and $\overline{\vartheta}_i$ represent respectively the minimum and the maximum value of each individual parameter. An uncertain LTI state space system depending on $\boldsymbol{\vartheta}$ has the form

$$\begin{aligned} \dot{x}(t) &= A(\boldsymbol{\vartheta})x(t) + B(\boldsymbol{\vartheta})u(t), \quad x(0) = x_0 \\ y(t) &= C(\boldsymbol{\vartheta})x(t) + D(\boldsymbol{\vartheta})u(t). \end{aligned} \tag{2.56}$$

In the above system, the value of the parameter is not allowed to vary with time, so that for each possible instance of $\boldsymbol{\vartheta}$, the resulting state space equations are linear and time invariant.

A more complex situation occurs when the parameter vector is a function of time, $\boldsymbol{\vartheta}(t) : \mathbb{R}_{\geq 0} \to \Theta$. In such a case, we have a *linear parameter varying* (LPV) system

$$\begin{aligned} \dot{x}(t) &= A(\boldsymbol{\vartheta}(t))x(t) + B(\boldsymbol{\vartheta}(t))u(t), \quad x(0) = x_0 \\ y(t) &= C(\boldsymbol{\vartheta}(t))x(t) + D(\boldsymbol{\vartheta}(t))u(t). \end{aligned} \tag{2.57}$$

Linear parameter varying systems are a particular case of *linear time-varying* systems, in which the time dependency is indirectly induced by the value of the vector function $\boldsymbol{\vartheta}(t)$. For the developments of this thesis, the discussion will be limited to uncertain or LPV systems with P = Q, i.e. square systems with the same number of inputs and outputs.

Linear systems depending on external parameters will be also described in terms of the descriptor system

$$\begin{aligned} E\dot{x}(t) &= A(\boldsymbol{\vartheta})x(t) + B(\boldsymbol{\vartheta})u(t) \\ y(t) &= C(\boldsymbol{\vartheta})x(t) \end{aligned}. \tag{2.58}$$

The derivations of this work will consider a particular structure for the matrices involved in the above descriptor, in which

$$\begin{aligned} E &= \begin{bmatrix} \mathbb{I}_{\mathrm{N}} & 0 \\ 0 & 0 \end{bmatrix} & A(\boldsymbol{\vartheta}) &= \begin{bmatrix} A_2 & B_2 \\ C_2(\boldsymbol{\vartheta}) & D_2(\boldsymbol{\vartheta}) \end{bmatrix} \\ B &= \begin{bmatrix} 0 \\ -\mathbb{I}_{\mathrm{P}} \end{bmatrix} & C(\boldsymbol{\vartheta}) &= \begin{bmatrix} C_1(\boldsymbol{\vartheta}) & D_1(\boldsymbol{\vartheta}) \end{bmatrix} \end{aligned}. \tag{2.59}$$

The descriptor system (2.58) with matrices defined as in (2.59) is commonly used to represent parameterized behavioral models [103], and will be exploited for the derivations of Chapter 5.

Under the assumption that $D_2(\boldsymbol{\vartheta})$ is nonsingular $\forall \boldsymbol{\vartheta} \in \Theta$, straightforward algebraic manipulations show that the descriptor (2.58) is equivalent to the state space

$$\Sigma = \left(\begin{array}{c|c} A_2 - B_2 D_2(\boldsymbol{\vartheta})^{-1} C_2(\boldsymbol{\vartheta}) & B_2 D_2(\boldsymbol{\vartheta})^{-1} \\ \hline C_1(\boldsymbol{\vartheta}) - D_1(\boldsymbol{\vartheta}) D_2(\boldsymbol{\vartheta})^{-1} C_2(\boldsymbol{\vartheta}) & D_1(\boldsymbol{\vartheta}) D_2(\boldsymbol{\vartheta})^{-1} \end{array} \right). \tag{2.60}$$

2.2.5 Frequency domain description of LTI systems and the impulse response

The state space representation provides an explanation for the input-output behavior of a dynamical system in terms of the state vector, and is therefore commonly referred to as *internal*.

For LTI systems, the concept of *transfer function* provides a tool to characterize the system behavior only in terms of the *external* signals, i.e. the input and the output. By means of the transfer function, the behavior of the system is explained in terms of an algebraic relation relating the Laplace domain representation of the input and the output signals. Taking the Laplace transform of the state space equations (2.33) for vanishing initial conditions gives

$$sX(s) = AX(s) + BU(s) \tag{2.61}$$

$$Y(s) = CX(s) + DU(s). \tag{2.62}$$

From the above, the following purely algebraic relations between the states, the input, and the output can be derived:

$$X(s) = (s\mathbb{I}_{\mathrm{N}} - A)^{-1} BU(s), \quad Y(s) = \mathsf{H}(s)U(s), \tag{2.63}$$

where

$$\mathsf{H}(s) = C(s\mathbb{I}_{\mathrm{N}} - A)^{-1} B + D \in \mathbb{C}^{\mathrm{P} \times \mathrm{Q}} \tag{2.64}$$

is the transfer function of the underlying LTI system. As the transfer function is derived by imposing vanishing initial conditions on the state vector for $t = 0$, it is

suitable to describe only the output contribution of the zero-state response of the system. When the transfer function representation is adopted, the knowledge of the state vector is not required. As a consequence, even if the LTI system behavior admits an infinity of equivalent state space representations, the associated transfer function is unique.

The transfer function (2.64) is always a rational function of the complex variable s with individual elements

$$\mathsf{H}_{i,j}(s) = \frac{N_{i,j}(s)}{D(s)}, \tag{2.65}$$

where the numerator and the denominator are polynomials of degree at most N. The denominator is common to all of the transfer function elements, as $D(s) = |s\mathbb{I} - A|$. Each of these elements can be therefore rewritten (dropping the i, j subscripts) as

$$\mathsf{H}(s) = \frac{a_M s^M + a_{M-1} s^{M-1} + ... + a_0}{b_N s^N + b_{N-1} s^{N-1} + ... + b_0}. \tag{2.66}$$

When it holds $M \leq N$, then the transfer function is *proper*. Other representations are available for $\mathsf{H}(s)$. The pole-zero form reads

$$\mathsf{H}(s) = k \frac{\prod_{m=1}^{M}(s - z_m)}{\prod_{n=1}^{N}(s - q_n)} \tag{2.67}$$

where the numbers z_m are the transfer function *zeros*, while the q_n are the transfer function *poles*. In case of matrix transfer functions, all the i, j elements of $\mathsf{H}(s)$ in (2.65) share the same set of common poles, as they represent the values of s for which $D(s)$ vanishes.

It is known that the set of admissible poles for a transfer function coincide with the eigenvalues of the state space matrix A, which remain the same under any similarity transformation. However, the pole-zero form (2.67) highlights the fact that, in case a pole is equal to one zero, a cancellation may take place, thus reducing the actual degree of the transfer function; as a result, some eigenvalues of A may be not poles of some transfer matrix elements.

The pole-residues form is another possible representation of $\mathsf{H}(s)$ which will be extensively exploited in the following. The general, assuming simple poles, form is

$$\mathsf{H}(s) = R_0 + \sum_{n=1}^{N} \frac{R_n}{s - q_n}, \quad R_i \in \mathbb{C}^{\mathrm{P}\times\mathrm{Q}}, \quad i = 0,1,...,N \tag{2.68}$$

where the *residues* R_i are real when $q_i \in \mathbb{R}$; in case of complex conjugate poles $q_i = q_{i+1}^* \in \mathbb{C}$, then $R_i = R_{i+1}^*$.

Although transfer functions hide the internal description of the LTI system by implicitly taking into account the role of the states, it is useful to express the zero-input response of state space (2.33) in the Laplace domain, for non-vanishing initial

conditions. By setting $u(t) = 0$, $\forall t$, and considering the initial condition $x(0) = x_0$, the unilateral Laplace transform is applied to the state and output signals, in order to obtain the representation

$$sX(s) = AX(s) + x_0 \tag{2.69}$$
$$Y(s) = CX(s) \tag{2.70}$$

from which

$$X(s) = \mathscr{L}\{e^{At}x_0\} = (s\mathbb{I} - A)^{-1}x_0, \quad Y(s) = CX(s). \tag{2.71}$$

This shows that the zero-input response in the Laplace domain has the same rational structure of the transfer function of $\mathsf{H}(s)$. When the eigenvalues of A have simple multiplicity, then each j-th component of the state vector can be expressed in the Laplace domain in pole-residues form

$$X_j(s) = \sum_{i=1}^{\mathrm{N}} \frac{c_i^j}{s - q_i} \tag{2.72}$$

where q_i are the transfer function poles and c_i^j are constants.

Another mathematical tool suitable to characterize the external behavior of a linear time invariant system is the *impulse response*. As opposed to the transfer function, the impulse response describes the system evolution in the time domain.

The impulse response is a matrix function $h(t) : \mathbb{R} \to \mathbb{R}^{\mathrm{P}\times\mathrm{Q}}$, that links the signals $u(t)$ and $y(t)$ through the convolution integral

$$y(t) = h(t) * u(t) = \int_{-\infty}^{\infty} h(t - \tau)u(\tau)d\tau. \tag{2.73}$$

Assuming from now on that $u(t), h(t) = 0\ \forall t < 0$, the above reduces to

$$y(t) = h(t) * u(t) = \int_{0}^{t} h(t - \tau)u(\tau)d\tau, \tag{2.74}$$

and each output component is obtained as a superposition of the individual input effects

$$y_i(t) = \sum_{j=1}^{\mathrm{Q}} \int_0^t h_{i,j}(t - \tau)u_j(\tau)d\tau. \tag{2.75}$$

For a LTI system, the transfer function is the Laplace transform of the impulse response

$$\mathsf{H}(s) = \mathscr{L}\{h(t)\} = \int_0^t h(t)e^{-st}dt. \tag{2.76}$$

2.2.6 Multiport representations of electrical networks

Up to now, we considered the input and the output vectors of a dynamical system as generic physical quantities. When an electrical network is considered, inputs and outputs are defined based on currents and voltages.

Assuming that the network is represented as a P-port, then the most common definitions of inputs and outputs are based on the following *multiport representations*, that relate voltages and currents in the Laplace domain.

- *Impedance representation.* The P inputs are the port currents $I(s)$, the outputs are the port voltages $V(s)$, that are related by the law

$$V(s) = Z(s)I(s). \tag{2.77}$$

The network function $Z(s)$ is the *impedance matrix*, with elements defined as

$$\begin{aligned} Z_{ii}(s) &= \frac{V_i(s)}{I_i(s)}, \quad I_k(s) = 0, \forall k \neq i \\ Z_{ij}(s) &= \frac{V_i(s)}{I_j(s)}, \quad I_k(s) = 0, \forall k \neq j. \end{aligned} \tag{2.78}$$

- *Admittance representation.* The P inputs are the port voltages $V(s)$, the outputs are the port currents $I(s)$, that are related by the law

$$I(s) = Y(s)V(s). \tag{2.79}$$

The network function $Y(s)$ is the *admittance matrix*, with elements defined as

$$\begin{aligned} Y_{ii}(s) &= \frac{I_i(s)}{V_i(s)}, \quad V_k(s) = 0, \forall k \neq i \\ Y_{ij}(s) &= \frac{I_i(s)}{V_j(s)}, \quad V_k(s) = 0, \forall k \neq j. \end{aligned} \tag{2.80}$$

- *Scattering representation.* The input are the *incident* waves $A(s)$, the output are the *reflected waves* $B(s)$, defined as

$$\begin{aligned} A_k(s) &= \frac{1}{2\sqrt{Z_k}}(V_k(s) + Z_k I_k(s)), \quad k = 1,2,...,\mathrm{P} \\ B_k(s) &= \frac{1}{2\sqrt{Z_k}}(V_k(s) - Z_k I_k(s)), \quad k = 1,2,...,\mathrm{P}; \end{aligned} \tag{2.81}$$

where Z_k is the k-th port reference impedance. Here we assume $Z_k = 50\Omega$, $k = 1,2,\ldots \mathrm{P}$. The *scattering matrix* is the input-output transfer function relating the vector of the incident waves $A(s)$ with the vector or the reflected waves $B(S)$

$$B(s) = S(s)A(s) \tag{2.82}$$

with elements obtained as

$$\begin{aligned} S_{ii}(s) &= \frac{B_i(s)}{A_i(s)}, \quad A_k(s) = 0, \forall k \neq i \\ S_{ij}(s) &= \frac{B_i(s)}{A_j(s)}, \quad A_k(s) = 0, \forall k \neq j. \end{aligned} \tag{2.83}$$

Also, the *hybrid representation* will be considered in this work, and will be explicitly defined when necessary. When both the impedance and the admittance matrices exist, they are related by the equations

$$Y(s) = Z^{-1}(s), \quad Z(s) = Y^{-1}(s). \tag{2.84}$$

By defining a diagonal matrix collecting the reference impedances, $Z_{\text{ref}} = \text{Diag}(Z_1, \ldots, Z_{\text{P}})$, the scattering, impedance and admittance matrices are related as follow

$$\begin{aligned} S(s) &= [Z_{\text{ref}}^{-1/2} Z(s) Z_{\text{ref}}^{-1/2} + \mathbb{I}_{\text{P}}]^{-1} [Z_{\text{ref}}^{-1/2} Z(s) Z_{\text{ref}}^{-1/2} - \mathbb{I}_{\text{P}}] \\ S(s) &= [Z_{\text{ref}}^{1/2} Y(s) Z_{\text{ref}}^{1/2} + \mathbb{I}_{\text{P}}]^{-1} [\mathbb{I}_{\text{P}} + Z_{\text{ref}}^{1/2} Y(s) Z_{\text{ref}}^{1/2}] \\ Y(s) &= Z_{\text{ref}}^{-1/2} [\mathbb{I}_{\text{P}} - S(s)][\mathbb{I}_{\text{P}} + S(s)]^{-1} Z_{\text{ref}}^{-1/2} \\ Z(s) &= Z_{\text{ref}}^{1/2} [\mathbb{I}_{\text{P}} - S(s)]^{-1} [\mathbb{I}_{\text{P}} + S(s)] Z_{\text{ref}}^{1/2} \end{aligned} \tag{2.85}$$

The *instantaneous power* absorbed by a P-port network reads

$$p(t) = \sum_{k=1}^{\text{P}} v_k(t) i_k(t) = v(t)^\top i(t) = i(t)^\top v(t). \tag{2.86}$$

For immittance representations, this expression translates to

$$p(t) = u(t)^\top y(t) \tag{2.87}$$

while for scattering representations

$$p(t) = a(t)^\top a(t) - b(t)^\top b(t) = u(t)^\top u(t) - y(t)^\top y(t) \tag{2.88}$$

2.3 Stability and passivity

This section provides some characterization of the qualitative system behavior around its equilibrium points (stability), and introduces the concept of passivity. The proposed material is classical, more detailed discussions can be found in [65], [5], [94], [51].

2.3.1 Stability

A review of the basic concepts related to *internal stability* characterization of dynamical systems is given next. Internal stability is explicitly defined in terms of the system state vector, in compliance with the definitions given in Sec. 2.2. Historically, the foundation of the internal stability concepts is due to Lyapunov, who proved that, for a generic system of ODEs like (2.28), the characterization of the equilibrium points can be performed by studying the properties of energy functions related to the state configurations. According to the Lyapunov stability theory, an equilibrium point is stable if any state trajectory starting sufficiently close to it is such that the internal energy of the system is non-increasing in time. This concept is mathematically represented in terms of the so-called *Lyapunov functions*.

Consider the following scenario involving an autonomous (time-invariant) dynamical system, associated with an equilibrium point X_e

$$\dot{x} = F(x), \qquad F(X_e) = 0; \tag{2.89}$$

Let $V(x) : \mathbb{R}^{\mathrm{N}} \to \mathbb{R}$ be a scalar continuously differentiable function of the states, and let $\mathcal{B}(X_e, r) = \{x : ||x - X_e||_2 < r\}$ be a spherical neighborhood centered at the equilibrium state X_e. When the state configuration evolves in time, the function $V(x(t))$ can be interpreted as a continuously differentiable function of t, which evolves along the state trajectories according to

$$\dot{V}(x) = \frac{dV(x(t))}{dt} = \sum_{i=1}^{\mathrm{N}} = \frac{\partial V}{\partial x_i}\frac{\partial x_i}{\partial t} = \sum_{i=1}^{\mathrm{N}} \frac{\partial V}{\partial x_i} F_i(x(t)) \tag{2.90}$$

The following two theorems, proved by Lyapunov, are of interest.

Theorem 2.3. *The equilibrium point X_e of (2.89) is stable if there exists a differentiable function of the states $V(x) : \mathbb{R}^{\mathrm{N}} \to \mathbb{R} \in C^1$ and a scalar $r > 0$ such that*

1. *$V(X_e) = 0$ and $V(x) > 0 \; \forall x \in \mathcal{B}(X_e, r)$,*
2. *$\dot{V}(x) \leq 0 \; \forall x \in \mathcal{B}(X_e, r)$.*

Theorem 2.4. *The equilibrium point X_e of (2.89) is asymptotically stable if there exists a differentiable function of the states $V(x) : \mathbb{R}^{\mathrm{N}} \to \mathbb{R} \in C^1$ and a scalar $r > 0$ such that*

1. *$V(X_e) = 0$ and $V(x) > 0 \; \forall x \in \mathcal{B}(X_e, r)$,*
2. *$\dot{V}(x) < 0 \; \forall x \in \mathcal{B}(X_e, r)$.*

The function $V(x)$ in the theorems is usually denoted as Lyapunov function. The two above theorems characterize the properties of the equilibrium point without relying on the explicit computation of the system state trajectories around X_e. As such, they provide a qualitative characterization of the system equilibria. However, the theorems provide only sufficient conditions to prove the stability (resp. asymptotic stability) of the equilibrium points. Moreover, for a general system of non-linear ODEs, no systematic procedure is available to determine the expression for a Lyapunov function able to satisfy the assumptions of the theorems.

For the particular case of LTI systems, additional theoretical results allow to easily characterize the internal stability. As already pointed out, to completely characterize the stability of a LTI system as (2.33), it sufficies to consider the equilibrium points X_e associated to the equation $AX_e = 0$; this equation is satisfied only if either $X_e \in \text{Null}(A)$ or $X_e = 0$. As the results of this thesis concern mostly asymptotically stable LTI systems, the results presented here will be referred to the only admissible asymtotically stable equilibrium point, i.e., the origin; this does not reduce the generality of the results, as those that would be obtained by considering $X_e \in \text{Null}(A)$ are identical.

It is a known result in the theory of LTI systems that a Lyapunov function certifying the asymptotic stability of the state $X_e = 0$, if exists, is a positive definite quadratic form

$$V(x) = x^\top P x, \qquad P = P^\top \succ 0. \tag{2.91}$$

The associated variation along the state trajectories is

$$\frac{dV(x(t))}{dt} = \dot{x}(t)^\top P x(t) + x(t)^\top P \dot{x}(t) = x(t)^\top [A^\top P + PA] x(t). \tag{2.92}$$

This shows that $\dot{V}(x)$ is negative definite in any neighborhood of the origin if and only if the matrix $Q = [A^\top P + PA]$ is negative definite. As $V(x)$ in (2.91) is positive definite by construction over $\mathbb{R}^{\mathrm{N}}$, a LTI system is asymptotically stable if and only if

$$\exists P = P^\top \succ 0 : \; A^\top P + PA \prec 0. \tag{2.93}$$

For simple stability, $\dot{V}(x)$ is allowed to be negative semi-definite; this means that the system is stable if and only if

$$\exists P = P^\top \succ 0 : \; A^\top P + PA \preceq 0. \tag{2.94}$$

The following Theorem also provides the way to characterize the asymptotic stability of system (2.33) in terms of the eigenvalues of the matrix A

Theorem 2.5. *Given system* (2.33) *and any matrix* $Q \in \mathcal{S}^{\mathrm{N}}_{++}$*, a solution* $P \in \mathcal{S}^{\mathrm{N}}_{++}$ *of the equation*

$$A^\top P + PA = -Q, \tag{2.95}$$

exists and is unique if and only if all the eigenvalues of A have strictly negative real part. In this case, A is denoted as Hurwitz.

The consequence of the above theorem is well-known: the knowledge of the eigenvalues of the matrix A is sufficient to state if a LTI system is asymptotically stable. As the eigenvalues of A are also the poles for the transfer function $\mathsf{H}(s)$, the asymptotic stability of the system can also be assessed by checking the negativity of the real part of the transfer function poles, if no cancellation between poles and zeros occurs.

2.3.2 Passivity

A dynamical system is passive if it is not able to generate energy on its own. The concept of *dissipativity* formalizes this idea in mathematical terms. Given the instantaneous electrical power $p(t)$ *entering* a P-port, defined by (2.86) we have the following

Definition 2.7. *System* (2.28) *is dissipative with respect to the supply rate* $p(t)$ *if there exists a non-negative scalar function of the states* $S : \mathbb{R}^{\mathrm{N}} \to \mathbb{R}^{+}$ *such that*

$$S(x(t_1)) \leq S(x(t_0)) + \int_{t_0}^{t_2} p(t)dt \tag{2.96}$$

for all $t_0 \leq t_1$ *and for all signals x,u,y satisfying the state space equations. If* $S(x)$ *exists, then it is called* storage function.

The storage function $S(x(t))$ represents a generalized energy function, in a way analogous to Lyapunov functions. The inequality (2.96) is called *dissipation inequality*. Under the assumption that the energy stored in the system is vanishing for a reference time instant $t = 0$, which implies $S(x(0)) = 0$, the dissipation inequality translates to

$$0 \leq S(x(t)) \leq \int_{0}^{t} p(t)dt = \mathcal{E}(t), \quad \forall t. \tag{2.97}$$

where $\mathcal{E}(t)$ is the energy dissipated by the system up to time t. The non-negativity of $\mathcal{E}(t)$ implies system passivity.

The dissipation inequality (2.96) can be expressed in differential form whenever the storage function $S(x)$ is differentiable; the differential form reads:

$$\frac{dS(x(t))}{dt} \equiv \dot{S}(x) \leq p(t), \quad \forall t. \tag{2.98}$$

Moreover, the *dissipation function* $d(t) = -\dot{S}(x) + p(t)$ can be interpreted as the instantaneous power dissipated by the dynamical system.

Storage functions, similarly to Lyapunov functions, are not unique. Indeed, for the generic case of nonlinear systems, it is proved that storage functions are also admissible Lyapunov functions in proximity of an equilibrium point provided that they are positive definite and meet additional technical conditions. As one could expect, determining a storage assessing the dissipativity of a nonlinear system is a nontrivial task.

For LTI systems, stronger theoretical results are available. In particular, it is proved that for stable linear time invariant systems, the class of admissible storage functions is reduced to the set of positive definite quadratic forms. For LTI systems in immittance representation, this leads to the following important result.

Theorem 2.6. *Let system* (2.33) *be controllable and observable. Then it is dissipative (passive) with respect to supply rate* (2.87) *if and only if there exists a matrix* $P \in \mathcal{S}^{\mathrm{N}}_{++}$ *such that*

$$Q = \begin{bmatrix} A^\top P + PA & PB - C^\top \\ B^\top P - C & -D - D^\top \end{bmatrix} \preceq 0 \tag{2.99}$$

The above theorem known as *Positive Real lemma* (PRL), states that for immittance linear time invariant systems, dissipativity can always be assessed by checking the feasibility of matrix inequality (2.99). The theorem can be derived by requiring that inequality (2.98) is verified with a positive-definite storage function $S(x) = x^\top P x$ for all of the possible configurations of the state and input vectors. For the system, an admissible dissipation function is

$$d(t) = -\begin{bmatrix} x \\ u \end{bmatrix}^\top Q \begin{bmatrix} x \\ u \end{bmatrix}. \tag{2.100}$$

As a necessary condition for the involved matrix to be negative semi-definite is that the upper-right block is negative semi-definite as well. Therefore the function $S(x)$, if it exists, plays also the role of Lyapunov function for system (2.33).

The following *Bounded Real lemma* (BRL) represents the equivalent counterpart of the PRL for LTI systems in scattering representation

Theorem 2.7. *Let system* (2.33) *be controllable and observable. Then it is dissipative (passive) with respect to supply rate* (2.88) *if and only if there exists a matrix* $P \in \mathcal{S}^{\mathrm{N}}_{++}$ *such that*

$$Q = \begin{bmatrix} A^\top P + PA + C^\top C & PB + C^\top D \\ B^\top P + D^\top C & -\mathbb{I}_{\mathrm{P}} + D^\top D \end{bmatrix} \preceq 0 \tag{2.101}$$

Here, the matrices Q and P have the same interpretation as in the positive real lemma. The main structural difference between the two theorems, which has practical implications, is the fact that in (2.101), the dependency of matrix Q on C and D is either quadratic or bilinear. The linear dependency on the state space matrices

can be recovered by applying the inverse Schur complement to condition (2.101), which is then converted to the following equivalent form

$$\begin{bmatrix} A^\top P + PA & PB & C^\top \\ B^\top P & -\mathbb{I}_{\mathrm{P}} & D^\top \\ C & D & -\mathbb{I}_{\mathrm{P}} \end{bmatrix} \preceq 0, \tag{2.102}$$

in which the dependency on all the state space output matrices is linear.

Passivity of LTI systems in immittance or scattering representations can be assessed also in terms of the properties of the associated transfer matrix $\mathsf{H}(s)$, by means of frequency domain criteria. The following definitions are of interest.

Definition 2.8. *A transfer matrix $\mathsf{H}(s)$ is Positive Real (PR) if it satisfies the following conditions*

1. $\mathsf{H}(s)$ *regular for* $\mathrm{R}\{s\} > 0$,
2. $\mathsf{H}^*(s) = \mathsf{H}(s^*) \quad \forall s \in \mathbb{C}$,
3. $\mathsf{H}^\star(s) + \mathsf{H}(s) \succeq 0 \quad$ *for* $\mathrm{R}\{s\} > 0$.

Definition 2.9. *A transfer matrix $\mathsf{H}(s)$ is Bounded Real (BR) if it satisfies the following conditions*

1. $\mathsf{H}(s)$ *regular for* $\mathrm{R}\{s\} > 0$,
2. $\mathsf{H}^*(s) = \mathsf{H}(s^*) \quad \forall s \in \mathbb{C}$,
3. $\mathbb{I}_{\mathrm{P}} - \mathsf{H}^\star(s)\mathsf{H}(s) \succeq 0 \quad$ *for* $\mathrm{R}\{s\} > 0$.

The first point in the above definitions requires that the transfer function $\mathsf{H}(s)$ has no poles in the open right-half complex plane; this implies that the matrix A of the associated state space (2.33) is required to be stable. The second point is equivalent to requiring that the impulse response of the system is real-valued. The third point taks a different form for immittance and scattering representations. The hermitian part of positive real transfer matrices is required to be positive semi-definite in the open right-half complex plane, whereas the singular values of a bounded real transfer matrix $\mathsf{H}(s)$ must be bounded by one over the same region.

Point 3 in both definitions 2.8, 2.9 is strictly related to the energy gain of the associated linear system. The following theorem states that positive realness and bounded realness provide a characterization for the passivity of LTI systems in immittance or scattering representations

Theorem 2.8. *An LTI system with transfer matrix $\mathsf{H}(s)$ is passive if and only if $\mathsf{H}(s)$ is Positive Real (immittance case) or Bounded Real (scattering case).*

Whenever the transfer function $\mathsf{H}(s)$ is rational, with no poles on the imaginary axis and is bounded for $s \to \infty$, then the fulfilment of Point 3 in both definitions 2.8, 2.9 can be equivalently required over the imaginary axis $j\mathbb{R}$ rather than over the open right-half complex plane. This means that whenever such a transfer function fulfills Points 1, 2 then it is

$$\begin{cases} \text{Bounded Real if and only if:} & \mathbb{I}_{\mathrm{P}} - \mathsf{H}^{\star}(j\omega)\mathsf{H}(j\omega) \succeq 0, \\ \text{Positive Real if and only if:} & \mathsf{H}^{\star}(j\omega) + \mathsf{H}(j\omega) \succeq 0. \end{cases} \tag{2.103}$$

Under the above conditions, the link between the frequency domain characterization of passivity and the fulfillment of the linear matrix inequalities involved in Theorems 2.7, 2.6 is provided by the celebrated *Kalman-Yakubovich-Popov lemma* (KYP)[2] [56, 105]

Theorem 2.9. *Let the pair (A, B) be controllable, with $A \in \mathbb{R}^{\mathrm{N}\times\mathrm{N}}$, $B \in \mathbb{R}^{\mathrm{N}\times\mathrm{P}}$, and let*

$$\Omega(A, B, P) = \begin{bmatrix} A^{\top}P + PA & PB \\ B^{\top}P & 0 \end{bmatrix}, \quad Z(j\omega) = (j\omega\mathbb{I}_{\mathrm{N}} - A)^{-1}B. \tag{2.104}$$

The following statements are equivalent for any matrix $G \in \mathcal{S}^{\mathrm{N}+\mathrm{P}}$:

1. *The following frequency domain inequality holds for all ω excluded those such that $j\omega$ is an eigenvalue of A*

$$\begin{bmatrix} Z(j\omega) \\ \mathbb{I}_{\mathrm{P}} \end{bmatrix}^{\star} G \begin{bmatrix} Z(j\omega) \\ \mathbb{I}_{\mathrm{P}} \end{bmatrix} \succeq 0 \tag{2.105}$$

2. *There exists a matrix $P \in \mathcal{S}^{\mathrm{N}}$ such that*

$$\Omega - G \preceq 0 \tag{2.106}$$

3. *There exists a solution of the Lur'e equations, that is, there exists matrices $P \in \mathcal{S}^{\mathrm{N}}$, $L \in \mathbb{R}^{(\mathrm{N}+\mathrm{P})\times\mathrm{P}}$ such that*

$$\Omega - G = -L^{\top}L \tag{2.107}$$

[2]The number of theoretical derivations and applications based on this lemma are so numerous and important that often some of the derived results go under the name of the KYP lemma itself. An example is the positive real lemma, that is often refferred to as Kalman-Yakubovich-Popov lemma. The interested reader is referred to [56] for an historical overview of the research developments that led to the formulation of Theorem 2.9 and for further discussions

Chapter 3

Rational fitting

This chapter provides an overview of most common rational fitting approaches. Rational approximation can be considered as the starting point for most developments and novel results documented in this thesis.

The motivations and the advantages offered by rational fitting problem are introduced, together with the classical Sanathanan-Koerner iteration and the celebrated Vector Fitting algorithm. Then, the multivariate rational fitting setting and the Parameterized Sanathanan-Koerner iteration are introduced in Sec. 3.2.1. Some contents of this last section are recent and include research topics covered by the author.

3.1 Rational fitting

The goal of the rational fitting techniques covered in this dissertation is to build a rational closed form approximation $\mathsf{H}(s)$ of a target function $\breve{\mathsf{H}}(s) \in \mathbb{C}^{\mathrm{P}\times\mathrm{P}}$ depending on the complex frequency. The target transfer function is known numerically in correspondence of K complex frequency sampling points

$$\breve{H}_k = \breve{\mathsf{H}}(s_k), \quad k = 1,2,\ldots,K. \tag{3.1}$$

These values represent the dataset upon which the approximation is built. The rational fitting process enforces the condition

$$\mathsf{H}(s_k) \approx \breve{\mathsf{H}}(s_k), \quad k = 1,2,\ldots,K. \tag{3.2}$$

where the approximation is performed by minimizing a suitable norm of the model-data error.

3.1.1 Problem linearization

Consider the situation in which the structure of the model function $\mathsf{H}(s) \in \mathbb{C}^{\mathrm{P}\times\mathrm{P}}$ is defined according to

$$\mathsf{H}(s) = \frac{\mathsf{N}(s)}{\mathsf{D}(s)} = \frac{\sum_{i=0}^{n} R_i \ f_i(s)}{\sum_{i=0}^{n} r_i \ g_i(s)}; \tag{3.3}$$

in the above $f_i(s)$, $g_i(s)$ are complex scalar basis functions, that can be chosen freely provided that $\mathsf{H}(s)$ is a rational function. The coefficients of the expansions, $R_i \in \mathbb{C}^{\mathrm{P}\times\mathrm{P}}$, $r_i \in \mathbb{C}$ are unknowns to be estimated during the rational fitting process. This model structure assumes that all of the entries of $\breve{\mathsf{H}}(s)$ can be approximated by considering a common denominator $\mathsf{D}(s)$.

In this case, the enforcement of (3.2) over the available data points can be performed by minimizing the following cost function

$$\min_{r_i,R_i} \sum_{k=1}^{K} \left\| \frac{\sum_{i=0}^{n} R_i \ f_i(s_k)}{\sum_{i=0}^{n} r_i \ g_i(s_k)} - \breve{H}_k \right\|_F^2 = \min_{r_i,R_i} \sum_{k=1}^{K} \|E_k\|_F^2 \tag{3.4}$$

where $\|\cdot\|_F$ is the Frobenius norm[1]. The rational dependency of the cost function defined in (3.4) on the coefficients r_i makes the approximation problem non-convex, and thus prone to exhibit multiple local sub-optimal solutions, with expected convergence problems during minimization.

One intuitive way to deal with this issue is to perform a linearization of the approximation condition (3.2) (first proposed in [70]), replacing it with the following

$$\mathsf{N}(s_k) \approx \mathsf{D}(s_k)\breve{H}(s_k), \quad k = 1,2,\dots K. \tag{3.5}$$

which can be enforced by minimizing

$$\min_{r_i,R_i} \sum_{k=1}^{K} \left\| \sum_{i=0}^{n} R_i \ f_i(s_k) - \left(\sum_{i=0}^{n} r_i \ g_i(s_k) \right) \breve{H}_k \right\|_F^2 = \min_{r_i,R_i} \sum_{k=1}^{K} \left\| \bar{E}_k \right\|_F^2 . \tag{3.6}$$

The minimizer of (3.6) can be found by simply solving a homogeneous least-squares problem involving the unknown coefficients, using appropriate constraints to rule out the vanishing solution. However, problems (3.4) and (3.6) are not equivalent, and the linearization introduces a bias in the coefficients estimation. To see this,

[1]Other norms can be chosen to measure the approximation error to be minimized by the rational approximation. The Frobenius norm is used here because it is also the one employed to derive most of the results of this thesis.

consider the vectors $e_k = \mathrm{vet}(E_k)$, $\bar{e}_k = \mathrm{vet}(\bar{E}_k)$; it holds that

$$\sum_{k=1}^{K} \|E_k\|_F^2 = \sum_{k=1}^{K} e_k^\star e_k, \tag{3.7}$$

$$\sum_{k=1}^{K} \left\|\bar{E}_k\right\|_F^2 = \sum_{k=1}^{K} \bar{e}_k^\star \bar{e}_k = \sum_{k=1}^{K} (\mathsf{D}(s_k)e_k)^\star \mathsf{D}(s_k)e_k = \sum_{k=1}^{K} |\mathsf{D}(s_k)|^2 e_k^\star e_k. \tag{3.8}$$

The above shows that the linearized cost function weights the original error components with the squared absolute value that the denominator function attains at each s_k.

3.1.2 The Sanathanan-Koerner iteration

The Sanathanan-Koerner (SK) algorithm [92] performs a rational approximation of the target function $\breve{\mathsf{H}}(s)$ exploiting model structure (3.3). The fitting process consists at iterating the estimation of the model $\mathsf{H}(s)$, by repeatedly enforcing a linearized version of (3.4). The idea behind the algorithm is to progressively reduce the bias introduced in the linearized fitting condition (3.5), by solving a sequence of suitably weighted least-squares problems.

Let ν be an iteration index and let $\mathsf{D}^0(s) = 1$. The Sanathanan-Koerner iteration solves the following convex problems

$$\begin{aligned}\min_{r_i^\nu, R_i^\nu} \sum_{k=1}^{K} \left\| \frac{\mathsf{N}^\nu(s_k) - \mathsf{D}^\nu(s_k)\breve{H}_k}{\mathsf{D}^{\nu-1}(s_k)} \right\|_F^2 = \\ = \min_{r_i^\nu, R_i^\nu} \sum_{k=1}^{K} \left\| \frac{\sum_{i=0}^{n} R_i^\nu \; f_i(s_k) - (\sum_{i=0}^{n} r_i^\nu \; g_i(s_k))\breve{H}_k}{\sum_{i=0}^{n} r_i^{\nu-1} \; g_i(s_k)} \right\|_F^2, \quad \nu = 1,2,\dots\end{aligned} \tag{3.9}$$

This optimization represents a least-squares problem in the current decision variables r_i^ν, R_i^ν, since at iteration ν the denominator function $\mathsf{D}^{\nu-1}(s)$ is numerically available as a result of the previous iteration. By employing the notation used in (3.7), it can be seen how the cost function minimized at each SK iteration can be written equivalently as

$$\sum_{k=1}^{K} e_k^\star \left(\frac{|\mathsf{D}^\nu(s_k)|^2}{|\mathsf{D}^{\nu-1}(s_k)|^2} \right) e_k. \tag{3.10}$$

The above cost function is equivalent to (3.7) at any iteration $\bar{\nu}$ for which it holds $\mathsf{D}^{\bar{\nu}}(s) = \mathsf{D}^{\bar{\nu}-1}(s)$, which represents a convergence condition for the SK iteration.

For what concerns the model structure, the SK iteration is usually performed by employing either canonical polynomial or partial fraction bases. Whenever it

is assumed that $\breve{\mathsf{H}}(s)$ can be adequately represented through a proper rational function, these two sets of bases are

$$\begin{cases} f_i = g_i = s^i & \text{Polynomial basis} \\ f_0 = g_0 = 1, \quad f_i = g_i = \frac{1}{s-q_i},\ i = 1,\dots,n & \text{Partial fraction basis.} \end{cases} \tag{3.11}$$

In both cases, choosing the above basis functions leads to a proper rational function $\mathsf{H}(s)$ of order at most n. When the partial fraction basis is employed, the algorithm is usually referred to as *Generalized Sanathanan-Koerner* iteration (GSK). In this case, some remarks are in order. The set of numbers $\{q_i\}$ representing the poles of the basis are often chosen to have negative real part, so that all the partial fractions are stable. Whenever q_i is complex, then q_{i+1} is chosen as its complex conjugate[2].

The partial fractions can also be used to define a different basis, $f_i = \phi_i(s)$, where the functions $\phi_i(s)$ are orthonormal rational functions constructed starting from $\frac{1}{s-q_i},\ i = 1,\dots n$, as explained in [34]; this improves the numerical conditioning of the optimization problem (3.9).

Using the partial fractions basis, both the rational functions $\mathsf{N}(s)$ and $\mathsf{D}(s)$ share the same set of poles $\{q_i\}$, that cancel out in $\mathsf{H}(s)$, whose actual poles and zeros coincide with the zeros of $\mathsf{D}(s)$ and $\mathsf{N}(s)$ respectively. Therefore, the partial fractions play only the role of basis functions, and their poles are not the poles of the approximating function. The result is that $\mathsf{H}(s)$ is expressed in *rational barycentric* form, widely adopted in interpolation problems [66], rational fitting algorithms [79], and model order reduction schemes [63].

When polynomials or partial fractions are used as bases, the coefficient r_0^ν can be fixed a priori to a known real value, in such a way that problems (3.9) do not admit the trivial zero optimal solution. Also, the condition $\mathsf{D}^0(s) = 1$, is easily achieved by additionally setting $r_i^0 = 0$ for $i = 1,2,\dots,n$. From a practical standpoint, the partial fraction basis performs better then the polynomial basis, due to the bad numerical conditioning properties of the latter for large values of n.

Figure 3.1 shows the results obtained by applying the GSK algorithm to a test case. The target function $\breve{\mathsf{H}}(s)$ represents the scattering parameters of a high-speed interconnect, that are modeled in this case setting $n = 25$. The top panel shows a comparison between the model $\mathsf{H}(s)$ and the reference data samples, in terms of real and imaginary components. The bottom panel shows the absolute value of the associated fitting error. The convergence index δ^ν for this example defined as

$$\delta^\nu = \frac{\left\|x^\nu - x^{\nu-1}\right\|_2}{\left\|x^{\nu-1}\right\|_2} \tag{3.12}$$

being $x^\nu = \left[r_1^\nu, r_2^\nu, \dots, r_n^\nu\right]$, is reported in Fig 3.2. As this index vanishes, the estimate of the denominator stabilizes, meaning that the algorithm has converged.

[2]The case $\breve{H}^*(s) \neq \breve{H}(s^*)$ for some s is not considered in this work.

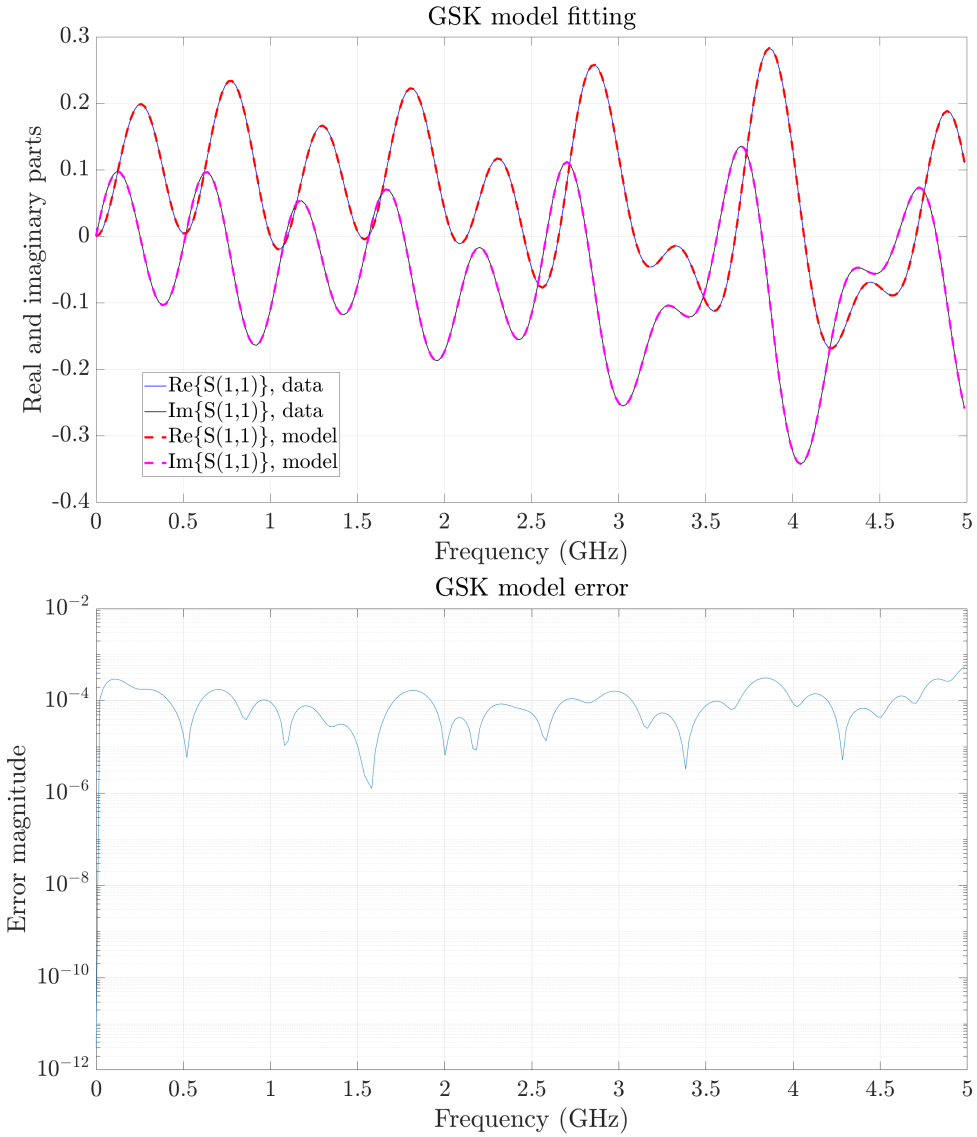

Figure 3.1: GSK modeling performace. The target rational function $\breve{\mathsf{H}}(s)$ represents the scattering parameters of a high-speed interconnection. Top panel: model-vs-data comparison. Bottom panel: absolute value of the error.

3.1.3 The Vector Fitting iteration

The Vector Fitting (VF) iteration represents one of the most widespread techniques in the field of macromodeling and model order reduction based on rational fitting. Since its introduction in 1999 [61], this algorithm has been subject of intensive research (see e.g. [34, 35, 60, 31, 59])

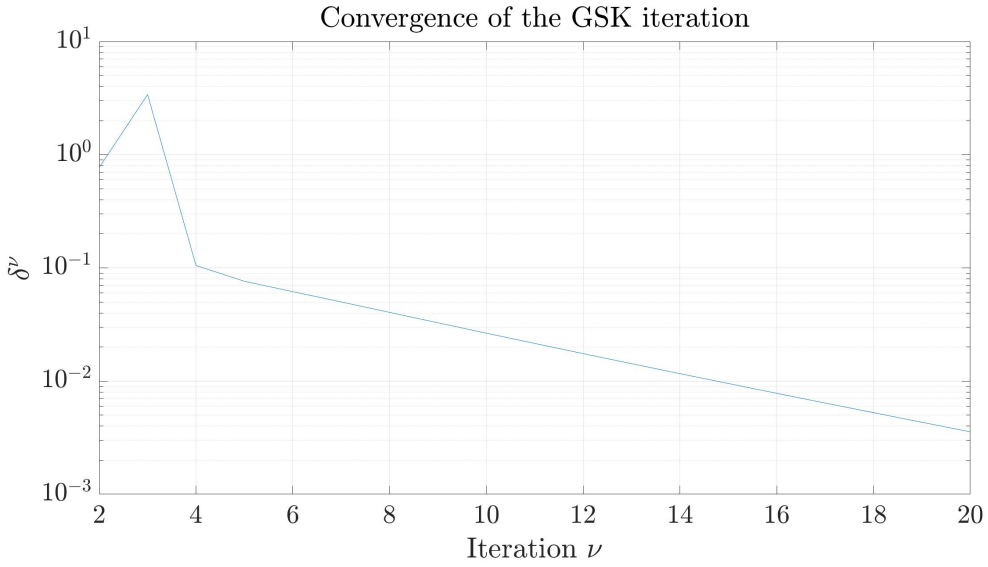

Figure 3.2: The convergence index δ^ν of the GSK iteration in a practical application.

The algorithm can be seen as an elegant reformulation of the GSK counterpart [62], in which the iterative re-weighting of the cost function is indirectly performed via relocation of the basis poles $\{q_i\}$.

In order to introduce the algorithm, it is convenient to take a closer look at (3.9) when the basis functions $f_i(s)$, $g_i(s)$ are defined as the partial fractions in (3.11). In this setting, the GSK optimization problem at each iteration is

$$\min_{r_i^\nu, R_i^\nu} \sum_{k=1}^{K} \left\| \frac{R_0^\nu + \sum_{i=1}^n \frac{R_i^\nu}{s_k - q_i} - (r_0^\nu + \sum_{i=1}^n \frac{r_i^\nu}{s_k - q_i}) H_k}{r_0^{\nu-1} + \sum_{i=1}^n \frac{r_i^{\nu-1}}{s_k - q_i}} \right\|_F^2, \quad \nu = 1,2,\dots. \tag{3.13}$$

For simplicity in the following derivation, suppose that $\breve{\mathsf{H}}(s)$ is a scalar function, so that both $\mathsf{N}^\nu(s)$ and $\mathsf{D}^\nu(s)$ admit the pole-zero form representation

$$\mathsf{N}^\nu(s) = G_N^\nu \frac{\prod_{i=1}^n (s - a_i^\nu)}{\prod_{i=1}^n (s - q_i)}, \quad \mathsf{D}^\nu(s) = G_D^\nu \frac{\prod_{i=1}^n (s - z_i^\nu)}{\prod_{i=1}^n (s - q_i)}, \tag{3.14}$$

where the gain and the poles of $\mathsf{N}(s)$ and $\mathsf{D}(s)$ are functions of the unknown coefficients R_i^ν, r_i^ν (here the explicit dependency is omitted for readability). Using this representation, the optimization problem is rewritten as

$$\min_{r_i^\nu, R_i^\nu} \sum_{k=1}^{K} \left\| \frac{G_N^\nu \frac{\prod_{i=1}^n (s_k - a_i^\nu)}{\prod_{i=1}^n (s_k - q_i)} - G_D^\nu \frac{\prod_{i=1}^n (s_k - z_i^\nu)}{\prod_{i=1}^n (s_k - q_i)} \breve{H}_k}{G_D^{\nu-1} \frac{\prod_{i=1}^n (s_k - z_i^{\nu-1})}{\prod_{i=1}^n (s_k - q_i)}} \right\|_F^2, \quad \nu = 1,2,\dots. \tag{3.15}$$

which is equivalent to

$$\min_{r_i^\nu, R_i^\nu} \sum_{k=1}^{K} \left\| \frac{G_N^\nu}{G_D^{\nu-1}} \frac{\prod_{i=1}^n (s_k - a_i^\nu)}{\prod_{i=1}^n (s_k - z_i^{\nu-1})} - \frac{G_D^\nu}{G_D^{\nu-1}} \frac{\prod_{i=1}^n (s_k - z_i^\nu)}{\prod_{i=1}^n (s_k - z_i^{\nu-1})} \breve{H}_k \right\|_F^2, \quad \nu = 1,2,\dots \quad . \tag{3.16}$$

The above formulation shows that at iteration ν the weighting procedure introduced by the GSK iteration leads to the minimization of a cost function equal to that defined in (3.6), provided that the basis functions are partial fractions defined as in (3.11), with poles $\{z_i^{\nu-1}\}$. These new poles are the zeros of the previously estimated denominator function, $\mathsf{D}^{\nu-1}(s)$.

The vector fitting iteration exploits this fact in order to avoid the explicit numerical weighting introduced by the SK scheme. In its basic formulation, the algorithm works as follows. An iteration-dependent model structure is defined as

$$\mathsf{H}^\nu(s) = \frac{\mathsf{N}^\nu(s)}{\mathsf{D}^\nu(s)} = \frac{R_0^\nu + \sum_{i=1}^n \frac{R_i^\nu}{s - q_i^\nu}}{r_0^\nu + \sum_{i=1}^n \frac{r_i^\nu}{s - q_i^\nu}}; \tag{3.17}$$

here, again, each R_i^ν and r_i^ν are model unknowns, together with R_0^ν. For $\nu = 1$, the basis poles $\{q_i^1\}$ are initialized to a predefined set. Then, the VF solves the sequence of optimization problems

$$\min_{r_i^\nu, R_i^\nu} \sum_{k=1}^{K} \left\| \underbrace{R_0^\nu + \sum_{i=1}^n \frac{R_i^\nu}{s_k - q_i^\nu}}_{\mathsf{N}^\nu(s)} - \underbrace{\left(r_0^\nu + \sum_{i=1}^n \frac{r_i^\nu}{s_k - q_i^\nu} \right)}_{\mathsf{D}^\nu(s)} \breve{H}_k \right\|_F^2, \quad \nu = 1,2,\dots \tag{3.18}$$

with

$$\mathsf{D}^{\nu-1}(s) \iff \left(\begin{array}{c|c} A & B \\ \hline C & D \end{array} \right) \to \{q_i^\nu\} = \mathrm{eig}(A - BD^{-1}C) \tag{3.19}$$

The iteration reaches a fixed point whenever it holds $\{q_i^{\bar{\nu}-1}\} = \{q_i^{\bar{\nu}}\}$, which is the convergence condition of the Vector Fitting algorithm. When it happens, the zeros of $\mathsf{D}^{\bar{\nu}}(s)$ coincide with its poles; this implies that the denominator coefficients $r_i^{\bar{\nu}}$ are identically zero for $i = 1, \dots, n$ and that $\mathsf{D}^{\bar{\nu}}(s) = r_0^{\bar{\nu}}$. Up to a normalization factor $r_0^{\bar{\nu}}$, the output model of the vector fitting scheme is then

$$\mathsf{H}(s) = \mathsf{N}^{\bar{\nu}}(s) = R_0^{\bar{\nu}} + \sum_{i=1}^{n} \frac{R_i^{\bar{\nu}}}{s_k - q_i^{\bar{\nu}}} \tag{3.20}$$

It is proved [68] that whenever $\breve{\mathsf{H}}(s)$ is a proper rational function of order n and the data samples H_k are noise-free, the VF convergence condition takes place in a single iteration.

In practical implementations, it is common to stop the algorithm either when a desired model-vs-data error is achieved, or when the difference between the basis poles of two successive iterations is small enough. This last approach is based on the definition of a small threshold ϵ, used to define the following convergence criterion

$$\delta^{\nu} = \frac{\|x^{\nu} - x^{\nu-1}\|_2}{\|x^{\nu-1}\|_2} \leq \epsilon \tag{3.21}$$

being $x^{\nu} = \left[r_1^{\nu}, r_2^{\nu}, \ldots, r_n^{\nu}\right]$.

As an application example, Fig. 3.3 shows the performance of the VF scheme when applied to the same fitting problem presented in sec. 3.1.2, setting $n = 25$. The model-vs-data error shows that the VF scheme guarantees an accuracy improvement of about 1 order of magnitude with respect to the GSK. Also, the convergence index decreases faster, as shown in Fig. 3.4

3.2 Multivariate rational fitting

Parameterized rational fitting computes an approximation for a function $\breve{\mathsf{H}}(s, \boldsymbol{\vartheta})$, which depends both on the Laplace variable and on a set of additional parameters $\boldsymbol{\vartheta} \in \Theta \subset \mathbb{R}^d$, where Θ is defined as in (2.55). In this case, the fitting is expected to return an approximating function $\mathsf{H}(s, \boldsymbol{\vartheta})$ whose dependency on the variable s is rational for each value of $\boldsymbol{\vartheta}$ belonging to Θ. Therefore, the approximation to be enforced in a parameterized rational fitting problem is

$$\mathsf{H}(s_k, \boldsymbol{\vartheta}_m) \approx \breve{\mathsf{H}}(s_k, \boldsymbol{\vartheta}_m) = \breve{H}_{k,m}, \quad k = 1,2,\ldots,K, \quad m = 1,2,\ldots M \tag{3.22}$$

where $\breve{H}_{k,m}$ are samples of the target function available at prescribed sampling points.

3.2.1 The PSK iteration

The Generalized Sanathanan-Koerner algorithm can be extended to the parameterized case, in order to perform multivariate rational fitting. The genaralization leads to the so-called Parameterized-Sanathanan-Koerner (PSK) algorithm, [33, 103, 102]

To illustrate the algorithm, the discussion is limited to the case of a model structure of the form

$$\mathsf{H}(s, \boldsymbol{\vartheta}) = \frac{\mathsf{N}(s, \boldsymbol{\vartheta})}{\mathsf{D}(s, \boldsymbol{\vartheta})} = \frac{\sum_{i=0}^{n} R_i(\boldsymbol{\vartheta})\ \varphi_i(s)}{\sum_{i=0}^{n} r_i(\boldsymbol{\vartheta})\ \varphi_i(s)} \tag{3.23}$$

where the basis functions $\varphi_i(s)$ are defined as the partial fractions. As the PSK iteration is one of the main numerical tools exploited for the derivations of this

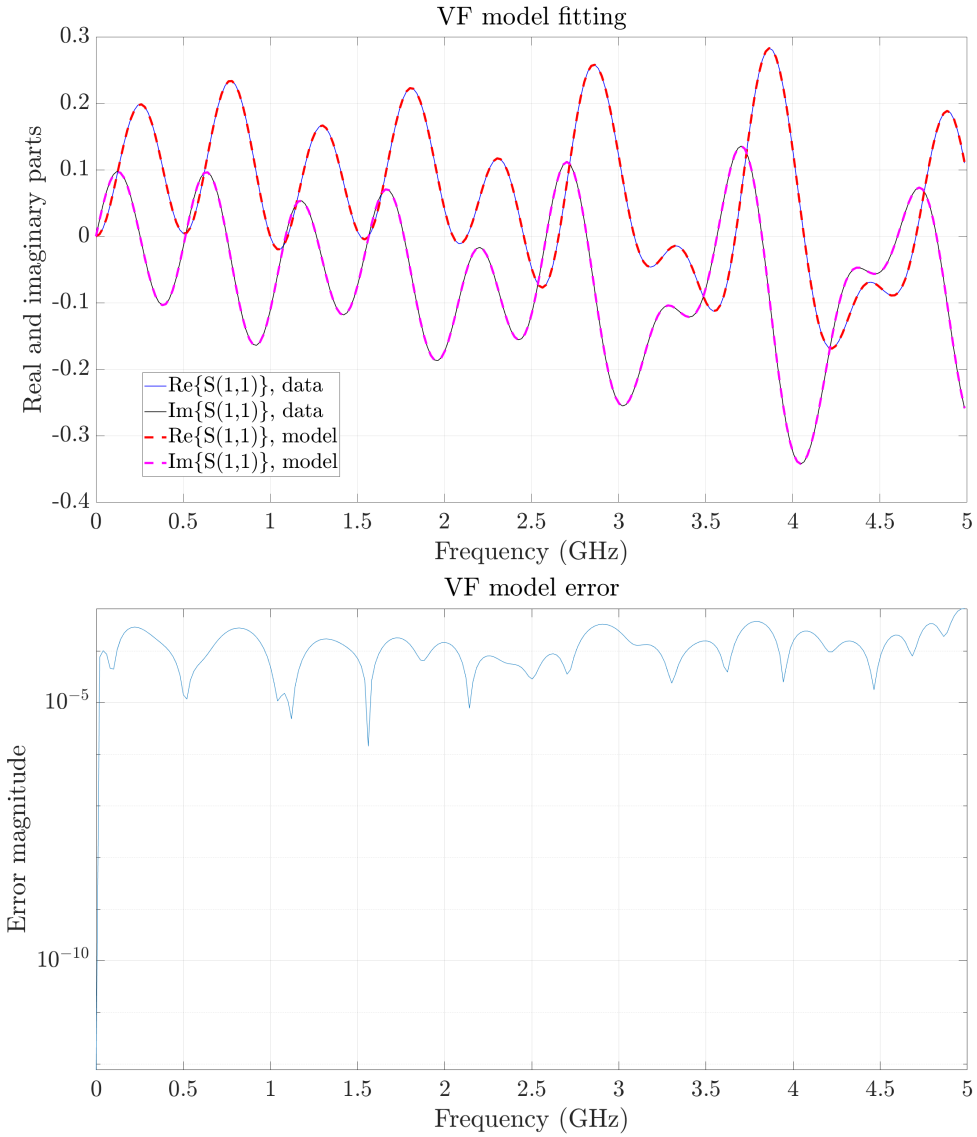

Figure 3.3: VF modeling performace. The target rational function $\breve{\mathsf{H}}(s)$ represents the scattering parameters of a high-speed interconnection, as in Fig 3.1. Top panel: model-vs-data comparison. Bottom panel: absolute value of the error.

thesis, it is worth defining the following modified partial fraction basis, used in practical implementations

$$\begin{cases} \varphi_i(s) = (s - q_i)^{-1}, & q_i \in \mathbb{R} \\ \varphi_i(s) = [(s - q_i)^{-1} + (s - q_i^*)^{-1}] & q_i \in \mathbb{C} \\ \varphi_{i+1}(s) = j[(s - q_i)^{-1} - (s - q_i^*)^{-1}] & q_{i+1} = q_i^* \in \mathbb{C} \end{cases} \tag{3.24}$$

with $\varphi_0(s) = 1$ and with $\mathrm{Re}\{q_i\} < 0 \,\forall\, i \neq 0$. As opposed to the standard partial

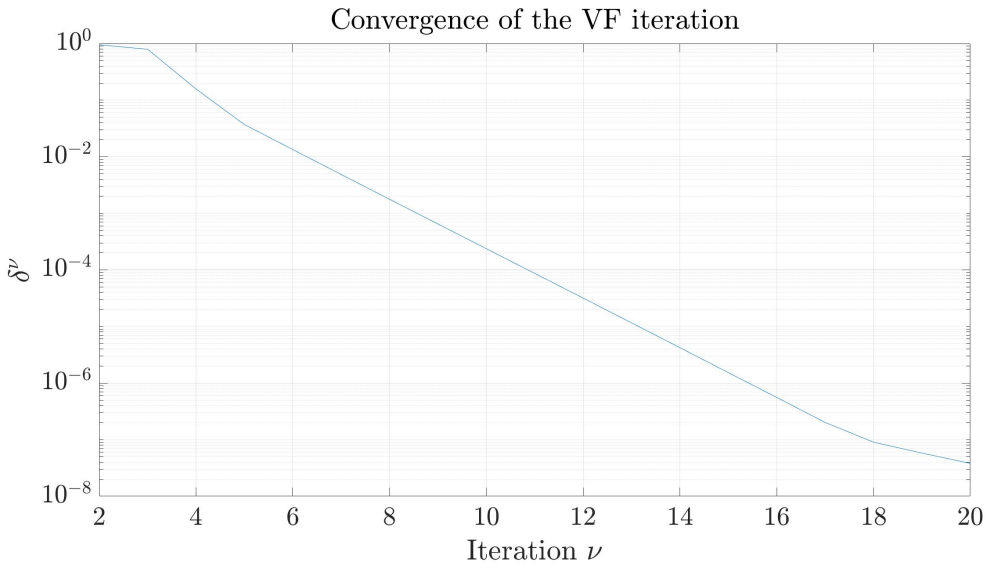

Figure 3.4: The convergence index δ^ν of the VF iteration in a practical application.

fraction basis (3.11), functions (3.24) allow to perform the model estimation working with real algebra [51].

The quantities $R_i(\boldsymbol{\vartheta}), r_i(\boldsymbol{\vartheta})$ are the parameterized residues associated to each partial fraction. They are unknown functions that must be found in such a way that the fitting condition (3.22) is enforced. To practically estimate these functions, it is assumed that they are structured as parameter-dependent basis functions expansions; in this dissertation, the interest will be limited to the case in which these functions are multivariate polynomials of the parameter vector $\boldsymbol{\vartheta}$. In order to keep the notation short, it is convenient to introduce a multi-index notation to identify each of the basis component.

Let $\xi_\ell(\vartheta_i)$ be the ℓ-th component of a univariate polynomial basis of the i-th parameter and let $\boldsymbol{\ell} = (\ell_1, \ell_2, \ldots, \ell_d)$ be a d dimensional multi-index. Then the multivariate polynomial basis $\xi_{\boldsymbol{\ell}}(\boldsymbol{\vartheta})$ is defined as

$$\xi_{\boldsymbol{\ell}}(\boldsymbol{\vartheta}) = \xi_{\ell_1}(\vartheta_1) \times \xi_{\ell_2}(\vartheta_2) \times \ldots \times \xi_{\ell_d}(\vartheta_d). \tag{3.25}$$

To define the PSK model structure, the order of the polynomial residues $R_i(\boldsymbol{\vartheta})$, $r_i(\boldsymbol{\vartheta})$ on each individual variable ϑ_i must be fixed; here, without loss of generality, we assume that these orders are equal for both N and D, and are identified by i-th entry of the multi-index

$$\overline{\boldsymbol{\ell}} = (\bar{\ell}_1, \ldots, \bar{\ell}_d), \tag{3.26}$$

so that the two functions can be expressed in terms of the basis components $\xi_{\boldsymbol{\ell}}(\boldsymbol{\vartheta})$ as

$$R_i(\boldsymbol{\vartheta}) = \sum_{\boldsymbol{\ell} \in \mathcal{I}_{\overline{\boldsymbol{\ell}}}} R_{i,\boldsymbol{\ell}}\ \xi_{\boldsymbol{\ell}}(\boldsymbol{\vartheta}), \quad r_i(\boldsymbol{\vartheta}) = \sum_{\boldsymbol{\ell} \in \mathcal{I}_{\overline{\boldsymbol{\ell}}}} r_{i,\boldsymbol{\ell}}\ \xi_{\boldsymbol{\ell}}(\boldsymbol{\vartheta}) \tag{3.27}$$

with unknown coefficients $R_{i,\boldsymbol{\ell}}$, $r_{i,\boldsymbol{\ell}}$, being

$$\mathcal{I}_{\overline{\boldsymbol{\ell}}} = \{\boldsymbol{\ell} \in \mathbb{N}^d : \boldsymbol{\ell} \leq \overline{\boldsymbol{\ell}}\} \tag{3.28}$$

the set of admissible multi-indices for the polynomial expansion, whose cardinality will be denoted hereafter as $V_{\overline{\boldsymbol{\ell}}}$.

Once the model structure is defined, the model is generated by solving the sequence of optimization problems

$$\begin{aligned}\min_{R^{\nu}_{i,\boldsymbol{\ell}}, r^{\nu}_{i,\boldsymbol{\ell}}} \sum_{m=1}^{M}\sum_{k=1}^{K} \left\| \frac{\mathsf{N}^{\nu}(s_k,\boldsymbol{\vartheta}_m) - \mathsf{D}^{\nu}(s_k,\boldsymbol{\vartheta}_m)\breve{H}_{k,m}}{\mathsf{D}^{\nu-1}(s_k,\boldsymbol{\vartheta}_m)} \right\|_F^2 = \\ = \min_{R^{\nu}_{i,\boldsymbol{\ell}}, r^{\nu}_{i,\boldsymbol{\ell}}} \sum_{m=1}^{M}\sum_{k=1}^{K} \left\| \frac{\sum_{i=0}^{n} R_i^{\nu}(\boldsymbol{\vartheta}_m)\ \varphi_i(s_k) - (\sum_{i=0}^{n} r_i^{\nu}(\boldsymbol{\vartheta}_m)\ \varphi_i(s_k))\breve{H}_{k,m}}{\sum_{i=0}^{n} r_i^{\nu-1}(\boldsymbol{\vartheta}_m)\ \varphi_i(s_k)} \right\|_F^2, \\ \nu = 1,2,\dots\end{aligned} \tag{3.29}$$

that represent the parameterized counterpart of (3.9). As in the SK and VF schemes, the iteration is stopped when the estimate of the denominator stabilizes; this means that the stopping criterion (3.21) can also be used in the parameterized setting, in which the vector x^{ν} collects all the denominator unknowns $r_{i,\boldsymbol{\ell}}$.

3.2.2 Estimation of the PSK coefficients

A compact matrix notation for (3.29) is readily obtained by collecting all elements of $R_{i,\boldsymbol{\ell}}$, $r_{i,\boldsymbol{\ell}}$ at iteration ν in a vector z^{ν}, obtaining the homogeneous least-squares form

$$\Psi^{\nu} z^{\nu} \approx 0, \tag{3.30}$$

that must be constrained to avoid the trivial vanishing solution, e.g. by setting $\|z^{\nu}\|_2 = 1$ and obtaining the optimal parameters as the right singular vector of Ψ^{ν} associated to the least singular value.

The matrix $\Psi^{\nu} \in \mathbb{C}^{KM\mathrm{P}^2 \times (n+1)(\mathrm{P}^2 V_{\overline{\boldsymbol{\ell}}} + V_{\overline{\boldsymbol{\ell}}})}$ is defined as

$$\Psi^{\nu} = \begin{bmatrix} \Gamma^{\nu} & & \Xi^{\nu}_{1,1} \\ & \ddots & \vdots \\ & \Gamma^{\nu} & \Xi^{\nu}_{\mathrm{P},\mathrm{P}} \end{bmatrix} \tag{3.31}$$

with individual blocks defined as

$$\begin{aligned} \Gamma^{\nu} &= W^{\nu-1} X, \\ \Xi^{\nu}_{i,j} &= -W^{\nu-1} \breve{H}_{i,j} X, \\ X &= \Phi \otimes J \end{aligned} \tag{3.32}$$

where $W^{\nu-1}$ and $\breve{H}_{i,j}$ are diagonal matrices collecting respectively the samples of the denominator available from previous iteration $D^{\nu-1}(s_k, \boldsymbol{\vartheta}_m)$ and the samples of the response $\breve{H}_{i,j}(s_k, \boldsymbol{\vartheta}_m)$, in correspondence of the available data points. The matrix X collects the products of frequency and parameter basis functions, individually stored in

$$\Phi = \begin{bmatrix} \varphi_0(s_1) & \cdots & \varphi_n(s_1) \\ \vdots & & \vdots \\ \varphi_0(s_K) & \cdots & \varphi_n(s_K) \end{bmatrix}, \quad J = \begin{bmatrix} \xi_{\mathbf{1}}(\boldsymbol{\vartheta}_1) & \cdots & \xi_{\bar{\boldsymbol{\ell}}}(\boldsymbol{\vartheta}_1) \\ \vdots & & \vdots \\ \xi_{\mathbf{1}}(\boldsymbol{\vartheta}_M) & \cdots & \xi_{\bar{\boldsymbol{\ell}}}(\boldsymbol{\vartheta}_M) \end{bmatrix} \tag{3.33}$$

In problem (3.30), the single elements of the model matrix $\mathsf{H}(s, \boldsymbol{\vartheta})$ cannot be estimated individually, due to the presence of the common denominator term. In fact, the matrix Ψ^{ν} exhibits a bordered block diagonal structure, which forces one to solve a coupled estimation problem in which the denominator and the denominator unknowns are computed concurrently. However, some algebraic manipulations inherited from the VF scheme [35], can be performed in order to reduce the computational cost burden of the procedure, as shown in [17]. For each i, j-th element of the target function, a QR factorization is performed as

$$Q^{\nu}_{i,j} R^{\nu}_{i,j} = \begin{bmatrix} \Gamma^{\nu} & \Xi^{\nu}_{i,j} \end{bmatrix} \tag{3.34}$$

where

$$R^{\nu}_{i,j} = \begin{bmatrix} \bullet & \bullet \\ 0 & T^{\nu}_{i,j} \end{bmatrix}. \tag{3.35}$$

Once available, the blocks $T^{\nu}_{i,j}$ are collected to build a least-squares problem of reduced size, which can be used to estimate the denominator coefficients $r^{\nu}_{i,\boldsymbol{\ell}}$ separately from the numerator counterparts. This reduced least-squares problem takes the form

$$\begin{pmatrix} T^{\nu}_{1,1} \\ \vdots \\ T^{\nu}_{\mathrm{P},\mathrm{P}} \end{pmatrix} x^{\nu} = \bar{T}^{\nu} x^{\nu} \approx 0, \tag{3.36}$$

where x^{ν} is the vector collecting the unknowns $r^{\nu}_{i,\boldsymbol{\ell}}$. Once x^{ν} is found, the remaining model unknowns $R_{i,\boldsymbol{\ell}}$ are found by solving problem

$$\min_{y^{\nu}} \sum_{i=1}^{\mathrm{P}} \sum_{j=1}^{\mathrm{P}} \left\| \Gamma^{\nu} y^{\nu}_{i,j} + \Xi_{i,j} x^{\nu} \right\|_2^2 \tag{3.37}$$

with vectors $y^{\nu}_{i,j}$ collecting all elements i, j of numerator matrix coefficients $R^{\nu}_{n,\boldsymbol{\ell}}$, and where the vector y^{ν} is an ensemble of all these unknowns

$$y^{\nu\top} = \begin{bmatrix} y^{\nu\top}_{1,1}, & \ldots, & y^{\nu\top}_{\mathrm{P},\mathrm{P}}. \end{bmatrix} \tag{3.38}$$

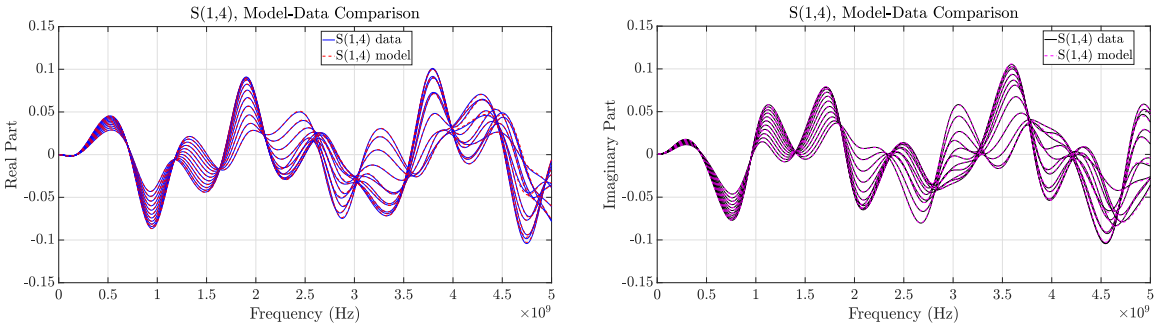

Figure 3.5: Performance of the PSK scheme when applied to model the scattering parameters of a parameterized multiconductor transmission line. See Sec. 4.6.2

Since at each iteration ν the knowledge of the coefficients $R_{i,\ell}$ is not required to set up and solve problem (3.36), the numerator estimation problem (3.37) can be solved only once the denominator estimate has stabilized, i.e., at the last PSK iteration $\bar{\nu}$. This significantly improves the algorithm efficiency, since the iteration requires only the computatution of the QR factorizations (3.34) and the solution of the small scale problem (3.36).

Several examples of application of the PSK scheme will be provided in this work. Fig. 3.5 anticipates the results that can be obtained by applying the algorithm for a multivariate rational fitting problem, for $d = 1$. The underlying data represent the scattering matrix parameters of a multiconductor transmission line system, that will be more thoroughly discussed in Sec. 4.6.2. The rational fitting quality guaranteed by the algorithm is remarkable. However, when the output approximation $\mathsf{H}(s, \boldsymbol{\vartheta})$ represents a parameterized transfer function, the plain PSK formulation is not able to guarantee stability and passivity of the associated model. A solution for this problem will be given in chapter 4.

3.2.3 Equivalent SPICE netlist

Model (4.8) admits a representation in terms of an equivalent SPICE netlist, as discussed in [52]. Assuming that the PSK model represents the scattering parameters of a P-port network, one way of synthesizing the equivalent netlist is as follows . First, decompose the model into two sub-blocks representing the individual numerator and denominator transfer functions, defined as

1. a scalar admittance $Y_D(s, \boldsymbol{\vartheta}) = \mathsf{D}(s, \boldsymbol{\vartheta})$, associated with instrumental port voltage and current variables v_D and i_D obeying

$$i_D = Y_D(s, \boldsymbol{\vartheta})\, v_D \quad \text{and} \quad v_D = Y_D^{-1}(s, \boldsymbol{\vartheta})\, i_D. \tag{3.39}$$

To handle the presence of multiple ports, the scalar denominator function is

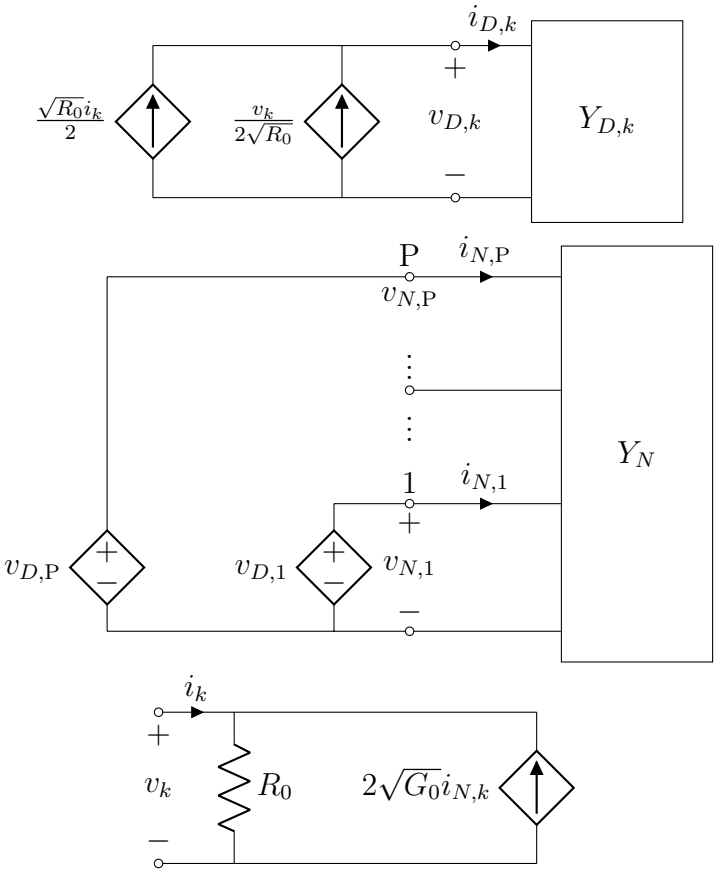

Figure 3.6: SPICE realization circuits. Top: denominator sub-block (k-th out of P instances). Middle: numerator sub-block. Bottom: external interface of the PSK model (k-th out of P ports, scattering representation, realized in Norton form).

represented as a diagonal P-ports

$$\mathsf{D}_{\otimes}(s,\boldsymbol{\vartheta}) = \mathbb{I}_{\mathrm{P}}\mathsf{D}_{\otimes}(s,\boldsymbol{\vartheta}) \tag{3.40}$$

realized as P separate and identical instances of Y_D, each associated with a pair of port voltages $v_{D,k}$ and currents $i_{D,k}$ for $k = 1,\dots,\mathrm{P}$. These port quantities are collected into the vectors $v_{\otimes}$ and $i_{\otimes}$ so that

$$i_{\otimes} = \mathsf{D}_{\otimes}(s,\boldsymbol{\vartheta})v_{\otimes}, \quad v_{\otimes} = \mathsf{D}_{\otimes}^{-1}(s,\boldsymbol{\vartheta})i_{\otimes}. \tag{3.41}$$

2. The numerator sub-block is considered as a P-port with admittance matrix $Y_N(s,\boldsymbol{\vartheta}) = \mathsf{N}(s,\boldsymbol{\vartheta})$ so that, by defining the instrumental port voltage and current vectors $v_N, i_N \in \mathbb{C}^{\mathrm{P}}$, we have

$$i_N = \mathsf{N}(s,\vartheta)\, v_N. \tag{3.42}$$

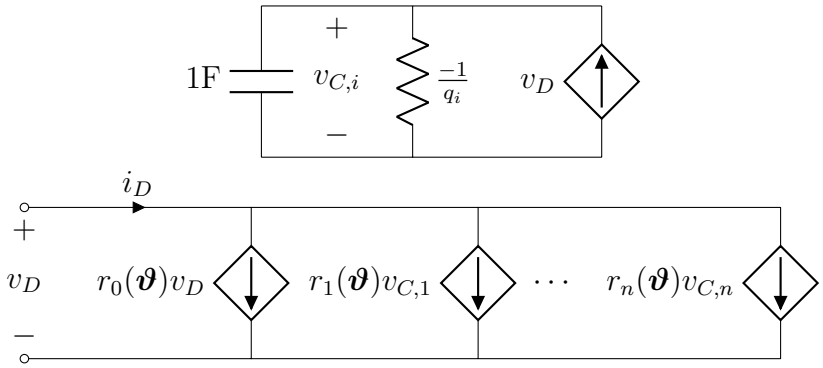

Figure 3.7: Synthesis of parameterized admittance block $\mathsf{D}(s,\boldsymbol{\vartheta})$. Top: elementary RC cell synthesizing the basis pole q_i. Bottom: external circuit interface.

3. Model (4.8) is assumed to be in scattering representation. Therefore,

$$B = \mathsf{H}(s,\boldsymbol{\vartheta})A = \mathsf{N}(s,\boldsymbol{\vartheta}) \cdot \mathsf{D}_{\otimes}^{-1}(s,\boldsymbol{\vartheta}) \cdot A. \tag{3.43}$$

where $A, B \in \mathbb{C}^P$ are the incident and reflected scattering wave vectors, defined as in (2.81).

Interconnection of the various blocks is realized as in Fig. 3.6 through dependent sources, by setting

- $i_{\otimes} = A$, so that the voltage vector at the output of the denominator block reads $v_{\otimes} = \mathsf{D}_{\otimes}^{-1}(s,\boldsymbol{\vartheta})\,A$. See Fig. 3.6 (top) , where a pair of controlled sources are used to synthesize each incident wave A_k;
- $v_N = v_{\otimes}$, so that $i_N = \mathsf{H}(s,\boldsymbol{\vartheta})\,A$, see Fig. 3.6 (middle);
- $B = i_N$, so that $B = \mathsf{H}(s,\boldsymbol{\vartheta})\,A$. See Fig. 3.6 (bottom), where a pair of current sources are used to realize the output components B_k in Norton form according to (2.81).

In the above setting, each of the involved transfer function elements can be synthesized following the same approach. We consider for example the synthesis of $\mathsf{D}(s,\boldsymbol{\vartheta})$, since the extension to $\mathsf{N}(s,\boldsymbol{\vartheta})$ and $\mathsf{D}_{\otimes}(s,\boldsymbol{\vartheta})$ is straightforward. From (4.8) and (3.27), we can write

$$i_D = \mathsf{D}(s,\boldsymbol{\vartheta})\,v_D = \sum_{i=0}^{n} j_{D,i} \tag{3.44}$$

where $j_{D,0} = r_0(\boldsymbol{\vartheta})\,v_D$ and

$$j_{D,i} = r_i(\boldsymbol{\vartheta})\,v_{C,i}, \quad \text{with} \quad v_{C,i} = (s-q_i)^{-1}\,v_D \tag{3.45}$$

for $i = 1, \ldots, n$. With real stable basis poles $q_i < 0$, the instrumental voltage $v_{C,i}$ is synthesized as a standard RC cell, see Fig. 3.7(top). Two coupled RC cells are used realize a pair of complex conjugate basis poles $q_{i+1} = q_i^*$, as in [55]. The instrumental currents $j_{D,i}$ are synthesized as Voltage-Controlled Current Sources (VCCS) with parameterized trans-conductance $r_i(\boldsymbol{\vartheta})$. Equation (3.44) is then realized as in Fig. 3.7(bottom).

Chapter 4

Multivariate passive macromodeling

This chapter presents a novel framework for the generation of reliable parameterized macromodels of passive devices, components, and sub-systems. The objective is to formulate a data-driven model order reduction scheme that, starting from frequency domain samples of the underlying system parameterized transfer function, returns certified passive parameterized surrogates. The method is thought to be non-intrusive, so that no closed form descriptions of the reference system are required to perform the model generation.

The reference data collection is performed according to the well-established workflow of passive univariate (i.e. parameter free) macromodeling. First, a physical description of the reference device is instantiated in CAD tools that can provide the required highly detailed descriptions of the structure behavior by directly solving the associated Maxwell's or, more generally, first-principle methods, as outlined in Sec. 1.1.1. Then, the electrical ports through which the device interacts with the outer environment are defined, and a finite-bandwidth characterization of the system is obtained by collecting samples of a specified network function, typically, in scattering representation. When the generation of a parameterized macromodel is required, the reference device network function is sampled in correspondence of a finite number parameter values.

To derive a macromodel valid for a single parameter configuration, a rational fitting process, such as the vector fitting scheme recalled in Sec. 3.1.3 ([79, 14, 69]) is commonly applied to the available data to generate a rational reduced order model of the network function. This model is then made available in the form of state space or equivalent SPICE netlist, and exploited to speed-up system level simulations by replacing the complex first-principle description. In Sec. 1.2.1, it has been highlighted that embedding parameterization into macromodels enables a number of desirable possibilities, including fast design optimization, statistical assessments and worst-case analyses. This motivates the interest to develope a parameterized counterpart for the above described univariate macromodeling approach.

It is known that physically passive devices must always be represented or modeled by certified passive equivalents. When it is not the case, the mathematical representation can be the root cause of nonphysical instabilities [46, 51], as outlined in Sec. 1.2.1. While for univariate macromodels robust post-processing passivity enforcement schemes [50, 32, 54] can be successfully applied to achieve model passivity, the same is not true in the more involved parameterized setting. In this case the property must be guaranteed for all of the possible parameter configurations of interest, in the sense that passivity must hold *uniformly* over the considered parameter set. This introduces significant technical difficulties that make passive parameterized macromodeling an open research topic. In fact, currently available state-of-the-art techniques are not able to guarantee the generation of parameterized macromodels that are concurrently accurate, compact and uniformly passive.

The available strategies are based either on *root macromodels interpolation* or on *multivariate rational fitting*. The ideas behind these two approaches and the related pros and cons are summarized below, before introducing our novel approach.

Parameterized macromodeling via root macromodel interpolation.

Root macromodels interpolation methods generate a passive reduced order parameterized model $\mathsf{H}(s,\boldsymbol{\vartheta})$ based on the availability of univariate (i.e. not depending on $\boldsymbol{\vartheta}$) macromodels. Various different implementations have been proposed [39, 41, 40, 91]. Most these approaches follow the general procedure discussed below.

A set of parameters of interest is defined according to (2.55). Then, a multidimensional grid with nodes $\boldsymbol{\vartheta}_g,\ g=1,\dots G$ is defined over this parameter space. For each node of the grid $\boldsymbol{\vartheta}_g$, the reference system transfer function $\breve{\mathsf{H}}(s,\boldsymbol{\vartheta})$ is sampled or measured leading to the samples

$$\tilde{H}_{k,g}=\tilde{\mathsf{H}}(j\omega_k,\boldsymbol{\vartheta}_g),\quad k=1,...K. \tag{4.1}$$

A rational fitting scheme, (such as VF, see Sec. 3.1.3) is then used to generate a *root* macromodel $\mathsf{H}_g(s)$ that verifies the approximation $\mathsf{H}_g(j\omega_k)\approx\mathsf{H}(j\omega_k,\boldsymbol{\vartheta}_g)$ over the available frequency samples. All root macromodels are then independently processed by standard algorithms [50, 32, 54] to enforce their passivity.

Once the passive root macromodels $\mathsf{H}_g(s),\ g=1,\dots G$ are available, the desired parameterized macromodel is obtained via interpolation

$$\mathsf{H}(s,\boldsymbol{\vartheta})=\sum_{g=1}^{G}\mathsf{H}_g(s)\lambda_g(\boldsymbol{\vartheta}). \tag{4.2}$$

It turns out that the interpolating functions $\lambda(\boldsymbol{\vartheta})$ can be chosen so that the resulting model $\mathsf{H}(s,\boldsymbol{\vartheta})$ is passive uniformly over Θ.

The procedure is simple, robust and straightforward. However, presents a number of drawbacks.

- The number of poles of $\mathsf{H}(s, \boldsymbol{\vartheta})$ is generally different and larger than the number of poles of each root macromodel, since the parameterized model is a weighted sum of the root macromodels. This parameter-dependent complexity is nonphysical and may introduce modeling artifacts (e.g. fictitious resonant behaviors).

- The model representation is not compact, since it requires the availability of G different macromodels. When G is large, the model compactness is inevitably lost, and the model must be returned in the form, for example, of large netlists embedding the individual roots descriptions.

The above described approach is based on transfer function. Other techniques have also been proposed to interpolate the corresponding state space matrices [41, 40, 91]. When interpolating the state space matrices, the complexity of the parameterized model is kept constant, but the model representation compactness is still lost. Additionally, the non-uniqueness of the state space representation can lead to inconsistent interpolation results. In [91], the problem is tackled by representing the root state space systems based on a common similarity transformation. However, robustness and scalability of this approach have not been documented yet.

Parameterized macromodeling via multivariate rational fitting

The second approach for the generation of passive parameterized macromodels seeks for an implicit and global parameterization of the structure behavior, obtained by means of multivariate rational fitting [33, 103]. The PSK iteration presented in Sec. 3.2.1 provides the reference framework for this approach. Its main advantages are a compact representation in terms of numerator and denominator coefficients, and a model order that is independent on $\boldsymbol{\vartheta}$.

The compactness of the model, however, introduces relevant technical difficulties when the rational approximation must ensure model stability and passivity uniformly in Θ. The basic formulation of the PSK algorithm does not guarantee these properties. A number of strategies have been therefore proposed to solve the problem, see e.g. [116, 114]

All of the currently available methods aimed at guaranteeing asymptotic stability of $\mathsf{H}(s, \boldsymbol{\vartheta})$ are based on the enforcement of the following condition

$$\mathsf{D}^{\star}(j\omega, \boldsymbol{\vartheta}) + \mathsf{D}(j\omega, \boldsymbol{\vartheta}) \geq 0 \quad \forall \boldsymbol{\vartheta} \in \Theta, \forall \omega. \tag{4.3}$$

As will be more rigorously discussed in Sec. 4.3, the above implies that the poles of model (4.8) are stable $\forall \boldsymbol{\vartheta} \in \Theta$. Sampling-based techniques [114, 115] try to enforce

condition (4.4) during the PSK iteration. At iteration ν these methods evaluate the previously estimated function $\mathsf{D}^{\nu-1}(j\omega, \boldsymbol{\vartheta})$ searching for parameter configurations $\boldsymbol{\vartheta}_v$ for which (4.4) is not verified. Then, they require

$$\mathsf{D}^{\nu\star}(j\omega, \boldsymbol{\vartheta}_v) + \mathsf{D}^{\nu}(j\omega, \boldsymbol{\vartheta}_v) \geq 0 \forall \omega, \tag{4.4}$$

by means of suitable linear constraints enforced on the coefficients $r^{\nu}_{i,\boldsymbol{\ell}}$. After the last iteration, the resulting denominator function $D^{\bar{\nu}}(j\omega, \boldsymbol{\vartheta})$ is sampled again over Θ. If (4.4) is still violated for some parameter configuration, the coefficients $r^{\bar{\nu}}_{i,\boldsymbol{\ell}}$ are iteratively perturbed until the violations are removed. This stability enforcement strategy is efficient and effective, but is not theoretically guaranteed to return uniformly stable models.

A more robust approach [116] for enforcing (4.4) relies in choosing uniformly positive parameter basis functions, $\xi_{\boldsymbol{\ell}}(\boldsymbol{\vartheta}) \geq 0 \ \forall \boldsymbol{\ell}$. In such a case it can be shown that (4.4) is verified if the following conditions are imposed on the model coefficients

$$\begin{cases} r_{i,\boldsymbol{\ell}} > 0 \ \forall \boldsymbol{\ell} \quad \text{if} \quad q_i \in \mathbb{R}, \\ -\alpha_i \cdot \mathrm{Re}\left\{r_{i,\boldsymbol{\ell}}\right\} \pm \beta_i \cdot \mathrm{Im}\left\{r_{i,\boldsymbol{\ell}}\right\} > 0 \ \forall \boldsymbol{\ell} \quad \text{if} \quad q_i = \alpha_i \pm j\beta_i. \end{cases} \tag{4.5}$$

The above linear constraints can be easily enforced while solving (3.36) using a convex formulation. Despite robust and reliable, this approach is conservative, since (4.5) are only sufficient conditions for (4.4), which in turn is a sufficient condition for uniform stability. Therefore, the constraints (4.5) may significantly restrict the set of parameterized models that can be identified, with a possible accuracy degradation.

When parameterized macromodels are obtained via PSK iteration, none of the current state-of-the-art approaches can guarantee theoretically their uniform passivity. Currently available strategies try to overcome this problem by enforcing model passivity in post-processing, similarly to what is commonly done for univariate macromodels. These techniques extend widespread passivity enforcement schemes [50, 32, 54] to the parameterized case, by sampling Θ in order to detect locations where the model is not passive, and to apply suitable model coefficients perturbations [114]. Under the assumption that a stable but not passive model $\mathsf{H}(s, \boldsymbol{\vartheta})$ is available (we assume a scattering representation), passivity is enforced by iteratively perturbing the model coefficients, in order to verify

$$\mathbb{I}_{\mathrm{P}} - \mathsf{H}^{\star}(j\omega, \boldsymbol{\vartheta}_v)\mathsf{H}(j\omega, \boldsymbol{\vartheta}_v) \succeq 0 \quad \forall \omega \in \mathbb{R} \tag{4.6}$$

in correspondence of a finite number of parameter configurations $\boldsymbol{\vartheta}_v$ where the above condition is violated. These parameter configurations are usually detected via adaptive sampling of the parameter space Θ. This approach is usually effective, but presents two main drawbacks

- There is no formal guarantee that the sampling procedure detects all of the parameter configurations $\boldsymbol{\vartheta}_v$ where (4.6) is violated

- The iterative perturbation enforces (4.6) based on non-exact (linearized) constraints, as in standard passivity enforcement schemes [50]. Removal of the passivity violations may require a large number of iterations and the process is not guaranteed to converge.

The proposed approach

The contribution of this chapter is to describe a novel constrained multivariate rational fitting scheme, that allows to overcome the above limitations and drawbacks, by providing accurate and compact models that are stable and passive by construction. The approach, first presented in [21, 20] can be summarized as follows.

1. The model structure is defined according to the PSK framework outlined in Sec. 3.2.1. This guarantees a compact model representation. The employed parameter-dependent basis functions, $\xi(\boldsymbol{\vartheta})$, are chosen to be multivariate Bernstein polynomials. This choice is not restrictive since any polynomial can be written in the Bernstein basis over a closed interval.

2. Stability conditions along frequency are expressed as a (continuously) parameterized linear matrix inequality structured according to the Positive Real Lemma 2.6. These LMIs are aimed at constraining only the coefficients of the denominator function, $\mathsf{D}(s, \boldsymbol{\vartheta})$. Contrary to (4.5) these conditions are necessary and sufficient to verify (4.4).

3. The above parameterized matrix inequality is cast into a finite number of standard (parameter-free) LMIs, that provide *sufficient conditions* for uniform stability. The discretization process is performed by taking advantage of the Bernstein polynomials properties.

4. The passivity conditions along frequency are expressed as another parameterized linear matrix inequality, by exploiting the Kalman-Yakubovich-Popov Lemma 2.9. This parameterized LMI constrains only the coefficients of the numerator function, $\mathsf{N}(s, \boldsymbol{\vartheta})$.

5. Similarly to point 3, the above parameter-dependent condition is discretized into a set of standard LMIs that provide *sufficient conditions* to guarantee the passivity of the model. This avoids the necessity of any sampling-based post-processing scheme.

6. The conservativity introduced by the discretization in points 3 and 5 is reduced by exploiting a special degree elevation property of Bernstein polynomials.

In the above list, the crucial steps are represented by the discretization process of the stability and passivity constraints, performed by applying the properties of the Bernstein polynomials used to parameterize the model coefficients. The usefulness of this properties for handling parameter-dependent LMIs has been also recently discussed in [67] in a more general setting.

From the numerical standpoint, the proposed modeling scheme requires computing

- the iterative low-complexity estimate of the model denominator constrained by the proposed set of LMIs, aimed at enforcing uniform stability (i.e., solving problem (3.36) subject to LMI constraints)
- the solution of a single higher-complexity semidefinite program for the identification of the numerator coefficients, which guarantees uniform model passivity (i.e., solving problem (3.37) subject again to LMI constraints)

As a result, the procedure is fully deterministic and robust, since no sampling of the parameter space is required to derive the required constraints. Since the formulation is convex, the involved optimization problems can be solved in polynomial time using standard optimization software.

The only drawback of the proposed approach is represented by the complexity of the models that can be processed. The scalability analysis and the numerical examples that are presented at the end of the chapter show that small and medium-scale models can be generated with modest time requirements .The method, however, does not scale favorably with the model complexity, intended as a cumulative contribution of model order (number of poles and parameter-dependent basis functions) and number of interface ports. This applicability limit is common to all the strategies that are based on the solution of semidefinite optimization problems, not only in the framework of model order reduction, but also in the general field of modern control system engineering and numerical linear algebra.

4.1 Problem statement

Consider a P-port passive LTI system, whose behavior depends on d physical or design parameters, collected in the vector $\boldsymbol{\vartheta} = (\vartheta_1, ..., \vartheta_d) \in \Theta$, defined as in (2.55). It is assumed that a highly accurate yet complex first-principle model is available for the P $\times$ P transfer function of the system, $\tilde{\mathsf{H}}(s, \boldsymbol{\vartheta})$, here assumed in scattering representation. The PSK algorithm is used to generate a compact parameterized macromodel $\mathsf{H}(s, \boldsymbol{\vartheta})$ that verifies the approximation

$$\mathsf{H}(j\omega_k, \boldsymbol{\vartheta}_m) \approx \tilde{\mathsf{H}}(j\omega_k, \boldsymbol{\vartheta}) = \tilde{H}_{k,m}, \quad k = 1, ...K, \quad m = 1, ..., M. \tag{4.7}$$

with model structure

$$\mathsf{H}(s,\boldsymbol{\vartheta}) = \frac{\mathsf{N}(s,\boldsymbol{\vartheta})}{\mathsf{D}(s,\boldsymbol{\vartheta})} = \frac{\sum_{i=0}^{n}\sum_{\boldsymbol{\ell}\in\mathcal{I}_{\bar{\boldsymbol{\ell}}}} R_{i,\boldsymbol{\ell}}\ \xi_{\boldsymbol{\ell}}(\boldsymbol{\vartheta})\ \varphi_i(s)}{\sum_{i=0}^{n}\sum_{\boldsymbol{\ell}\in\mathcal{I}_{\bar{\boldsymbol{\ell}}}} r_{i,\boldsymbol{\ell}}\ \xi_{\boldsymbol{\ell}}(\boldsymbol{\vartheta})\ \varphi_i(s)}. \tag{4.8}$$

The necessary and sufficient conditions for the passivity of a generic scattering or immittance LTI system in terms of its transfer matrix are given in 2.9 and 2.8. In the parameterized setting, the conditions must be verified over the whole parameter space, so that the model is uniformly passive if and only if

1. $\mathsf{H}(s,\boldsymbol{\vartheta})$ regular for $\mathrm{Re}\{s\} > 0 \quad \forall\boldsymbol{\vartheta}\in\Theta$
2. $\mathsf{H}^*(s,\boldsymbol{\vartheta}) = \mathsf{H}(s^*,\boldsymbol{\vartheta}) \quad \forall s\in\mathbb{C},\ \forall\boldsymbol{\vartheta}\in\Theta$
3. $\Phi(s,\boldsymbol{\vartheta}) \succeq 0 \quad$ for $\mathrm{Re}\{s\} > 0,\ \forall\boldsymbol{\vartheta}\in\Theta$

and

$$\Phi(s,\boldsymbol{\vartheta}) = \begin{cases} \mathbb{I}_{\mathrm{P}} - \mathsf{H}^{\star}(s,\boldsymbol{\vartheta})\mathsf{H}(s,\boldsymbol{\vartheta}) & \text{scattering,} \\ \mathsf{H}^{\star}(s,\boldsymbol{\vartheta}) + \mathsf{H}(s,\boldsymbol{\vartheta}) & \text{immittance.} \end{cases} \tag{4.9}$$

Without loss of generality, we will only consider the Bounded Realness case for Condition 3 in the following, since Positive Realness can be achieved with a straightforward adaptation. Noticing that the realness condition 2 is enforced by construction by adopted model structure (4.8), the uniform passivity is verified when the model $\mathsf{H}(s,\boldsymbol{\vartheta})$ fulfils also Conditions 1 and 3; this leads to the formalization of the following two problems.

Problem 4.1. *Estimate the model coefficients $r_{i,\boldsymbol{\ell}}$, so that Condition 1 is fulfilled* (uniform stability)

Problem 4.2. *Assuming uniform stability, estimate the model coefficients $R_{i,\boldsymbol{\ell}}$, so that Condition 3 is fulfilled* (uniform passivity).

Notice that, in agreement with available literature concerning passive parameterized macromodeling, uniform stability is obtained by constraining the estimate of the denominator $\mathsf{D}(s,\boldsymbol{\vartheta})$, and provides a necessary prerequisite to uniform passivity. The latter is controlled by constraining all model coefficients.

4.2 State space parameterization

The main enabling factors for the proposed solution for problems 4.1 and 4.2 are represented by

1. A particular choice of the parameter dependent basis functions $\xi_{\boldsymbol{\ell}}(\boldsymbol{\vartheta})$ used to parameterize the model.

2. The definition of two state space realizations for both model numerator $\mathsf{N}(s,\boldsymbol{\vartheta})$ and $\mathsf{D}(s,\boldsymbol{\vartheta})$, interpreted as individual transfer functions.

This section presents the necessary mathematical tools and definitions that are exploited in the proposed formulation.

4.2.1 Bernstein model parameterization

In the following, the parameter-dependent basis functions $\xi_{\boldsymbol{\ell}}(\boldsymbol{\vartheta})$ entering model structure (4.8) will be defined as multivariate Bernstein polynomials. For $d = 1$,

$$b_{\ell}^{\bar{\ell}}(\vartheta) = \binom{\bar{\ell}}{\ell} \vartheta^{\ell}(1-\vartheta)^{\bar{\ell}-\ell}, \quad \ell = 0, \dots, \bar{\ell} \tag{4.10}$$

is the ℓ-th Bernstein polynomial of degree $\bar{\ell}$ in the scalar variable ϑ. For $d > 1$, the basis function $\xi_{\boldsymbol{\ell}}(\boldsymbol{\vartheta})$ can be chosen to be the $\boldsymbol{\ell}$-th multivariate Bernstein polynomial of multi-degree $\overline{\boldsymbol{\ell}}$, defined as

$$\xi_{\boldsymbol{\ell}}(\boldsymbol{\vartheta}) \equiv b_{\boldsymbol{\ell}}^{\overline{\boldsymbol{\ell}}}(\boldsymbol{\vartheta}) = b_{\ell_1}^{\bar{\ell}_1}(\vartheta_1) \times \cdots \times b_{\ell_d}^{\bar{\ell}_d}(\vartheta_d) \tag{4.11}$$

where $\overline{\boldsymbol{\ell}}$ is defined as in (3.26). Given a multivariate polynomial matrix function expressed in Bernstein basis

$$F(\boldsymbol{\vartheta}) : \mathbb{R}^d \to \mathbb{R}^{m \times n} = \sum_{\boldsymbol{\ell} \in \mathcal{I}_{\overline{\boldsymbol{\ell}}}} F^{\boldsymbol{\ell}}\, b_{\boldsymbol{\ell}}^{\overline{\boldsymbol{\ell}}}(\boldsymbol{\vartheta}) \tag{4.12}$$

the elements of the set $\{F^{\boldsymbol{\ell}} : \boldsymbol{\ell} \in \mathcal{I}_{\overline{\boldsymbol{\ell}}}\}$, in short $\{F^{\boldsymbol{\ell}}\}$, are referred to as *control points*.

The following properties of Bernstein polynomials [13] will be exploited in the proposed derivations. First, these polynomials are non-negative and represent a partition of unity for any arbitrary number of variables d and any maximum degree $\overline{\boldsymbol{\ell}}$

$$b_{\boldsymbol{\ell}}^{\overline{\boldsymbol{\ell}}}(\boldsymbol{\vartheta}) \geq 0 \quad \forall \boldsymbol{\ell} \in \mathcal{I}_{\overline{\boldsymbol{\ell}}}, \qquad \sum_{\boldsymbol{\ell} \in \mathcal{I}_{\overline{\boldsymbol{\ell}}}} b_{\boldsymbol{\ell}}^{\overline{\boldsymbol{\ell}}}(\boldsymbol{\vartheta}) = 1, \quad \forall \boldsymbol{\vartheta} \in \Theta. \tag{4.13}$$

Due to these properties, all the values attained by functions (4.12) are obtained through a convex combination of the control points $\{F^{\boldsymbol{\ell}}\}$.

Any multivariate Bernstein polynomial of degree $\overline{\boldsymbol{\ell}}$ admits a representation in terms of a higher order Bernstein polynomial, that can be found via the *degree elevation* formula. Given a Bernstein polynomial $p(\boldsymbol{\vartheta})$ of degree $\overline{\boldsymbol{\ell}}$ and a degree increment $\boldsymbol{e} = (e_1, \dots, e_2) \geq \mathbf{0}$, $p(\boldsymbol{\vartheta})$ can be expressed equivalently as

$$p(\boldsymbol{\vartheta}) = \sum_{\boldsymbol{\ell} \in \mathcal{I}_{\overline{\boldsymbol{\ell}}}} p^{\boldsymbol{\ell}}\, b_{\boldsymbol{\ell}}^{\overline{\boldsymbol{\ell}}}(\boldsymbol{\vartheta}) = \sum_{\boldsymbol{\gamma} \in \mathcal{I}_{\overline{\boldsymbol{\gamma}}}} g^{\boldsymbol{\gamma}}\, b_{\boldsymbol{\gamma}}^{\overline{\boldsymbol{\gamma}}}(\boldsymbol{\vartheta}), \qquad \overline{\boldsymbol{\gamma}} = \overline{\boldsymbol{\ell}} + \boldsymbol{e}. \tag{4.14}$$

The new coefficients $g^{\boldsymbol{\gamma}}$ are convex combinations of the coefficients $p^{\boldsymbol{\ell}}$

$$g^{\boldsymbol{\gamma}} = \sum_{\boldsymbol{s}\in\mathcal{S}} \frac{\binom{\bar{\boldsymbol{\ell}}}{\boldsymbol{s}}\binom{\boldsymbol{e}}{\boldsymbol{\gamma}-\boldsymbol{s}}}{\binom{\bar{\boldsymbol{\ell}}+\boldsymbol{e}}{\boldsymbol{\gamma}}} p^{\boldsymbol{s}}, \quad \boldsymbol{\gamma}\in\mathcal{I}_{\overline{\boldsymbol{\gamma}}}, \tag{4.15}$$

where the sum is performed over the set of multi-indices $\mathcal{S} = \{\boldsymbol{s} : \boldsymbol{s} = \max(\boldsymbol{0}, \boldsymbol{\gamma} - \boldsymbol{e}), \dots, \min(\bar{\boldsymbol{\ell}}, \boldsymbol{\gamma})\}$. Lastly, given two Bernstein polynomials $p(\boldsymbol{\vartheta})$, $g(\boldsymbol{\vartheta})$ of total degree $\bar{\boldsymbol{\ell}}$ and $\overline{\boldsymbol{\gamma}}$ respectively, their product $h(\boldsymbol{\vartheta})$ is another polynomial of total degree $\overline{\boldsymbol{\beta}} = \bar{\boldsymbol{\ell}} + \overline{\boldsymbol{\gamma}}$, with coefficients $h^{\boldsymbol{\beta}}$ defined as

$$h^{\boldsymbol{\beta}} = \sum_{\boldsymbol{s}\in\mathcal{S}} \frac{\binom{\bar{\boldsymbol{\ell}}}{\boldsymbol{s}}\binom{\overline{\boldsymbol{\gamma}}}{\boldsymbol{\beta}-\boldsymbol{s}}}{\binom{\bar{\boldsymbol{\ell}}+\overline{\boldsymbol{\gamma}}}{\boldsymbol{\beta}}} p^{\boldsymbol{s}} g^{\boldsymbol{\beta}-\boldsymbol{s}}, \quad \boldsymbol{\beta}\in\mathcal{I}_{\overline{\boldsymbol{\beta}}} \tag{4.16}$$

where $\mathcal{S} = \{\boldsymbol{s} : \boldsymbol{s} = \max(\boldsymbol{0}, \boldsymbol{\beta} - \overline{\boldsymbol{\gamma}}), \dots, \min(\bar{\boldsymbol{\ell}}, \boldsymbol{\beta})\}$.

4.2.2 State space formulations

The transfer function $\mathsf{D}(s, \boldsymbol{\vartheta})$ can be realized in state space form as [103]

$$\mathsf{D}(s,\boldsymbol{\vartheta}) \leftrightarrow \Sigma_{\mathsf{D}} = \left(\begin{array}{c|c} A_1 & B_1 \\ \hline C_1(\boldsymbol{\vartheta}) & D_1(\boldsymbol{\vartheta}) \end{array}\right), \tag{4.17}$$

where the constant matrices A_1, B_1 are

$$A_1 = \operatorname{blkdiag}\{A_{1,i}\} \in \mathbb{R}^{n\times n} \tag{4.18}$$

$$B_1 = [\dots, B_{1,i}, \dots]^\top \in \mathbb{R}^n, \tag{4.19}$$

and

$$A_{1,i} = \begin{cases} q_i, & q_i \in \mathbb{R} \\ \begin{bmatrix} \sigma_i & \omega_i \\ -\omega_i & \sigma_i \end{bmatrix}, & q_i = \sigma_i \pm j\omega_i \in \mathbb{C} \end{cases} \tag{4.20}$$

$$B_{1,i} = \begin{cases} 1, & q_i \in \mathbb{R} \\ \begin{bmatrix} 2 & 0 \end{bmatrix}, & q_i = \sigma_i \pm j\omega_i \in \mathbb{C} \end{cases} \tag{4.21}$$

By construction, the pair (A_1, B_1) is controllable and A_1 is stable, as $\operatorname{Re}\{q_i\} < 0\ \forall i$. Under the choice of basis functions (4.11), the matrices describing the output equations are available as Bernstein polynomials and read

$$C_1(\boldsymbol{\vartheta}) = \sum_{\boldsymbol{\ell}\in\mathcal{I}_{\bar{\boldsymbol{\ell}}}} C_1^{\boldsymbol{\ell}}\, b_{\boldsymbol{\ell}}^{\bar{\boldsymbol{\ell}}}(\boldsymbol{\vartheta}), \quad C_1^{\boldsymbol{\ell}} = [r_{1,\boldsymbol{\ell}}, \dots, r_{n,\boldsymbol{\ell}}] \in \mathbb{R}^{1\times n} \tag{4.22}$$

$$D_1(\boldsymbol{\vartheta}) = \sum_{\boldsymbol{\ell}\in\mathcal{I}_{\bar{\boldsymbol{\ell}}}} D_1^{\boldsymbol{\ell}}\, b_{\boldsymbol{\ell}}^{\bar{\boldsymbol{\ell}}}(\boldsymbol{\vartheta}), \quad D_1^{\boldsymbol{\ell}} = r_{0,\boldsymbol{\ell}} \in \mathbb{R}. \tag{4.23}$$

Using a similar construction, the numerator transfer function $\mathsf{N}(s,\boldsymbol{\vartheta})$ is realized as

$$\mathsf{N}(s,\boldsymbol{\vartheta}) \leftrightarrow \Sigma_{\mathsf{N}} = \left(\begin{array}{c|c} A & B \\ \hline C_2(\boldsymbol{\vartheta}) & D_2(\boldsymbol{\vartheta}) \end{array}\right) \tag{4.24}$$

where $A = \mathbb{I}_{\mathrm{P}} \otimes A_1$ and $B = \mathbb{I}_{\mathrm{P}} \otimes B_1$ and

$$C_2(\boldsymbol{\vartheta}) = \sum_{\boldsymbol{\ell} \in \mathcal{I}_{\bar{\boldsymbol{\ell}}}} C_2^{\boldsymbol{\ell}}\, b_{\boldsymbol{\ell}}^{\bar{\boldsymbol{\ell}}}(\boldsymbol{\vartheta}) \qquad\qquad C_2^{\boldsymbol{\ell}} \in \mathbb{R}^{\mathrm{P}\times n\mathrm{P}}, \tag{4.25}$$

$$D_2(\boldsymbol{\vartheta}) = \sum_{\boldsymbol{\ell} \in \mathcal{I}_{\bar{\boldsymbol{\ell}}}} D_2^{\boldsymbol{\ell}}\, b_{\boldsymbol{\ell}}^{\bar{\boldsymbol{\ell}}}(\boldsymbol{\vartheta}) \qquad\qquad D_2^{\boldsymbol{\ell}} = R_{0,\boldsymbol{\ell}} \in \mathbb{R}^{\mathrm{P}\times\mathrm{P}}. \tag{4.26}$$

Given a multi-index $\boldsymbol{\ell}$, matrix $C_2^{\boldsymbol{\ell}}$ collects the entries of the model coefficients $R_{i,\boldsymbol{\ell}}$, $i > 0$ with a suitable ordering. The pair (A, B) inherits the controllability property from (A_1, B_1). All of the eigenvalues of A are stable.

4.3 Uniform stability enforcement

This section presents a solution for Problem 4.1 and derives a set of algebraic and convex constraints providing a guaranteed uniform stability of the model.

Due to the adopted model structure (4.8), uniform stability is enforced by constraining all the zeros of the denominator $\mathsf{D}(s,\boldsymbol{\vartheta})$ to be placed in the open left-half complex plane, as these zeros coincide with the parameter-dependent model poles. The denominator $\mathsf{D}(s,\boldsymbol{\vartheta})$ satisfies by construction Conditions 1, 2 of Sec. 4.1 since it is a real rational function with poles having strictly negative real part. If we can construct this function so that it verifies also the immittance dissipativity condition (3)

$$\mathsf{D}^{\star}(s,\boldsymbol{\vartheta}) + \mathsf{D}(s,\boldsymbol{\vartheta}) \succeq 0 \quad \text{for } \mathrm{Re}\,\{s\} > 0,\ \forall \boldsymbol{\vartheta} \in \Theta \tag{4.27}$$

then it becomes a certified uniformly Positive Real function. Since any PR function is also minimum phase [110] with stable zeros, enforcing this condition guarantees indirectly the uniform stability of the model $\mathsf{H}(s,\boldsymbol{\vartheta})$. Note that, under the adopted model structure, this condition can be restricted to the imaginary axis, as

$$\mathsf{D}^{\star}(j\omega,\boldsymbol{\vartheta}) + \mathsf{D}(j\omega,\boldsymbol{\vartheta}) \geq 0 \quad \forall \boldsymbol{\vartheta} \in \Theta, \forall \omega, \tag{4.28}$$

since $\mathsf{D}(s,\boldsymbol{\vartheta})$ is asymptotically stable and bounded for $s \to \infty$, without poles on the imaginary axis $s = j\omega$.

This fact has been repeatedly exploited in the literature to generate stable parameterized macromodels [114, 116, 52]. From the numerical point of view, (4.28) is not suitable to be enforced directly, as it represents an infinite number of constraints to be verified over the entire continuous frequency-parameter space. In what follows, we propose an approach to overcome this issue.

Considering the realization (4.17) and defining $Z_1(j\omega) = (j\omega\mathbb{I}_\mathrm{P} - A_1)^{-1}B_1$, Condition (4.28) is reformulated as

$$Z_1(j\omega)^\star C_1(\boldsymbol{\vartheta})^\top + C_1(\boldsymbol{\vartheta})Z_1(j\omega) + 2D_1(\boldsymbol{\vartheta}) \geq 0, \tag{4.29}$$

that must hold $\forall\boldsymbol{\vartheta} \in \Theta, \forall\omega$, or in the more compact matrix form

$$\begin{bmatrix} Z_1(j\omega) \\ \mathbb{I}_\mathrm{P} \end{bmatrix}^\star \begin{bmatrix} 0 & -C_1(\boldsymbol{\vartheta})^\top \\ -C_1(\boldsymbol{\vartheta}) & -2D_1(\boldsymbol{\vartheta}) \end{bmatrix} \begin{bmatrix} Z_1(j\omega) \\ \mathbb{I}_\mathrm{P} \end{bmatrix} \leq 0. \tag{4.30}$$

Since the pair (A_1, B_1) is controllable, we can exploit the equivalence between points 1 and 2 in the KYP lemma 2.9 to replace this frequency domain inequality with the equivalent algebraic condition

$$\begin{aligned} &\forall\boldsymbol{\vartheta} \in \Theta, \quad \exists L(\boldsymbol{\vartheta}) \in \mathbb{S}_n : \\ &\Omega(A_1, B_1, L(\boldsymbol{\vartheta})) - \begin{bmatrix} 0 & C_1(\boldsymbol{\vartheta})^\top \\ C_1(\boldsymbol{\vartheta}) & 2D_1(\boldsymbol{\vartheta}) \end{bmatrix} \preceq 0, \end{aligned} \tag{4.31}$$

where $\Omega(A_1, B_1, L(\boldsymbol{\vartheta}))$ is defined as in Theorem 2.9 and $L(\boldsymbol{\vartheta})$ plays the role of a parameter-dependent matrix that can be used to define a quadratic storage function.

Condition (4.31) represents a robust LMI condition in which the variables are the instrumental matrix $L(\boldsymbol{\vartheta})$ and the denominator coefficients $r_{i,\boldsymbol{\ell}}$ entering the denominator output matrices according to (4.22)-(4.23). Although this condition is convex, solving (3.36) to find the denominator coefficients while enforcing (4.31) for all $\boldsymbol{\vartheta} \in \Theta$ is numerically infeasible task. The application of the KYP lemma removed the dependency of the constraints on the variable ω, but the passivity condition still depends continuously on the parameter vector $\boldsymbol{\vartheta}$.

The problem is tackled by constraining the class of the instrumental matrices $L(\boldsymbol{\vartheta})$ to belong to a finite-dimensional subspace. In particular, a Bernstein polynomials expansion is adopted to define the structure of such a matrix, as

$$L(\boldsymbol{\vartheta}) = \sum_{\boldsymbol{\ell}\in\mathcal{I}_{\bar{\boldsymbol{\ell}}}} L^{\boldsymbol{\ell}}\, b^{\bar{\boldsymbol{\ell}}}_{\boldsymbol{\ell}}(\boldsymbol{\vartheta}), \quad L^{\boldsymbol{\ell}} \in \mathbb{S}_n \quad \forall\boldsymbol{\ell} \in \mathcal{I}_{\bar{\boldsymbol{\ell}}}, \tag{4.32}$$

based on a set of unknown symmetric matrix coefficients $\{L^{\boldsymbol{\ell}}\}$. Using (4.32), (4.31) turns into

$$\begin{aligned} &\forall\boldsymbol{\vartheta} \in \Theta\,, \exists L^{\boldsymbol{\ell}} \in \mathbb{S}_n,\, \boldsymbol{\ell} \in \mathcal{I}_{\bar{\boldsymbol{\ell}}} : \\ &S(\boldsymbol{\vartheta}) = \sum_{\boldsymbol{\ell}\in\mathcal{I}_{\bar{\boldsymbol{\ell}}}} S^{\boldsymbol{\ell}}\, b^{\bar{\boldsymbol{\ell}}}_{\boldsymbol{\ell}}(\boldsymbol{\vartheta}) \preceq 0, \end{aligned} \tag{4.33}$$

with

$$S^{\boldsymbol{\ell}} = \Omega(A_1, B_1, L^{\boldsymbol{\ell}}) - \begin{bmatrix} 0 & C_1^{\boldsymbol{\ell}\top} \\ C_1^{\boldsymbol{\ell}} & 2D_1^{\boldsymbol{\ell}} \end{bmatrix} \in \mathbb{S}_{n+1}. \tag{4.34}$$

Since all elements of the Bernstein basis are nonnegative, $b_{\boldsymbol{\ell}}^{\bar{\boldsymbol{\ell}}}(\boldsymbol{\vartheta}) \geq 0 \ \forall \boldsymbol{\ell} \in \mathcal{I}_{\bar{\boldsymbol{\ell}}}$, then (4.31) is entailed by the following sufficient conditions

$$S^{\boldsymbol{\ell}} \preceq 0 \qquad \forall \boldsymbol{\ell} \in \mathcal{I}_{\bar{\boldsymbol{\ell}}} \tag{4.35}$$

that can be used as a set of parameter-independent LMI constraints to be enforced during the estimation of the model denominator coefficients. Therefore, the proposed solution for uniform stability enforcement amounts at solving the following semi-definite program

$$\min_{x^\nu} \left\| \bar{T}^\nu x^\nu \right\|_2 \qquad \text{s.t.} \quad S^{\boldsymbol{\ell}} \preceq 0 \quad \forall \boldsymbol{\ell} \in \mathcal{I}_{\bar{\boldsymbol{\ell}}}, \tag{4.36}$$

which replaces the unconstrained least squares problem (3.36). The optimization problem (4.36) is a semidefinite program that can be solved through off-the-shelf convex optimization solvers.

Computational complexity analysis

Some considerations about the computational complexity of the proposed approach are in order. The solution of (4.36) involves $(n+1)V_{\bar{\boldsymbol{\ell}}}$ unknown model coefficients and $V_{\bar{\boldsymbol{\ell}}}((n+1)^2+n+1)/2$ instrumental variables. The size of the regressor matrix is $\mathrm{P}^2 V_{\bar{\boldsymbol{\ell}}} n \times V_{\bar{\boldsymbol{\ell}}} n$, as in (3.36). The size of the symmetric matrices entering the constraints is $n+1$, and the number of matrix constraints is $V_{\bar{\boldsymbol{\ell}}}$. As one could expect, the method suffers from a curse of dimensionality for large dimensions of the design space d, as both the number of denominator unknowns and the cardinality $V_{\bar{\boldsymbol{\ell}}}$ of the admissible indices grows exponentially with d. Nevertheless, as experimentally proved later in Sec. 4.6, the solution of (4.36) requires affordable (desktop-level) computational power when making use of state-of-the-art convex optimization solvers, at least when d is limited to few units.

We conclude this section by highlighting that both (4.32) and (4.35) do introduce some level of conservativity in the constraints when compared to the fully parameterized form (4.31). It will be shown in Sec. 4.5 that this amount can be effectively controlled and reduced thanks to the degree elevation property of the Bernstein polynomials.

4.4 Uniform passivity enforcement

In this section, a solution for Problem 4.2 of Sec. 4.1, addressing the uniform passivity enforcement of the model, is proposed. In the assumed scattering representation, enforcing the uniform passivity is the same as enforcing the model transfer function $\mathsf{H}(s,\boldsymbol{\vartheta})$ to be Bounded Real throughout the design space Θ. One prerequisite for this qualification is that the model is uniformly stable; therefore,

we assume that the coefficients x^ν defining $\mathsf{D}(s,\boldsymbol{\vartheta})$ have already been found by solving the convex program (4.36). For this reason, the following derivations will be focused on the identification of the numerator coefficients $R_{i,\boldsymbol{\ell}}$, assuming that the denominator coefficients are fixed and numerically available.

The non-expansivity Condition 3 of Sec. 4.1 can be replaced by the equivalent restriction to the imaginary axis

$$\mathsf{H}^\star(j\omega,\boldsymbol{\vartheta})\mathsf{H}(j\omega,\boldsymbol{\vartheta}) \preceq \mathbb{I}_\mathrm{P} \quad \forall\omega\in\mathbb{R},\, \forall\boldsymbol{\vartheta}\in\Theta, \tag{4.37}$$

similarly to (4.28). The exploitation of the model structure (4.8) allows to express the above as

$$\begin{aligned}&\mathsf{N}^\star(j\omega,\boldsymbol{\vartheta})\mathsf{N}(j\omega,\boldsymbol{\vartheta}) - \mathbb{I}_\mathrm{P}\,\mathsf{D}^\star(j\omega,\boldsymbol{\vartheta})\mathsf{D}(j\omega,\boldsymbol{\vartheta}) \preceq 0, \\ &\forall\omega\in\mathbb{R},\, \forall\boldsymbol{\vartheta}\in\Theta.\end{aligned} \tag{4.38}$$

Also in this case, the numerator and the denominator transfer functions can be expressed in terms of their state space realizations, as in Sec. 4.3. Before proceeding, a Multi-Input Multi-Output (MIMO) realization of the auxiliary system $\mathbb{I}_\mathrm{P}\mathsf{D}(s,\boldsymbol{\vartheta})$ appearing in (4.38) must be defined. This MIMO realization replicates the SISO denominator $\mathsf{D}(s,\boldsymbol{\vartheta})$ over the diagonal of the $\mathrm{P}\times\mathrm{P}$ matrix. The desired realization can be obtained as

$$\begin{aligned}\mathbb{I}_\mathrm{P}\mathsf{D}(s,\boldsymbol{\vartheta}) &\leftrightarrow \left(\begin{array}{c|c} \mathbb{I}_\mathrm{P}\otimes A_1 & \mathbb{I}_\mathrm{P}\otimes B_1 \\ \hline \mathbb{I}_\mathrm{P}\otimes C_1(\boldsymbol{\vartheta}) & \mathbb{I}_\mathrm{P}\otimes D_1(\boldsymbol{\vartheta}) \end{array}\right) \\ &= \left(\begin{array}{c|c} A & B \\ \hline C_\otimes(\boldsymbol{\vartheta}) & D_\otimes(\boldsymbol{\vartheta}) \end{array}\right),\end{aligned} \tag{4.39}$$

where all state space matrices are numerically available as the denominator coefficients have already been found. Here, the matrices A and B are the same entering the numerator state space Σ_N [103]. By defining $Z(j\omega) = (j\omega\mathbb{I}_{n\mathrm{P}} - A)^{-1}B$ and using (4.39), (4.24), condition (4.38) is cast into

$$\begin{bmatrix} Z(j\omega) \\ \mathbb{I}_\mathrm{P}\end{bmatrix}^\star \Big(X_2(\boldsymbol{\vartheta}) - X_\otimes(\boldsymbol{\vartheta})\Big) \begin{bmatrix} Z(j\omega) \\ \mathbb{I}_\mathrm{P}\end{bmatrix} \preceq 0, \tag{4.40}$$

which must hold $\forall\boldsymbol{\vartheta}\in\Theta$ and $\forall\omega$, where the auxiliary matrices are defined as

$$X_\mu(\boldsymbol{\vartheta}) = \begin{bmatrix} C_\mu^\top(\boldsymbol{\vartheta}) \\ D_\mu^\top(\boldsymbol{\vartheta})\end{bmatrix} \begin{bmatrix} C_\mu(\boldsymbol{\vartheta}) & D_\mu(\boldsymbol{\vartheta})\end{bmatrix}, \tag{4.41}$$

being μ a place-holder for the subscripts $\{2,\otimes\}$. As the pair (A,B) is controllable, the application of Theorem 2.6 allows to transform (4.52) into the equivalent parameter-dependent algebraic condition

$$\begin{aligned}&\forall\boldsymbol{\vartheta}\in\Theta, \quad \exists P(\boldsymbol{\vartheta})\in\mathbb{S}_{n\mathrm{P}}: \\ &X_2(\boldsymbol{\vartheta}) - X_\otimes(\boldsymbol{\vartheta}) + \Omega(A,B,P(\boldsymbol{\vartheta})) \preceq 0,\end{aligned} \tag{4.42}$$

that can be understood as an ad-hoc formulation of Theorem 2.7 for stable transfer functions which are parameterized according to the PSK model structure (4.8).

Condition (4.42) is analogous to (4.31), with the additional complication that the numerator unknowns that are embedded in the parameterization of $C_2(\boldsymbol{\vartheta})$, $D_2(\boldsymbol{\vartheta})$ enter quadratically in $X_2(\boldsymbol{\vartheta})$. However, (4.42) can be reformulated as a LMI. In first place, $X_{\otimes}(\boldsymbol{\vartheta})$ is rewritten as a sum of Bernstein polynomials of total degree $\overline{\boldsymbol{m}} = 2\overline{\boldsymbol{\ell}}$

$$X_{\otimes}(\boldsymbol{\vartheta}) = \sum_{\boldsymbol{m} \in \mathcal{I}_{\overline{\boldsymbol{m}}}} X^{\boldsymbol{m}}\, b_{\boldsymbol{m}}^{\overline{\boldsymbol{m}}}(\boldsymbol{\vartheta}) \tag{4.43}$$

being $X^{\boldsymbol{m}}$ symmetric matrix coefficients. Due to the numerical availability of the denominator coefficients $r_{i,\boldsymbol{\ell}}$, each $X^{\boldsymbol{m}}$ can be computed exactly as the product of polynomials in Bernstein basis, using formula (4.16). Then, applying the inverse Schur complement to (4.42), the equivalent LMI condition is obtained

$$\left[\begin{array}{c|c} \Omega(A, B, P(\boldsymbol{\vartheta})) - X_{\otimes}(\boldsymbol{\vartheta}) & \begin{bmatrix} C_2(\boldsymbol{\vartheta}) & D_2(\boldsymbol{\vartheta}) \end{bmatrix}^{\top} \\ \hline \begin{bmatrix} C_2(\boldsymbol{\vartheta}) & D_2(\boldsymbol{\vartheta}) \end{bmatrix} & -\mathbb{I}_{\mathrm{P}} \end{array}\right] \preceq 0 \tag{4.44}$$

which must be fulfilled $\forall \boldsymbol{\vartheta} \in \Theta$. As a third step, the degree elevation property of Bernstein polynomials (4.14) is applied to the off-diagonal blocks of (4.44). Specifically, $C_2(\boldsymbol{\vartheta})$ and $D_2(\boldsymbol{\vartheta})$ are rewritten as sums of Bernstein polynomials of total degree $\overline{\boldsymbol{m}}$ using the minimal degree-$\overline{\boldsymbol{\ell}}$ expansions (4.25)-(4.26); the result is rewritten compactly in the form

$$Y(\boldsymbol{\vartheta}) = \sum_{\boldsymbol{m} \in \mathcal{I}_{\overline{\boldsymbol{m}}}} Y^{\boldsymbol{m}}\, b_{\boldsymbol{m}}^{\overline{\boldsymbol{m}}}(\boldsymbol{\vartheta}) = \sum_{\boldsymbol{\ell} \in \mathcal{I}_{\overline{\boldsymbol{\ell}}}} \begin{bmatrix} C_2^{\boldsymbol{\ell}\top} \\ D_2^{\boldsymbol{\ell}\top} \end{bmatrix}\, b_{\boldsymbol{\ell}}^{\overline{\boldsymbol{\ell}}}(\boldsymbol{\vartheta}). \tag{4.45}$$

The entries of the matrix coefficients $Y^{\boldsymbol{m}}$ are linear combinations of the numerator coefficients embedded in $R_{i,\boldsymbol{\ell}}$. Lastly, the following structure for the instrumental matrix $P(\boldsymbol{\vartheta})$ is enforced

$$P(\boldsymbol{\vartheta}) = \sum_{\boldsymbol{m} \in \mathcal{I}_{\overline{\boldsymbol{m}}}} P^{\boldsymbol{m}}\, b_{\boldsymbol{m}}^{\overline{\boldsymbol{m}}}(\boldsymbol{\vartheta}), \quad P^{\boldsymbol{m}} \in \mathbb{S}_{n\mathrm{P}} \quad \forall \boldsymbol{m} \in \mathcal{I}_{\overline{\boldsymbol{m}}}. \tag{4.46}$$

Due to this assumption, all terms in (4.44) are Bernstein polynomials of total degree $\overline{\boldsymbol{m}}$, meaning that (4.44) can be rewritten as

$$F(\boldsymbol{\vartheta}) = \sum_{\boldsymbol{m} \in \mathcal{I}_{\overline{\boldsymbol{m}}}} F^{\boldsymbol{m}}\, b_{\boldsymbol{m}}^{\overline{\boldsymbol{m}}}(\boldsymbol{\vartheta}) \preceq 0 \quad \forall \boldsymbol{\vartheta} \in \Theta, \tag{4.47}$$

using (4.45) and (4.46) where the symmetric matrix coefficients

$$F^{\boldsymbol{m}} = \begin{bmatrix} \Omega(A, B, P^{\boldsymbol{m}}) - X^{\boldsymbol{m}} & Y^{\boldsymbol{m}} \\ Y^{\boldsymbol{m}\top} & -\mathbb{I}_{\mathrm{P}} \end{bmatrix} \in \mathbb{S}_g \tag{4.48}$$

have of size $g = \mathrm{P}n + 2\mathrm{P}$. Finally, due to the sign properties of the Bernstein polynomials, (4.44) is verified whenever the following set of linear matrix inequalities holds

$$F^{\boldsymbol{m}} \preceq 0, \quad \forall \boldsymbol{m} \in \mathcal{I}_{\overline{\boldsymbol{m}}}. \tag{4.49}$$

The above conditions can be easily coupled with the numerator estimation problem (3.37). The unconstrained least-squares system in the unknown variables Y^{ν} is thus replaced by the following LMI-constrained convex program

$$\min_{y_{i,j}^{\nu}} \sum_{i=1}^{\mathrm{P}} \sum_{j=1}^{\mathrm{P}} \left\| \Gamma^{\nu} y_{i,j}^{\nu} + \Xi_{i,j} x^{\nu} \right\|_2^2 \quad \text{s.t.} \quad F^{\boldsymbol{m}} \preceq 0, \quad \forall \boldsymbol{m} \in \mathcal{I}_{\overline{\boldsymbol{m}}}. \tag{4.50}$$

Computational complexity analysis

A set of numerator coefficients that guarantees the model uniform passivity can be obtained by solving (4.50). The row size of the data matrices entering (4.50) depends on the amount of training data samples. If the reference structure is reciprocal, then the cost function involved in the problem can be modified to estimate only the lower (upper) triangular elements of the numerator transfer function $\mathsf{N}(s, \boldsymbol{\vartheta})$; in this case the problem involves $V_{\overline{\boldsymbol{m}}}(n+1)(\mathrm{P}^2/2 + \mathrm{P}/2)$ unknowns and $V_{\overline{\boldsymbol{m}}}(\mathrm{P}^2 n^2/2 + \mathrm{P}n/2)$ instrumental variables. Therefore, the complexity of the problem depends not only on the total number $V_{\overline{\boldsymbol{m}}}$ of terms of the multivariate Bernstein basis used to model the passivity constraints, but also on the size of the system P of the device under modeling. This means that the proposed method is practically applicable only to small-medium scale devices. This limitation is expected, since it is a characteristic of all the passivity constraints formulation based on PR and BR lemmas.

We remark that the proposed derivations assume that the output matrices of Σ_{D} and Σ_{N} are expressed as Bernstein polynomials with common total degree $\overline{\boldsymbol{\ell}}$. If this assumption is dropped, the proposed method is still applicable, since the entries of the matrix function (4.44) can be expressed as Bernstein polynomial series of the same degree, by elevating the degree of the lower order terms.

Remark 4.1. When models in immittance representation are of interest, the proposed passivity enforcement scheme can be applied as well. In this case, the positive realness of the model transfer function is verified whenever

$$\mathsf{H}^{\star}(j\omega, \boldsymbol{\vartheta}) + \mathsf{H}(j\omega, \boldsymbol{\vartheta}) \succeq 0, \quad \forall \omega \in \mathbb{R}, \ \forall \boldsymbol{\vartheta} \in \Theta. \tag{4.51}$$

Expressing the above in terms of the state space realization of N and D leads to

$$\begin{bmatrix} Z(j\omega) \\ \mathbb{I}_{\mathrm{P}} \end{bmatrix}^{\star} \left(\begin{bmatrix} C_{\otimes}^{\top}(\boldsymbol{\vartheta}) \\ D_{\otimes}^{\top}(\boldsymbol{\vartheta}) \end{bmatrix} \begin{bmatrix} C_2(\boldsymbol{\vartheta}) & D_2(\boldsymbol{\vartheta}) \end{bmatrix} + \begin{bmatrix} C_2^{\top}(\boldsymbol{\vartheta}) \\ D_2^{\top}(\boldsymbol{\vartheta}) \end{bmatrix} \begin{bmatrix} C_{\otimes}(\boldsymbol{\vartheta}) & D_{\otimes}(\boldsymbol{\vartheta}) \end{bmatrix} \right) \begin{bmatrix} Z(j\omega) \\ \mathbb{I}_{\mathrm{P}} \end{bmatrix} \succeq 0. \tag{4.52}$$

The above condition is linear in the numerator unknowns embedded in $C_2(\boldsymbol{\vartheta})$ and $D_2(\boldsymbol{\vartheta})$. Applying the KYP lemma 2.6 with instrumental matrix $P(\boldsymbol{\vartheta})$ defined as in (4.46) leads to a parameterized LMI condition in the numerator coefficients and the symmetric matrices $P^{\boldsymbol{m}}$, which is frequency-independent. The condition can be then discretized into $V_{\bar{\boldsymbol{m}}}$ standard LMIs similar to (4.49) and enforced while solving (3.37). Differently from the scattering case, each of the involved LMIs is of size $\mathrm{P}n + \mathrm{P}$, since no application of the Schur complement is required to recover linearity in the problem unknowns.

4.5 Reducing conservativity

The pair of semidefinite optimization problems (4.36) and (4.50), when solved sequentially, provide a set of model coefficients that guarantee the uniform bounded realness of $\mathsf{H}(s, \boldsymbol{\vartheta})$ over Θ. All the steps leading to the linear matrix inequalities (4.35) and (4.49) are based on a sequence of necessary and sufficient implications, with two exceptions. The first is the restriction of the instrumental matrices $L(\boldsymbol{\vartheta})$ and $P(\boldsymbol{\vartheta})$ to a particular polynomial structure. This imposition reduces the space of storage functions that can be found to provide stability or passivity certificates for the model. This translates to a restriction of the set of models that can be generated. Therefore, the polynomial structure of the instrumental matrices introduces some conservativity in the modeling algorithm.

A second reason for conservativity stems from the discretization of (4.33) into (4.35) and of (4.47) into (4.49). With reference to the latter, the discretization process is conservative since $F(\boldsymbol{\vartheta})$ can be uniformly negative semi-definite even if some of the coefficients $F^{\boldsymbol{m}}$ are not. In this section, this limitation is analyzed in detail, and an effective methodology to reduce the introduced conservativity is proposed. This methodology allows to improve the overall model accuracy that can be achieved by the proposed approach.

Consider the replacement of (4.47) with the finite set of constraints (4.49). Let $\mathcal{F}$ be the set of matrices spanned by $F(\boldsymbol{\vartheta})$ as $\boldsymbol{\vartheta}$ spans the design space Θ. Since $F(\boldsymbol{\vartheta})$ is expressed as an expansion into Bernstein polynomial basis, $\mathcal{F}$ is a subset of the convex hull of the control points $\{F^{\boldsymbol{m}}\}$

$$\mathcal{F} = \{x : x = F(\boldsymbol{\vartheta}), \boldsymbol{\vartheta} \in \Theta\} \subseteq \mathrm{Conv}(\{F^{\boldsymbol{m}}\}). \tag{4.53}$$

The enforcement of (4.49) guarantees uniform passivity by requiring that the matrix coefficients $F^{\boldsymbol{m}}$ are individually negative semi-definite, in such a way that

$$F^{\boldsymbol{m}} \in \mathbb{S}_g^- \Rightarrow \mathrm{Conv}(\{F^{\boldsymbol{m}}\}) \subseteq \mathbb{S}_g^- \Rightarrow \mathcal{F} \subseteq \mathbb{S}_g^-. \tag{4.54}$$

The level of conservativity depends on the distance between $\mathcal{F}$ and the boundary of $\mathrm{Conv}(\{F^{\boldsymbol{m}}\})$. The larger this distance, the larger the degree of conservativity in

the passivity (stability) enforcement. Therefore, reduction of this distance will lead to a reduction of conservativity and to an improved model accuracy. Fortunately, the properties of Bernstein polynomials come at hand for this task, since it is well known that, for any matrix function in form (4.12), the set of control points (the matrix coefficients in the Bernstein expansion) converge uniformly to the value of the expanded function under repeated application of the degree elevation property [71, 38, 86]. This is graphically illustrated in Fig 4.1.

Let us apply this property to the present passivity (stability) enforcement case. We define $\boldsymbol{e} = \boldsymbol{m} + (e, \ldots, e)$. Then for any e we can always write

$$F(\boldsymbol{\vartheta}) = \sum_{\boldsymbol{m} \in \mathcal{I}_{\overline{\boldsymbol{m}}}} F^{\boldsymbol{m}}\, b_{\boldsymbol{m}}^{\overline{\boldsymbol{m}}}(\boldsymbol{\vartheta}) = \sum_{\boldsymbol{e} \in \mathcal{I}_{\overline{\boldsymbol{e}}}} F^{\boldsymbol{e}}\, b_{\boldsymbol{e}}^{\overline{\boldsymbol{e}}}(\boldsymbol{\vartheta}), \tag{4.55}$$

where the new control points $\{F^{\boldsymbol{e}}\}$ are obtained as convex combinations of $\{F^{\boldsymbol{m}}\}$ according to (4.15). We have

$$\mathcal{F} \subseteq \mathrm{Conv}(\{F^{\boldsymbol{e}}\}) \subseteq \mathrm{Conv}(\{F^{\boldsymbol{m}}\}), \quad \forall e \in \mathbb{N}. \tag{4.56}$$

For increasing e, we have the uniform convergence property [71]

$$\lim_{e \to \infty} \{F^{\boldsymbol{e}}\} = F(\boldsymbol{\vartheta}) \tag{4.57}$$

with a convergence rate $1/e$, see Fig. 4.1. For any given e, we can therefore replace (4.50) with a less conservative optimization problem

$$\min_{y_{i,j}^{\nu}} \sum_{i=1}^{\mathrm{P}} \sum_{j=1}^{\mathrm{P}} \left\| \Gamma^{\nu} y_{i,j}^{\nu} + \Xi_{i,j} x^{\nu} \right\|_2^2 \quad \text{s.t.} \quad F^{\boldsymbol{e}} \preceq 0, \quad \forall \boldsymbol{e} \in \mathcal{I}_{\overline{\boldsymbol{e}}} \tag{4.58}$$

where the constraint $F^{\boldsymbol{e}} \preceq 0$ becomes practically equivalent to (4.47) for sufficiently large e.

Switching to (4.58) does not modify the number of decision variables in the optimization. However, the number of LMI constraints increases becoming $V_{\overline{\boldsymbol{e}}}$, implying that conservativity reduction comes with an increase in computational cost. As a beneficial side effect, the degree elevation property may also lead to a relaxation of the structure imposed on the instrumental matrix $P(\boldsymbol{\vartheta})$, thereby addressing the first source of conservativity discussed at the beginning of this section. If applying the degree elevation *after* imposing a given structure of the storage function (4.46), this structure will not change even if expressed as a higher degree polynomial, and the dimension of the space spanned by the allowed storage functions will remain the same. Conversely, if a new degree-elevated structure

$$P(\boldsymbol{\vartheta}) = \sum_{\boldsymbol{e} \in \mathcal{I}_{\overline{\boldsymbol{e}}}} P^{\boldsymbol{e}}\, b_{\boldsymbol{e}}^{\overline{\boldsymbol{e}}}(\boldsymbol{\vartheta}), \quad P^{\boldsymbol{e}} \in \mathbb{S}_{n\mathrm{P}} \quad \forall \boldsymbol{e} \in \mathcal{I}_{\overline{\boldsymbol{e}}} \tag{4.59}$$

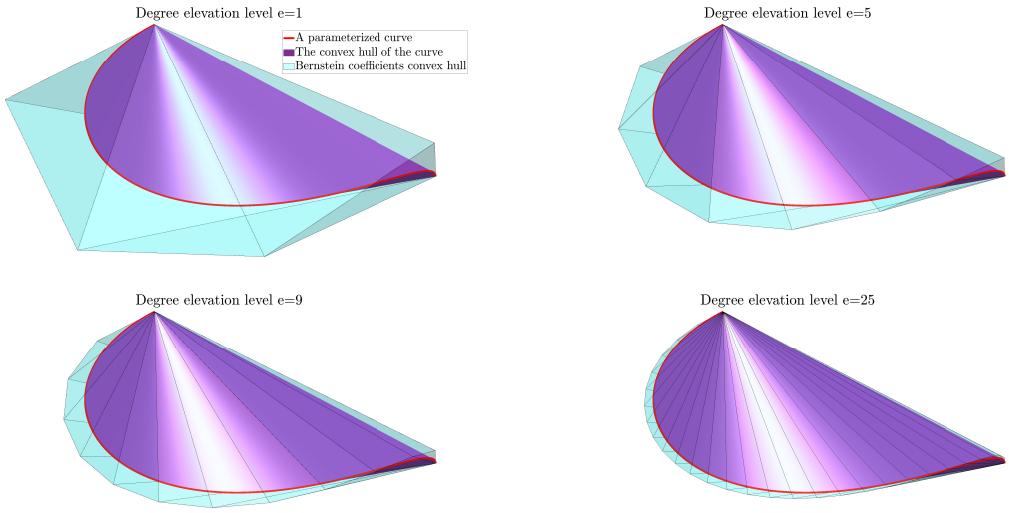

Figure 4.1: Graphical demonstration of the degree elevation effects. The red line represents the set $\mathcal{F}$ of the values attained by a function defined according to (4.12) for $d = 1$, $\overline{\ell} = 4$ and $F^\ell \in \mathbb{R}^3$; the purple volume is the convex hull of $\mathcal{F}$; the light blue polyhedra are the convex hulls of the control points $\{F^\ell\}$ for different levels of degree elevation. As the degree of the representation increases, the polyhedron approaches the underlying set $\mathcal{F}$, thus providing better and better outer approximations. Figure reproduced from [21] © 2022 IEEE.

of total degree $\overline{\boldsymbol{e}}$ is used since the beginning, all the corresponding control points $P^{\boldsymbol{e}}$ will provide independent degrees of freedom in a degree-$\overline{\boldsymbol{e}}$ expansion, therefore increasing the space of allowed storage functions enabling certification of model passivity (stability). Since polynomials converge to any arbitrary smooth multivariate function on a compact domain, this second strategy practically removes the limitations of the imposed polynomial structure on $P(\boldsymbol{\vartheta})$, as far as e is sufficiently large.

In our experiments, we observed that the degree elevation process is very effective in reducing the conservativity of the passivity constraints (4.49). Conversely, we did not observe relevant advantages in applying the same strategy to improve the stability constraints (4.36).

4.6 Numerical examples

The proposed passive parameterized macromodeling strategy is experimentally tested in this section. A number of numerical tests of increasing complexity are considered, in order to investigate the performance and the applicability limits

of proposed approach. All experiments have been performed using a workstation equipped with 32 GB of memory and a 3.3 GHz Intel i9-X7900 CPU using a prototypal MATLAB implementation.

All tests are based on the following settings. The denominator coefficients x^ν are always computed by solving problem (4.36), while the numerator coefficients y^ν are estimated at the last iteration by solving problem (4.58) with a given level of degree elevation e. When solving this problem, the structure of the matrix $P(\boldsymbol{\vartheta})$ is always defined as in (4.59); this implies that the number of variables involved in the problem is proportional to the number of considered constraints, i.e. $V_{\overline{\boldsymbol{e}}}$). The above mentioned semi-definite programs are handled via the YALMIP toolbox [73], exploiting the MOSEK interior point method for conic problems [6].

Iterations are stopped when the convergence index $\delta^\nu \leq 10^{-3}$ as defined in (3.21); the evolution of δ^ν over iterations is displayed below for each test case, in order to monitor convergence based on the stabilization of denominator coefficients. With reference to a given transfer function element $\mathsf{H}^{i,j}$ and the associated reference data $\breve{H}^{i,j}$, an overall error index is defined as

$$\epsilon_{i,j} = \max_{m=1,\dots,M} \sqrt{\frac{1}{K}\sum_{k=1}^{K}\left|\frac{\mathsf{H}^{i,j}(j\omega_k,\boldsymbol{\vartheta}_m) - \breve{H}^{i,j}_{k,m}}{\tilde{H}^{i,j}_{k,m}}\right|^2}, \tag{4.60}$$

which is representative of the worst case relative error of the model against the data over the design space.

In the considered datasets, the frequency-parameter spaces are sampled over logarithmically or linearly spaced grids. However, the proposed technique can be applied also in case the data are obtained according to some adaptive sampling strategy which leads to unstructured data distribution. Additionally, in some application scenarios, some a priori knowledge of the transfer function properties (e.g. degree of smoothness or resonance and anti-resonance locations) may be exploited to reduce the number K of frequency samples retrieved for each parameter configuration. This is not restrictive for the applicability of the method, provided that the data samples are sufficient to fully characterize the structure behavior.

As a final remark, notice that the automated selection of the model hyperparameters $\bar{\boldsymbol{\ell}}$ and n is still an open problem. In the following examples, this selection was performed in a preprocessing stage with a basic trial and error strategy.

4.6.1 An integrated inductor

In this test case a 2-port, 1.5 turns integrated inductor, parameterized by its side-length $\boldsymbol{\vartheta} \in [1.02, 1.52]$ mm is considered. The structure, schematically depicted

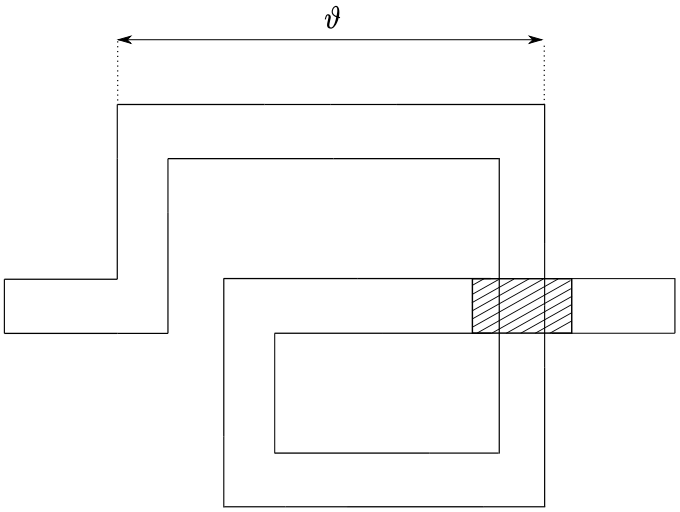

Figure 4.2: A 1.5-turn integrated inductor parameterized by the side-length $\boldsymbol{\vartheta} \in [1.02, 1.52]$ mm. Drawing is not to scale. Figure reproduced from [21] © 2022 IEEE.

in Fig. 4.2, is characterized in terms of its scattering parameters[1] in the bandwidth $[0.1, 12]$ GHz. A total of $M = 11$ parameter configurations are available as training data obtained from the solver Sonnet [97], with each dataset including $K = 477$ logarithmically distributed frequency samples.

These training data are used to generate a passive parameterized macromodel of dynamic order $n = 7$, using degree $\bar{\ell} = 2$ polynomials to represent the dependence of the model responses on the inductor side-length. With these settings, the solution of the semi-definite program (4.36) required 0.22 s on average for the 7 performed iterations. Figure 4.3 shows the evolution of the convergence index (3.21) as the iteration number increases.

At the last iteration $\bar{\nu} = 7$, problem (4.58) was solved for different values of the degree elevation level $e = 1, ...,50$, in order to show the effect of the proposed conservativity reduction. Fig. 4.4 reports the trend of the optimal cost function resulting from the solution of (4.58), as a function of e. This figure confirms the effectiveness of degree elevation in the reduction of the conservativity of passivity constraints, since the residual norm of the cost function is reduced by almost one order of magnitude. The corresponding CPU time requirements are depicted in Fig. 4.5, as a function of the total number of variables involved in the optimization, which in turn depends on the degree elevation order e. For this small-scale example, the computational time is modest even in the case $e = 50$, which is associated to a

[1]Data provided by Prof.Madhavan Swaminathan (Georgia Institute of Technology, USA)

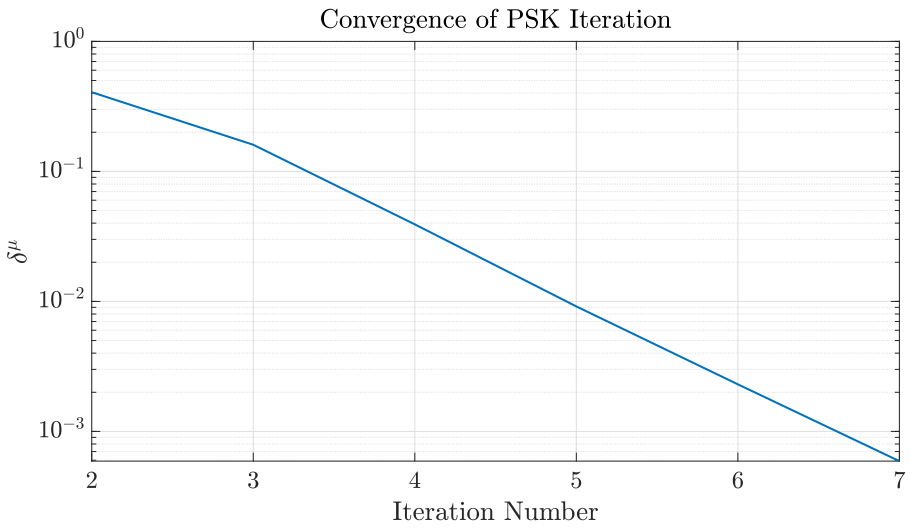

Figure 4.3: Integrated inductor. Normalized deviation of the denominator coefficients estimates, as a function of the iteration index ν. Figure reproduced from [21] © 2022 IEEE.

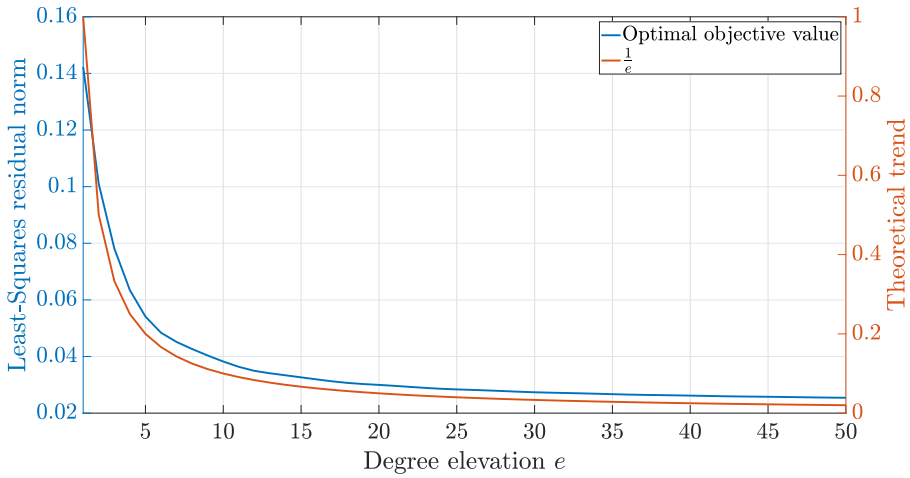

Figure 4.4: Integrated inductor. Residual norm of the constrained numerator coefficients estimation problem, as a function of the degree elevation level e. The experimental results are compared to a reference asymptotic $1/e$ trend, which is expected based on the theory [71]. Figure reproduced from [21] © 2022 IEEE.

total of 5847 unknowns.

Considering as an example the model obtained for $e = 50$, the non-expansivity condition 3 of the model was verified a-posteriori . Therefore, the model singular values were computed over a finely sampled frequency-parameter grid, using 3000 log-spaced frequency values in the bandwidth $[0, 10^{11}]$ Hz, and 3000 linearly spaced samples in the design space. The maximum observed singular value resulted less

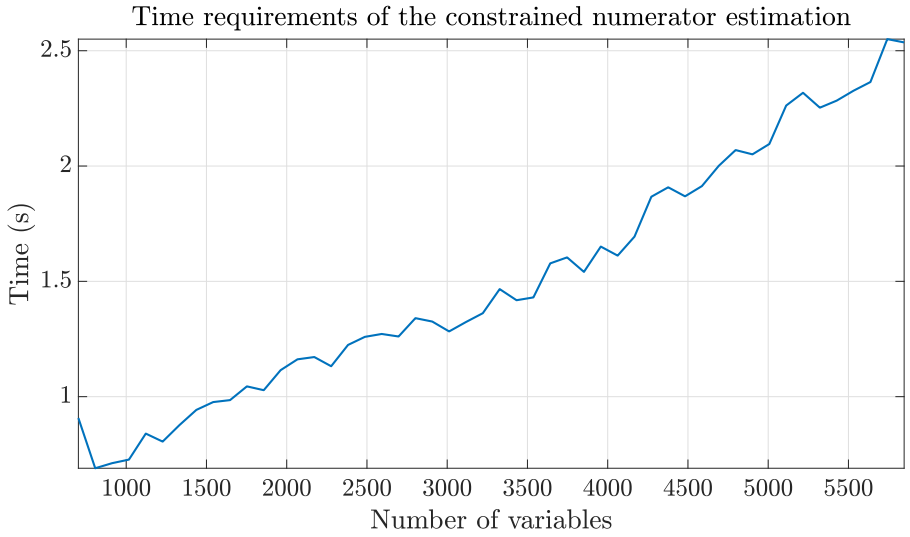

Figure 4.5: Integrated inductor. Time required to solve problem (4.58) as a function of the number of decision variables; the latter is directly proportional to the degree elevation e. Figure reproduced from [21] © 2022 IEEE.

than one, with a passivity margin $1 - \sigma_{\max} = 3 \times 10^{-10}$.

The quality of the resulting model (for the case $e = 50$) is confirmed by comparing the model responses to the training data in Fig. 4.6. Finally, Fig. 4.7 reports the relative error index $\epsilon_{2,1}$ as a function of the degree elevation e. The figure reports also the error that would be obtained by generating a model without enforcing any passivity constraint. It can be observed that starting from $e \approx 6$ the proposed approach is able to achieve a model accuracy that is not distinguishable from the unconstrained case. In conclusion, proposed framework is able to guarantee uniform model passivity by construction, with no accuracy degradation, and with limited overhead in computing time, at least for this small-scale example.

4.6.2 A multiconductor transmission line with variable coupling length

This second test case provides an academic example with a distributed coupling parameter. It consists of a multiconductor transmission line with two differential pairs, each made of two equal parallel wires (radius of copper core $r_w = 0.5$ mm and dielectric coating $r_e = 0.8$ mm). The two differential pairs are placed next to each other, so that the wire centers form a square with adjacent center-to-center distance equal to 1.61 mm . The total length of the interconnect is $L = 10$ cm, but the coupling between the two pairs in the corresponding per-unit-length matrices is considered only over a portion of the length $L_c = \vartheta \in \Theta = [20, 40]$ mm, which is the independent parameter considered for this study. The lines are considered

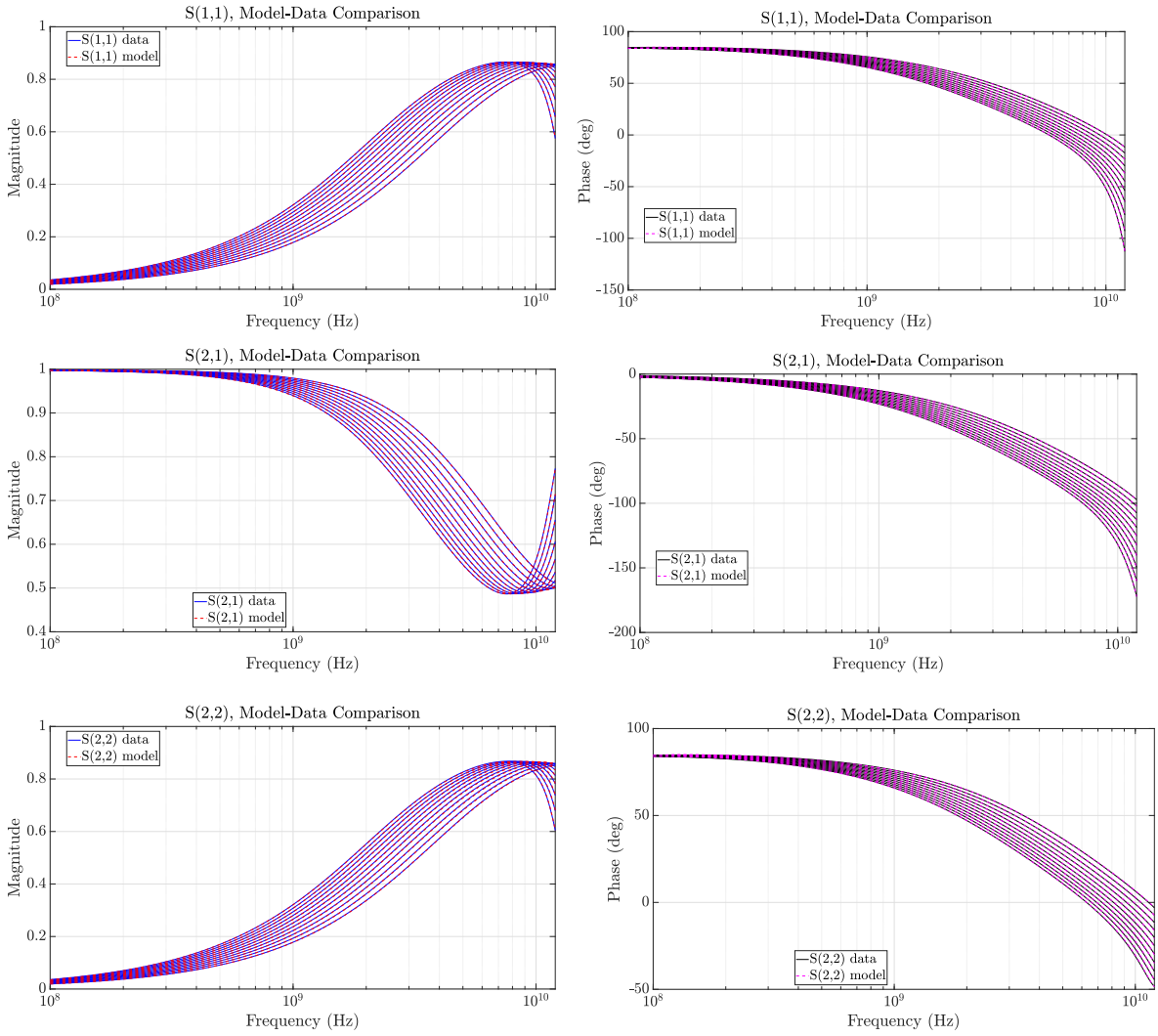

Figure 4.6: Integrated inductor. Comparison between parameterized model responses and training data for a degree elevation level $e = 50$; all the $M = 11$ parameter configurations are shown. Figure reproduced from [21] © 2022 IEEE.

as uncoupled for the remaining length $L - L_c$. Figure 4.8 provides a graphical description for the structure. This example is selected to illustrate the shifting of the resonances as ϑ changes, and the capability of the model to track such resonances (the parameterized model poles) thanks to the adopted model structure.

The design space is sampled with $M = 11$ linearly spaced values. For each parameter configuration a total of $K = 499$ logarithmically spaced frequency samples of the 4×4 scattering matrix are extracted in the bandwidth $[0.01, 5]$ GHz. These samples are used to generate a model of dynamic order $n = 28$, whereas numerator $\mathsf{N}(s, \boldsymbol{\vartheta})$ and denominator $\mathsf{D}(s, \boldsymbol{\vartheta})$ are parameterized by Bernstein polynomials of

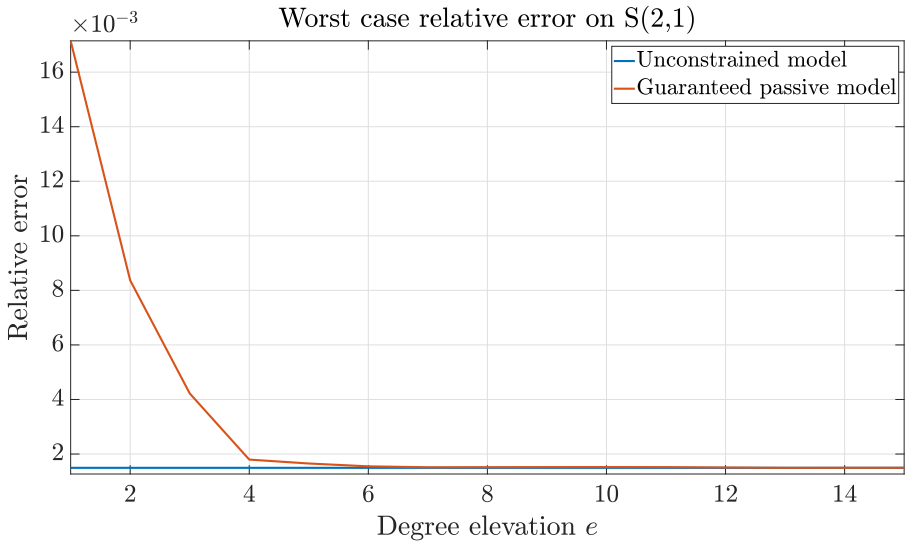

Figure 4.7: Integrated inductor. Relative error $\epsilon_{2,1}$ for different degree elevation levels e. The blue line reports the corresponding error for a model generated without enforcing any passivity constraint. Figure reproduced from [21] © 2022 IEEE.

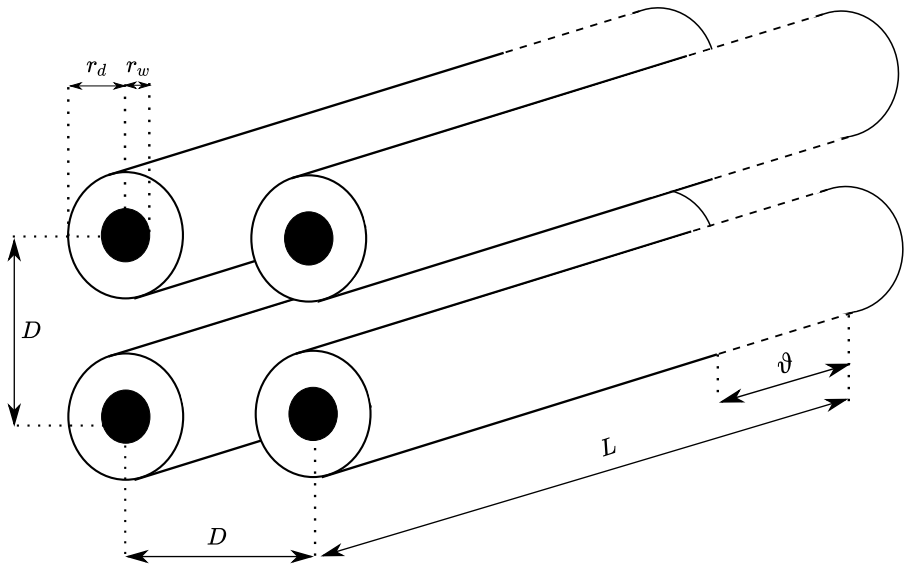

Figure 4.8: A partially-coupled multiconductor transmission line system. The parameter ϑ represents the length of the coupling. The drawing is not to scale. Figure reproduced from [21] © 2022 IEEE.

order 4 and 2, respectively.

The convergence of the identification algorithm is demonstrated in Fig. 4.9, where the value of δ^ν for $\nu \geq 1$ is reported. For this example, 10 different models

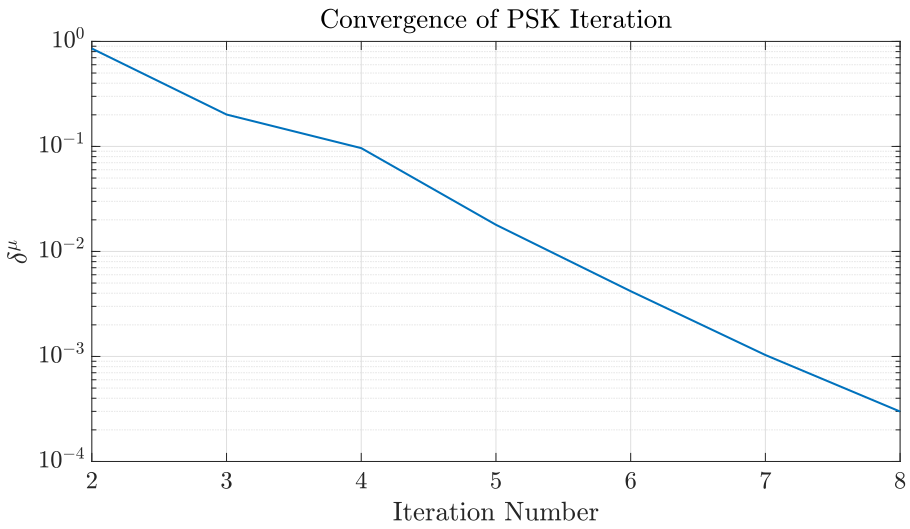

Figure 4.9: Coupled transmission line. Evolution of the convergence index δ^ν through iterations. Figure reproduced from [21] © 2022 IEEE.

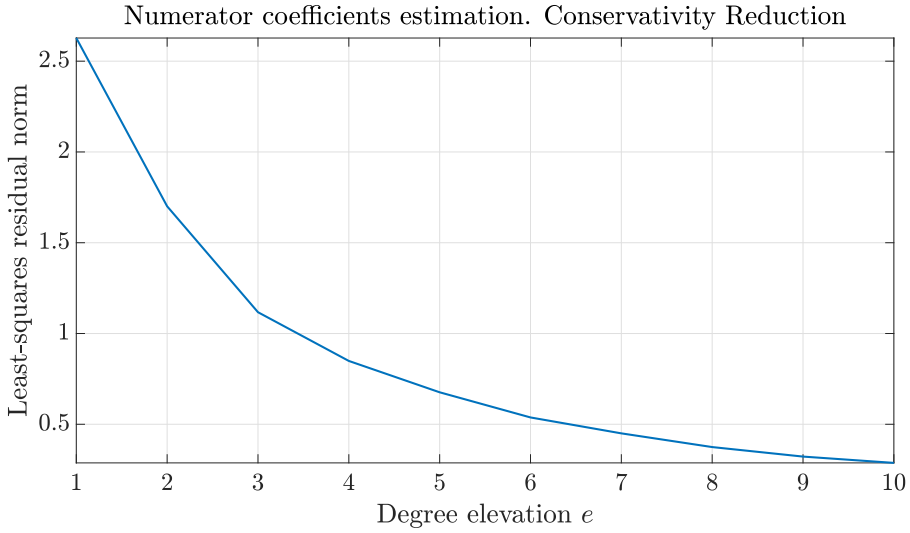

Figure 4.10: Coupled transmission line. Optimal values of the cost function in (4.58) for various degree elevation levels. Figure reproduced from [21] © 2022 IEEE.

were built, solving each time problem (4.58) with different levels of degree elevation $e = 1,2,\ldots,10$. Figure 4.10 reports the optimal cost function value from the solution of problem (4.58) for different degree elevation levels e. The average time required to solve problem (4.36) is 0.72 s, while the time required to solve (4.58) depends on the degree elevation level. The actual runtimes for this test case are reported in Fig. 4.11.

Figure 4.12 reports the modeling results obtained with $e = 10$ for the entire first

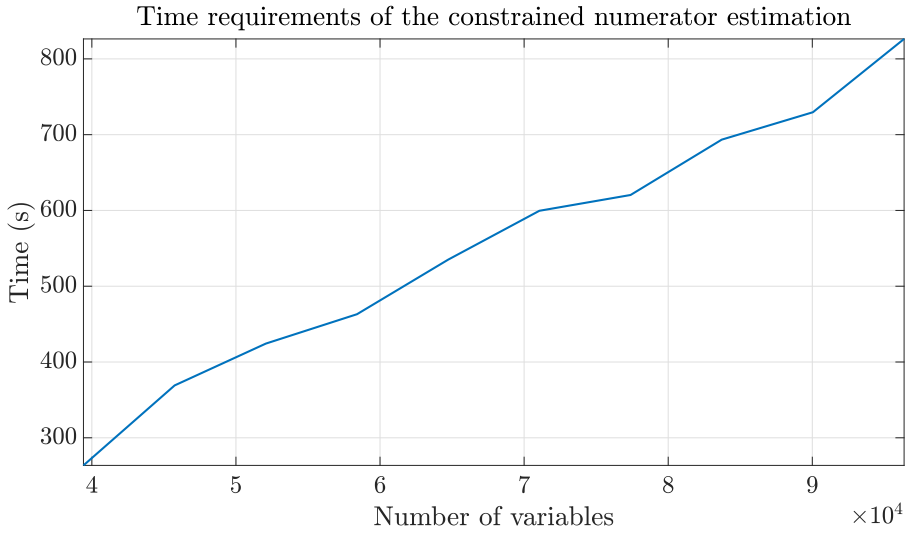

Figure 4.11: Coupled transmission line. Time required to solve problem (4.58) as a function of the number of decision variables corresponding to the various degree elevation levels reported in Fig. 4.10. The increase in the number of variables is mostly due to the increased order of the instrumental polynomial matrix $P(\boldsymbol{\vartheta})$. Figure reproduced from [21] © 2022 IEEE.

column of the scattering matrix, while Fig. 4.13 depicts the model relative error $\epsilon_{2,1}$ as a function of the degree elevation e. These results confirm that also for this case the error approaches the limit corresponding to the unconstrained (hence not guaranteed passive) model, computed using the same training dataset. A graphical representation of the model parameterized poles trajectories is given in Fig 4.14, computed over a very fine sweep of the free parameter $\vartheta \in \Theta$. As expected, all the poles are stable with a negative real part, uniformly in the parameter space. The presence of bifurcations further confirms the effectiveness of the proposed approach in modeling non-smooth poles behaviors, thanks to the implicit parameterization provided by the adopted model structure.

4.6.3 A two-parameter high-speed PCB link

This test case considers a 2-parameter structure, namely a high-speed stripline link running through two PCBs attached by a connector and the corresponding via fields, first presented in [87]. A schematic layout of the structure is depicted in Fig. 4.15. The PCB substrate has permittivity $\epsilon_r = 3$ and $\tan\delta = 0.002$. The vertical vias are parameterized by the pad radius $\vartheta_1 \in [100, 300]$ μm and the associated antipad radius $\vartheta_2 \in [400, 600]$ μm. See [87] for full details.

The scattering parameters of the structure are available from a field solver (courtesy of Prof. Schuster, TUHH, Germany) at $K = 250$ frequency points linearly

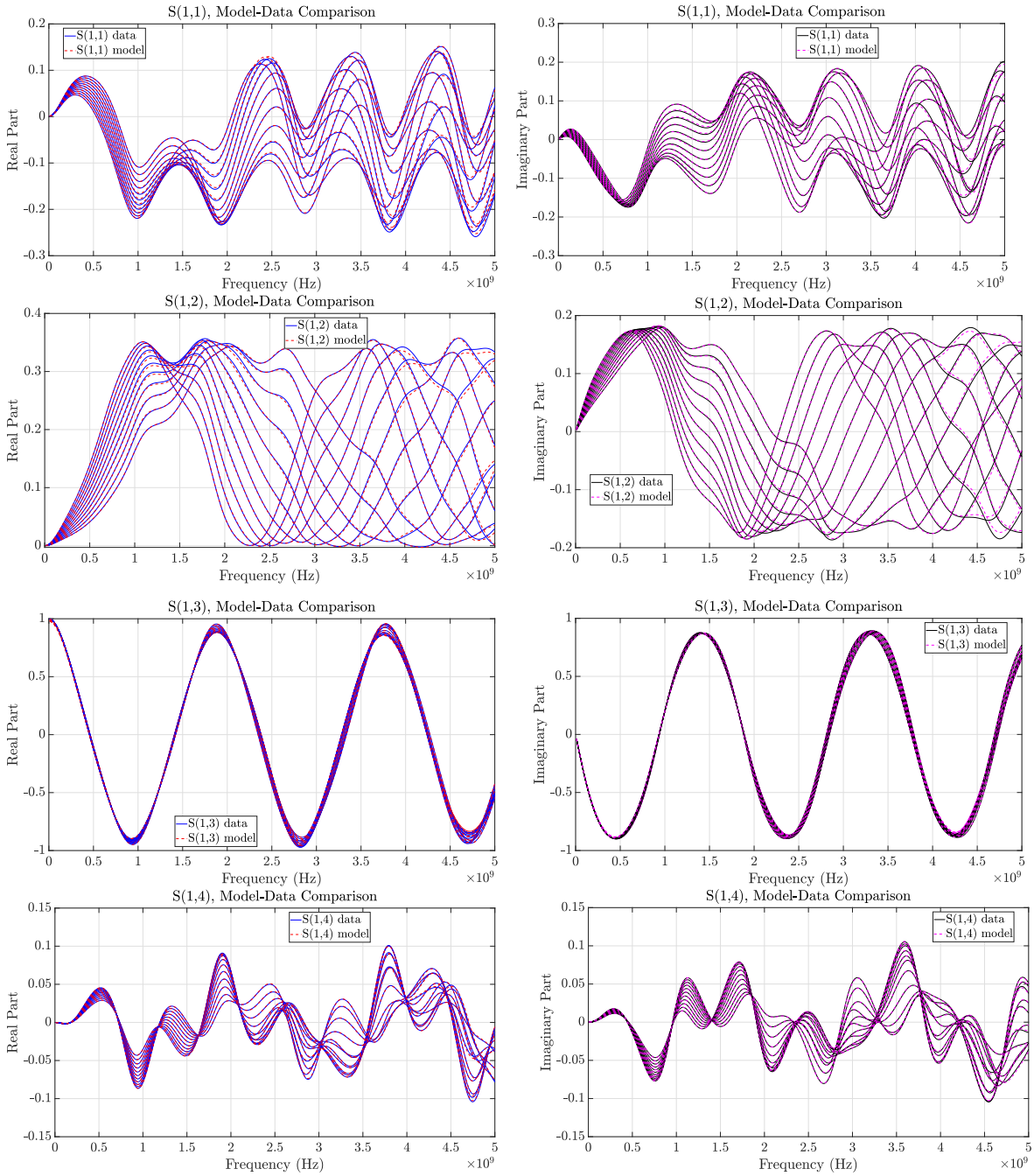

Figure 4.12: Partially coupled transmission line. Fitting results for the first-column of the transfer matrix. The elements that are not shown here exhibit similar trends and a comparable model accuracy. Figure reproduced from [21] © 2022 IEEE.

spaced in the interval $[0.02, 5]$ GHz, and over a 9×9 uniform grid in the parameter space. These data are used to generate a parameterized macromodel with $n = 25$

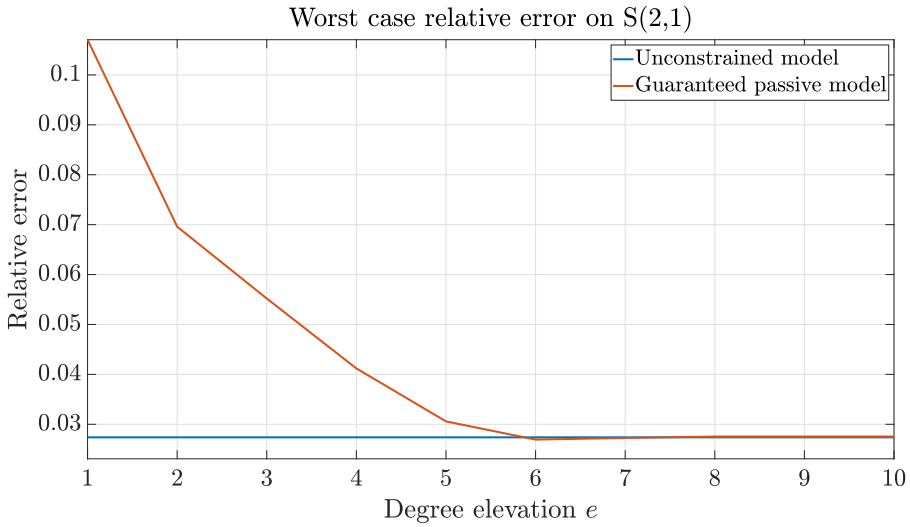

Figure 4.13: Coupled transmission line. Relative error $\epsilon_{2,1}$ for the passive models based on different degree elevations, compared to the error of the model obtained without enforcing any passivity constraint. Figure reproduced from [21] © 2022 IEEE.

poles and polynomial order of numerator and denominator $\overline{\ell} = (3,2)$.

The convergence of the denominator coefficient estimation is illustrated by plotting δ^{ν} in Fig. 4.16. With the considered model structure, the time required to solve (4.36), averaged over the 8 PSK iterations amounts to 1.5 s. For this example, a number of possible degree elevations levels e ranging from 1 to 25, was considered. The time required to build each of the 25 models is depicted in Fig. 4.17. Observe that, although the time requirements for this example are larger, the solver scales favourably with the increase in the number of instrumental variables induced by the higher degree elevations (almost linearly, at least up to 10^5 variables). The value of the optimal cost function value of the semi-definite program (4.50) for different values of e is reported in Fig. 4.18, and confirms the same decreasing trend that has been observed in single-parameter test cases.

For the case $e = 25$, a visual comparison between the parameterized model frequency response and the reference data is provided in Fig. 4.19, considering a subset of 14 random parameter configurations out of the available 81. Also in this case, the accuracy of the model is remarkable throughout the considered frequency band, with no visual difference between model and data on this scale. Finally, Fig. 4.20 reports the relative error $\epsilon_{1,1}$ for different degree elevations. Also for this case the error stabilizes to the same error of the unconstrained (non-passive) model; this occurs at about $e = 15$.

In order to assess the influence of the design parameters on the time-domain

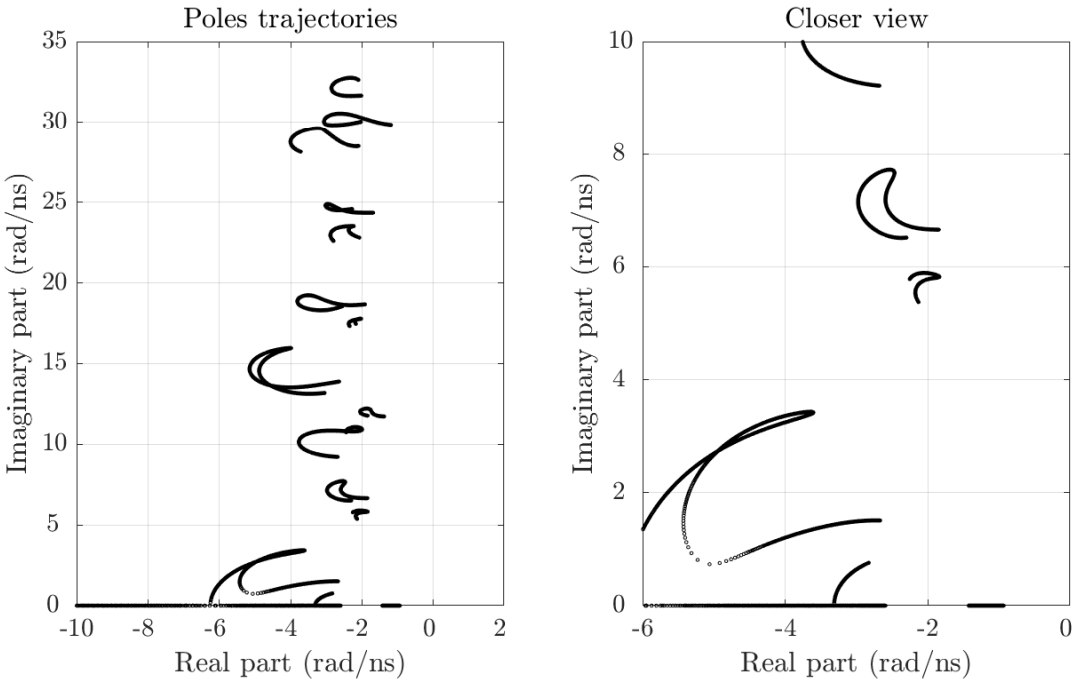

Figure 4.14: Parameterized poles trajectories of the coupled transmission line model. Left panel: in-band poles. Right panel: enlarged view on the low-frequency region. Figure reproduced from [21] © 2022 IEEE.

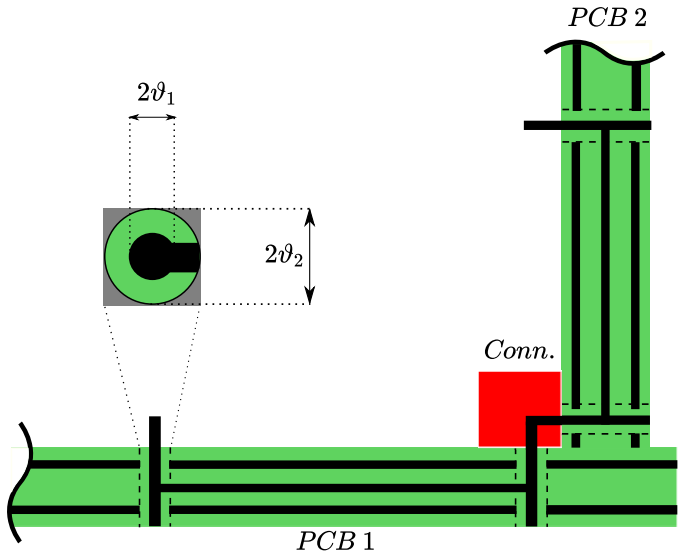

Figure 4.15: High-speed PCB stripline interconnect parameterized by via pad and antipad radii. Drawing for illustration only and not to scale. Figure reproduced from [21] © 2022 IEEE.

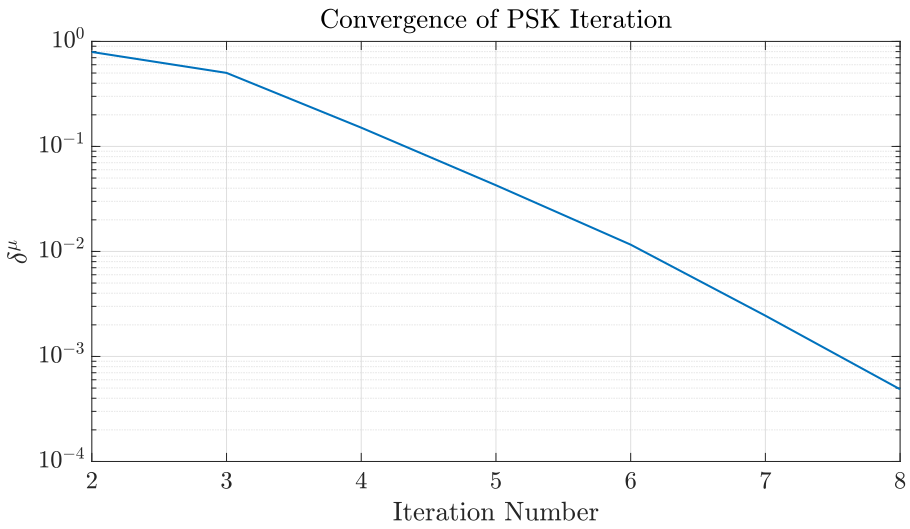

Figure 4.16: High-speed link. Convergence of denominator coefficients estimates through iterations. Figure reproduced from [21] © 2022 IEEE.

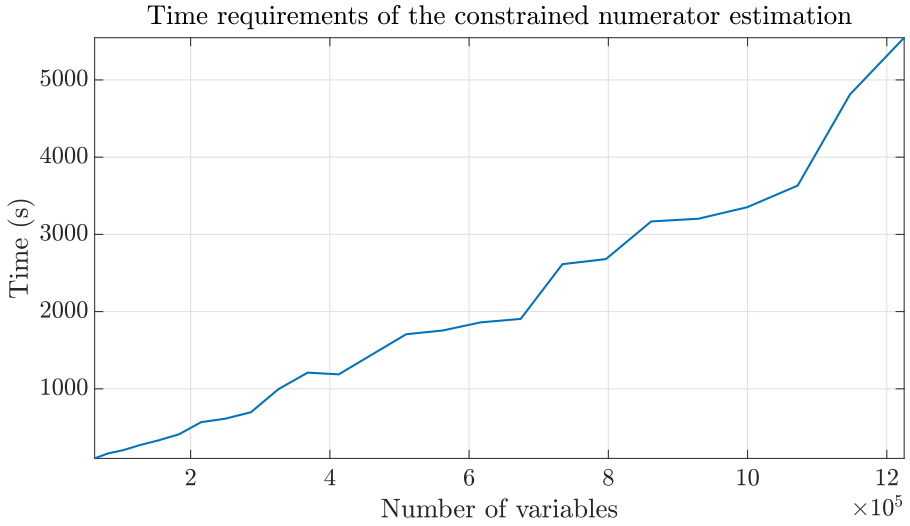

Figure 4.17: High-speed link. Time required to enforce the model passivity, as a function of the number of variables required by different degree elevation levels. Figure reproduced from [21] © 2022 IEEE.

responses, and to demonstrate the efficiency of the parameterized models in a typical use case scenario, a transient simulation of the equivalent parameterized SPICE circuit synthesized from the model was performed. The simulation setup includes a 50Ω voltage driver launching a pulse sequence with amplitude 1 V, period $T = 3$ ns, rise and fall time 200 ps, and bit duration 0.8 ns. The receiver side is instead terminated by a RC parallel load, with $R = 1$ kΩ and $C = 2$ pF. The pad radius was

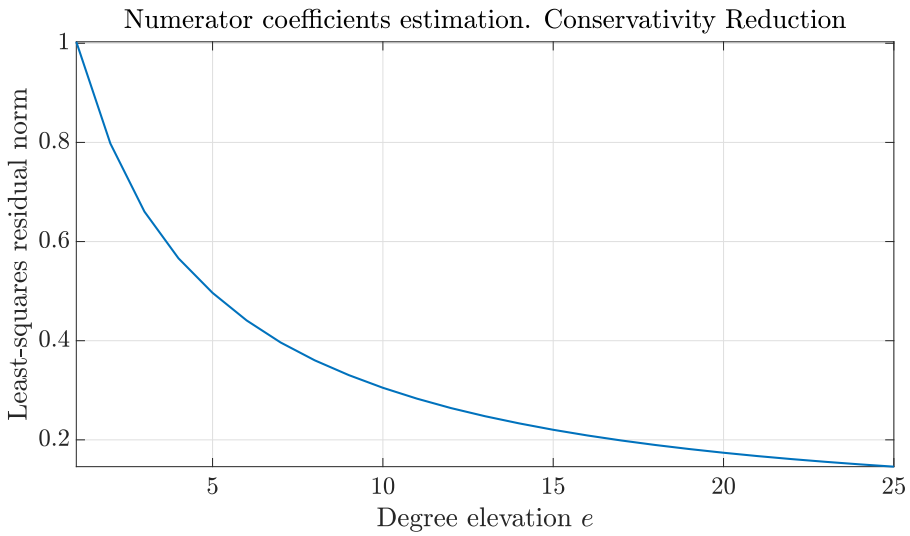

Figure 4.18: High-speed link. Cost function reduction for increasing degree elevation during passivity enforcement. Figure reproduced from [21] © 2022 IEEE.

fixed to $\vartheta_1 = 300$ μm, and the antipad radius was allowed to vary; in particular a linear sweep of 8 configurations within its allowed range was considered. The results of the simulation are depicted in Fig. 4.21, where the voltage signals at the receiver are shown. The time requirements of each simulation amounted to 0.5 s using the freeware LTSPICE solver.

4.6.4 Modeling behaviors with parameter dependent complexity

In this experiment, we test the robustness of the proposed approach when used for modeling structures whose in-band complexity is parameter-dependent. This situation occurs e.g. when the free parameters of the model are related to the electrical size of the underlying structure. Since model (4.8) has a fixed number of poles, modeling this kind of systems requires using a model order n equal to the largest required by the response behavior. We show experimentally that the proposed approach is robust to this kind of over-parameterization.

To this aim, we model a lossy copper microstrip transmission line in the bandwidth [0,20] GHz. The microstrip is characterized by a width $w = 150$ μm, a height $t = 30\mu$m and is placed over a dielectric with relative permittivity $\epsilon_r = 4.1$ and loss tangent $\tan\delta = 0.02$. We let the length of the line vary in the interval $L \in [6.5, 14.8]$ mm, inducing the required parameter dependent complexity in the considered bandwidth.

To build the model, we fixed the line length and we sampled the 2×2 scattering matrix of the line in correspondence of $K = 400$ logarithmically spaced frequency

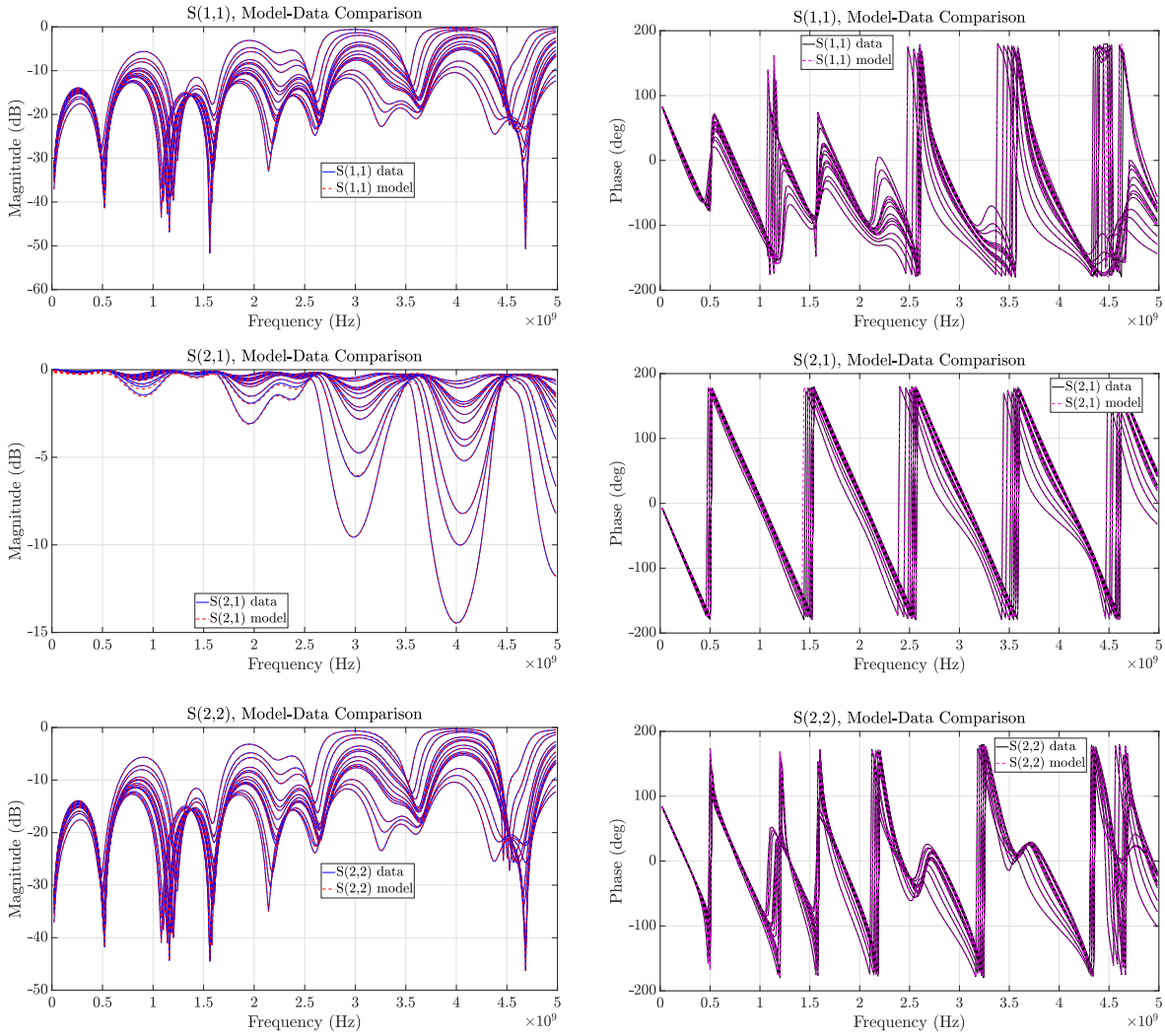

Figure 4.19: High-speed link. Comparison of model responses ($e = 25$) with the corresponding raw data over a random subset of 14 out of the total 81 available frequency responses. Figure reproduced from [21] © 2022 IEEE.

values. We repeated the procedure $M = 20$ times, for different parameter values extracted randomly with uniform probability over the parameter space, including also the interval extremal points. We used 18 out of the 20 available parameterized responses to generate a model of order 12, using Bernstein polynomials of order $\bar{\ell} = 7$ for both numerator and denominator. The remaining 2 were used for model validation. The modeling stage required 35 seconds, 15 of which were necessary to solve (4.58), with a degree elevation level $e = 50$.

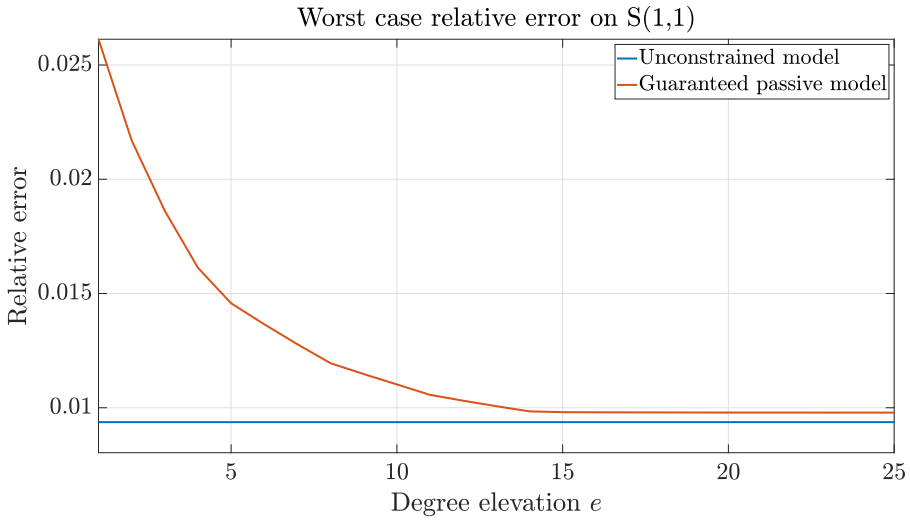

Figure 4.20: High-speed link. Evolution of the relative error $\epsilon_{1,1}$ for the passive models with different degree elevations, compared to the unconstrained model error. Figure reproduced from [21] © 2022 IEEE.

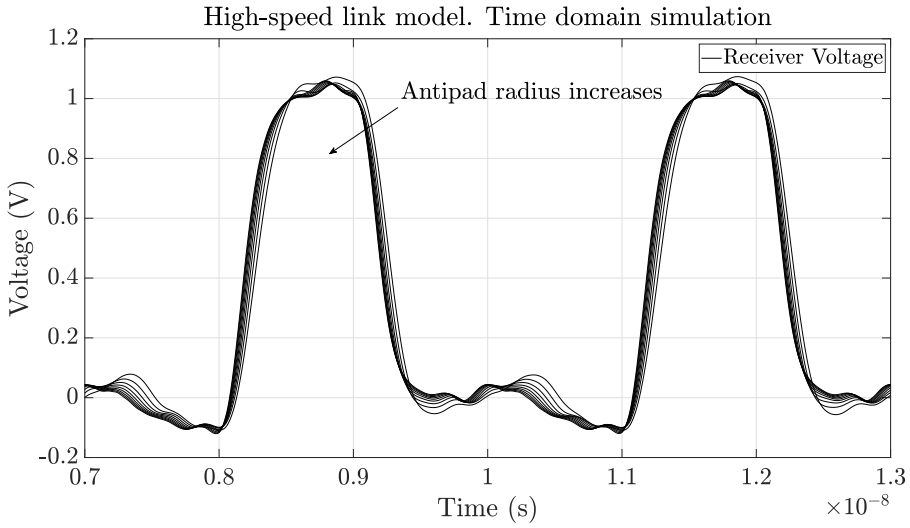

Figure 4.21: Parameterized transient analysis of the high-speed link equivalent circuit. The simulation is performed by considering eight different antipad radius configurations in the interval [400,600]μm, while keeping fixed the pad radius to 300μm. Two periods of the output signal are shown. Figure reproduced from [21] © 2022 IEEE.

The proposed approach resulted to be robust to the over-parameterization, returning an accurate model. The model accuracy is shown in Fig. 4.22 for all of the 20 available responses and in Fig. 4.23 for the extremal points of the parameter

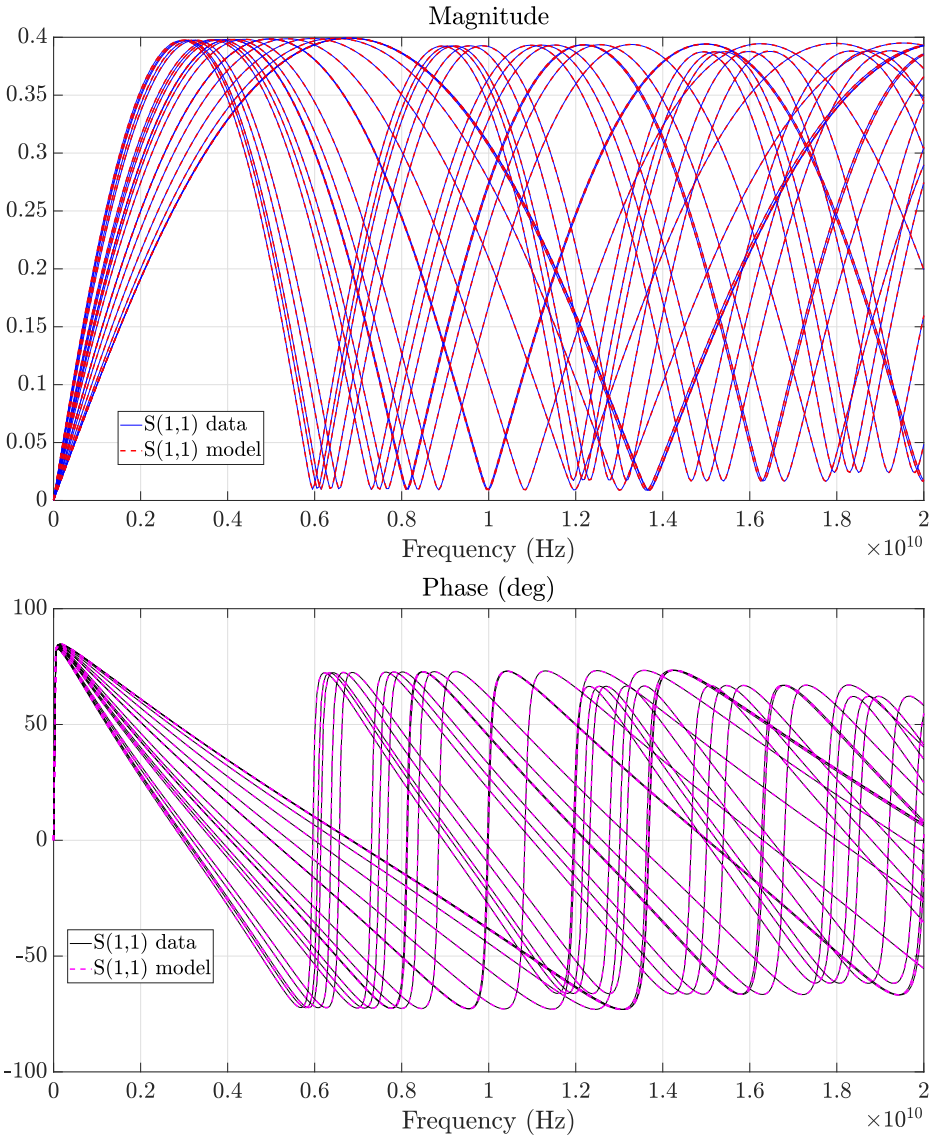

Figure 4.22: Modeling of a transmission line with varying length. Top panel: reflection coefficient magnitude. Bottom panel: reflection coefficient phase.

space. As can be seen in Fig. 4.24, the model poles exhibit smooth and regular trajectories within the modeling bandwidth. In order to match the proper dynamic order of the responses, for some of the parameter values the trajectories exceed the bandwidth limit. When this happens the poles evolve according to more involved yet controlled behaviors.

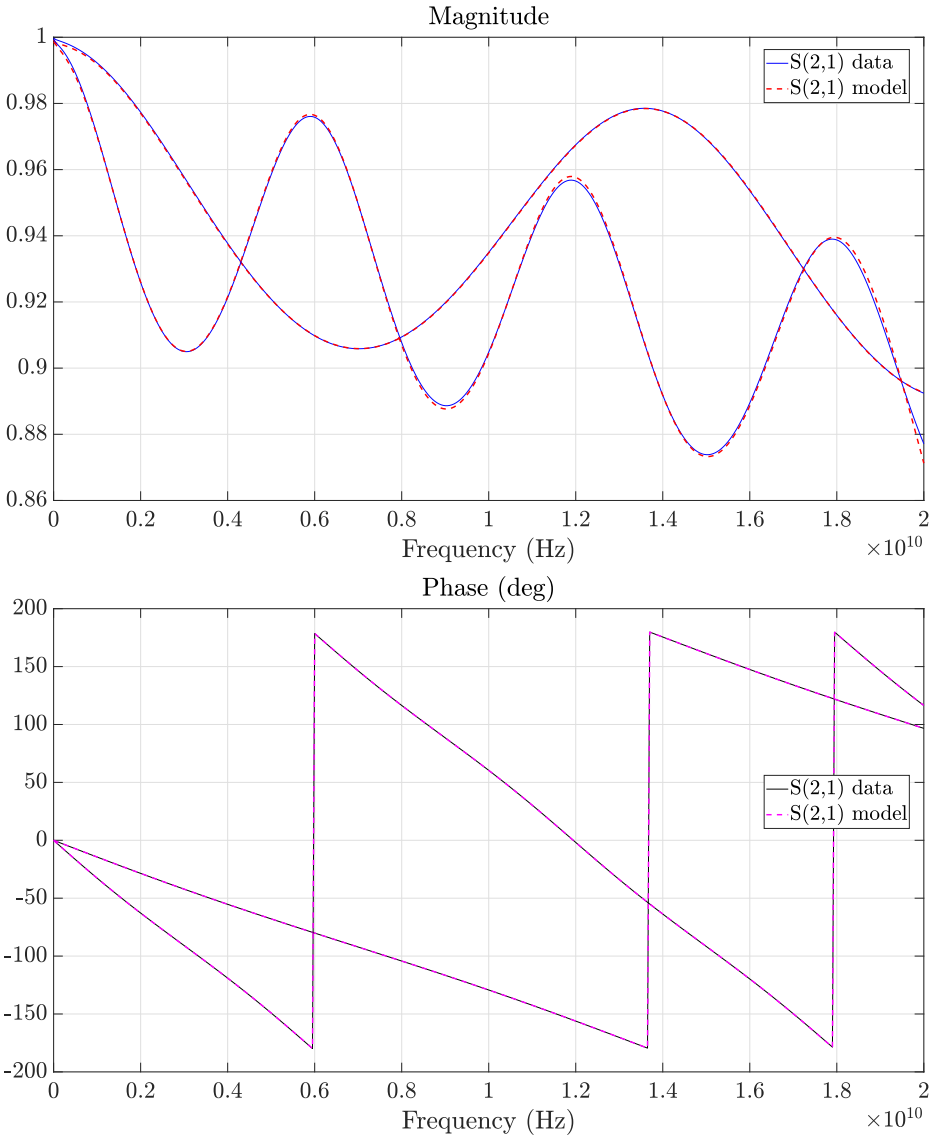

Figure 4.23: Modeling of a transmission line with varying length. Top panel: agreement between model and data transmission magnitude at the extremal points of the parameter space. Bottom panel: same as top, but for the phase.

4.6.5 Comparison with state-of-the-art techniques

We consider the same test case of Sec. 4.6.4 and the same dataset to compare the modeling performance of the proposed approach with those of root macromodels interpolation and multivariate rational fitting combined with sampling-based stability and passivity enforcement schemes. For the latter case, we applied the strategy proposed in [114], generating a model with $n = 12$ and $\overline{\ell} = 7$. The model generation required 146 s, while the passivity enforcement step converged in 126 s,

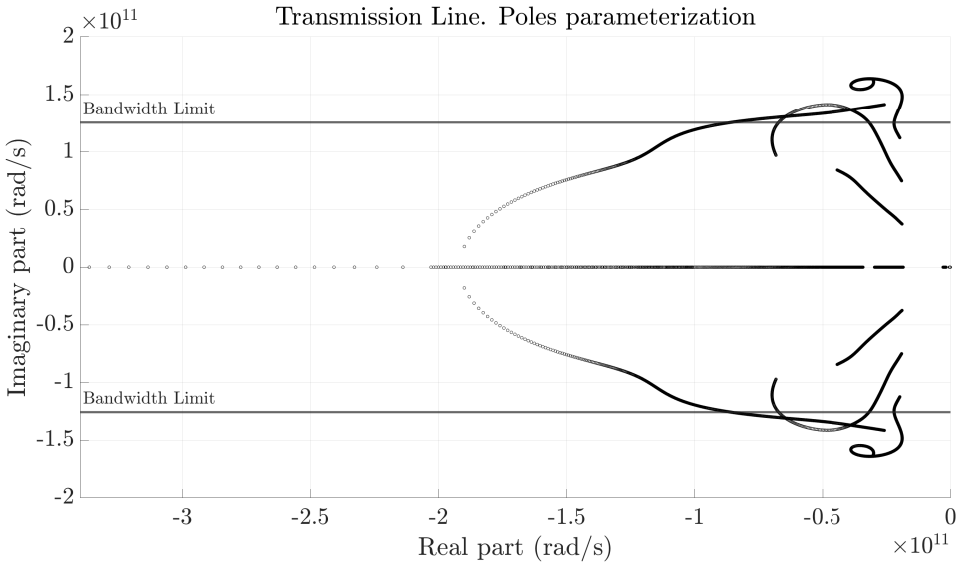

Figure 4.24: Modeling of a transmission line with varying length. The parameterized poles of the macromodel obtained by means of the proposed approach. To model the parameter-dependent complexity of the behavior with a constant dynamic order n, for some parameter configuration the poles exceed the bandwidth limit, according to involved yet controlled trajectories.

resulting in time requirements that are about 5× larger than those of the proposed approach.

To apply the root macromodels interpolation strategy, we used the vector fitting algorithm and the passivity enforcement scheme described in [50] to generate 18 univariate passive macromodels in correspondence of the parameter configurations exploited to train the PSK models. To predict the response of the system for a line length validation value L_v, we used the following formula

$$H(s, L_v) = \alpha H(s, L_1) + (1 - \alpha) H(s, L_2), \tag{4.61}$$

$$\alpha = 1 - (L_v - L_1)/(L_2 - L_1), \quad L_1 < L_2 \tag{4.62}$$

being L_1 and L_2 the nearest parameter values for which root macromodels are available. The results of the comparison are shown in Fig. 4.25 for $L_v = 8.2$ mm (top panel) and for $L_v = 0.112$ mm (bottom panel). The results show that the proposed approach returns a model that is practically indistinguishable from that obtained vie post-processing passivity enforcement. On the other hand, the approach based on the root macromodels returns less accurate predictions, even if the associated model is of order $2n = 24$.

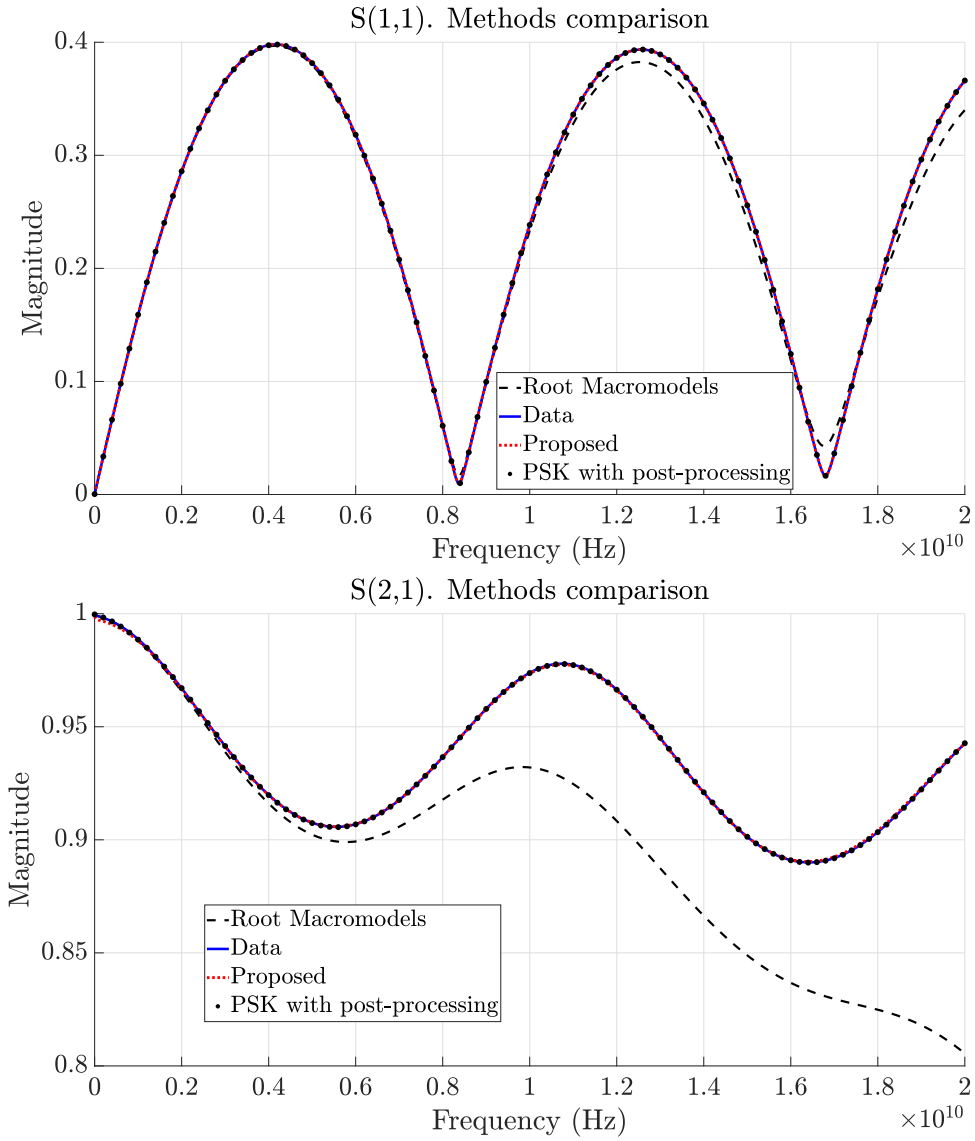

Figure 4.25: Modeling of a transmission line with parameterized length via different techniques. Top panel reflection coefficient for the length validation value $L_v = 8.2$ mm. Bottom panel: transmission coefficient for the length validation value $L_v = 0.112$ mm. The proposed approach matches the results obtained via multivariate rational fitting combined with sampling-based stability and passivity enforcement. The prediction obtained combining root macromodels lacks of accuracy and returns a macromodel of order $2n$.

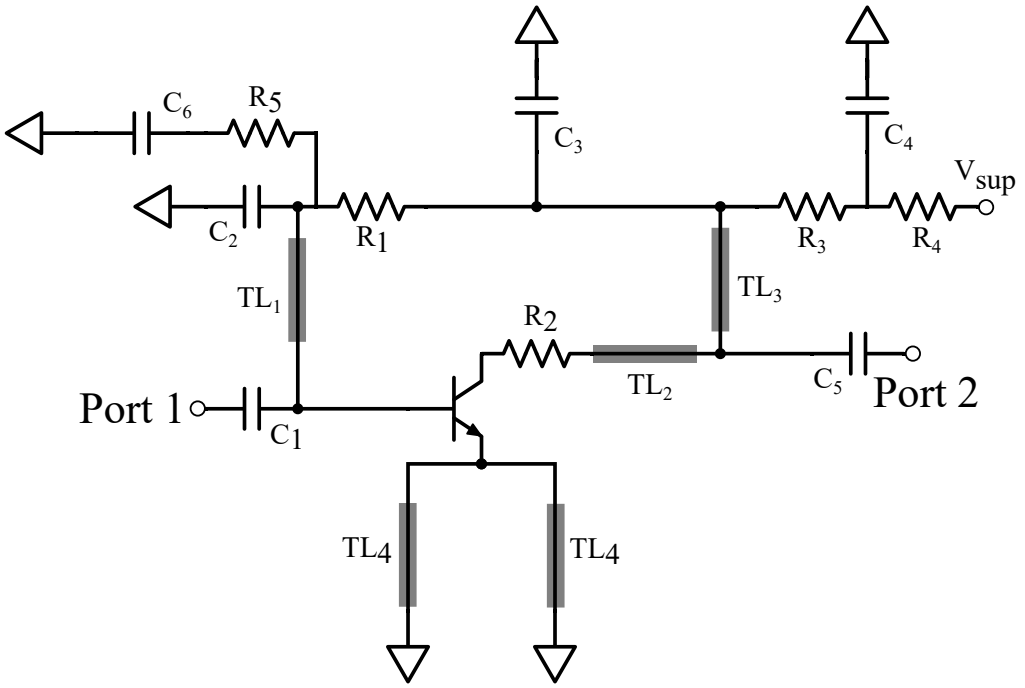

Figure 4.26: The LNA circuit schematic.

4.6.6 Stability constraints. Scalability and conservativity assessment.

This last example is aimed at assessing experimentally the conservativity induced by the stability enforcement scheme proposed in Sec. 4.3, and its scalability in case of many parameters. The assessment is performed by considering a test-bench already studied in [116], in order to compare the proposed method with the one based on the enforcement of (4.5). The device under test is the Low Noise Amplifier (LNA) depicted in Fig. 4.26, first presented in [25]. The circuit depends on $d = 7$ design parameters, which are listed in Table 4.1, and includes both lumped elements and lossy transmission lines.

For this example, the proposed parameterized macromodeling approach is applied to generate a reduced-order small-signal surrogate of the amplifier. Since the device is active, the passivity constraints derived in section 4.4 are not applicable.

A fixed operating point $\mathrm{V_{SUP}} = 4.5$ V is considered to construct a small-signal linearized model. A total of $M = 1400$ parameter configurations are chosen according to a latin-hypercube distribution in the design space. For each fixed configuration, the reflection coefficient at the amplifier input port is sampled at $K = 701$ logarithmically spaced frequency points in the interval [1,10] GHz. Only 595 parameter configurations are exploited to generate a parameterized macromodel with $n = 10$ and $\bar{\boldsymbol{\ell}} = (1, 1, 1, 1, 1, 1, 2)$, while the remaining samples are left for model

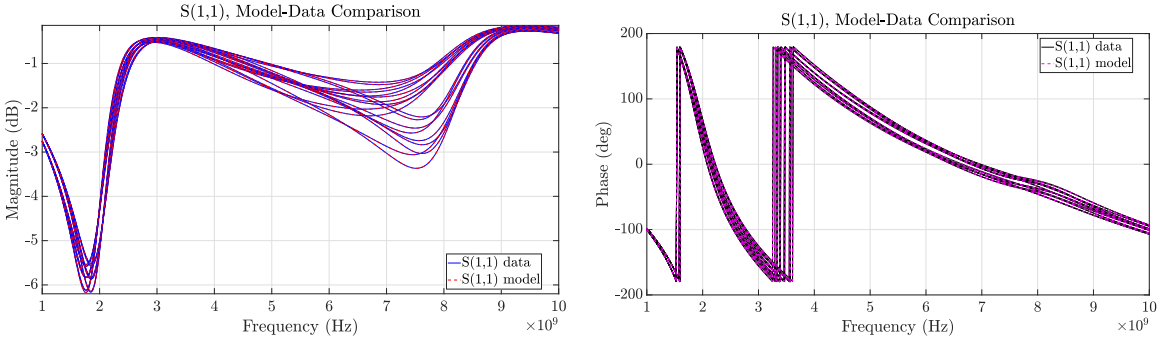

Figure 4.27: LNA example. Comparison between model responses and validation data over 19 different frequency responses, randomly selected in the design space.

validation.

With this configuration, the modeling algorithm reaches the stopping threshold $\delta^{\nu} = 10^{-3}$ in only 3 iterations. The average time to solve (4.36) is 6 s, and the relative error index results $\epsilon = 1.42 \times 10^{-3}$, confirming that the model is highly accurate also in correspondence of the validation samples. In Fig. 4.27, a visual comparison between the model and the data is provided for 19 different randomly-selected validation responses.

In order to show the low degree of conservativity of the proposed stability constraints, the experiment performed in [116], where the uniform stability is enforced by imposing a sign inequality directly on the denominator coefficients $r_{n,\boldsymbol{\ell}}$ during the model generation, was repeated here with the novel stability constraints. For this purpose, the same LNA device was considered and the dimension of the design space was reduced to $d = 5$, by taking into account only the first five parameters listed in Table 4.1. A model was built by setting $n = 16$ and $\overline{\boldsymbol{\ell}} = (1,1,1,1,1)$, as in

Table 4.1: Free parameters considered for the modeling of the LNA test case. First six parameters: parasitic inductances and capacitances of the transistor. Parameter h is the substrate thickness for lines TL_1, TL_2, TL_3.

#	Parameter ϑ_i	$\vartheta_{i,\min}$	$\vartheta_{i,\max}$
1	L_b (nH)	0.88	1.32
2	L_c (nH)	0.88	1.32
3	L_e (nH)	0.20	0.30
4	C_{cb} (pF)	0.0016	0.0024
5	C_{be} (pF)	0.064	0.096
6	C_{ce} (pF)	0.064	0.096
7	h (mm)	0.45	0.55

the referenced article.

The stop criterion $\delta^{\nu} = 10^{-3}$ was met after 4 iterations, with an average computing time required to solve (4.36) equal to 1.2 s. The relative error index of the resulting model read $\epsilon = 6.36 \times 10^{-5}$; the same index for a model based on [116] was $\epsilon = 1.94 \times 10^{-2}$. Thus, the proposed technique provides a decrease of the worst case relative error of about 3 orders of magnitude, while guaranteeing the uniform model stability by construction. This improvement is attained in approximately the same runtime.

4.7 Discussion

The modeling framework described in this chapter provides a major improvement with respect to to standard techniques for the generation of passive parameterized macromodels. The proposed approach generates compact parameterized macromodels that are at the same time characterized by minimal complexity and guaranteed passive by construction. These features can not be guaranteed concurrently by previously available methods based on root macromodels interpolation or multivariate rational fitting with stability and passivity enforced by perturbation or post-processing.

Before the results of this research were presented, the main limiting factor for the generation of certified passive macromodels in the PSK framework was represented by the difficulty in handling numerically the parameterized Bounded Realness condition (4.37). The derivations of this section show that such a difficulty can be overcome by taking advantage of the PSK model structure combined with the specific choice of the Bernstein basis for model parameterization. These two elements, when combined, allow to derive a specific formulation for the dissipation function of the model, and to enforce its semi-definiteness by means of discretized sufficient conditions. Some advancements in similar directions were preliminarly presented in [116] for what concerns the stability enforcement; then, a preliminary formulation of the passivity constraints was given in [20]. In the paper [21], the ideas were gathered and presented with the same level of detail of this section.

The degree elevation property of the Bernstein polynomials is fundamental to derive both the discretized sufficient conditions for passivity and to address a strategy for the reduction of their conservativeness. The straightforward link between the polynomial degree used to represent the constraints and their conservativity becomes a valuable trade-off parameter that can be tuned to reach the desired compromise between model accuracy and generation time.

As shown in Sec. 4.6, the method is efficient and reliable to generate surrogates for devices of modest dimensions and limited number of parameters. Unfortunately, the benefits of the proposed method come with an unfavourable scaling of its demand for computational power, as the complexity of the model increases, both

in terms of electrical ports and of number of free parameters.The computational complexity of the interior point method used to solve problem (4.58) strongly depends on the specific algorithm implementation and on the possibility to exploit the particular problem structure. For instance, we noticed that for the problem of interest the MOSEK interior point implementation outperforms competing publicly available SDP solvers based on the same algorithm (e.g. SEDUMI or SDPT3). It is thus difficult to estimate rigorously which are the limitations of the proposed approach in terms of resulting model complexity. Based on our experience, using the hardware described in Sec. 4.6, we were able to solve problem (4.58) in less then one hour to generate models with $n\mathrm{P}d < 100$, using a degree elevation level e that practically nullifies the conservativity induced by the constraints discretization. A passive model generation is guaranteed also for larger problems, at the price of longer runtimes. Notice however, that even sampling-based post-processing schemes for passivity enforcement become more and more expensive and unreliable as the dimension of the design space increases beyond few units.

Chapter 5

Small signal and linear parameter varying models

This chapter reports a series of novel results concerning the generation of macromodels for fast small signal analysis of nonlinear systems and analog Circuit Blocks (CBs). Specifically, the presented techniques apply to systems designed to behave almost linearly under prescribed operating conditions, that will be denoted henceforth as *mildly nonlinear*. Typical examples are, Low-Noise Amplifiers (LNA), Operational Amplifiers (OPA), and Low DropOut (LDO) voltage regulators, which are ubiquitous in electronic products.

As outlined in Sec. 1.1.2, analog circuit blocks in advanced design stages are commonly represented by netlists that translate the physical device description into an equivalent circuit. As in modern Systems-on-Chip (or Systems-in-Package), CBs operate at very low voltage supply levels, within miniaturized volumes, the resulting equivalent circuit characterization must account for coupling and parasitic effects due to layout and packaging. This leads to highly complex CB representations that limit the possibility to perform system-level simulations, e.g., for stability assessment or performance optimization. In this view, reduced order behavioral models of analog circuit blocks represent enabling factors for performing such simulations in a fast and accurate way.

In the available literature, a variety of modeling frameworks have been proposed to approximate the behavior of CBs for nonlinear simulations; among them, the classical Hammerstein-Wiener model structure identification [93], trajectory piecewise linear approaches [88], Volterra series based methods [84], X Parameters [89], and neural networks [78, 77]. These approaches are all characterized by specific advantages and drawbacks from the point of view of model complexity, degree of accuracy, and training time requirements. This is because, when dealing with nonlinear systems, the range of admissible behaviors is so broad and heterogeneous that any effective modeling strategies should be tailored with respect to the characteristics of the device, having in mind the application of interest. In this Chapter,

we restrict the focus on mildly nonlinear circuits, that are deliberately designed to operate as linear as possible in the neighborhood of some prescribed working point. Our objective is to derive surrogate models that can replace these devices for simulations that meet the small signal assumption. This assumption is commonly verified in practically relevant situations, for example when stability assessment or power management optimization of large scale systems must be performed.

When the small signal assumption is verified, the mildly nonlinear circuit block can be replaced by a linearized model, which mimics the reference nonlinear behavior though a set of linear differential equations. The exploitation of such a linear model guarantees drastic reduction in terms of description complexity and high accuracy in transient analyses for small deviations around the operating point [83]. Additionally, due to the linear structure, a linearized model ensures that fundamental physical properties, such as stability, can be easily guaranteed by construction. As a drawback, linearized models are not suitable to perform nonlinear analyses, such as harmonic distortion, that can be in principle modeled by using nonlinear models (e.g. based on Volterra series).

Capitalizing on the multivariate rational fitting framework presented in chapter 4, we propose a methodology to generate linearized behavioral models that replace the reference CB description for small signal analyses in which either

1. The operating point of the device is unknown a priori but kept constant during a transient simulation

2. The operating point of the device is unknown a priori and allowed to vary during a transient simulation.

In both cases, the models are constructed from frequency-domain samples of multiple small-signal responses corresponding to a set of static operating points (bias levels) in a given design range. The PSK iteration is used to build a multivariate rational approximation for the target bias-dependent small signal transfer function. This data acquisition procedure has the advantage of being relatively inexpensive. Therefore, we apply the framework of chapter 4, where the operating point plays the role of the parameter $\boldsymbol{\vartheta}$.

For applications involving constant but uncertain bias, the modeling approach is analogue to the one of chapter 4, with the difference that only uniform stability constraints are enforced during the model generation. The second application scenario involving nonstationary operating conditions is tackled by representing the reduced order parameterized model as a Linear Parameter Varying (LPV) system. In this case, the dependency of the model on the bias condition is induced in real-time using a feed-through term resulting from a low-pass filtering operation on the port signals. This operation is performed at negligible computational cost.

The main technical contribution of the proposed modeling approach is related to asymptotic stability of the resulting LPV models. By making use of Lyapunov

theory and of the results derived in Chapter 4, it is possible to ensure the quadratic stability of the surrogate LPV models [24], which entails the asymptotic stability under any possible time-varying bias conditions within a proper design range. Also in this case, parameterizing the model coefficients through multivariate Bernstein polynomials, guarantees quadratic stability by enforcing a finite number of LMIs during the model estimation.

The approach is validated experimentally in Section 5.3 over a set of test cases involving low dropout voltage regulators. The results show that the linear structure of the models combined with their low complexity representation guarantee major speedup, in real time while at the same time preserving the accuracy of the predictions.

5.1 Equivalent linearized surrogates for mildly nonlinear systems

Consider a P-port nonlinear electrical system that admits a description in terms of a state space representation

$$\begin{aligned} \dot{\xi}(t) &= F(\xi(t), u(t)), \\ \eta(t) &= G(\xi(t), u(t)), \end{aligned} \tag{5.1}$$

where $u, \eta \in \mathbb{R}^{\mathrm{P}}$ denotes the input and output signals, $\xi, \dot{\xi} \in \mathbb{R}^{\mathrm{N}}$ are the internal state vector and its time derivative, and F, G are C^1-smooth maps. The above state space is the same as (2.28), rewritten here for convenience. Although description (5.1) is suitable to describe a broader class of systems, in the following the discussion will be focused on nonlinear circuit blocks that admit a SPICE netlist representation. Without loss of generality, we restrict our attention to immittance representations.

An *affine linearized model* provides an approximation of the input output properties of (5.1) in proximity of a prescribed operating condition. More specifically, such a model is intended to replace (5.1) whenever the following assumptions are met

1. The system signals can be decomposed as

$$u(t) = U_0 + \tilde{u}(t), \quad \xi(t) = \Xi_0 + \tilde{\xi}(t), \quad \eta(t) = Y_0 + \tilde{\eta}(t). \tag{5.2}$$

   where (U_0, Ξ_0, Y_0) are constant quantities hencefoth denoted as *DC components* (defining the bias level or operating point) and $\tilde{u}(t), \tilde{y}(t), \tilde{\xi}(t)$ are small signals.

2. The triplet of constant quantities (U_0, Ξ_0, Y_0) identifies a unique asymptotically stable equilibrium point, corresponding to the static input U_0 with (U_0, Ξ_0, Y_0) being the stationary solution of (5.1)

$$\begin{aligned} 0 &= F(\Xi_0, U_0), \\ Y_0 &= G(\Xi_0, U_0) \end{aligned} \tag{5.3}$$

3. $\tilde{u}(t) \equiv 0$ for $t \leq 0$, and thus

$$u(t) = U_0, \quad \xi(t) = \Xi_0, \quad \eta(t) = Y_0, \quad \forall t \leq 0. \tag{5.4}$$

The above conditions reflect those that are encountered whenever a small signal analysis of a device obeying equations (5.1) is performed in standard SPICE solvers. In particular, assumption 1 represents the small-signal operating condition; assumption 2 requires that the operating point of the device is well-defined and that the small signal analysis is carried out in proximity of such operating point. Finally assumption 3 is compliant with the fact that at the reference time instant $t = 0$ the small signals are vanishing and that the system quantities are initialized according to (5.3).

Around the operating point (U_0, Ξ_0, Y_0), the nonlinear system can be linearized following the steps recalled in Sec 2.2.3. The process leads to the local linear model

$$\begin{aligned} \dot{\tilde{\xi}}(t) &\approx \tilde{A}\,\tilde{\xi}(t) + \tilde{B}\,\tilde{u}(t) \quad , \tilde{\xi}(0) = 0 \\ \tilde{\eta}(t) &\approx \tilde{C}\,\tilde{\xi}(t) + \tilde{D}\,\tilde{u}(t), \end{aligned} \tag{5.5}$$

where $\tilde{A}$, $\tilde{B}$, $\tilde{C}$, $\tilde{D}$ are computed as in (2.51) and (2.54). The above small signal model approximates the behavior of the signals deviations from the equilibrium. From an input output point of view, state space (5.5) provides an approximation for the map $\tilde{u}(t) \to \tilde{\eta}(t)$.

As the dimension N of ξ can be large when highly detailed descriptions of the underlying device are considered, model order reduction techniques can be applied to reduce the complexity of the linear system explaining the small-signal dynamics. This leads to a *small-signal reduced-order model* of (5.1)

$$\begin{aligned} \dot{\tilde{x}}(t) &= A\,\tilde{x}(t) + B\,\tilde{u}(t), \quad \tilde{x}(0) = 0 \\ \tilde{y}(t) &= C\,\tilde{x}(t) + D\,\tilde{u}(t), \end{aligned} \tag{5.6}$$

Clearly, the above model is valid only in a neighborhood of the equilibrium point induced by the DC component U_0. In this dissertation, we consider the situation in which the nonlinear maps F and G are not available in closed form, since encrypted

indirectly into the netlist describing the nonlinear circuit. Thus, the reduced-order small signal model can be constructed by means of rational fitting techniques, starting from a set of samples of the small-signal transfer function.

$$\breve{H}_k = \tilde{\mathsf{H}}(j\omega_k) = \tilde{C}(j\omega_k I - \tilde{A})^{-1}\tilde{B} + \tilde{D}, \quad k = 1, \dots K. \tag{5.7}$$

computed at a discrete set of frequencies ω_k by means of an AC sweep performed within the SPICE solver where the circuit description is available. The fitting process returns a small-signal reduced order transfer function $\mathsf{H}(s) \approx \tilde{\mathsf{H}}(s)$ with order $n \ll \mathrm{N}$, which can be readily cast in the state space form (5.6)

5.1.1 Affine linearized models

System (5.6) provides only a compact model for predicting the small signal behavior, but it cannot be used as a direct replacement of (5.1) in circuit simulation environments. This is because, even if the reduction process preserves the accuracy of the mapping from $\tilde{u}(t)$ to $\tilde{\eta}(t)$, in a global circuit simulation both the the DC and the small signal components act concurrently on the circuit. This means that a model aimed at replacing (5.1) must accurately reproduce the input-output map $\tilde{u}(t) + U_0 \to \tilde{\eta}(t) + Y_0$. This requires a consistent embedding of the desired bias level.

A straightforward modification of (5.6) allows to obtain a model that meets this requirement, which is the affine linearized model, defined as follows

$$\begin{aligned} \dot{x}(t) &= Ax(t) + Bu(t), \qquad x(0) = X_0 \\ y(t) &= Cx(t) + Du(t) + Y_C, \end{aligned} \tag{5.8}$$

where vectors X_0, Y_C are defined as

$$Y_C = Y_0 - (CX_0 + DU_0) \quad \text{and} \quad X_0 = -A^{-1}BU_0. \tag{5.9}$$

Comparing (5.8) with (5.6), one can observe that

1. model (5.8) is subject to the total input $u(t) = U_0 + \tilde{u}(t)$ and not only to the small-signal component $\tilde{u}(t)$;

2. the output contains the constant term Y_C, which is needed to provide matching between (5.1) and (5.8) under stationary conditions $u(t) \equiv U_0$, $x(t) \equiv X_0 \implies y(t) \equiv Y_0$;

3. similarly to (5.2), we can split the signals $x(t)$ and $y(t)$ as

$$x(t) = X_0 + \tilde{x}(t), \quad y(t) = Y_0 + \tilde{y}(t), \tag{5.10}$$

where, according to the initial conditions entering (5.8), $\tilde{x}(t) = 0$ and $\tilde{y}(t) = 0$ for $t \leq 0$. This means that the circuit is at rest for $t \leq 0$, when only the constant DC input U_0 is applied.

Under the above conditions, the original nonlinear circuit block described by (5.1) can be replaced by model (5.8) in circuit simulation environments under assumptions 1, 2, 3. Using (5.8) instead of (5.1), however, one has to define the initial condition on the surrogate model X_0 as in (5.9) in order to guarantee that the constant components U_0 and Y_0, match exactly the input and output levels defining the operating point of (5.1).

The signal $\tilde{y}(t) = y(t) - Y_0$ approximates the actual small-signal component $\tilde{\eta}(t)$ with an error introduced by the linearization and model reduction procedures. With reference to Fig. 5.1, which illustrates the above affine linearization process in the scalar (one-port) static case, we remark that both models (5.6) and (5.8) should be considered as valid approximations of (5.1) only if the deviations from the equilibrium point are sufficiently small. If this assumption is not verified, then different modeling strategies should be adopted, see e.g. [72].

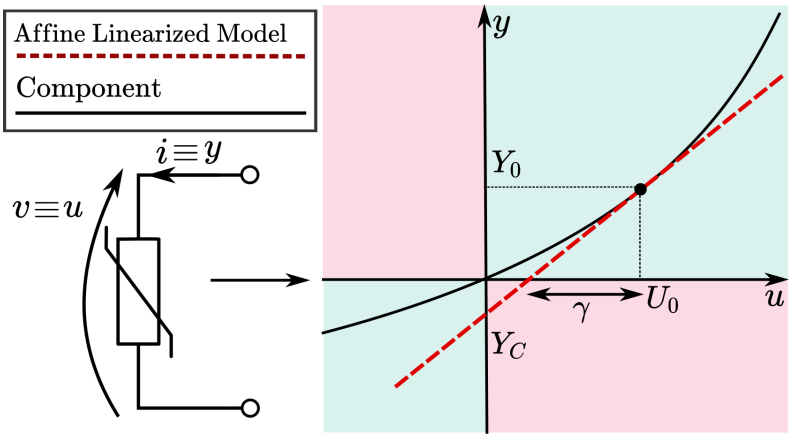

Figure 5.1: The linearized affine model of a nonlinear dissipative static component in admittance representation. The presence of the biasing input U_0 allows to derive a local model around the operating point, corresponding to a constant output Y_0. The linearized model characteristic is affine, with a non-zero output Y_C obtained with a vanishing input voltage. Figure adapted from [19] © 2020 IEEE.

5.1.2 Bias-dependent linearized models

Affine linearized models (5.8) can be used to replace efficiently the native circuit block description (5.1), as far as all signals are bounded in a neighborhood of some operating point. Nevertheless, from a system level point of view, the DC working condition of the device is often not known a priori, but is imposed by the

interconnection of all the external subsystems and terminations connected to the circuit electrical ports. When the outer environment conditions are modified, the operating point of the circuit block may change in such a way that a predetermined affine linearized model results to be inadequate.

To guarantee that the model is defined according to the actual operating point within the simulation scenario of interest, the affine linearized state space (5.8) should be generalized in order to explicitly embed the dependency of the equations on the correct bias level [82], [18]. The following derivations show how to generate parameterized affine models that can be used in simulation scenarios in which the CB works under an uncertain uncertain operating point.

Model structure definition

The parameterized rational fitting framework presented in chapter 4 allows to generate models that retain such a feature, albeit with minimal modifications of the modeling procedure. The first adaptation to be taken into account is conceptual. A parameterized affine macromodel should depend on the operating point, univocally determined by the value of the constant input component U_0 acting on the circuit for $t \leq 0$. Assuming that the value U_0^i of the input DC component at the i-th electrical port is known to belong to a prescribed interval $[\underline{U}_0^i, \overline{U}_0^i]$, a set of admissible bias conditions can be defined as

$$\mathcal{U}_0 = [\underline{U}_0^1, \overline{U}_0^1] \times [\underline{U}_0^2, \overline{U}_0^2] \times \cdots \times [\underline{U}_0^{\mathrm{P}}, \overline{U}_0^{\mathrm{P}}]. \tag{5.11}$$

The set $\mathcal{U}_0$, called in the following *bias space*, represents a particular case of (2.55), in which the parameter configurations of interest represent different operating points of the circuit. Thus, in the considered modeling framework, the DC component U_0 assumes the meaning of *both* an uncertain parameter *and* an input component.

In order to be compliant with the settings of Section 5.1, it is necessary to assume that each bias condition $U_0 \in \mathcal{U}_0$ is associated to a unique asymptotically stable equilibrium point $\Xi_0 = \Xi_0(U_0)$ fulfilling (5.3). Therefore, by omitting for brevity the dependency on the state configuration Ξ_0 in matrices (2.51) and (2.54), the small signal transfer function associated to (5.5) can be parameterized by $U_0 \in \mathcal{U}_0$ as follows

$$\tilde{\mathsf{H}}(s, U_0) = \tilde{D}(U_0) + \tilde{C}(U_0)(sI_N - \tilde{A}(U_0))^{-1}\tilde{B}(U_0). \tag{5.12}$$

A reduced order small signal model that embeds the closed form dependency on the bias condition can be obtained starting from samples of (5.12), computed at discrete bias-frequency configurations

$$\tilde{H}_{k,m} = \tilde{\mathsf{H}}(j\omega_k, U_{0m}), \quad k = 1, ...K, \quad m = 1, ..., M \tag{5.13}$$

that are again computed by performing a series of AC sweeps of the original circuit for different bias conditions U_{0m}. Dataset (5.13) is analogous to the one involved

in (4.7), and therefore the PSK iteration can be used to generate the model. The novel technical derivations of this chapter will be derived using the PSK model structure in Bernstein polynomial basis

$$\mathsf{H}(s,U_0)=\frac{\mathsf{N}(s,U_0)}{\mathsf{D}(s,U_0)}=\frac{\sum_{i=0}^{n}\sum_{\boldsymbol{\ell}\in\mathcal{I}_{\bar{\boldsymbol{\ell}}}}R_{i,\boldsymbol{\ell}}\,b_{\boldsymbol{\ell}}^{\bar{\boldsymbol{\ell}}}(U_0)\,\varphi_i(s)}{\sum_{i=0}^{n}\sum_{\boldsymbol{\ell}\in\mathcal{I}_{\bar{\boldsymbol{\ell}}}}r_{i,\boldsymbol{\ell}}\,b_{\boldsymbol{\ell}}^{\bar{\boldsymbol{\ell}}}(U_0)\,\varphi_i(s)}. \tag{5.14}$$

Other choices of the parameter-dependent basis functions are allowed, as will be shown in a practical application at the end of this section. The model transfer function (5.14) admits the state space realization

$$\mathsf{H}(s,U_0)\leftrightarrow\left(\begin{array}{c|c}A-BD_{\otimes}^{-1}C_{\otimes} & -BD_{\otimes}^{-1}\\ \hline C_2-D_2D_{\otimes}^{-1}C_{\otimes} & D_2D_{\otimes}^{-1}\end{array}\right)=\left(\begin{array}{c|c}A_M(U_0) & B_M(U_0)\\ \hline C_M(U_0) & D_M(U_0)\end{array}\right). \tag{5.15}$$

The above is obtained starting from (4.24) and (4.39), as explained in [103]. The involved matrices are defined as in Chapter (4.25), (4.26), (4.39), and their explicit dependency on U_0 in the left side of the equality is omitted for readability.

When the PSK modeling framework is applied to generate parameterized small signal models, the only difference occurring between (5.14) and the model structure exploited in Chapter 4 for the modeling of passive devices is represented by the nature of the uncertain parameters; all the other symbols and quantities retain the same meaning and the same interpretation that have been introduced in chapter 4.

Stability enforcement

The considered model structure is such that the stability enforcement strategy introduced in 4.3 can be applied with no modifications in order to obtain a uniformly stable macromodel throughout $\mathcal{U}_0$. This condition reflects the preliminary assumption that $\tilde{A}(U_0)$ must be asymptotically stable for all the considered bias configurations. As Bernstein polynomials are defined in the unit interval, the bias space $\mathcal{U}_0$ must be normalized to the unitary hypercube for (5.14) to be consistent. Otherwise, different available strategies can also be employed to guarantee model stability, e.g. the one proposed in [112].

Modeling of parameterized DC correction

Once model (5.14) is generated, it must be augmented with the affine correction term, suitably parameterized over the bias space, that allows to recover the reference circuit DC output $Y_0(U_0)=G(\Xi,U_0),\ U_0\in\mathcal{U}_0$. The parameterized DC correction term $Y_C(U_0)$ is defined upon state space (5.15) and $Y_0(U_0)$ as

$$Y_C(U_0)=Y_0(U_0)-(C_MX_0+D_MU_0)\quad\text{and}\quad X_0=-A_M^{-1}B_MU_0, \tag{5.16}$$

and can be determined using the small-signal reduced order model and the full-order device netlist. For a set of bias configurations $U_{0,j} \in \mathcal{U}_0,\ j = 1, \dots J$, the reference system DC output values $Y_{0j} = Y_0(U_{0j})$ are computed with a parameterized DC analysis. Then, the samples of the required map can be defined as

$$Y_{Cj} = Y_{0j} - (C_M X_0 + D_M U_{0j}), \quad j = 1, \dots J. \tag{5.17}$$

As the complexity of DC analysis is usually modest and so is that of the model evaluation, a large number J of samples can be retrieved with small computational effort. Once these data are gathered, standard interpolation techniques can be used to generate a model for the required parameterized DC correction term $Y_C(U_0)$. This interpolation procedure can be performed with arbitrary choice of basis functions, simply via least-squares estimation. The approach is straightforward and further details can be found in [82], [18]. Once the approximation of $Y_C(U_0)$ is available, the overall parameterized affine model is assembled as

$$\begin{aligned} \dot{x}(t) &= A_M(U_0)x(t) + B_M(U_0)u(t), \qquad x(0) = X_0 = -A_M^{-1}B_M U_0, \\ y(t) &= C_M(U_0)x(t) + D_M(U_0)u(t) + Y_C(U_0). \end{aligned} \tag{5.18}$$

The following example shows how the proposed procedure can be used to generate a bias-dependent linearized model of an LDO circuit.

Bias-dependent linearized equivalent of a post-layout LDO circuit

This example shows how bias-dependent linearized models can be used to drastically speedup small-signal simulations of circuit blocks in advanced stage of design, as anticipated in Sec 1.2.1. The presented results have been documented in [18].

We consider the Only-MOS regulator design proposed in [74] depicted in Fig. 5.2. The circuit was instantiated in Cadence environment, including the layout description [1]. The design is characterized by low quiescent current and is intended for low-power applications, with a maximum nominal load current $I_L = 10$ mA and a minimum rated input voltage $V_{DD} = 0.9$ V. The circuit was designed according to the reference specifications, making use of a 40 nm CMOS process. The resulting layout takes a 0.0045 mm^2 area.

For fixed bias configuration, the circuit block is characterized in terms of its small signal hybrid matrix $\tilde{\mathsf{H}}(s)$:

$$\begin{bmatrix} i_1 \\ v_2 \end{bmatrix} = \tilde{\mathsf{H}}(s) \begin{bmatrix} v_1 \\ i_2 \end{bmatrix}, \tag{5.19}$$

where port 1 denotes the supply voltage and the port 2 the regulated voltage. For this example, the admissible DC bias conditions for the supply voltage at port 1 are

[1] We thank Dr. Pedro Filipe Leite Correia De Toledo for providing the circuit design

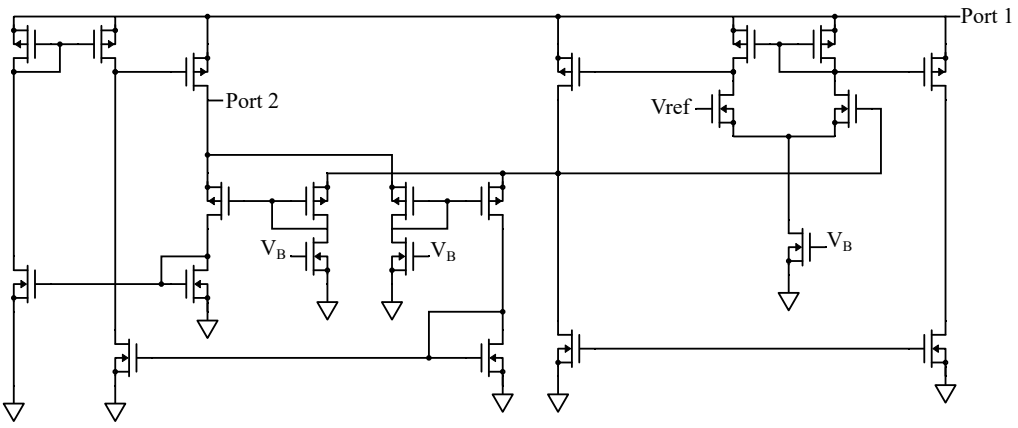

Figure 5.2: A Only-MOS LDO circuit schematic designed with 40 nm CMOS process

$V_{DD} \equiv U_0^1 \in [0.9, 1.1]$ V. At port 2, the admissible DC values for the load current are instead $I_L \equiv U_0^2 \in [0, 10]$ mA.

A parameterized small signal-model for the circuit, valid for the above defined bias space, was obtained by applying the PSK algorithm of Sec. 3.2.1. A parameterized AC sweep was applied to the post-layout netlist to sample $\tilde{\mathsf{H}}(s, U_0)$ (defined as in (5.12)) in correspondence of a 25×25 square grid over $\mathcal{U}_0$. For each bias configuration, $K = 125$ logarithmically spaced samples of the frequency response were retrieved over the bandwidth $[0, 10]$ GHz. A subset of 208 parameters configuration were used to perform model generation, setting $n = 9$ and inducing the parameterization by choosing $\xi_\ell(U_0)$ as multivariate Chebyshev polynomials, of multidegree $\boldsymbol{\ell}_N = (4,4)$ for the numerator and $\boldsymbol{\ell}_D = (3,3)$ for the denominator. Model stability has been enforced in this case using the sampling-based strategy proposed in [112].

Fig. 5.3 shows the result of the multivariate rational fitting for one element of the hybrid matrix, proving that the accuracy of the model is excellent for all of the cosidered bias configurations.

Once the parameterized rational function $\mathsf{H}(s, U_0)$ is available, the parameterized correction term $Y_C(U_0)$ is computed to augment the small signal model with the affine correction term. The required samples Y_{Cj} are computed via parameterized DC analysis using formula (5.17) and $Y_C(U_0)$ is reconstructed via multivariate Chebyshev polynomials least-squares regression, performed on the available data. The results of this regression for the DC correction at Port 2 are shown in Fig. 5.4 (left panel), together with the residual fitting error (right panel). The accuracy of the approximation if excellent throughout the bias space, with a maximum error around 2.5×10^{-3}.

Finally, $\mathsf{H}(s, U_0)$ and $Y_C(U_0)$ are assembled to generate final model (5.18). The state space model is cast into an equivalent SPICE netlist having a few kB size, against the 30 MB of the post-layout original circuit netlist. In order to evaluate

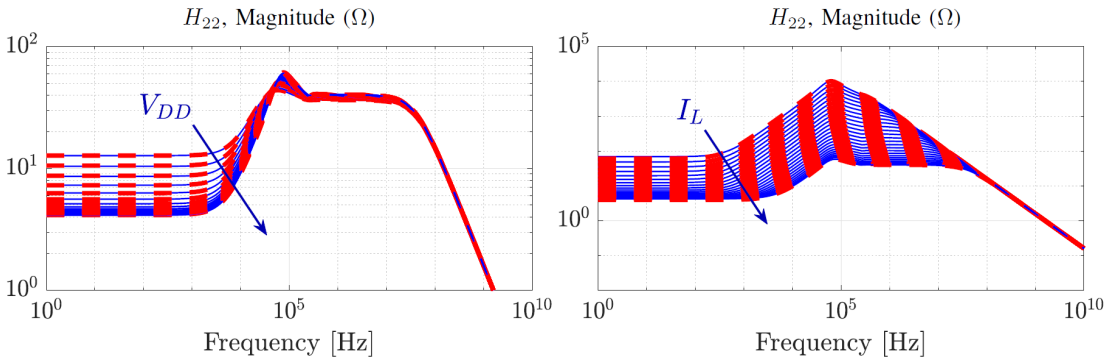

Figure 5.3: Comparison between reference data (blue solid lines) and reduced order small signal model (dashed red lines) for the post-layout LDO circuit. Left panel: fixed bias current $I_L = 10$ mA, with varying DC voltage within the bias space. Right panel: the same by fixing $V_{DD} = 1$ V and varying I_L. Reproduced from [18] © 2019 IEEE.

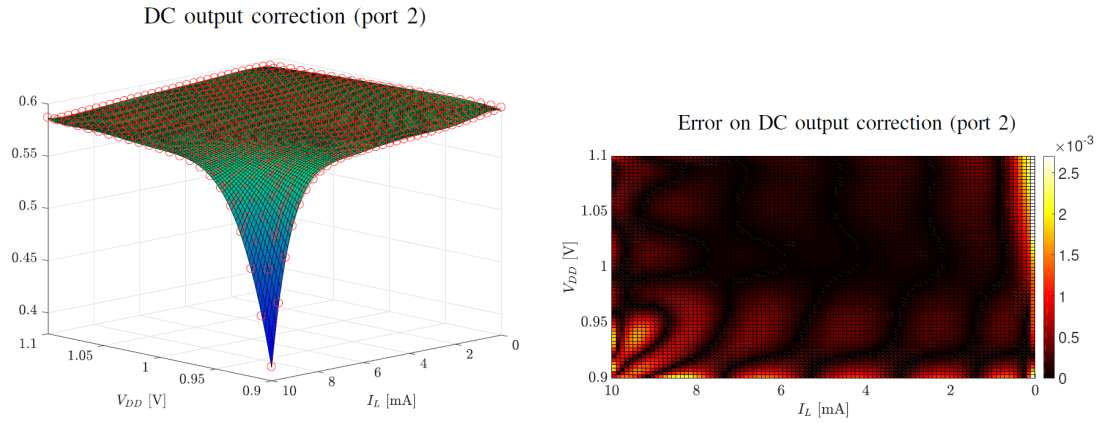

Figure 5.4: The parameterized DC correction $Y_C(U_0)$ for the second port of the post-layout LDO test case. Right panel: reference data Y_{Cj} (red dots) against the resulting curve fitting (solid surface). Right panel: residual fitting error. Reproduced from [18] © 2019 IEEE.

the effectiveness of the complexity reduction, we performed a small signal transient simulations by fixing the bias configuration with $V_{DD} = 1$ V and $I_L = 5$ mA, and comparing the reference circuit response with that of the macromodel. The simulation is performed by superimposing two sequential pulses of amplitude ±25 mV and width 25μs to the V_{DD} bias. The results of the simulation are shown in Fig. 5.5, and confirm the excellent agreement between the reference circuit and the model. Simulating the post-layout netlist required 63 s, while only 93 ms were required by the model. The equivalent speed-up factor is in this case about 675×.

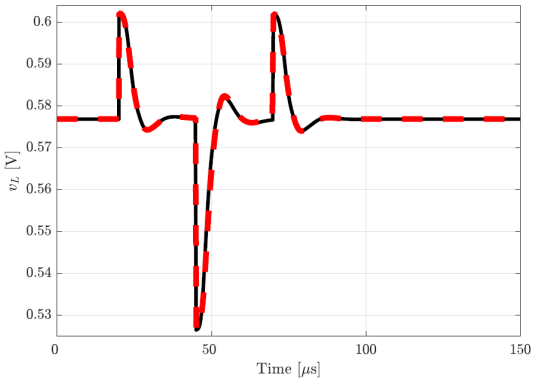

Figure 5.5: A small signal transient simulation. Affine linearized model (dashed red lines) against reference post-layout LDO circuit (solid black line). The model simulation was 675× faster than the native circuit description. Reproduced from [18] © 2019 IEEE.

5.2 Non-stationary operating conditions: the time-varying approximation

The steps leading from (5.8) to (5.18) provide a linearized model that can be used in place on the original nonlinear circuit for small signal analyses with constant but uncertain operating point. However, during small-signal system level simulations, the bias condition of the CB may be nonstationary, for example due to a change of the loading conditions imposed by the terminations, or due to the effect of some control operation aimed at tuning the operating point to meet some performance goal, such as minimization of the power consumption. When the rate of variation of the operating condition is slower than that of the small signals components, the device evolution can be characterized by linearizing (5.1) around a trajectory determined by the istantaneous operating condition. This concept is formalized in the next derivations.

Let us assume that the input signal can be decomposed into a time-varying bias term and a small-signal component, by generalizing (5.2) into

$$u(t) = U_0(t) + \tilde{u}(t), \tag{5.20}$$

where

- $U_0(t)$, from now on called *bias component*, is a slowly varying signal. Its rate of variation limit will be further characterized below in Assumption 5.1. It is also assumed that the amplitude of $U_0(t)$ is not necessarily small, but that

$$U_0(t) \in \mathcal{U}_0 \quad \forall t. \tag{5.21}$$

- $\tilde{u}(t)$ is a small-signal input with $\tilde{u}(0) = 0$.

When the input signal is defined as above, the time invariant model (5.8) is not adequate to represent the dynamics of (2.28), as the changes of the bias component $U_0(t)$ may induce the circuit block to operate in correspondence of different operating points.

The derivations contained in this section are based on the following assumption

Assumption 5.1. *For each $t^* \geq 0$, the nonlinear equation*

$$F(\xi, U_0(t^*)) = 0 \tag{5.22}$$

has a unique solution $\xi = \Xi_0(t^*)$, and a small constant $\delta_\xi > 0$ exists such that each solution of (5.1) corresponding to input (5.20), obeys the inequality

$$||\xi(t^*) - \Xi_0(t^*)||_2 \leq \delta_\xi. \tag{5.23}$$

Assumption 5.1 requires that the response of the nonlinear system is sufficiently fast to respond to the variations of the input bias component in such a way that the corresponding time-varying local equilibrium point tracks continuously the evolution of $U_0(t)$. This assumption is satisfied when the spectrum of $U_0(t)$ is limited to sufficiently low frequencies. The implications of this requirement will be documented on a practical example presented Section 5.3. If Assumption 5.1 is verified, at each time instant the system trajectory $(\xi(t), u(t))$ is confined to a neighborhood of the particular state-input configuration $(\Xi_0(t), U_0(t))$ which satisfies

$$\begin{aligned} 0 &= F(\Xi_0(t), U_0(t)), \\ Y_0(t) &= G(\Xi_0(t), U_0(t)). \end{aligned} \tag{5.24}$$

If δ_ξ is small enough and (5.24) holds, the small-signal dynamics of (5.1) can be approximated by the time-varying linearization

$$\begin{aligned} \dot{\tilde{\xi}}(t) &\approx F'_\Xi(\Xi_0(t), U_0(t)) \cdot \tilde{\xi}(t) + F'_U(\Xi_0(t), U_0(t)) \cdot \tilde{u}(t), \\ \tilde{\eta}(t) &\approx G'_\Xi(\Xi_0(t), U_0(t)) \cdot \tilde{\xi}(t) + G'_U(\Xi_0(t), U_0(t)) \cdot \tilde{u}(t), \end{aligned} \tag{5.25}$$

with $\tilde{\xi}(0) = 0$. In view of the one-to-one correspondence between $\Xi_0(t)$ and $U_0(t)$, (5.25) can be rewritten as

$$\begin{aligned} \dot{\tilde{\xi}}(t) &\approx \tilde{A}(U_0(t)) \cdot \tilde{\xi}(t) + \tilde{B}(U_0(t)) \cdot \tilde{u}(t), \quad \tilde{\xi}(0) = 0 \\ \tilde{\eta}(t) &\approx \tilde{C}(U_0(t)) \cdot \tilde{\xi}(t) + \tilde{D}(U_0(t)) \cdot \tilde{u}(t), \end{aligned} \tag{5.26}$$

where $\tilde{A}, \tilde{B}, \tilde{C}, \tilde{D}$ are defined as in (2.54) (2.51). From (5.26) it can be seen that, under Assumption 1, the instantaneous value of the matrices entering (5.26) is

the same as the one attained by the matrices defining parameterized small signal transfer function (5.12), provided that $U_0(t) \in \mathcal{U}_0,\ \forall t$. Therefore, the parameterized modeling procedure of Sec. 5.1.2 can be easily generalized to generate a reduced order model that mimics the desired map $U_0(t) + \tilde{u}(t) \to Y_0(t) + \tilde{\eta}(t)$.

The proposed modeling procedure can be summarized as follows:

1. gather the frequency samples (5.13) of the small signal transfer function at prescribed fixed values of the bias component;

2. synthesize a reduced-order parameterized transfer function in the form of (5.14) exploiting the PSK iteration;

3. cast the parameterized transfer function into the state space (5.15) or into an equivalent netlist, (not covered here, see [51]). Up to this step, the procedure is the same as for standard parameterized macromodeling flows.

4. during a transient simulation, extract the bias input component $U_0(t)$ from the total input $u(t)$ and use this time-varying bias to instantiate the model parameters in (5.15) by setting $U_0 = U_0(t)$ at each time step.

As a result, the precedure returns a LPV affine model

$$\begin{aligned} \dot{x}(t) &= A_M(U_0(t))x(t) + B_M(U_0(t))u(t), \qquad x(0) = X_0 = -A_M^{-1}B_M U_0(0), \\ y(t) &= C_M(U_0(t))x(t) + D_M(U_0(t))u(t) + Y_C(U_0(t)). \end{aligned} \tag{5.27}$$

that represents a generalization of (5.15) to the time-varying case. Provided that the value of $U_0(t)$ is known at each time instant, and that Assumption 5.1 is verified, the model can be used to replace the original circuit block in a small signal analysis with nonstationary operating conditions. Adopting the reduction process, the state space matrices in (5.15) have small size, and significant simulation speedup is expected.

However, to exploit model (5.27) in system-level simulations, the two following issues need to be addressed

- when the dynamics of the nonlinear system (5.1) are known to be stable when subject to input of the type (5.20), this stability must be inherited by model 5.27. Indeed, even if the "frozen-time" model (5.15) is guaranteed to be uniformly stable for *constant* configurations of $U_0 \in \mathcal{U}_0$, the stability of dynamics 5.27 it is not guaranteed when a time variation $U_0(t)$ takes place [119]. Therefore, the model generation must include some kind of appropriate constraints that guarantee the desired property.

- during runtime operation, the bias component $U_0(t)$ must be estimated starting from the evolution of the full input $u(t)$, in order to provide a valid instantaneous parameterization of the time-varying model.

These two issues will be addressed in sections 5.2.1, 5.2.2, providing a reliable framework for the generation of LPV linearized macromodels.

As a last observation, notice that up to now the discussion has been focused on the generation of linearized models in which the variation of the operating point is induced by slowly varying components of the electrical quantities imposed at the circuit block interfaces. Model structure (5.27) can also be exploited to take into account changes of the circuit operating point induced by external environmental parameters on which (5.1) depends, e.g., on temperature. In this scenario, a known instantaneous profile of the external parameter, such as a temperature profile induced by heating, can be considered during runtime. Alternatively, coupled electro-thermal or even multiphysics simulation, where the parameters are obtained as a result of a co-simulation of an associated thermal or multiphysics model, are also enabled by the proposed model structure.

In both the above-mentioned scenarios, the actual parameter value is available in some form as a variable that is independent on the electrical port signals. Therefore, there is no need to estimate in real time the actual working condition based on the input signal $u(t)$, and the exploitation of the proposed model structure is more straightforward. In Section 5.3, an example of the first scenario, where a given temperature profile is applied at runtime, is presented. Coupled multiphysics simulations are left as a future investigation.

5.2.1 Self-parameterized model structure

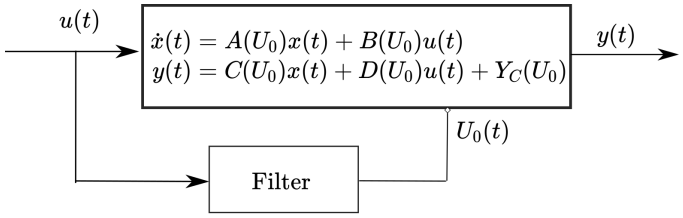

Figure 5.6: The proposed model structure augmented with a low-pass filter aimed at extracting the bias component and providing the instantaneous parameterization to the linearized dynamics. Reproduced from [22] © 2021 IEEE.

During a transient analysis, the signal decomposition (5.20) is not defined uniquely, as the only available numerical quantity is the full input signal $u(t)$ at the circuit interface. Therefore, the exploitation of (5.20) is practically applicable only in view of an automated procedure aimed at isolating the bias and the small signal components, as (5.27) requires the availability of the instantaneous input bias component $U_0(t)$, to be provided as a parameter for the affine state.

When Assumption 5.1 holds, the spectrum of $U_0(t)$ is confined to a sufficiently narrow low-frequency band, and the proposed time-varying linearization can be

applied. It is thus intuitive that the required parameterization can be obtained from the input signal by means of a low-pass filter aimed at extracting the value of the instantaneous bias component. The resulting model structure is depicted in Fig. 5.6,

The design of such a filter should be compliant with the requirements of our main assumption; in particular, it must provide a parameterization such that (5.23) holds with sufficiently small δ_ξ. However, since the non-linear equations (5.1) are not available in closed form, no analytical methods based on the native circuit description can be exploited to derive an exact characterization of the frequency domain properties that $U_0(t)$ must fulfill, in order to maintain the validity of the proposed approximation. Due to this limitation, only heuristic criteria based on experimental (simulated) data regarding the circuit under modeling can be employed to design the filter. The following procedure is proposed:

1. Build the low-order small-signal transfer function (5.14).
2. Sample the poles of the transfer function over the bias space $\mathcal{U}_0$. This operation is not computationally expensive since the order n of the model is small.
3. Determine the angular frequency ω_p of the slowest pole of the parameterized transfer function.
4. Set the cut-off frequency of the filter $\omega_c = \rho\,\omega_p$, with $\rho \leq 0.1$
5. Build a second order Butterworth filter of with gain and cut-off frequency ω_c.

The above procedure is aimed at guaranteeing a sufficiently slow variation of the bias parameter, in compliance with previous results concerning LPV models derived from frozen-parameter configurations of the underlying system, see e.g. [30], [107], [4]. Whenever an a-priori knowledge of the frequency content of the bias input $U_0(t)$ is available, it can be used to tune the value of the ratio ρ.

In principle, time-domain data could also be exploited in the design of the desired filter, based for example on the maximization of the accuracy of the model against reference time domain training samples. In the proposed framework, retrieving time domain data from the original circuit description is extremely expensive in terms of time requirements, as will be shown in the experimental section. Additionally, due to the non-linear nature of equations (2.28), time-domain approaches would not provide additional warranties of accuracy when the model is subject to input profiles that are different from those used to guide filter design. Time-domain approaches are thus impractical and beyond the scope of this work.

5.2.2 Quadratic stability constraints

In section 4.3, a method for the enforcement of uniform stability of LTI parameterized macromodels has been presented. However, the method is based upon the frequency domain conditions (4.28), and can be used only to enforce the asymptotic stability of Linear Time Invariant reduced order models; the addressed methodology, when applied to generate the affine LPV macromodel (5.27) does not guarantee that the dynamics of the resulting state space is stable irrespectively of the time domain profile of the parameter $U_0(t)$. Therefore, some stronger conditions are required.

The characterization of the stability properties of LPV systems has been subject of intensive research in the fields of robust control and gain scheduling, see for instance [15], [90], [118], [43]. A standard approach is to embed in the modeling procedure the search for a Lyapunov function, which guarantees that the resulting system is *quadratically stable*, meaning that is exponentially stable and admits a quadratic parameter-independent Lyapunov function. This strong characterization entails the asymptotic stability of system (5.27) under any possible time domain evolution of the parameters $U_0(t)$. We refer to [95], for a complete theoretical framework.

This approach can be incorporated in the PSK algorithm in order to enforce the required stability properties to equations (5.27). This section shows that the enforcement of quadratic stability can be achieved by constraining the iterative PSK denominator estimation problem (3.36) with a suitable set of LMI constraints, that represent a particular case of those introduced in 4.3 for the LTI case.

The derivation of such constraints exploits two known results. The first is the equivalence between the affine state space formulation (5.27) and the descriptor realization [103]

$$\underbrace{\begin{bmatrix}\mathbb{I}_{n\times \mathrm{P}} & 0\\ 0 & 0\end{bmatrix}}_{E}\begin{bmatrix}\dot{x}\\ \dot{w}\end{bmatrix} = \underbrace{\begin{bmatrix}A & B\\ C_{\otimes}(U_0(t)) & D_{\otimes}(U_0(t))\end{bmatrix}}_{\mathcal{A}(U_0(t))}\begin{bmatrix}x\\ w\end{bmatrix} + \underbrace{\begin{bmatrix}0\\ -\mathbb{I}_{\mathrm{P}}\end{bmatrix}}_{\mathcal{B}} u$$

$$y = \underbrace{\begin{bmatrix}C_2(U_0(t)) & D_2(U_0(t))\end{bmatrix}}_{\mathcal{C}(U_0(t))}\begin{bmatrix}x\\ w\end{bmatrix} + Y_C(U_0(t)) \tag{5.28}$$

which holds since the structure of (5.27) is compliant with (2.60). The equivalence also requires that $D_{\otimes}(U_0) \neq 0$ for all $U_0 \in \mathcal{U}_0$, a condition that will be guaranteed by the proposed stability conditions, as will be clear from the following derivations. Therefore, the descriptor system (5.28) is well-posed, regular, and impulse-free.

The second available result needed to perform our derivations is the following [24, Theorem 2.4.4], which provides the conditions that (5.28) must satisfy in order to be quadratically stable.

Theorem 5.1 (quadratic stability for descriptor systems)**.** *The descriptor LPV system*

$$E \begin{bmatrix} \dot{x} \\ \dot{w} \end{bmatrix} = \mathcal{A}(U_0(t)) \begin{bmatrix} x \\ w \end{bmatrix} \tag{5.29}$$

is quadratically stable if there exists

$$Q(U_0) = \begin{bmatrix} Q_1 & 0 \\ Q_2(U_0) & Q_3(U_0) \end{bmatrix} \tag{5.30}$$

with $Q_1 \in \mathcal{S}_{++}^{(n\mathrm{P})}$, $Q_2 : \mathcal{U}_0 \to \mathbb{R}^{\mathrm{P}\times n}$ *and* $Q_3 : \mathcal{U}_0 \to \mathbb{R}^{\mathrm{P}\times \mathrm{P}}$ *such that the inequality*

$$\mathcal{A}(U_0)^\top Q(U_0) + Q(U_0)^\top \mathcal{A}(U_0) \prec 0 \quad \forall U_0 \in \mathcal{U}_0. \tag{5.31}$$

holds

Theoretically, Theorem 5.1 provides sufficient conditions that (5.28) must satisfy to be quadratically stable. Nevertheless, these conditions can not be enforced directly while generating the model, for two main reasons:

1. The entries $C_\otimes$ and $D_\otimes$ of the state matrix $\mathcal{A}(U_0)$ are defined upon the unknown model coefficients, according to (4.39). Considering these coefficients and $Q(U_0)$ as unknown variables, (5.31) becomes a *non-convex* bilinear matrix inequality (BMI) and thus cannot be solved efficiently as the number of unknowns becomes large.

2. Condition (5.31) is required to hold uniformly over the whole parameter space $\mathcal{U}_0$, imposing an infinite set of constraints.

In view of these considerations, enforcing (5.31) would translate in the necessity to perform the model generation while imposing an infinite number of BMI constraints, in order to guarantee the quadratic stability of (5.28). This approach is computationally impractical.

In order to make (5.28) compatible with the requirements of Theorem 5.1, a simplified set of sufficient conditions is derived. The derivations are similar to those of Section 4.3. Also in this case, the properties of the Bernstein polynomials are used to parameterize the model structure. It is shown that this strategy provides a guarantee for the quadratic stability through a *finite* set of LMIs.

The main result about the quadratic stability enforcement is given and proved in the following.

Theorem 5.2 (Sufficient conditions for quadratic stability)**.** *The LPV system* (5.28) *is quadratically stable if there exists* $\overline{Q}_1 \in \mathcal{S}_{++}^n$ *such that*

$$\begin{bmatrix} A_1^\top \overline{Q}_1 + \overline{Q}_1 A_1 & \overline{Q}_1 B_1 - C_1^{\boldsymbol{\ell}\top} \\ B_1^\top \overline{Q}_1 - C_1^{\boldsymbol{\ell}} & -2D_1^{\boldsymbol{\ell}} \end{bmatrix} \prec 0 \quad \forall \boldsymbol{\ell} \in \mathcal{I}_{\bar{\boldsymbol{\ell}}}. \tag{5.32}$$

Proof: Consider first the descriptor state matrix associated to (5.28) for the single-input-single-output case, P = 1

$$\mathcal{A}(U_0) = \begin{bmatrix} A_1 & B_1 \\ C_1(U_0) & D_1(U_0) \end{bmatrix}. \tag{5.33}$$

Applying Theorem 5.1 to the matrix $\mathcal{A}$ from (5.33) and defining

$$Q = \begin{bmatrix} \overline{Q}_1 & 0 \\ 0 & -1 \end{bmatrix}$$

shows that (5.33) is quadratically stable if $\overline{Q}_1 = \overline{Q}_1{}^{\top} \succ 0$ obeys the inequalities

$$\begin{bmatrix} A_1^{\top}\overline{Q}_1 + \overline{Q}_1 A_1 & \overline{Q}_1 B_1 - C_1(U_0)^{\top} \\ B_1^{\top}\overline{Q}_1 - C_1(U_0) & -2D_1(U_0) \end{bmatrix} \prec 0 \quad \forall U_0 \in \mathcal{U}_0. \tag{5.34}$$

Expanding $C_1(U_0)$ and $D_1(U_0)$ according to their definitions, (4.22) and (4.23), leads to the equivalent condition

$$\begin{bmatrix} A_1^{\top}\overline{Q}_1 + \overline{Q}_1 A_1 & \overline{Q}_1 B_1 - \sum\limits_{\boldsymbol{\ell}\in\mathcal{I}_{\bar{\boldsymbol{\ell}}}} b_{\boldsymbol{\ell}}^{\bar{\boldsymbol{\ell}}}(U_0)\cdot C_1^{\boldsymbol{\ell}\top} \\ B_1^{\top}\overline{Q}_1 - \sum\limits_{\boldsymbol{\ell}\in\mathcal{I}_{\bar{\boldsymbol{\ell}}}} b_{\boldsymbol{\ell}}^{\bar{\boldsymbol{\ell}}}(U_0)\cdot C_1^{\boldsymbol{\ell}} & -2\sum\limits_{\boldsymbol{\ell}\in\mathcal{I}_{\bar{\boldsymbol{\ell}}}} b_{\boldsymbol{\ell}}^{\bar{\boldsymbol{\ell}}}(U_0)\cdot D_1^{\boldsymbol{\ell}} \end{bmatrix} \prec 0 \tag{5.35}$$

that must hold $\forall U_0 \in \mathcal{U}_0$. In view of (4.13), one has

$$A_1 = A_1 \sum_{\boldsymbol{\ell}\in\mathcal{I}_{\bar{\boldsymbol{\ell}}}} b_{\boldsymbol{\ell}}^{\bar{\boldsymbol{\ell}}}(U_0), \quad B_1 = B_1 \sum_{\boldsymbol{\ell}\in\mathcal{I}_{\bar{\boldsymbol{\ell}}}} b_{\boldsymbol{\ell}}^{\bar{\boldsymbol{\ell}}}(U_0) \tag{5.36}$$

so that (5.35) shapes into

$$\sum_{\boldsymbol{\ell}\in\mathcal{I}_{\bar{\boldsymbol{\ell}}}} b_{\boldsymbol{\ell}}^{\bar{\boldsymbol{\ell}}}(U_0) \begin{bmatrix} A_1^{\top}\overline{Q}_1 + \overline{Q}_1 A_1 & \overline{Q}_1 B_1 - C_1^{\boldsymbol{\ell}\top} \\ B_1^{\top}\overline{Q}_1 - C_1^{\boldsymbol{\ell}} & -2D_1^{\boldsymbol{\ell}} \end{bmatrix} \prec 0, \ \forall U_0 \in \mathcal{U}_0 \tag{5.37}$$

Due to (4.13), condition (5.37) is entailed by the discrete set of LMIs (5.32). This proves the result for the case P = 1.

The general case P > 1 is proved by applying Theorem 5.1 to the matrix $\mathcal{A}(U_0)$ whose blocks are defined in (4.39), and by defining the matrix

$$Q = \begin{bmatrix} \mathbb{I}_{\mathrm{P}} \otimes \overline{Q}_1 & 0 \\ 0 & -\mathbb{I}_{\mathrm{P}} \end{bmatrix},$$

where $\overline{Q}_1 = Q_1^{*\top} \succ 0$ is a matrix that satisfies (5.34). Condition (5.31) shapes into

$$\mathcal{S} \prec 0 \quad \forall U_0 \in \mathcal{U}_0, \tag{5.38}$$

with

$$\mathcal{S} = \begin{bmatrix} \mathbb{I}_{\mathrm{P}} \otimes (A_1^\top \overline{Q}_1 + \overline{Q}_1 A_1) & \mathbb{I}_{\mathrm{P}} \otimes (\overline{Q}_1 B_1 - C_1(U_0)^\top) \\ \mathbb{I}_{\mathrm{P}} \otimes (B_1^\top \overline{Q}_1 - C_1(U_0)) & -\mathbb{I}_{\mathrm{P}} \otimes (2D_1(U_0)) \end{bmatrix}$$

A similarity transformation $\bar{\mathcal{S}} = T^\top \mathcal{S} T$, where T is an appropriate permutation matrix, leads to

$$\bar{\mathcal{S}} = \mathbb{I}_{\mathrm{P}} \otimes \begin{bmatrix} A_1^\top \overline{Q}_1 + \overline{Q}_1 A_1 & \overline{Q}_1 B_1 - C_1(U_0)^\top \\ B_1^\top \overline{Q}_1 - C_1(U_0) & -2D_1(U_0) \end{bmatrix} \tag{5.39}$$

which is a block-diagonal repetition of (5.34), being thus negative definite, along with $\mathcal{S}$, whenever $\overline{Q}_1$ satisfies (5.32). This completes the proof.■

Theorem 5.2 provides sufficient conditions, that once verified, guarantee that the affine LPV system (5.27) is quadratically stable. These conditions can be enforced very easily during the model generation. Indeed, conditions (5.32) represent a finite set of small-size LMIs, that can be enforced while solving (3.36); the resulting optimization problem is

$$\min_{x^\nu} \left\| \bar{T}^\nu x^\nu \right\|_2 \qquad \text{s.t.} \quad \begin{bmatrix} A_1^\top \overline{Q}_1 + \overline{Q}_1 A_1 & \overline{Q}_1 B_1 - C_1^{\boldsymbol{\ell}\top} \\ B_1^\top \overline{Q}_1 - C_1^{\boldsymbol{\ell}} & -2D_1^{\boldsymbol{\ell}} \end{bmatrix} \prec 0 \quad \forall \boldsymbol{\ell} \in \mathcal{I}_{\overline{\boldsymbol{\ell}}},\ \overline{Q}_1 \succ 0 \tag{5.40}$$

analogous to (4.36), with the difference that only one positive definite constant instrumental matrix $\overline{Q}_1$ must be found while identifying the denominator coefficients. Therefore, the number of variables involved in the problem is $n(n+1)/2+(n+1)V_{\overline{\boldsymbol{\ell}}}$. Some remarks about the proposed procedure are in order.

Remark 5.1. In order to cast (5.31) into a convex condition, the structure of the Lyapunov function $Q(U_0)$ entering Theorem 5.1 has been simplified by imposing $Q_3(U_0) \equiv -1$ and $Q_2(U_0) \equiv 0$. This could be the cause of some degree of conservatism by over-constraining the model coefficients, and, in turn, the allowed parameterized poles trajectories. However, in practice, no significant loss of accuracy have been in observed in models generated applying the proposed method, as experimentally confirmed by the results presented in Section 5.3.

Remark 5.2. In the proposed formulation of Theorem 5.1, the state space realization associated to model structure (5.14) has been considered. The properties of the Bernstein polynomials defining the state space matrices allowed for the discretization of the continuous parameter-dependent quadratic stability condition. However, for the applicability of the proposed quadratic stability enforcement approach, the basis functions $\xi_{\boldsymbol{\ell}}(U_0)$ are not required to be necessarily Bernstein polynomials; every choice of basis such that

$$\sum_{\boldsymbol{\ell} \in \mathcal{I}_{\overline{\boldsymbol{\ell}}}} \xi_{\boldsymbol{\ell}}(U_0) = 1, \quad \xi_{\boldsymbol{\ell}}(U_0) \geq 0 \ \forall \boldsymbol{\ell} \in \mathcal{I}_{\overline{\boldsymbol{\ell}}}, \quad U_0 \in \mathcal{U}_0 \tag{5.41}$$

is compatible with the proposed quadratic stability constraints.

Remark 5.3. In the proposed framework, it is assumed that for any fixed configuration of the bias component $U_0 \in \mathcal{U}_0$, the nonlinear system (5.1) operates around a stable operating point defined by equations (5.3). The enforcement of the quadratic stability constraints (5.32) guarantees that the parameterized macromodel inherits this property. Nevertheless, it is known that when active devices are interconnected with certain (even passive) termination networks, the behavior of the interconnected system may be unstable. It is thus relevant to ask if a certain circuit block and the associated affine linearized equivalent (5.8) are both stable (or unstable) under the same loading conditions.

This may not be the case in general, due to the unavoidable discrepancies between the local behavior of the reference circuit and that of the macromodel; these differences are due to the errors introduced by both the linearization process and by the modeling algorithm used to generate the reduced order model. However, provided that the linearization does not introduce significant errors, and that the order reduction approximation $\mathsf{H}(s, U_0) \approx \tilde{\mathsf{H}}(s, U_0)$ holds with sufficient accuracy, then it may be argued that a termination that drives the macromodel to instability will do the same with the original circuit, and vice versa. Notice that the linear structure of the surrogate is such that the unstable behaviors is qualitatively different from that of the reference nonlinear system.

This situation occurs in the following example. Consider the common emitter amplifier circuit depicted in Fig.5.7; for this circuit, a linearized macromodel is derived around the stable equilibrium point enforced by the bias signal V_{cc}. The input-output small signal transfer function has a maximum gain about 5.2. Applying the procedure of [49, Sec. 4.1], a passive two-port network that leads the amplifier to instability can be found. Interconnecting this network with the macromodel leads to an unstable system, in this case with a pair of complex conjugate poles with positive real part $p_{1,2} = +166 \pm j628$ rad/s. By interconnecting both the macromodel and the original amplifier with the considered termination, and performing a a transient analysis using a sinusoidal excitation $v_s(t)$ with amplitude 1 μV and frequency 100 Hz, it is observed that instability occurs in both the situations. The resulting output voltages are depicted in Fig. 5.8. As can be observed, the results of the simulation are in agreement only up to a finite time horizon (about 80 ms). For later times, the actual amplifier undergoes saturation, making the small-signal assumption invalid.

Remark 5.4. The proposed set of linearized quadratic stability constraints (5.32) can be seen as more general (yet restrictive) conditions for ensuring the uniform stability of standard LTI parameterized macromodels, where the parameters are constant. These are obviously a particular case of LPV systems, where time variation of the parameters is suppressed.

It is interesting to note that both (4.28) and proposed conditions (5.32) provide

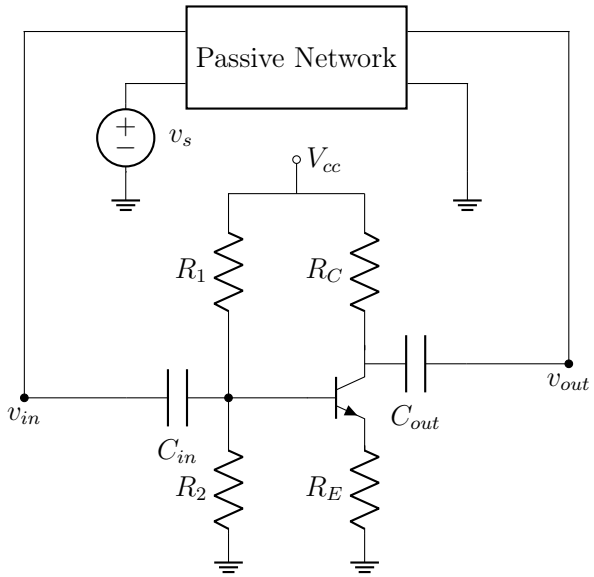

Figure 5.7: A common emitter amplifier ($C_{in} = C_{out} = 10$ μF, $R_1 = 4$ kΩ , $R_2 = 1$ kΩ, $R_C = 110$ Ω, $R_E = 20$ Ω and $V_{cc} = 10$ V) interconnected with a passive two-port network (see text). Reproduced from [22] © 2021 IEEE.

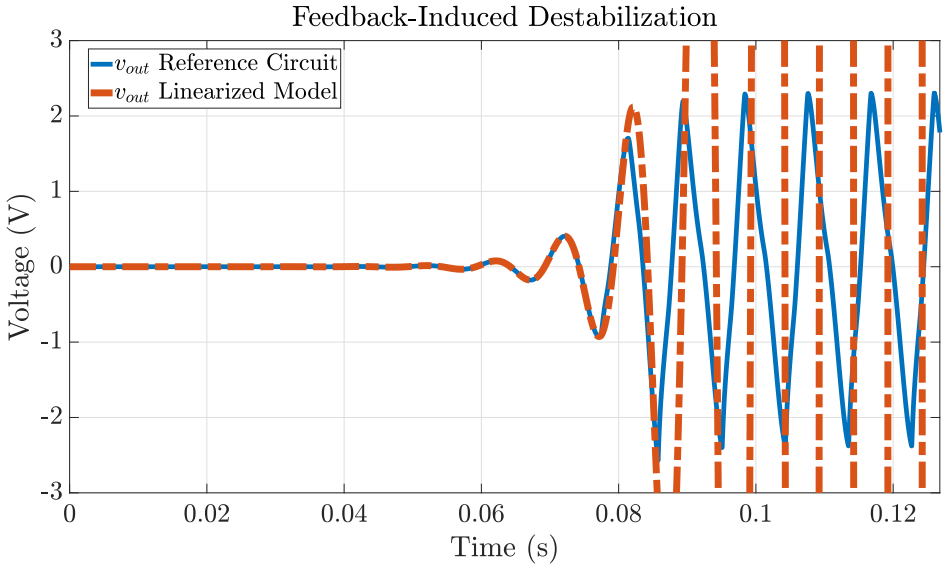

Figure 5.8: Transient analysis of the unstable electrical network depicted in Fig. 5.7. Reference nonlinear circuit and linearized model are in agreement up to a given time horizon, after which the small-signal assumption does not hold. Reproduced from [22] © 2021 IEEE.

a certification of model stability based on energetic properties of the model denominator function $\mathsf{D}(s, U_0)$. In short, if $\mathsf{D}(s, U_0)$ represents a passive system, then its inverse is also passive and both zeros and poles have a negative real part [53]. The proposed LMI conditions (5.32) provide a characterization of denominator passivity in terms of the Positive Real Lemma 2.6, analogously to (4.31), with the additional assumption that the employed storage function is constant.

5.3 Numerical examples

This section validates the proposed approach on a number of relevant test cases, showing the effectiveness and the limitations of the parameter varying modeling setting. The experiments are focused on two different Low Dropout Regulator (LDO) designs; this class of reference devices was chosen due to its relevance in modern electronic power distribution systems, in which they are heavily employed to guarantee different levels of stabilized reference voltages for the system components.

Two different LDOs designs are considered as test cases. The first was first presented in [75], and is treated in Sec 5.3.1. We will refer in the following as to LDO-A. The second is the post-layout LDO design already presented in Sec. 5.1.2. Here it is studied under nonstationary operating conditions. This test case will be denoted as LDO-B, and is considered in Sec. 5.3.2 and 5.3.3.

5.3.1 LDO-A

The first example provides a proof-of-concept validation of the proposed modeling framework. As reference circuit, a CMOS LDO regulator design, first proposed in [75] and depicted in 5.9, is considered.

The circuit schematic was instantiated in the LTSpice environment, without taking into account any additional layout description or packaging parasitics. This regulator provides a nominal output voltage $V_L = 2.8$ V for load currents values $I_L \in [0, 50]$ mA, with a minimum recommended DC input voltage $V_{DD} = 2.9$ V.

The circuit was modeled through its 2-port hybrid representation, considering as port variables the input voltage (port 1) and the load current (port 2). For this test case, the reference load current was fixed to $U_0^2 \equiv I_L = 10$ mA, while the input voltage was allowed to vary within the set $U_0^1(t) \equiv V_{DD}(t) \in [2.85, 3]$ V, in order to stress the non-linear degradation of the power supply rejection at low input voltages. The considered bias space is therefore the set $\mathcal{U}_0 = [2.85, 3]$ V $\times$ 10 mA.

The bias space was sampled by collecting $M = 20$ distinct small-signal frequency responses at different DC levels of the input voltage, and a reduced order model with order $n = 8$ was extracted by applying the quadratic stability constraints (5.32). $\mathsf{N}(s, U_0)$ and $\mathsf{D}(s, U_0)$ were both parameterized by means of third order Bernstein polynomials. The frequency-domain fitting required 6.2 s.

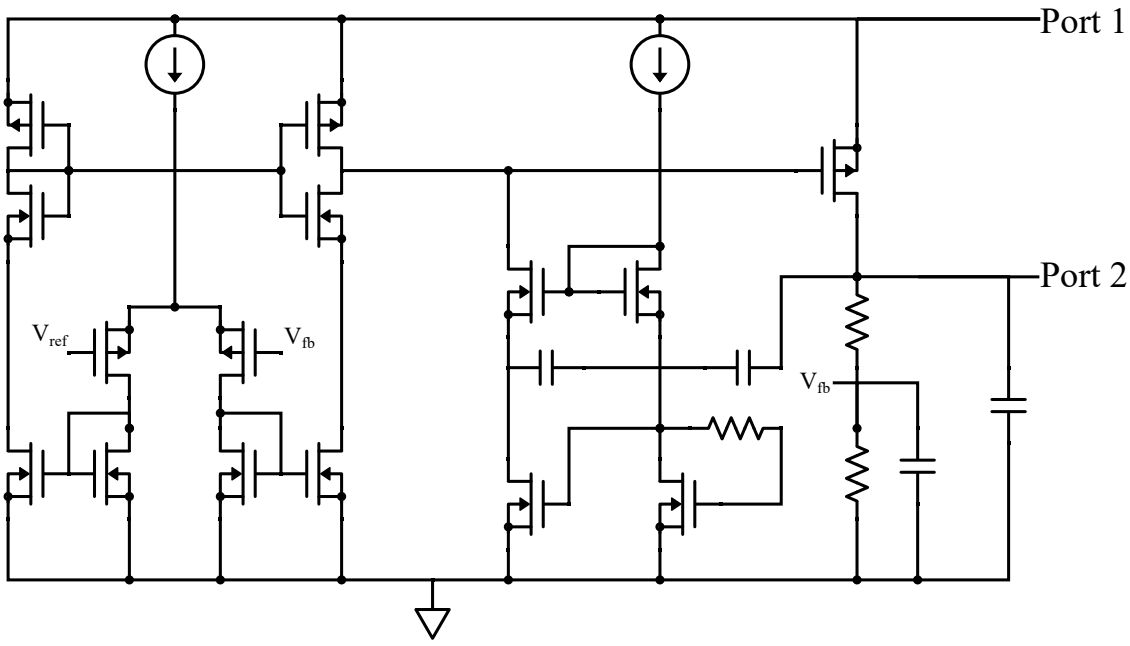

Figure 5.9: LDO-A. Circuit schematic

Figure 5.10 reports the results for two elements of the matrix transfer function, confirming the excellent accuracy of the model against the reference data. A low-pass filter with $\rho = 0.05$ and a cut-off frequency $\omega_c = 2\pi 800$ rad/s completes the model structure according to Fig. 5.6. The model was finally synthesized as a behavioral netlist, implemented in the LTSpice environment.

A set of transient analyses was performed in order to compare the performance of the proposed LPV behavioral model with the reference transistor-level schematic. To this aim, the following testing input signals were defined

$$\begin{aligned} u^1(t) &= a_1 \sin(2\pi f_1 t) + \frac{b}{1 + e^{-k(t-0.09)}} + 2.85 \text{ V} \\ u^2(t) &= a_2 \sin(2\pi\sqrt{2} f_1 t) + I_L \end{aligned} \tag{5.42}$$

where coefficients $a_1 = 5$ mV, $a_2 = 1$ mA and $f_1 = 10$ kHz define the small signal quantities. A variation of the operating point is induced by the second term in $u^1(t)$, with a slew rate parameterized by $b = 0.15$ V and by the shape factor k. A transient analysis was repeated for $k = 100, 200, \ldots, 1000$, in order to assess the ability of the model to track increasingly faster operating point variations. The considered bias profiles are depicted in Fig. 5.11.

The regulated voltage returned by the model prediction was compared with the transistor-level reference for the ten considered test cases, by computing the RMS value of the corresponding deviation. The results are reported in the top panel of Fig 5.12, while the bottom panel reports the transient regulated voltage

of model and true circuit for one case $k = 500$ (similar results were obtained for all values of k). It can be observed that the error remains well under control for all the considered bias profiles, although it increases slightly for faster bias variations. This behavior is expected, since faster variations are likely to be more difficult to track by the low-pass filter.

The necessity of a LPV model structure that embeds time-varying small-signal parameters is confirmed by Fig. 5.13. Here, the transient results obtained by a fixed model with LTI structure and constant state space matrices defined by a prescribed operating point $U_0^1 = 2.85$ V are reported, by letting the input bias component switch according to (5.42) with $k = 500$. In this experiment, the evolution of the bias component is not tracked by the model. The results show that the LTI model is not able to reproduce the correct voltage regulation behavior of the original circuit as the input voltage drifts to a higher value. On the other hand, the proposed LPV model structure adaptively tracks the operating point variation and recovers both the trend and the small signal variations of the output voltage (bottom panel of Fig. 5.12).

5.3.2 LDO-B

This second example is focused on a more realistic application scenario for the proposed modeling framework, and takes into account the LDO circuit design already considered in 5.1.2, which includes the parasitics characterization resulting from the circuit layout extraction. Similarly to the LDO-A circuit of Sec. 5.3.1, the device was modeled as a 2P system in hybrid representation. For this test case, a fixed bias level of the input voltage to $U_0^1 \equiv V_{DD} = 0.9$ V was considered, while the load current was allowed to span the entire operating range, so that $U_0^2 \equiv I_L \in [0, 10]$ mA. A model with $n = 9$ parameterized poles was derived starting from $M = 50$ frequency responses, obtained at different load current configurations, using a polynomial order $\bar{\ell} = 5$ for numerator and denominator. The model generation time was 8.6 s. The accuracy of the fitting is confirmed in Fig. 5.14, where no visible difference between the model and the reference small-signal responses can be noted, throughout the entire bias space. Finally, a low-pass filter with cut-off frequency $\omega_c = 2\pi 500$ rad/s was added to complete the LPV model structure (Fig. 5.6).

The resulting LPV model was used to simulate a transition from a low-power ($I_L = 0.5$ mA) to a higher consumption state $I_L = 2$ mA, with a transition time $\Delta t = 6$ ms. A time-varying noise signal with flat power spectrum limited to the band $1-10$ kHz and amplitude 0.2 mA was added to the output current, to represent a small-signal variation around I_L. Similarly, a 20 mV small-signal variation with the same bandwidth was added to the input voltage.

The model was istantiated as an equivalent SPICE netlist in the LTSpice environment. The numerically computed regulated voltage is provided in Fig. 5.15, where the model response against the reference device data are compared. The

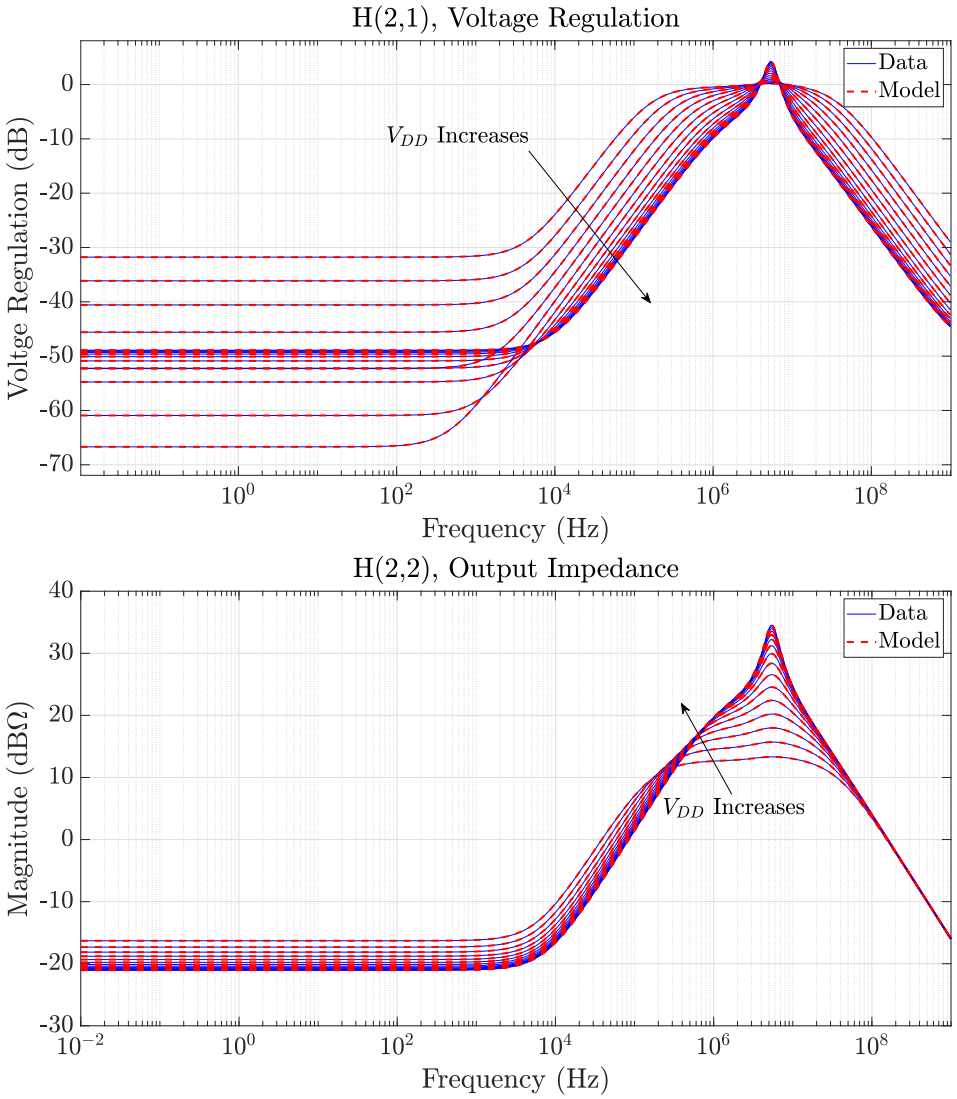

Figure 5.10: Two elements of the transfer function for the LDO-A test case. The parameterization is induced by the DC value of the input voltage. Both training and validation samples are shown. Reproduced from [22] © 2021 IEEE.

results show that the model is accurate for the whole simulation length, and that the accuracy is preserved during the transition. The reference transistor-level simulation was performed using Cadence 6.1.7-64b + Spectre 18.1.0-64b enviroment into a HP Proliant DL580 Server featuring 72-parallel-CPU Intel Xeon Gold 6140M and 128GB RAM. The total run-time was approximately 13 minutes. The same transient analysis using the proposed model was performed in LTSpice on a different machine, equipped with Intel Core i9 7900X CPU and 64 GB of RAM. The resulting runtime was 16 s, corresponding to a 50× speed up.

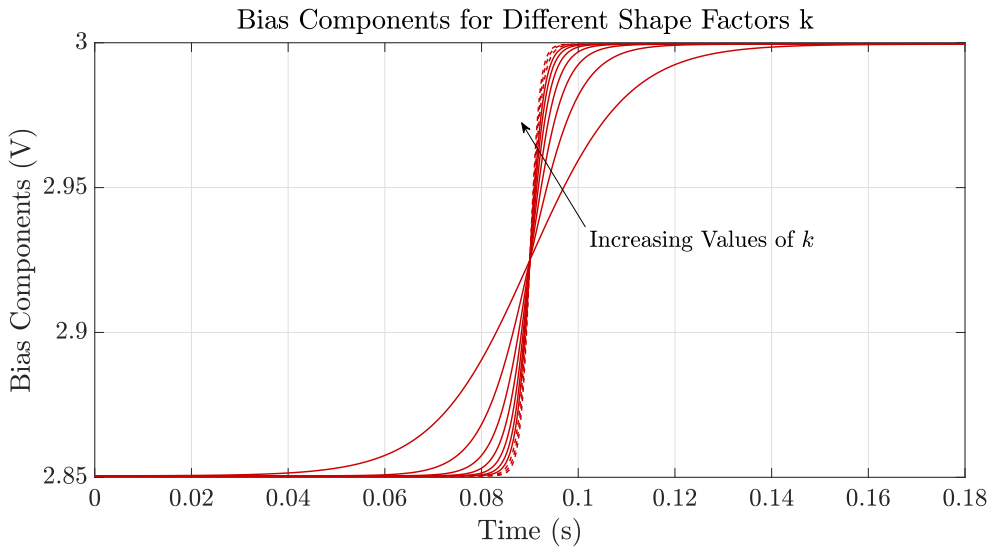

Figure 5.11: Time variation of the the bias component $U_0^1(t)$ for the LDO-A test case, for different values of k = 100,200,...,1000. Reproduced from [22] © 2021 IEEE.

To further validate the model, an additional operating point variation scenario was simulated, by switching the load current from $I_L = 5$ mA to $I_L = 8$ mA in $\Delta t = 6$ ms, and using a small-signal component with amplitude 0.5 mA. The results are reported in Fig. 5.16. Also in this case the LPV model is in full agreement with the reference data, confirming the validity of the proposed approach.

5.3.3 Modeling a temperature-dependent behavior

This last experiment represents a proof of concept of how the proposed LPV model structure can be adapted and exploited to track variations of environmental quantities during a transient analysis. The LDO-B was analyzed by performing a transient analysis including a time variation of the device temperature. The LPV model was constructed by fixing the DC levels of the port variables to $V_{DD} = 1$ V and $I_L = 50$ μA, and by collecting a set of $M = 26$ parameterized small-signal transfer functions for a broad range of operating temperature conditions $T \in [-25,100]$ °C. This data was used to generate a model with dynamic order $n = 8$ and third-order parameterization to capture the temperature dependence in the model. The modeling procedure required 6.8 s. The resulting model accuracy is illustrated in Fig. 5.18. Additionally, a model with the same order was generated by enforcing the uniform stability constraints proposed in [53] for parameterized LTI macromodels, in place of (5.32); in Fig. 5.19 the output impedance of the two models are compared for different temperature values, showing that no visible degradation of the accuracy is induced when the constraints from [53] are replaced

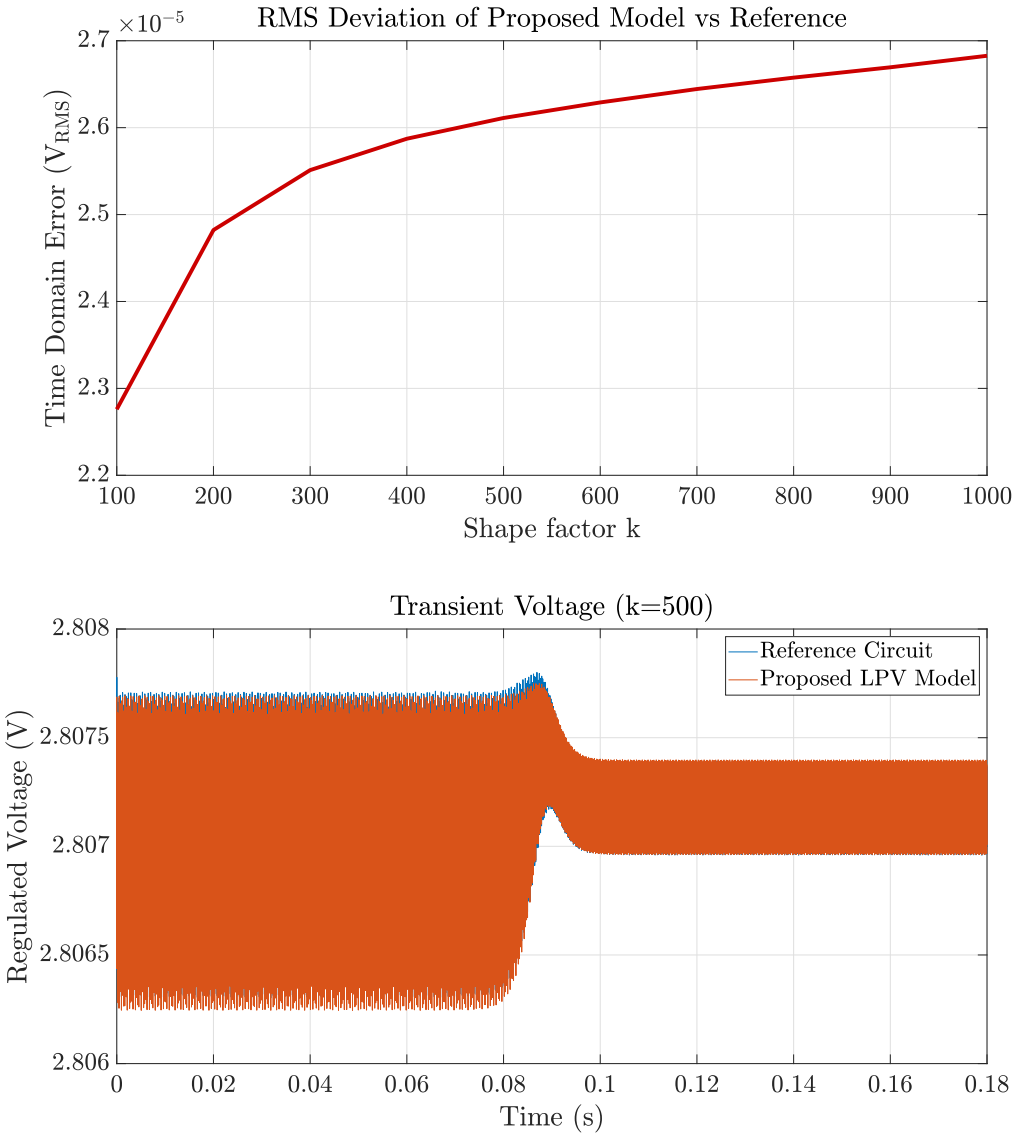

Figure 5.12: LDO-A test case. Top panel: RMS deviation of model wrt transistor-level response, as a function of the slew rate of input bias variation (see Fig. 5.11). Bottom panel: transient regulated voltages of model and transistor-level circuit for the case $k = 500$. Reproduced from [22] © 2021 IEEE.

by the proposed constraints (5.32).

For this illustrative example, the real-time temperature parameterization is injected directly into the model coefficients by making use of the temperature profile shown in Fig. 5.17, which simulates the variation induced by a CPU heating [76]. A

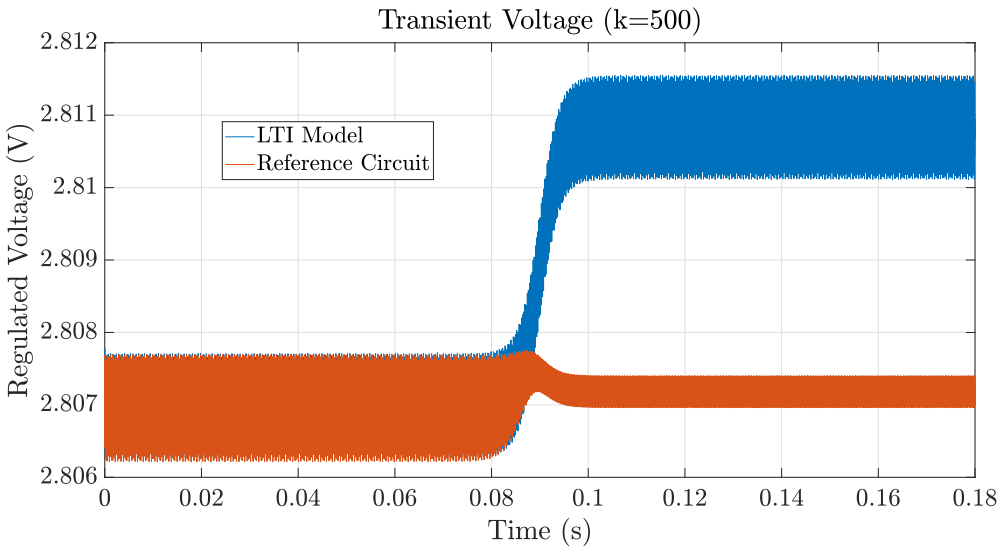

Figure 5.13: LDO-A test case: as in Fig. 5.12 (bottom panel), but using a fixed LTI model, with constant state space matrices. This model cannot track the variation of the operating point as the input bias component switches to another DC level. Reproduced from [22] © 2021 IEEE.

band-limited small-signal component was also added to the input voltage, with amplitude 30 mV and power spectrum limited to 100 Hz, with a peak around the line frequency at 50 Hz. A reference transient response was computed in the Cadence environment. Due to the extremely long duration of the transient, this simulation required approximately 24 hours to be performed.

The proposed model was instantiated and simulated with LTSpice in about 20 minutes, with a speed-up of about 100×. Figure 5.20 compares the transient evolution of the regulated voltage for both proposed model and transistor-level reference over two different time windows associated to different local temperature values. The figure reports also the results of a transient simulation performed with an ad hoc solver written in MATLAB and based on a simple backward Euler integration of the LPV model. Although this code is prototypal and non-optimized, the entire simulation required only 44 s, with further speedup with respect to a conventional SPICE implementation. Both reference and the two LPV model simulations provided compatible results, with no visible loss of accuracy.

5.4 Discussion

This chapter presented a macromodeling framework for mildly nonlinear systems and analog circuit blocks. The approach is aimed at generating macromodels that can replace the reference devices for small-signal operation, both with constant and

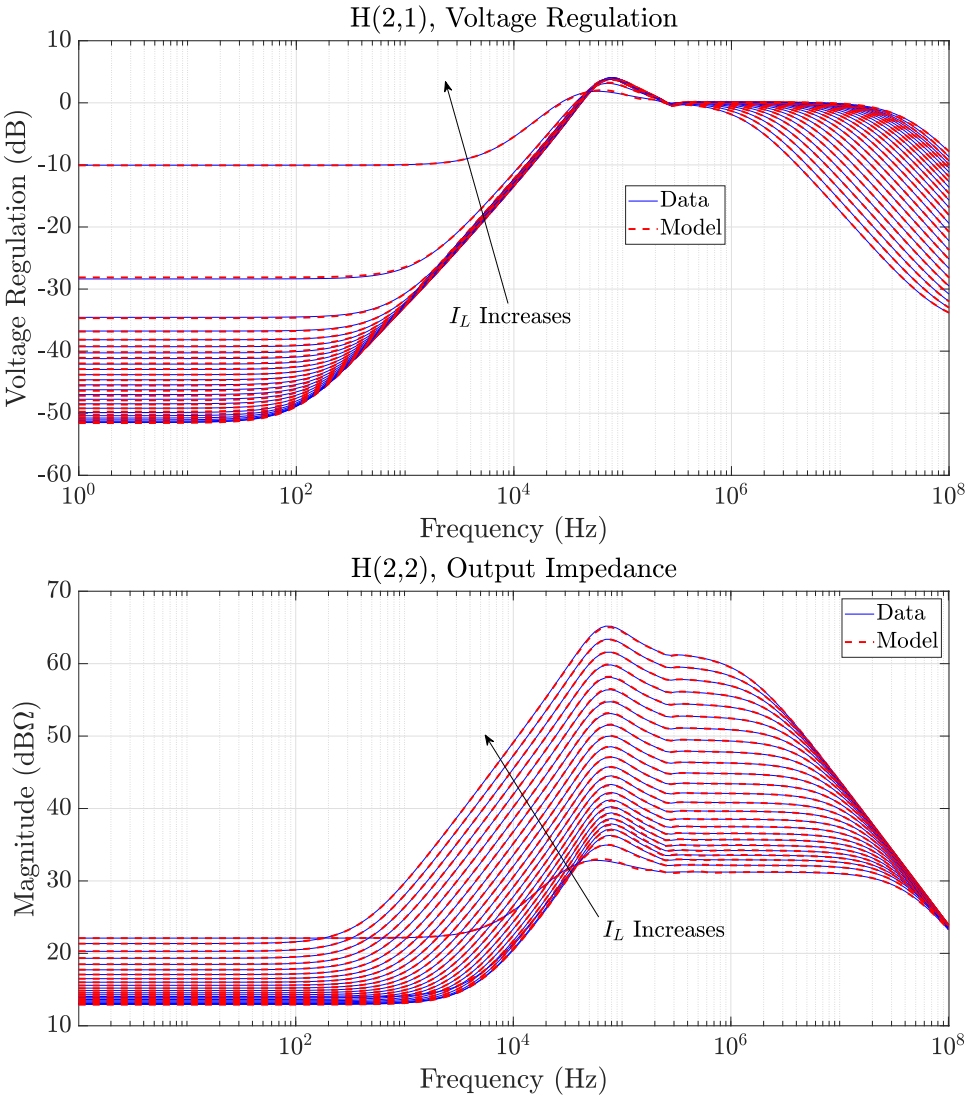

Figure 5.14: Two frequency responses of the LDO-B test case. The parameterization is induced by the DC value of the load current in the range [0,10] mA. Only validation samples are shown. Reproduced from [22] © 2021 IEEE.

nonstationary operating conditions. The modeling procedure is non intrusive and does not require performing expensive time domain simulations of the native circuit descriptions to perform training. The model structure is inherited from the passive parameterized macromodeling setting presented in chapter 4 and augmented with suitable affine output terms. In the proposed approach, the model coefficients are parameterized by the value of the input DC components at the device electrical ports, which determine the operating point.

To reconstruct the reference behavior when the device is subject to time-dependent

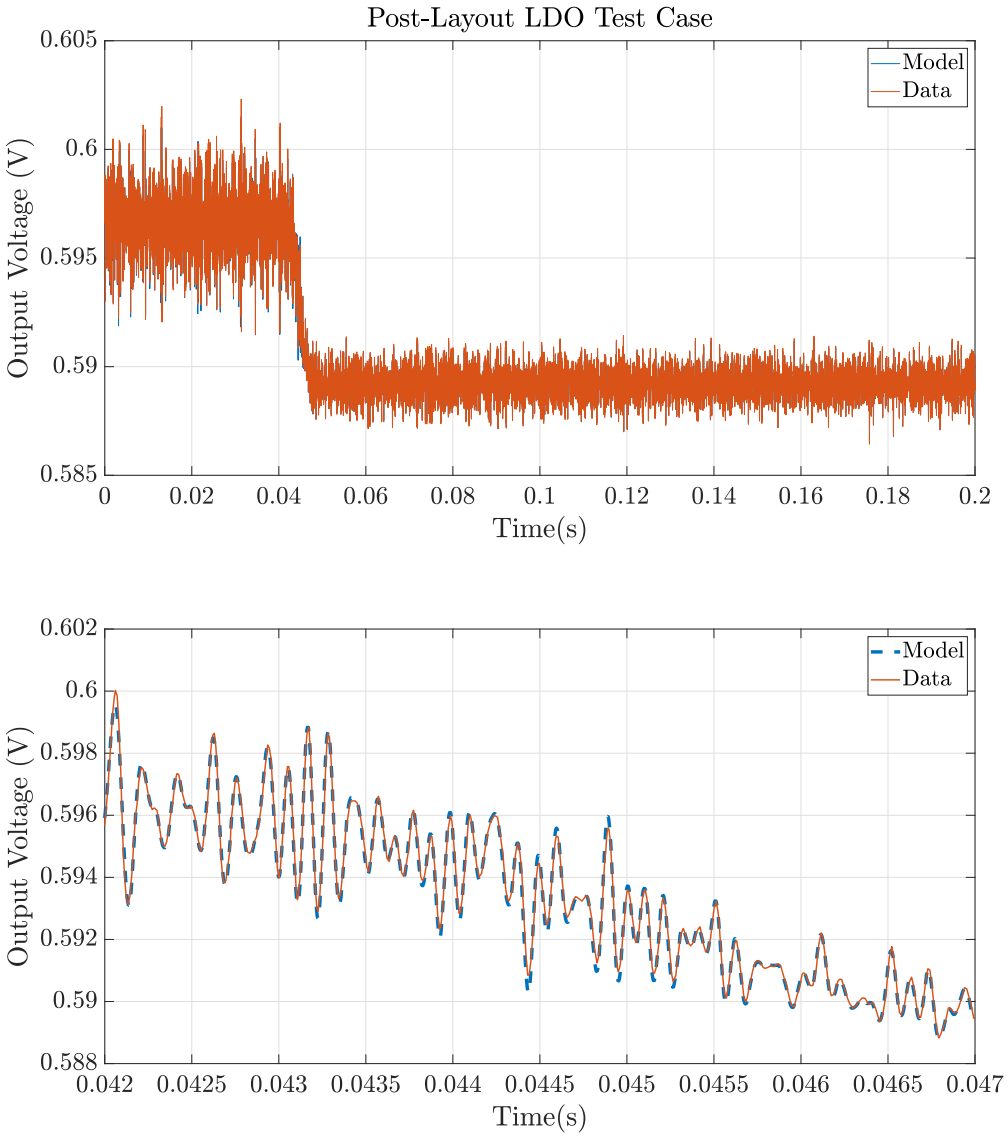

Figure 5.15: LDO-B test case. Top panel: regulated output voltage during an operating point transition from $I_L = 0.5$ mA to $I_L = 2$ mA; bottom panel: zoom on the transition time window. Reproduced from [22] © 2021 IEEE.

bias trajectories, we proposed to update online the value of the model coefficients, based on the instantaneous operating point condition. The resulting model is represented as a LPV system that automatically extracts the input DC components from the port signals in order to perform online self-parameterization. The asymptotic stability of the dynamics is guaranteed by enforcing the existence of a parameter-independent Lyapunov function for the model during its generation. This stability

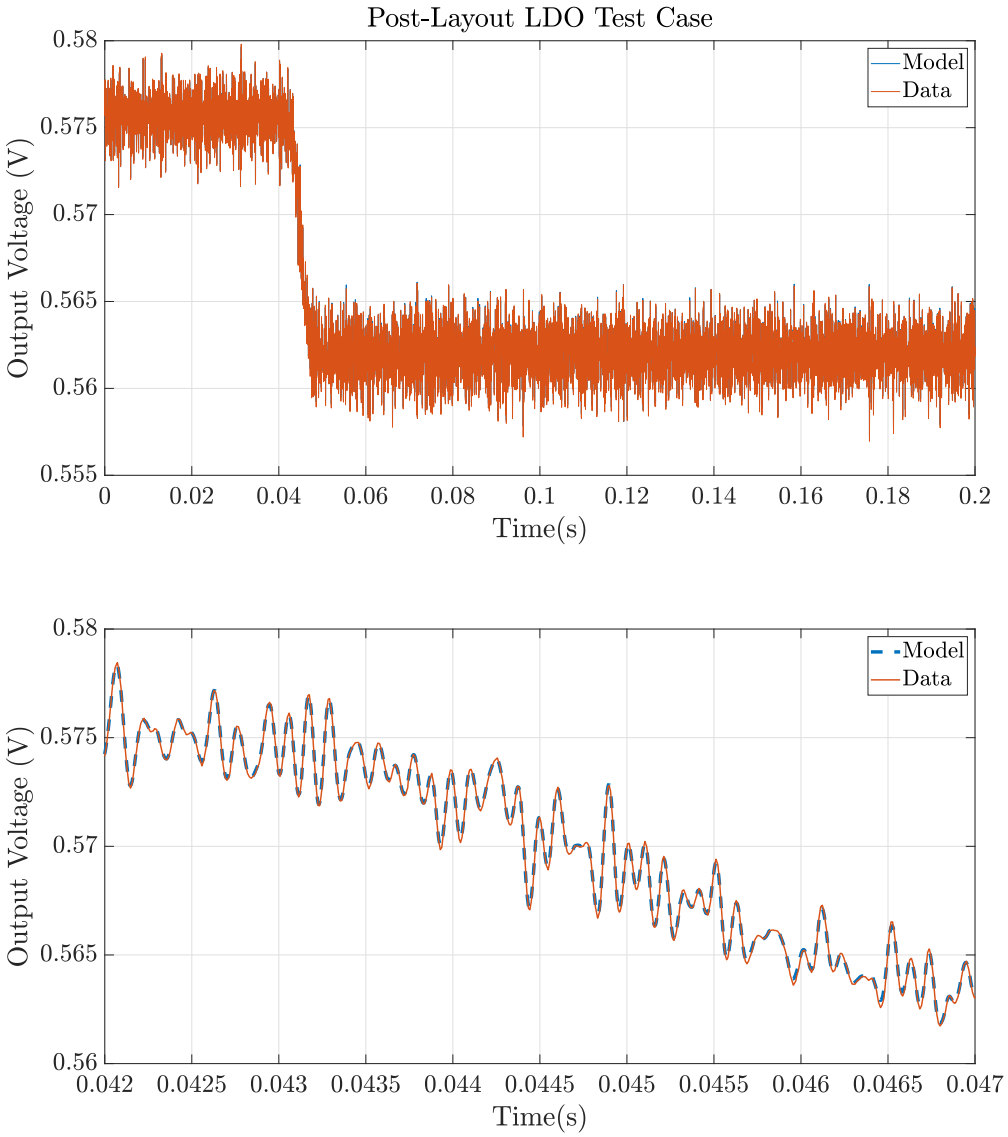

Figure 5.16: LDO-B. As in Fig. 5.15, but for an operating point transition from $I_L = 5$ mA to $I_L = 8$ mA. Reproduced from [22] © 2021 IEEE.

assessment is performed numerically by solving suitable semidefinite programs when estimating the model coefficients, similarly to what is done in Sec 4.3.

The modeling approach proved to be effective in a number of relevant test cases involving LDOs. The resulting surrogates are accurate and guarantee significant gains in terms of transient simulation speedup.

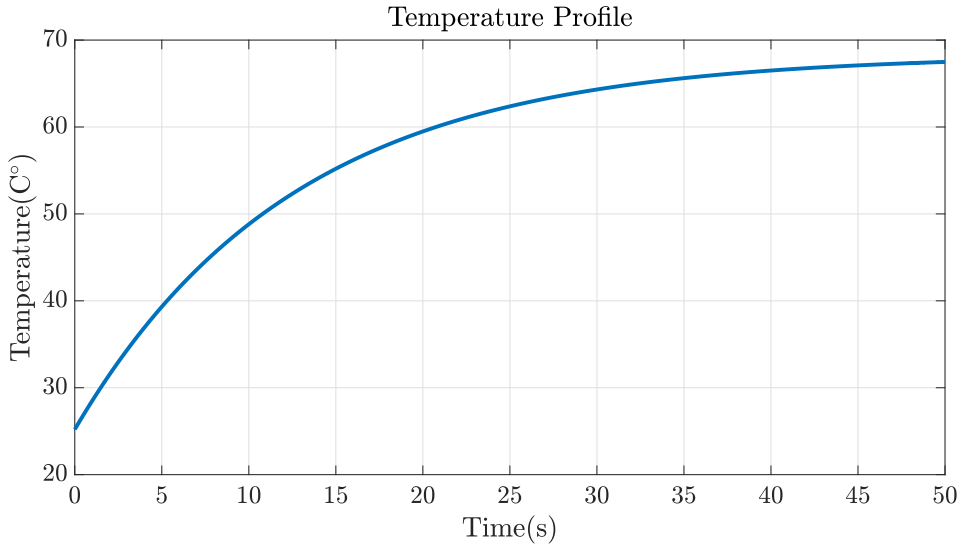

Figure 5.17: The temperature profile used to perform the transient analysis LDO-B under time-varying environmental conditions. Reproduced from [22] © 2021 IEEE.

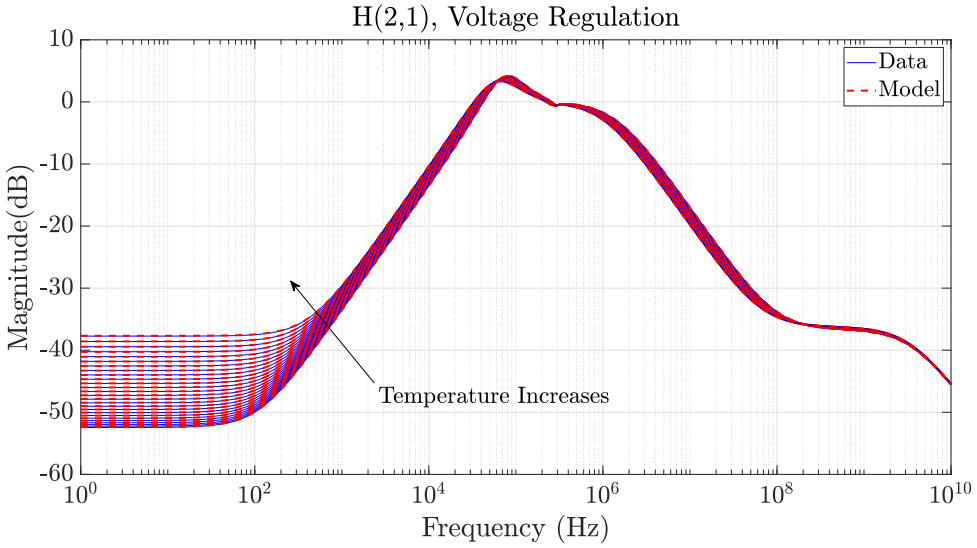

Figure 5.18: Validation of LDO-B model, parameterized by device temperature. The figure compares the model with the reference small-signal voltage regulation transfer function, for the temperature operating range $T \in [-25{,}100]$ °C. Reproduced from [22] © 2021 IEEE.

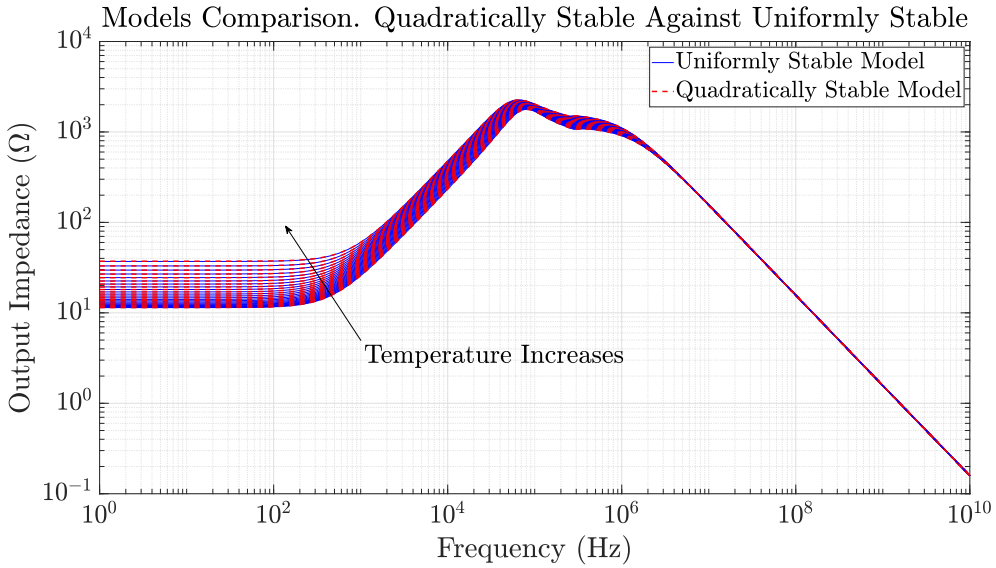

Figure 5.19: Comparison between the output impedance of two models of the LDO-B circuit, obtained by enforcing the uniform stability constraints as in [53] and the proposed quadratic stability constraints (5.32) respectively. Reproduced from [22] © 2021 IEEE.

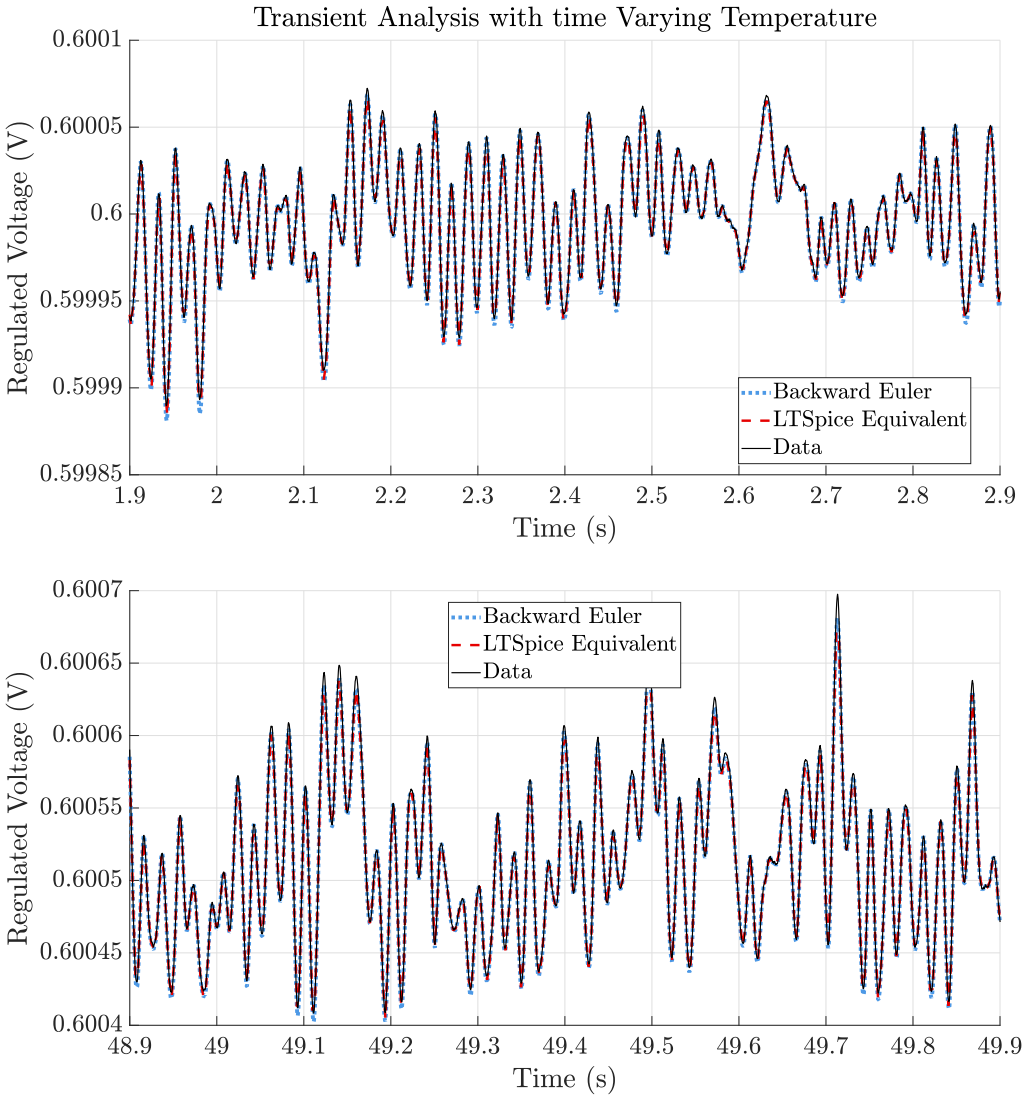

Figure 5.20: Transient analysis of the post-layout LDO with time-varying temperature over three time windows extracted from the whole simulation, representative of different instantaneous temperature values. Top panel: $T \approx 32°C$. Bottom panel: $T \approx 68°C$. Reproduced from [22] © 2021 IEEE.

Chapter 6

System modeling during on-line operation

All the macromodeling approaches discussed up to this point rely on the availability of frequency response samples (possibly swept over a parameter space of interest) of the underlying systems. The parameterized models are obtained via multivariate rational fitting, and in particular, exploiting the PSK iteration.

In certain scenarios however, there can be interest in generating reduced order models of systems for which samples of the frequency response are not available, either because no mathematical descriptions of the reference system are available, or because they can be computed only by performing Fourier analysis of prohibitively long and/or non-stationary time series data. In such situations, it is necessary (or convenient), to perform the model order reduction process in the time domain, by directly exploiting the availability of a set of real or virtual measurements of the system input and output signals.

Black box modeling of dynamical systems starting from input-output time series is a classical topic in the field of system identification, and a number of standard approaches, such as those based on autoregressive models or state space identification, are well established in the literature [72]. Time domain data have also been exploited in the model order reduction framework, e.g. in [36, 29], and [47].

This chapter presents an approach to generate reduced order models of systems starting from time-domain input-output data, sampled while the system is operating in real time (through measurements or highly accurate simulations). The proposed approach is designed to generate models when the available data are retrieved under the following conditions

- During the data acquisition, all the input signals possibly act on the system at the same time. Thus, their individual effect on the output signals is not directly observable from the data.

- The system is not at rest when the data acquisition starts. This implies that

the output signals embed free response components deriving from non-zero initial conditions.

The above conditions exist whenever the system under modeling can be monitored, but the user has no direct control on the input signals; therefore, no systematic experiments can be performed by arbitrarily designing the excitation time series required to build the model.

The described scenario is common in several applications, such as the two following notable examples.

- In the context of power systems, it is desirable to derive models describing the dynamics of complex grids starting from data provided by Phasor Measurement Units (PMU) [104, 37]; performing an online model generation and validation is in this case particularly valuable, since generators and loads acting on the distribution networks cannot be shut down or disconnected at will just for defining a controlled identification environment.

- In the field of computational haemodynamics, the derivation of patient-specific models of the cardiovascular system based on measured or simulated data (transient pressure and blood flow rates) represents an attractive opportunity to perform clinical diagnoses or what-if analyses. As training data are blood pressure and flow within the human cardiovascular system, it is obvious that they can be acquired only during on-line operation (i.e. while the patient is still alive!) and there is no possibility to control the physical signals involved in the modeling procedure.

For both applications, the proposed algorithm discussed in this chapter is suitable for estimating the small-signal reduced-order model (5.6) of the underlying systems during online operation, thus providing an alternative time-domain framework for the generation of local linearized equivalents described in Chapter 5.

The proposed modeling algorithm is based on the Time Domain Vector Fitting scheme (TDVF) first presented in [47] and recalled here in section 6.1.1, suitably reformulated to take into account the online data acquisition requirements. The resulting scheme, called Real Time Vector Fitting (RTVF) [23], is described in Sec 6.1.

6.1 Real-Time Vector Fitting

6.1.1 Background on Time-Domain Vector Fitting

Consider a dynamical system $\mathcal{D}$ operating in real time, with input $u(t) \in \mathbb{R}^{\mathrm{P}}$ and output $y(t) \in \mathbb{R}^{\mathrm{P}}$. The (unknown) system internal state vector is denoted as

$x(t) \in \mathbb{R}^{\mathrm{N}}$. It is assumed that set of samples of the input output vectors

$$u(t_k), y(t_k) \quad k = 1, ..., K \tag{6.1}$$

collected at constant sampling rate F_s, is available as a result of measurements or simulations. Without loss of generality, is is assumed that $t_1 = 0$ in the following. All derivations will hold if $t_1 \neq 0$, provided that the time variable is redefined as $t \leftarrow t - t_1$.

When the underlying system $\mathcal{D}$ is LTI, the relation between the input and output signals is defined by the system transfer function according to

$$Y(s) = \tilde{\mathsf{H}}(s)U(s), \tag{6.2}$$

When $\mathcal{D}$ is mildly nonlinear and operates under small signal regime, then $\tilde{\mathsf{H}}(s)$ may be regarded as a small signal transfer function as in (5.7). A reduced order model $\mathsf{H}(s) \approx \tilde{\mathsf{H}}(s)$ can be determined from the samples (6.1) through one of the several available data-driven model order reduction methods. Specifically, the standard Time Domain Vector Fitting (TDVF) scheme [51, 47, 48], which represents the starting point of the successive derivations, can be applied to generate the desired model $\mathsf{H}(s)$ whenever

- a time series of each output $y_{mj}(t)$ at port m, excited by a single input component $u_j(t)$ placed at port j, is available, under the constraint that this input is acting alone, i.e. $u(t)_{k\neq j} = 0$.
- each of the above time series must be generated with $u_j(0) = 0$, in such a way that the system is at rest when the observation starts, and

$$y_{lj}(0) \equiv 0, \quad x(0) \equiv 0. \tag{6.3}$$

If the data are compliant with the above requirements, then a model for $\tilde{\mathsf{H}}(s)$ can be generated via the standard TDVF algorithm. For convenience, we briefly recall this algorithm and its properties below.

The first step is to choose the order n of the model. Then, as in all vector fitting schemes, some initial estimate of the dominant system poles $\{q_i,\, i = 1, \ldots, n\}$ is performed. Usually, such poles are initialized randomly as real or complex conjugate pairs, provided that $\mathrm{Re}\,\{q_i\} < 0$ and $|q_i| < \Omega$, where Ω is the modeling bandwidth of interest [51, 58]. Based on the training data, TDVF constructs the approximation

$$r_0 \cdot y_{mj}(t) + \sum_{i=1}^{n} r_i \cdot y_{mj}^{(i)}(t) \approx R_{mj}^{(0)} \cdot u_j(t) + \sum_{i=1}^{n} R_{mj}^{(i)} \cdot u_j^{(i)}(t) \tag{6.4}$$

for $t = t_k$ with $k = 1, \ldots, K$, where $R_{mj}^{(i)}$ and r_i are unknown coefficients that can be determined through a linear least squares solution. In (6.4), the superscript $^{(i)}$

indicates the result of the single-pole convolution

$$z^{(i)}(t) = \int_0^t e^{q_i(t-\tau)} z(\tau) d\tau \tag{6.5}$$

where $z(t)$ is a generic signal with $z(0) = 0$. The regression problem (6.4) corresponds to the Laplace-domain relation

$$Y_{mj}(s) \approx \mathsf{H}_{mj}(s)\, U_j(s) = \frac{R_{mj}^{(0)} + \sum_{i=1}^{n} \dfrac{R_{mj}^{(i)}}{s - q_i}}{r_0 + \sum_{i=1}^{n} \dfrac{r_i}{s - q_i}} \cdot U_j(s) \tag{6.6}$$

In the above formula, the elements $\mathsf{H}_{lj}(s)$ are recognized to be structured exactly as in (3.17), for a fixed iteration index ν. After the unknowns of the problem are found, the poles relocation step can be performed exactly as for the VF frequency domain counterpart, until some convergence condition is verified, as reported in section 3.1.3.

6.1.2 Fitting real-time transient signals

Consider now the situation in which the system under modeling operates in real time, with input and output data (6.1) acquired during system operation. As data acquisition may begin at an arbitrary time instant, the assumption (6.3), which requires that the system is at rest when the acquisition starts, is evidently too restrictive; the output samples $y(t)$ may include contributions from both the zero-input and the zero-state response, due to non-vanishing initial conditions. Therefore the relations required by (6.3) are not met and the system description through an input-output transfer function is not sufficient. A suitable parameterization of the zero-state response contribution is required. Moreover, assuming that the system input signal can not be controlled, it is expected that all the input channels act concurrently on the system. Therefore, standard TDVF cannot be applied in such a situation.

Assuming that the system under observation is mildly nonlinear,however, it is always possible to decompose the inputs, outputs and states vectors according to

$$\begin{aligned} u(t) &= u_0 + \tilde{u}(t), \\ y(t) &= y_0 + \tilde{y}(t), \\ x(t) &= x_0 + \tilde{x}(t), \end{aligned} \tag{6.7}$$

where

$$u_0 = u(0), \quad x_0 = x(0), \quad y_0 = y(0) \tag{6.8}$$

are considered as non-necessarily vanishing initial conditions and $\tilde{u}(t)$, $\tilde{y}(t)$, $\tilde{x}(t)$ are small signal components.

Notice that the signal decomposition (6.7) is different from the similar one already defined in (5.2). In the latter, the small signal quantities are defined as deviations from the actual operating point defined by equations (5.3). In (6.7), instead, the small signals represent the deviation of the associated vectors from the values that they assume when the system observation starts. This change of reference point is necessary for the definition of the small signals in the considered scenario, as the constant quantities defining the equilibrium point of the reference system cannot be inferred by the time domain observations.

The derivations of this section show that an approximation for the small signal transfer function $\tilde{\mathsf{H}}(s)$, defined as in (5.7) with respect to the actual operating point of the system, can be obtained starting from the signal decomposition (6.7). The Real Time Vector Fitting scheme, introduced next generalizes the standard TDVF by allowing the presence of non-vanishing initial conditions, as in (6.8), and the presence of inputs acting concurrently, as in common system operation conditions.

6.1.3 Modeling non-vanishing initial conditions

A consistent formulation of the online operation scenario would require to decompose the observations of the output signal $y(t)$ into its zero-state and zero-input contributions. This decomposition is not straightforward, because the system quantities defining the operating point, and, in particular, the equilibrium configuration of the system $\mathcal{D}$, are unknown.

To describe the role of the unknown initial state, we first consider a generic LTI system in state space form:

$$\begin{aligned} \dot{x}(t) &= Ax(t) + Bu(t), \\ y(t) &= Cx(t) + Du(t), \end{aligned} \tag{6.9}$$

by requiring that A is non-singular (the system has no poles at the origin). Plugging the signal definitions (6.7) into (6.9) gives

$$\dot{x}(t) = \dot{\tilde{x}}(t) = A(x_0 + \tilde{x}(t)) + B(u_0 + \tilde{u}(t)) \tag{6.10}$$

$$\tilde{y}(t) + y_0 = C(x_0 + \tilde{x}(t)) + D(u_0 + \tilde{u}(t)). \tag{6.11}$$

The output (6.11) is rewritten as the superposition of the constant and the time-dependent small-signal components as

$$y_0 = Cx_0 + Du_0, \tag{6.12}$$

$$\tilde{y}(t) = C\tilde{x}(t) + D\tilde{u}(t), \quad \forall t \geq 0. \tag{6.13}$$

Two situations may occur:

1. The system is at constant steady-state for $t = 0$ (equivalently, $\forall t \leq 0$). If this is the case, all small-signal components are zero for $t = 0$ and (6.10) reduces to

$$Ax_0 + Bu_0 = 0 \quad \rightarrow \quad x_0 = -A^{-1}Bu_0. \tag{6.14}$$

The above provides the initial state condition x_0, from which one understands that the triplet (x_0, u_0, y_0) corresponds to the actual operating point of system (6.9). Note that a constant steady-state operation is allowed since A is assumed to be nonsingular. Coupling (6.10) with (6.14), for $t > 0$, the small-signal components satisfy the state space equations

$$\dot{\tilde{x}}(t) = A\tilde{x}(t) + B\tilde{u}(t). \tag{6.15}$$

The sets of equations (6.13) and (6.15) provide the small-signal transfer function $\tilde{\mathsf{H}}(s)$ in terms of the state space matrices:

$$\tilde{\mathsf{H}}(s) = C(s\mathbb{I}_\mathrm{P} - A)^{-1}B + D = \frac{\tilde{\mathsf{N}}(s)}{\tilde{\mathsf{D}}(s)} \tag{6.16}$$

with $\tilde{\mathsf{D}}(s) = |s\mathbb{I}_\mathrm{P} - A|$. In order to build a rational approximation for $\tilde{\mathsf{H}}(s)$ the initial conditions u_0, y_0 can be subtracted from the input and output signals, and a zero-state modeling scheme, such as basic TDVF can be applied based only on small-signal components $\tilde{u}(t)$, $\tilde{y}(t)$.

2. A second situation occurs when the system is *not* operating under constant steady-state conditions for $t < 0$. In this case, (6.14) is not verified and

$$x_0 \neq -A^{-1}Bu_0. \tag{6.17}$$

Therefore, even if the initial conditions u_0, y_0 are removed from the input and output signals, the corresponding small-signal output $\tilde{y}(t)$ still includes a contribution from the initial state. This contribution is analyzed next.

The system evolution in terms of small-signal state components can be obtained by integrating equation (6.10) for $t > 0$ as

$$\tilde{x}(t) = \int_0^t e^{A(t-\tau)}(B\tilde{u}(\tau) + Ax_0 + Bu_0)d\tau. \tag{6.18}$$

Equation (6.18) can also be rewritten as

$$\begin{aligned}\tilde{x}(t) = &\int_0^t e^{A(t-\tau)}B\tilde{u}(\tau)d\tau \\ &+ \left[e^{At} - \mathbb{I}_\mathrm{P}\right]\underbrace{(x_0 + A^{-1}Bu_0)}_{T},\end{aligned} \tag{6.19}$$

where the contribution of the state initial condition is highlighted. Notice that if a steady-state condition holds for $t \leq 0$, the second component of (6.19) vanishes, as $T = 0$, and the associated solution coincides with the solution of the small-signal system (6.15). The term T can therefore be interpreted as the deviation of the actual initial state x_0 and the equilibrium state that would stand if the system were operating under steady-state conditions, excited by the constant input u_0.

Computing the Laplace transform of (6.19) gives

$$\tilde{X}(s) = (s\mathbb{I}_{\mathrm{P}} - A)^{-1} B\, \tilde{U}(s) + \left[(s\mathbb{I}_{\mathrm{P}} - A)^{-1} - s^{-1}\mathbb{I}_{\mathrm{P}}\right] T. \tag{6.20}$$

Plugging (6.20) in (6.13) one obtains

$$\tilde{Y}(s) = C\tilde{X}(s) + D\tilde{U}(s) = \tilde{\mathsf{H}}(s)\tilde{U}(s) + \Gamma_0(s), \tag{6.21}$$

where $\tilde{\mathsf{H}}(s)$ is given by (6.16). Additionally,

$$\Gamma_0(s) = (C(s\mathbb{I}_{\mathrm{P}} - A)^{-1} - s^{-1}C)\, T = \frac{\tilde{\mathsf{G}}(s)}{s \cdot \tilde{\mathsf{D}}(s)}, \tag{6.22}$$

where $\tilde{\mathsf{G}}(s)$ is an unknown polynomial vector. Equation (6.21) can be therefore rewritten as

$$\tilde{Y}(s) = \frac{\breve{\mathsf{N}}(s)}{\tilde{\mathsf{D}}(s)}\, \tilde{U}(s) + \frac{\tilde{\mathsf{G}}(s)}{s \cdot \tilde{\mathsf{D}}(s)}\,. \tag{6.23}$$

The terms in (6.23) are characterized by the same denominator $\tilde{\mathsf{D}}(s)$ up to a pole at $s = 0$, representing the non-vanishing initial conditions contribution. A self-consistent vector fitting scheme to estimate model $\mathsf{H}(s) \approx \tilde{\mathsf{H}}(s)$ can now be formulated, by properly taking into account the presence of the additional term $\Gamma_0(s)$ in (6.21).

6.1.4 Model structure and implementation

Starting from the Laplace domain expression of the small signal output (6.23), the RTVF scheme is now introduced based on the following steps.

1. The observations are reconstructed by using a model of the form

$$\tilde{Y}(s) \approx \frac{\mathsf{N}(s)}{\mathsf{D}(s)}\, \tilde{U}(s) + \frac{\mathsf{G}(s)}{s \cdot \mathsf{D}(s)}\,. \tag{6.24}$$

   where N, D and G are approximations computed trough VF iteration.

2. Both $\mathsf{N}(s)$ and $\mathsf{D}(s)$ are expanded in the standard rational barycentric form, as in (6.6), using the initial set of poles q_i; in particular, the components of the unknown vector $G(s)$ are expanded as:

$$G_j(s) = b_i^{(0)} + \sum_{i=1}^{n} \frac{b_i^{(i)}}{s - q_i} \quad \forall j = 1, \ldots, \mathrm{P}\,. \tag{6.25}$$

3. The case of multiple inputs acting concurrently on the system is handled by exploiting the superposition principle to express each output term $\tilde{Y}_m(s)$ in terms of all input components $\tilde{U}_j(s)$.

Applying the above guidelines leads to the formulation of the fitting conditions (6.24) as

$$\tilde{Y}_m(s) \approx \sum_{j=1}^{\mathrm{P}} \frac{R_{lj}^{(0)} + \sum_{i=1}^{n} \dfrac{R_{mj}^{(i)}}{s-q_i}}{r_0 + \sum_{i=1}^{n} \dfrac{r_i}{s-q_i}} \cdot \tilde{U}_j(s) + \\ + \frac{b_m^{(0)} + \sum_{i=1}^{n} \dfrac{b_m^{(i)}}{s-q_i}}{s \cdot \left(r_0 + \sum_{i=1}^{n} \dfrac{r_i}{s-q_i} \right)} \quad \forall m = 1, \ldots, \mathrm{P}. \tag{6.26}$$

In (6.26), the terms $R_{mj}^{(i)}$ are the mj-th entries of the unknown matrix coefficients $R^{(i)}$ defining the numerator transfer function $\mathsf{N}(s)$ of the model $\mathsf{H}(s)$ expressed in barycentric form. The unknowns r_i are common to all transfer matrix entries; therefore, a set of common poles can be enforced for the model. Finally, the unknowns $b_m^{(i)}$ allow for a parameterization of the zero-input response in barycentric form, as written in (6.24).

Linearizing the fitting condition with respect to the denominator $\mathsf{D}(s)$ and performing the inverse Laplace transform returns the following time-domain fitting condition for $t \geq 0$:

$$r_0 \cdot \tilde{y}_m(t) + \sum_{i=1}^{n} r_i \cdot \tilde{y}_m^{(i)}(t) \\ \approx \sum_{j=1}^{\mathrm{P}} \left[R_{mj}^{(0)} \cdot \tilde{u}_j(t) + \sum_{i=1}^{n} R_{mj}^{(i)} \cdot \tilde{u}_j^{(i)}(t) \right] \\ + b_m^{(0)} \cdot \Theta(t) + \sum_{i=1}^{n} b_m^{(i)} \Theta^{(i)}(t), \ \forall m = 1, \ldots, \mathrm{P} \tag{6.27}$$

where, $\Theta(t)$ represents the Heaviside step function.

Writing (6.27) for $t = t_k$, with $k = 1, \ldots, K$, one obtains the RTVF fitting condition in compact matrix form

$$- \phi_m \cdot r + \sum_{j=1}^{\mathrm{P}} \psi_j \cdot r_{mj} + \beta \cdot b_l \approx 0 \quad \forall m = 1,2,...,\mathrm{P}\,, \tag{6.28}$$

where the vectors collecting the unknown coefficients are

$$r = \begin{bmatrix} r_0 \\ \vdots \\ r_n \end{bmatrix}, \; r_{mj} = \begin{bmatrix} R_{mj}^{(0)} \\ \vdots \\ R_{mj}^{(n)} \end{bmatrix}, \; b_m = \begin{bmatrix} b_m^{(0)} \\ \vdots \\ b_m^{(n)} \end{bmatrix}, \tag{6.29}$$

and the matrices that collect the filtered signal samples defined as in (6.5) are

$$\phi_m = \begin{bmatrix} \tilde{y}_m(t_1) & \tilde{y}_m^{(1)}(t_1) & \dots & \tilde{y}_m^{(n)}(t_1) \\ \vdots & \vdots & \ddots & \vdots \\ \tilde{y}_m(t_k) & \tilde{y}_m^{(1)}(t_K) & \dots & \tilde{y}_m^{(n)}(t_K) \end{bmatrix} \tag{6.30}$$

$$\psi_j = \begin{bmatrix} \tilde{u}_j(t_1) & \tilde{u}_j^{(1)}(t_1) & \dots & \tilde{u}_j^{(n)}(t_1) \\ \vdots & \vdots & \ddots & \vdots \\ \tilde{u}_j(t_k) & \tilde{u}_j^{(1)}(t_K) & \dots & \tilde{u}_j^{(n)}(t_K) \end{bmatrix} \tag{6.31}$$

$$\beta = \begin{bmatrix} 1 & \Theta^{(1)}(t_1) & \dots & \Theta^{(n)}(t_1) \\ \vdots & \vdots & \ddots & \vdots \\ 1 & \Theta^{(1)}(t_K) & \dots & \Theta^{(n)}(t_K) \end{bmatrix}, \tag{6.32}$$

where the functions $\Theta^{(i)}(t)$ entering β are the step responses of the partial fractions defining (6.25) computed for unitary residues. By additionally defining

$$\Delta = \begin{bmatrix} \psi_1 & \dots & \psi_{\mathrm{P}} & \beta \end{bmatrix}, \;\; a_m = \begin{bmatrix} r_{m1}^\top & \dots & r_{m\mathrm{P}}^\top & b_m^\top \end{bmatrix}^\top \tag{6.33}$$

and collecting all components, the fitting condition (6.28) is expressed through the compact matrix notation

$$\begin{bmatrix} \Delta & 0 & \dots & 0 & \phi_1 \\ 0 & \Delta & \dots & 0 & \phi_2 \\ \vdots & \vdots & \ddots & \vdots & \vdots \\ 0 & 0 & \dots & \Delta & \phi_{\mathrm{P}} \end{bmatrix} \begin{bmatrix} a_1 \\ a_2 \\ \vdots \\ a_{\mathrm{P}} \\ r \end{bmatrix} \approx 0. \tag{6.34}$$

As common to other vector fitting schemes, standard techniques can be used to avoid the vanishing trivial solution, using e.g. the SVD as outlined in Sec. 2.1.2, or tailored non-triviality constraints, as explained in [57, 51]. Once (6.34) is solved, the zeros z_i of the denominator $\mathsf{D}(s)$ are computed as in (3.19) and used to define the partial fractions basis for the next iteration. The iteration is performed until convergence of the poles estimates. A pseudocode for the proposed scheme is given in Algorithm 1. The final steps (lines 8–10) find the residues of the final rational model based on the fixed poles obtained from the pole relocation process (lines

1–7). In line 10, the vector $\tilde{y}_m$ collects all time samples of the m-th small-signal output component.

Due to the particular structure of the least-squares problem (6.34), in order to improve the algorithm efficiency, the coefficients r can be computed separately from the unknowns a_m, by performing a number P of QR factorizations, as outlined for the PSK algorithm in section 3.2.1; to see this, notice that the structure of (6.34) is the same as that of (3.31). Therefore, the same decoupled estimation procedure can be applied also in this case.

Algorithm 1 The RTVF algorithm

Input: Time samples $u(t_k)$, $y(t_k)$, sampling frequency F_s, starting poles $\{q_1, \ldots, q_n\}$, maximum iteration number $\bar{\nu}$

Output: Estimated transfer function $\mathsf{H}(s)$

1: Compute $\tilde{u}(t_k) \leftarrow u(t_k) - u(t_1)$, $\tilde{y}(t_k) \leftarrow y(t_k) - y(t_1)$
2: **for** $\nu = 1, .., \bar{\nu}$ **do**
3: Compute filtered signals $\tilde{y}_m^{(i)}(t_k)$, $\tilde{u}_m^{(i)}(t_k)$, $\Theta^{(m)}(t_k)$ according to (6.5).
4: Build and solve the least squares problem (6.34)
5: Compute the zeros z_i of denominator $\mathsf{D}(s)$
6: Set $q_i \leftarrow z_i$
7: **end for**
8: Set $\mathsf{D}(s) = 1$
9: Compute filtered signals $\tilde{u}_m^{(i)}(t_k)$, $\Theta^{(i)}(t_k)$
10: Build matrix Δ and solve $\Delta a_m \approx \tilde{y}_m$ for $m = 1, \ldots, \mathrm{P}$
11: **return:** $\mathsf{H}(s) = \mathsf{N}(s)$, where $\mathsf{N}_{mj}(s)$ is numerator of (6.6)

6.2 Assessing the performance of RTVF

This section presents a set of numerical results for validation and performance assessment of the RTVF scheme. First, performance is analyzed on several synthetically-generated high order and large-size LTI test systems. These experiments are aimed at evaluating the consistency of the fitting algorithm when it is used to identify systems with rational transfer function, both in case of noiseless and noisy measurements.

Once the RTVF scheme is validated, two practical application in power systems modeling are discussed: the estimation of the dynamics of an individual generator, and a black-box model of an aggregated power distribution network. Additionally, an application in the field of computational haemodynamics is presented. The power system applications were studied in collaboration with Prof. Luca Daniel and Dr. Samuel Chevalier (MIT), while the cardiovascular application was studied together with Prof. Piero Triverio (University of Toronto) and Elisa Fevola (Politecnico di Torino). These collaborations were intended to extended the field of

applicability of the developed techniques in a multidisciplary setting.

6.2.1 Consistency

The RTVF consistency is tested by running a systematic experimental campaign over a set of synthetic randomly generated LTI reference systems, with the objective of checking whether RTVF provides accurate estimates of all system poles. All modeled systems shared the same dynamic order $n = 10$, with number of ports P ranging from 2 to 30. The set of input-output data are generated as colored noise with flat power spectrum up to angular frequency $\omega_{\max}$, corresponding to the fastest pole of the reference system. The sampling frequency was fixed to $F_s = 10\,\omega_{\max}/2\pi$, and the total number of collected samples was $K = 5000$ in all cases. The modeling window started at sample $k = 250$.

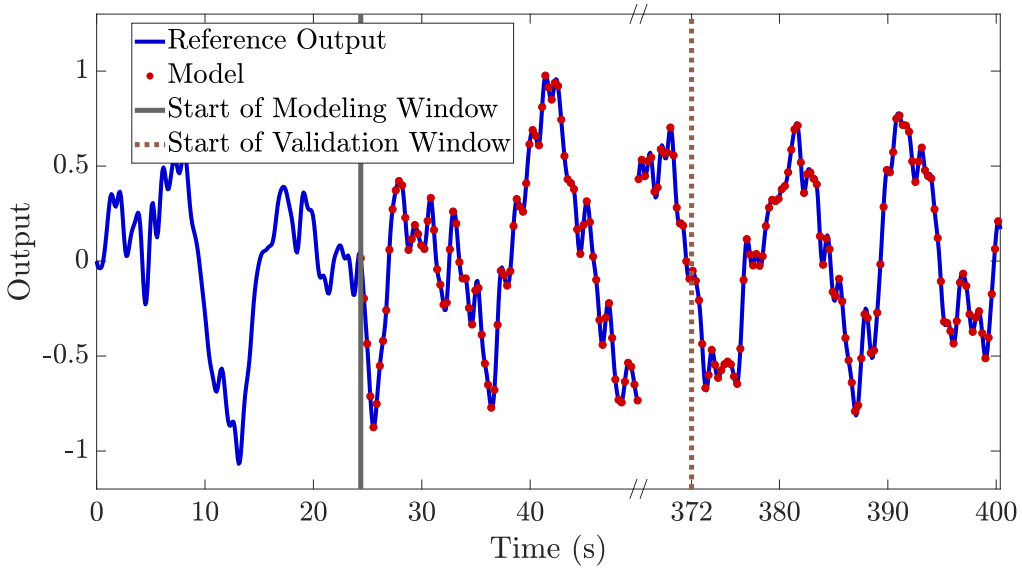

Figure 6.1: Time domain modeling results for a synthetic test case with P = 2. The modeling window starts after 24 s, the validation window starts at 372 s. Reproduced from [23] © 2021 IEEE.

Three metrics were used to assess performance of RTVF:

- the consistency of the pole estimates, as measured by the Hausdorff distance[1] $d_H(\mathcal{P}, \mathcal{Q})$ between the set of exact poles $\mathcal{P} = \{p_1, \ldots, p_n\}$ of the true system

[1]The *Hausdorff distance* between two sets $\mathcal{P}$ and $\mathcal{Q}$ is defined as

$$d_H(\mathcal{P}, \mathcal{Q}) = \max\{\sup_{p\in\mathcal{P}} \inf_{q\in\mathcal{Q}} ||p - q||, \sup_{q\in\mathcal{Q}} \inf_{p\in\mathcal{P}} ||p - q||\}. \tag{6.35}$$

and the set of numerically computed poles $\mathcal{Q} = \{q_1, \ldots, q_n\}$;

- the worst-case time domain output error, computed as

$$E_\infty = \max_{l=1,\ldots,\mathrm{P}} ||y_l - \breve{y}_l||_\infty, \tag{6.36}$$

- and the RMS-normalized maximum error, computed as

$$E_\infty^{\mathrm{RMS}} = \max_{i=1,\ldots,\mathrm{P}} \frac{||y_l - \breve{y}_l||_\infty}{||\breve{y}_l||_2}. \tag{6.37}$$

The experiments show that RTVF recovered the system poles almost exactly, with a set distance $d_H(\mathcal{P}, \mathcal{Q}) \leq 10^{-10}$ for all 29 test cases. Similar results were obtained from the output errors: both E_∞ and E_∞^{RMS} were less than 10^{-11}. As Fig. 6.1 shows, there is no visible difference between the model and the output data samples. In this idealized setting, the RTVF scheme proved to be effective and consistent with the expectations.

To further stress the algorithm, the presence of measurement noise on the input and output signals is considered for the case where $\mathrm{P} = 2$, $n = 10$. Signal corruption is performed by adding a vector of zero-mean Gaussian random variables x_n to any input or output small-signal vector $\tilde{x}$ as

$$\tilde{x}_N = \tilde{x} + x_n, \tag{6.38}$$

with a prescribed signal to noise ratio

$$\alpha = \mathrm{SNR} = 20 \log \frac{\mathrm{RMS}\{\tilde{x}\}}{\mathrm{RMS}\{x_n\}}. \tag{6.39}$$

In the experiments, an increasing levels of SNR, ranging from 10 dB to 100 dB, with resolution steps of 2 dB, is considered. For each level of SNR, $R = 50$ different synthetic systems are modeled, and the average *Signal to Error Ratio* (SER) is computed both in time and frequency domain. This metric is defined as follows. Let z be a vector collecting the samples of either a reference time-domain output signal or a target frequency-domain transfer matrix element, and z_M the corresponding response of one of the R models. Then for this signal the SER is defined as

$$\mathrm{SER} = 20 \log \frac{\mathrm{RMS}\{z\}}{\mathrm{RMS}\{z - z_M\}}. \tag{6.40}$$

For any fixed SNR level, the time-domain TD-SER is computed by averaging the performance induced by (6.40) over the R models and the two output signals. The frequency-domain FD-SER is computed in the same way, by averaging over the transfer matrix elements. These two metrics are shown in Fig. 6.2.

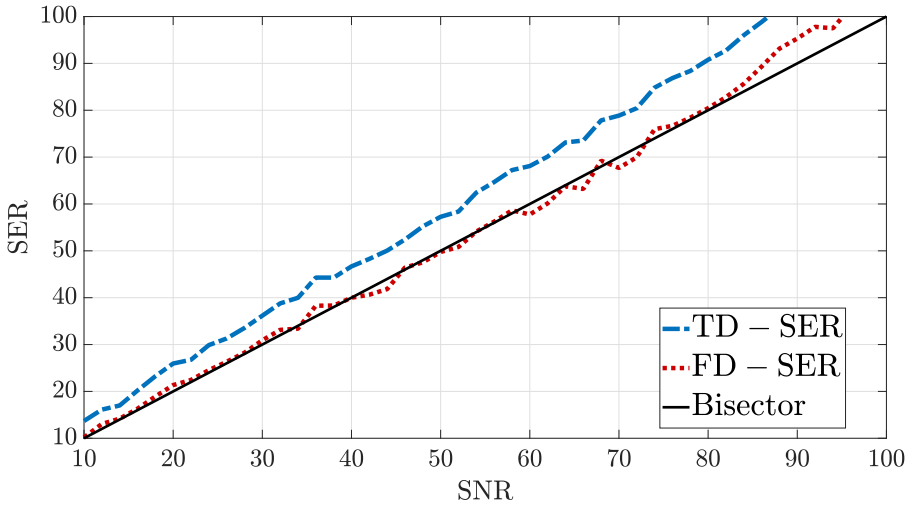

Figure 6.2: The trend of TD − SER and FD − SER against the SNR. Reproduced from [23] © 2021 IEEE.

The meaning of the SER being above or below the black line threshold is that RTVF is either rejecting or amplifying the presence of the noise on the data, respectively. Since the TD-SER is always above the plane bisector (solid black line), RTVF is able to partially reject the presence of measurements noise in the training data. This noise rejection property is expected, since the basis functions involved in the estimation procedure effectively filter the noisy input and output signals via (6.5). On the other hand, FD-SER follows the bisector almost exactly, confirming also a good frequency-domain accuracy.

The noise-corrupted training input signals for a representative test case for SNR = 16 are depicted in the top panel of Fig. 6.3, whereas the corresponding extracted model is validated against the reference time-domain output in the bottom panel. Even with this significant amount of noise, the time-domain prediction capabilities of the model are excellent.

6.2.2 Generator Modeling in the IEEE 39-Bus System

In order to test the performance of RTVF in a simulated power system setting, we apply the algorithm to estimate the local dynamic of a synchronous generator. The generator is considered as a component of the larger IEEE 39-Bus New England system (taken from [8] and depicted in Fig. 6.7) where it operates interacting with other subsystems. A reference physics-based nonlinear model for the generator is used to simulate its online operation under realistic load fluctuations and to collect the training data samples. Fig. 6.4 shows the interconnection of the machine and the related controllers with the outer network. The modeled machine is enclosed

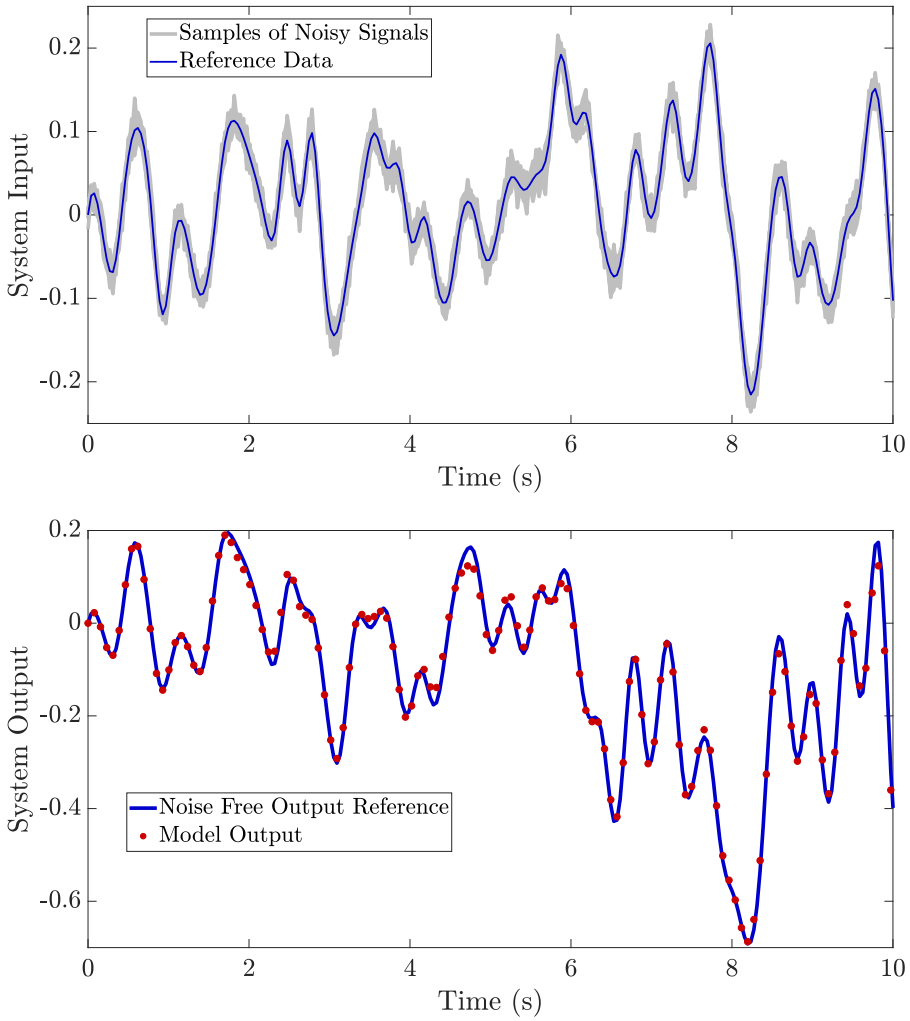

Figure 6.3: Top panel: corrupting one training input signal (solid line) with SNR=16 (a cloud of $R = 50$ different realizations are depicted in a grey shade). Bottom panel: response of a time domain model extracted from one noisy data realization (SNR=16) compared to the reference noise-free signal. Reproduced from [23] © 2021 IEEE.

in the grey box. For a complete characterization of the reference generator model see [23]. For the present discussion, it is sufficient to recall that the model is of dynamic order N = 15.

In order to reproduce a realistic modeling scenario, we sample the instantaneous magnitude and the phase of the voltage and current signals at the generator interface. This is done in order to mimic the data acquisition performed via Phase Measurement Units (PMU) in actual applications. The acquisition returns samples of the time-dependent voltage $\mathrm{V}(t)e^{j\theta(t)}$ and current $\mathrm{I}(t)e^{j\phi(t)}$ phasors. The data

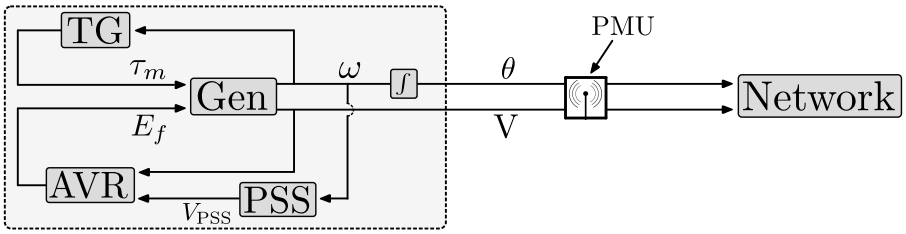

Figure 6.4: Generator modeling example. The figure shows the interaction between the generator, its three controllers, and the network. The PMU collects data at the generator's point of connection. Reproduced from [23] © 2021 IEEE.

are used to model a single generator's closed-loop dynamics, with input and output defined as

$$u(t) = \begin{bmatrix} \mathrm{V}(t) \\ \theta(t) \end{bmatrix} \quad y(t) = \begin{bmatrix} \mathrm{I}(t) \\ \phi(t) \end{bmatrix} \tag{6.41}$$

The RTVF algorithm is run to generate a MIMO model with P = 2 and various reduced orders n. In order to validate the quality of the model generated in the absence of measurement noise, we compare the model responses to the time and frequency domain references provided by the exact machine equations (known analytically in the frequency domain). The results are provided in Fig. 6.5 and show that the model accuracy is excellent in both the time and frequency domains, even though the reduced model order (in this case $n = 9$) is significantly less than the machine's true model order.

Algorithm 2 Measurement Noise Application

Input: Voltage & current signals $\mathrm{V}(t)$, $\mathrm{I}(t)$, $\theta(t)$, $\phi(t)$; desired SNR
Output: Noisy voltage & current signals $\mathrm{V}_n(t)$, $\mathrm{I}_n(t)$, $\theta_n(t)$, $\phi_n(t)$
1: $\sigma_{\mathrm{V}n} \leftarrow \mathrm{RMS}\left\{\mathrm{V}(t) - \mathrm{E}\left\{\mathrm{V}(t)\right\}\right\} \cdot 10^{-\mathrm{SNR}/20}$
2: $\sigma_{\mathrm{I}n} \leftarrow \mathrm{RMS}\left\{\mathrm{I}(t) - \mathrm{E}\left\{\mathrm{I}(t)\right\}\right\} \cdot 10^{-\mathrm{SNR}/20}$
3: $\mathrm{V}_n(t) \leftarrow \mathrm{V}(t) + \sigma_{\mathrm{V}n} \cdot \eta(t)$
4: $\mathrm{I}_n(t) \leftarrow \mathrm{I}(t) + \sigma_{\mathrm{I}n} \cdot \eta(t)$
5: $\theta_n(t) \leftarrow \theta(t) + \sigma_{\mathrm{V}n} \cdot \eta(t) / \mathrm{E}\left\{\mathrm{V}(t)\right\}$
6: $\phi_n(t) \leftarrow \phi(t) + \sigma_{\mathrm{I}n} \cdot \eta(t) / \mathrm{E}\left\{\mathrm{I}(t)\right\}$
Return: $\mathrm{V}_n(t)$, $\mathrm{I}_n(t)$, $\theta_n(t)$, $\phi_n(t)$

Robustness to measurement Noise

In order to further gauge the practical effectiveness of RTVF, artificial measurement noise is applied to the voltage and current signals measured by the PMU. To apply this noise, the procedure outlined in Algorithm 2 is implemented; in the algorithm, $\eta(t)$ represents an AWG noise vector. An SNR level is first specified in

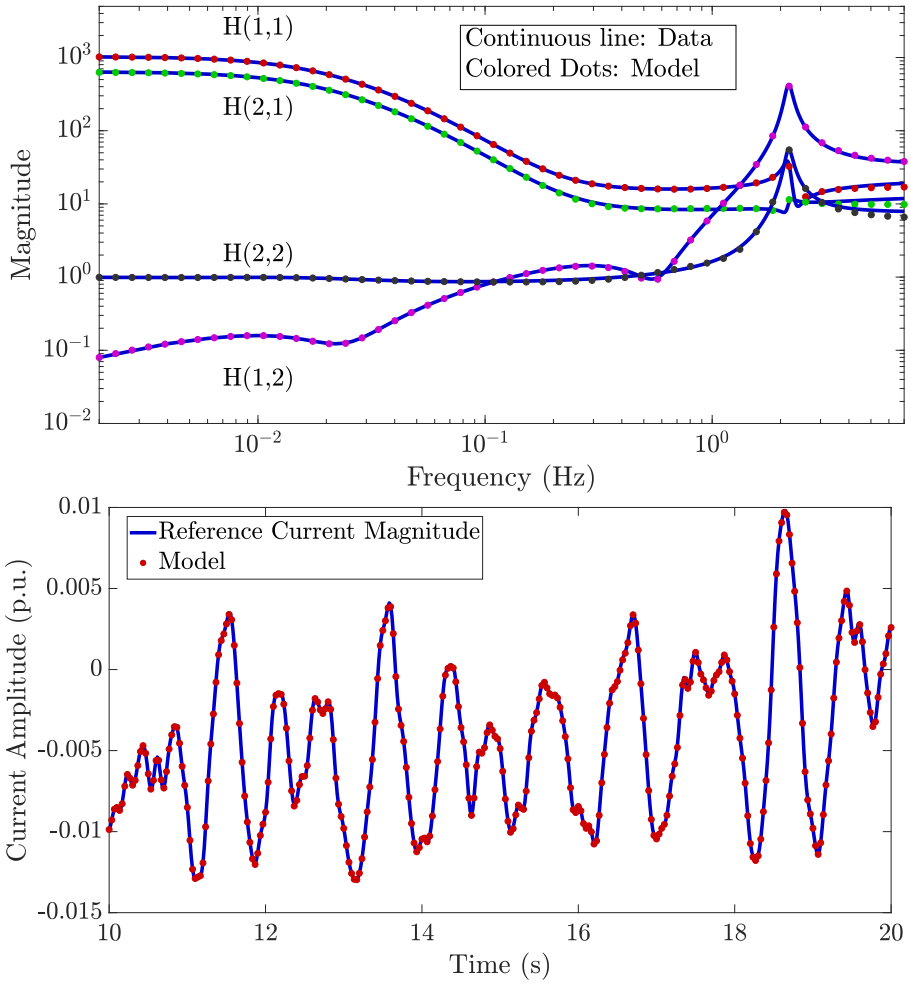

Figure 6.5: Noise-free generator model extraction. Top panel: frequency domain validation of the generator model (order $n = 9$) compared to exact (linearized) frequency response. Bottom panel: the time domain validation of the model against the current magnitude reference output. Reproduced from [23] © 2021 IEEE.

terms of magnitude (V, I) signals, and the proper amount of noise is then added. Next, noise with an appropriate standard deviation is applied to the phase signals (θ, ϕ), such that the total vector error (TVE) in the complex plane would be a circular cloud. In other words, an "equivalent" amount of noise is applied to both the magnitude and phase data, relative to the specified SNR value.

Top and bottom panels of Fig. 6.6 report the frequency- and time-domain fitting performance of a RTVF model of order $N = 7$ obtained for SNR = 32dB. Compared to the performance in the noise-free setting (Fig. 6.5), these results show that the frequency-domain model accuracy is still quite acceptable, and that the accuracy in the time domain seems to be not affected by the presence of noise. The experiments

confirm that the time prediction capabilities of RTVF models extracted from noisy signals are potentially adequate for power system applications.

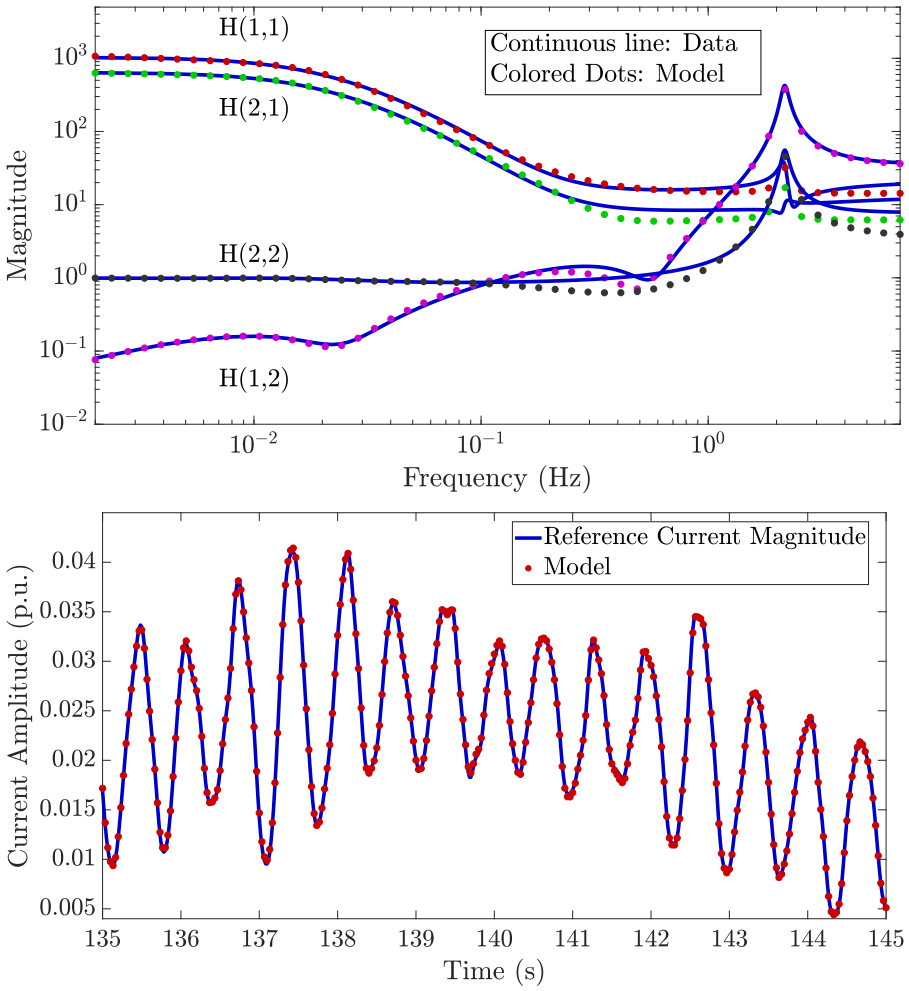

Figure 6.6: Generator model training from noisy data (SNR = 32). Top panel: frequency responses. Bottom panel: small signal current magnitude. Reproduced from [23] © 2021 IEEE.

6.2.3 Wide Area Monitoring in the IEEE 39-Bus System

As a third experiment, the ability of RTVF to perform "wide area" monitoring in the 39-Bus system via predictive modeling. The objective is to derive a black-box of a portion of a large-scale power system, using as identification signals the voltage and current phasors at the interface nodes. To do so, a simulated current flowing across line 16-19 is measured, as shown in Fig. 6.7, along with the voltage perturbations on bus 16. Subsequently, the resulting time domain data (i.e., V(t),

$\theta(t)$, I(t), $\phi(t)$) are used to model the linearized dynamics of the grey box depicted in Fig. 6.7, consisting of two generators, a load, and their interconnecting lines. The proposed approach is here compared with the ARX modeling [28, 99] and the standard Time Domain Vector Fitting scheme applied without the inclusion of initial conditions estimation.

The data are collected at a 60 Hz sampling rate for a total duration of 500 seconds, using the training subset $t \in [100,360]$ s to generate the models using the three considered methods. The dynamics of this wide area had $N = 30$ full order states, but using the ambient PMU data, a reduced order model of dynamic order $n = 13$ is generated.

The results are shown in Fig. 6.8, where the accuracy of the models is evaluated by comparing the output current magnitude and phase against the reference time domain data. The presented results are compared to time domain validation data, that are not used for model generation, and that are therefore meaningful to validate the prediction capabilities of the model.; for the sake of visualization, we used a different y-axis scale for the current magnitude signal returned by the ARX model (right y-axis in the figure top panel). It can be observed that the proposed RTVF method outperforms ARX and TDVF algorithms, providing highly accurate predictions. Notice that, in principle, the application of TDVF in its standard formulation is not even conceivable in the considered scenario due to the presence of concurrent inputs, which are here handled by implementing an extended TDVF algorithm according to the modified scheme of Sec. 6.1.4. Nevertheless, the experiments confirm that including the effect of the initial conditions is crucial to derive a meaningful model. This is even more evident when the frequency responses of the models are compared with those of the reference system, as reported in Fig. 6.9 for the two off-diagonal elements of the transfer matrix. The remarkable accuracy of the RTVF model proves its effectiveness for aggregated power system modeling, even at the wide area level. The same performance are not achieved by the ARX and TDVF algorithms.

6.2.4 Boundary conditions estimation for human arterial systems simulation

This last example provides a proof of concept of how the proposed vector fitting scheme can be applied successfully in the field of computational haemodynamics. This example is quite relevant since computational models of the cardiovascular system have become a valuable tool for the study and investigation of cardiovascular diseases [42] even in a patient-specific context where the geometry of cardiovascular system to be analyzed is reconstructed from 3D radiology images.

Often, cardiovascular computational analyses are required only for localized portions of the human body; therefore, it is a common practice to perform accurate analyses of the arterial regions of interest, neglecting the remaining part of the

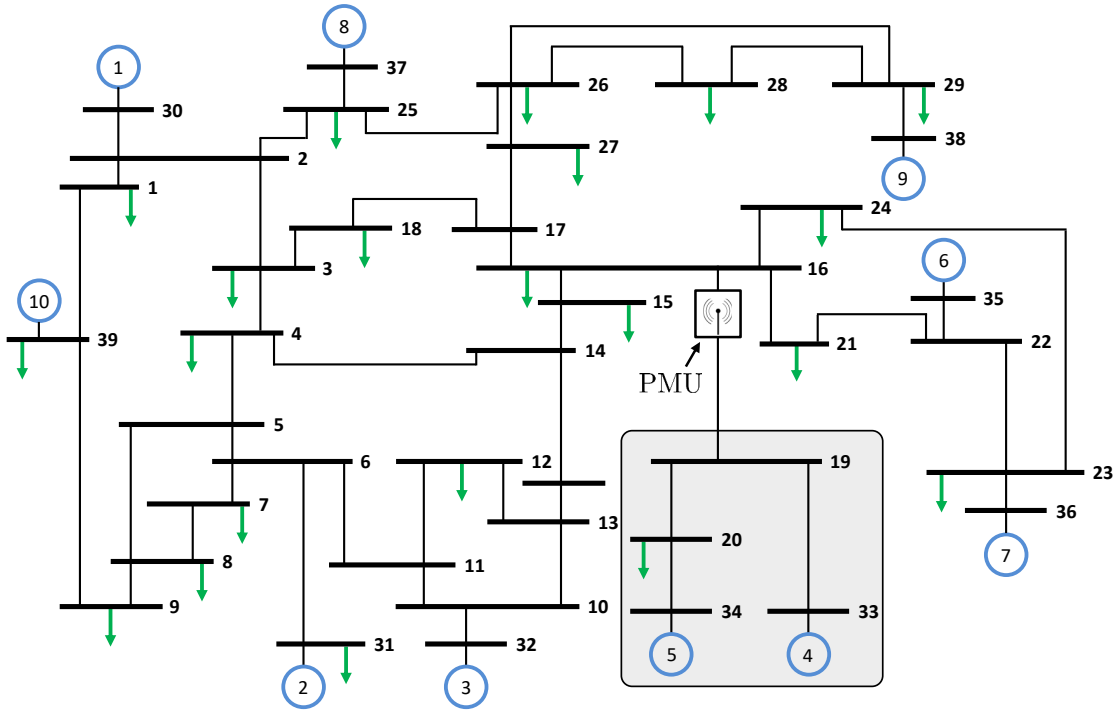

Figure 6.7: IEEE 39-bus New England system. The area depicted by the grey box, which geographically corresponds to a region in southern Massachusetts, US, is used to test RTVF's ability to perform wide area predictive modeling. Reproduced from [23] © 2021 IEEE.

cardiovascular system. This practice becomes necessary when the simulations are performed based on very precise yet complex fluid dynamics models, that require high computational power to be performed. When these conditions are met, the arterial system is truncated at the limits of the regions for which accurate simulations are required; in correspondence of the truncation points, denoted as *outlets*, proper boundary conditions must be enforced to take into account the proper dynamic relationship between blood pressure and flow.

These boundary conditions can be either estimated starting from closed form descriptions of the physics governing the cardiovascular system, or from measured or simulated data. This latter scenario is of particular interest, because building arterial system models starting from patient-specific data represents an interesting approach to perform clinical diagnosis and what-if analyses, e.g., predicting the consequences of surgical actions.

In this example of application of the RTVF algorithm, a set of boundary conditions models are derived from time domain samples of the blood flow and pressure at prescribed outlet points of the arterial system. The data come from the full simulation of a 1D arterial model comprising the largest 55 human arteries, shown

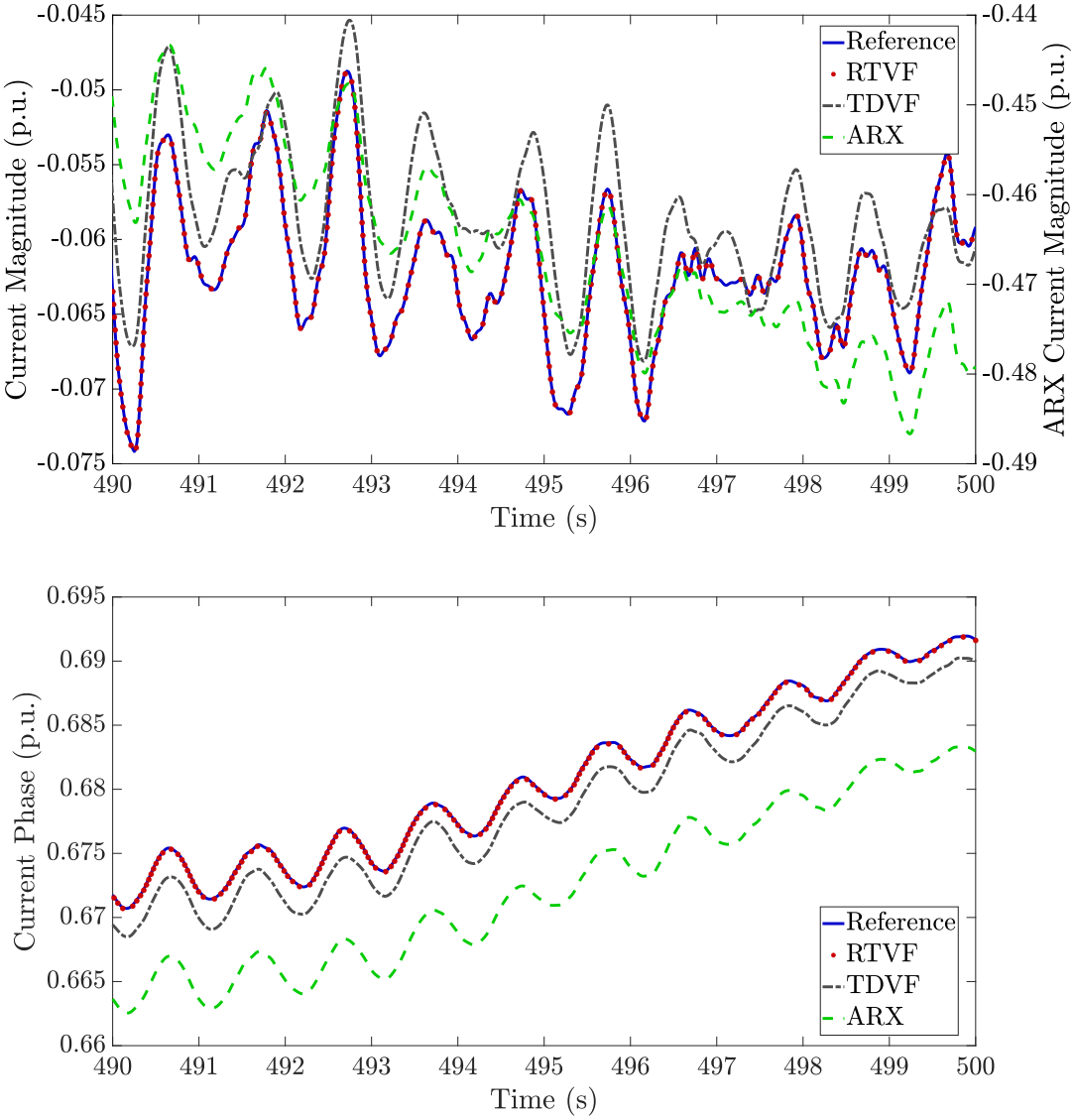

Figure 6.8: Wide area test case. Time domain validation of models derived by means of RTVF, ARX, and TDVF without inclusion of the initial conditions estimate. Top panel: Current magnitude deviation (note that the left y-axis applies to RTVF and TDVF, while right y-axis refers to ARX; the latter has difficulties in producing a sound approximation, especially at low frequencies). Bottom panel: Current phase deviation. Reproduced from [23] © 2021 IEEE.

in Fig. 6.10. The full order model is simulated via the Nektar 1-D solver [2]. The blood flow evolution is described by means of the Navier-Stokes partial differential equations including nonlinear phenomena. Further details about the problem

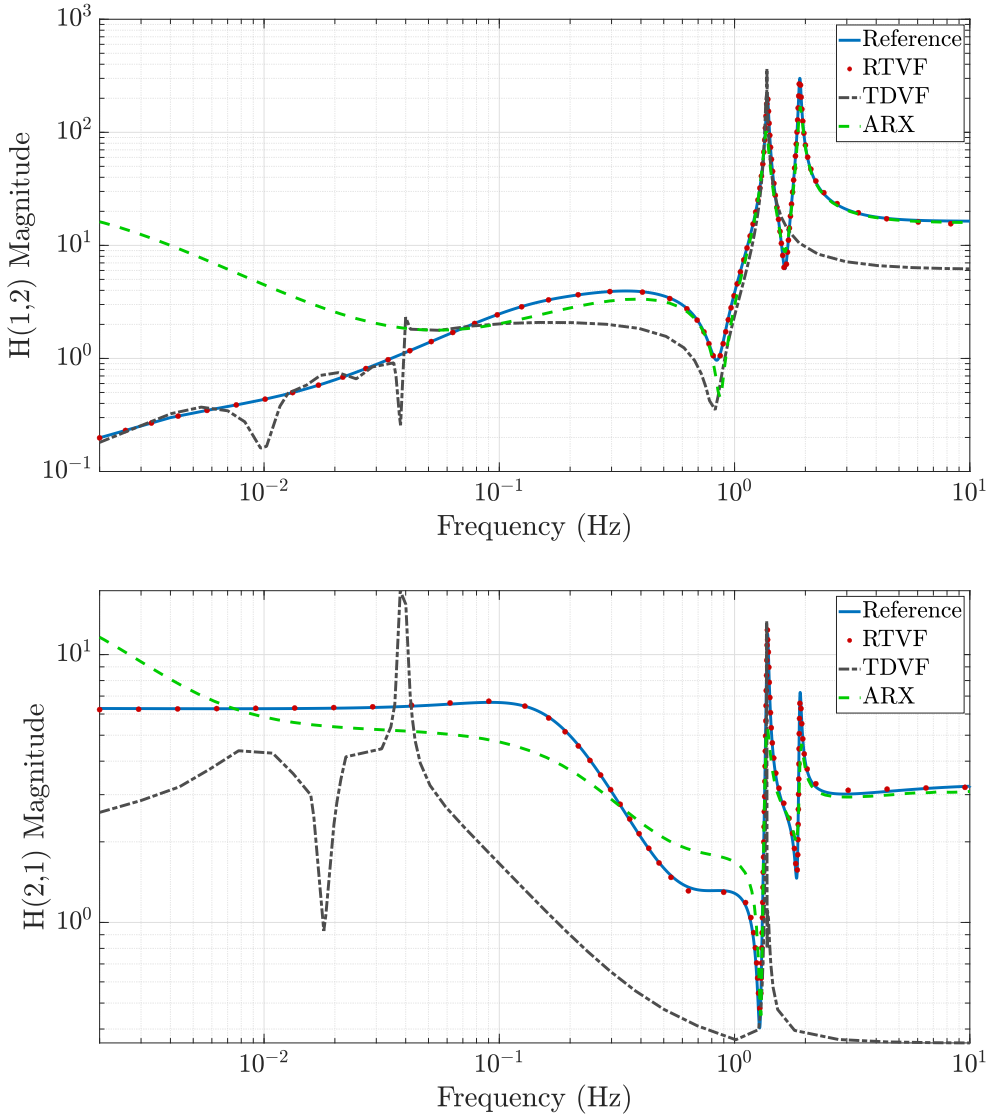

Figure 6.9: Selected transfer functions elements estimated by the RTVF, TDVF and ARX models, compared to the reference (exact) responses. Reproduced from [23] © 2021 IEEE.

physics descriptions can be found in [2].

Although the involved phoenomena are nonlinear, standard approaches for the estimation of suitable boundary conditions are based on the exploitation of LTI model structures. The most common approach is represented by the Windkessel model [85], which admits a representation in terms of first order ordinary differential equations. In particular, the Windkessel model admits a representation in terms of RRC circuit due to the duality that holds between the hydraulic and electrical

domains. This suggests that behavioral models of higher order can be suitable to obtain better estimates for the dynamics imposed by the required boundary conditions at the outlet interfaces.

With reference to Fig. 6.10, the Nektar solver was used to collect samples of the blood pressure and flow in correspondence of segment 19 (Left subclavian artery), and suitable LTI models for the corresponding boundary conditions were built, considering the blood flow as input and the blood pressure as output.

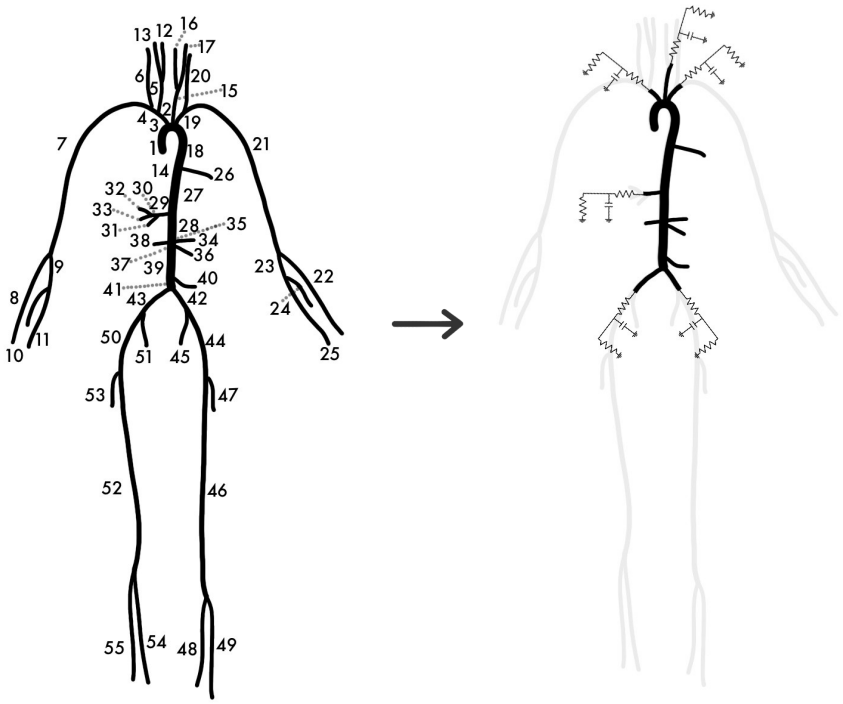

Figure 6.10: The arterial system model simulated in the Nektar 1-D solver. Left: the full arterial system. Right: the truncated arterial system with first order (Windkessel) outlet boundary conditions used in place of the native description. Courtesy of E. Fevola, Politecnico di Torino.

The available time domain data are sampled with $F_s = 1$ kHz and represent realistic signal waveforms that are encountered in healthy humans circulatory systems. The trend of the acquired blood flow signal is shown in Fig. 6.11. In order to simulate a realistic scenario in which boundary conditions are estimated based on *in vivo* patient specific measurements, the model generation is performed by using a subset of the available data, considering non-vanishing initial conditions.

Four different models with increasing dynamic order $n = 1,2,5,8$ were generated using the time window samples $t \in [5,11]$ s, applying the RTVF modeling scheme. The case $n = 1$ corresponds to a first order model structure equivalent to the standard Windkessel model outlet boundary condition. The resulting models

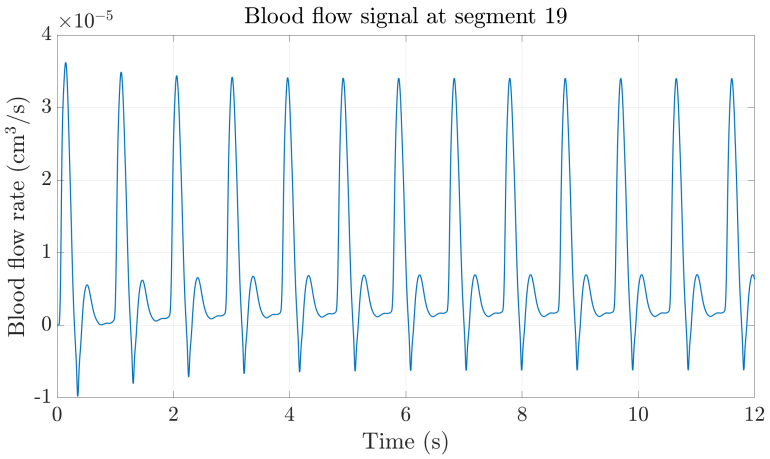

Figure 6.11: The blood flow signal in correspondence of segment 19 of the arterial system. The time window $t \in [5,11]$ is used to extract behavioral models for the outlet boundary conditions.

performance are shown in Fig. 6.12 for the cases $n = 1,2$. The higher order models performance are shown instead in Fig. 6.13.

The presented plots show that the accuracy of the model approximation increases significantly with the model order, reaching remarkable levels of accuracy for the case $n = 8$, both over training data and over time samples that do not belong to the modeling window. This confirms that the proposed approach can be successfully exploited to generate behavioral black box boundary conditions of arbitrary complexity, also taking into account realistic modeling scenarios with non-vanishing initial conditions.

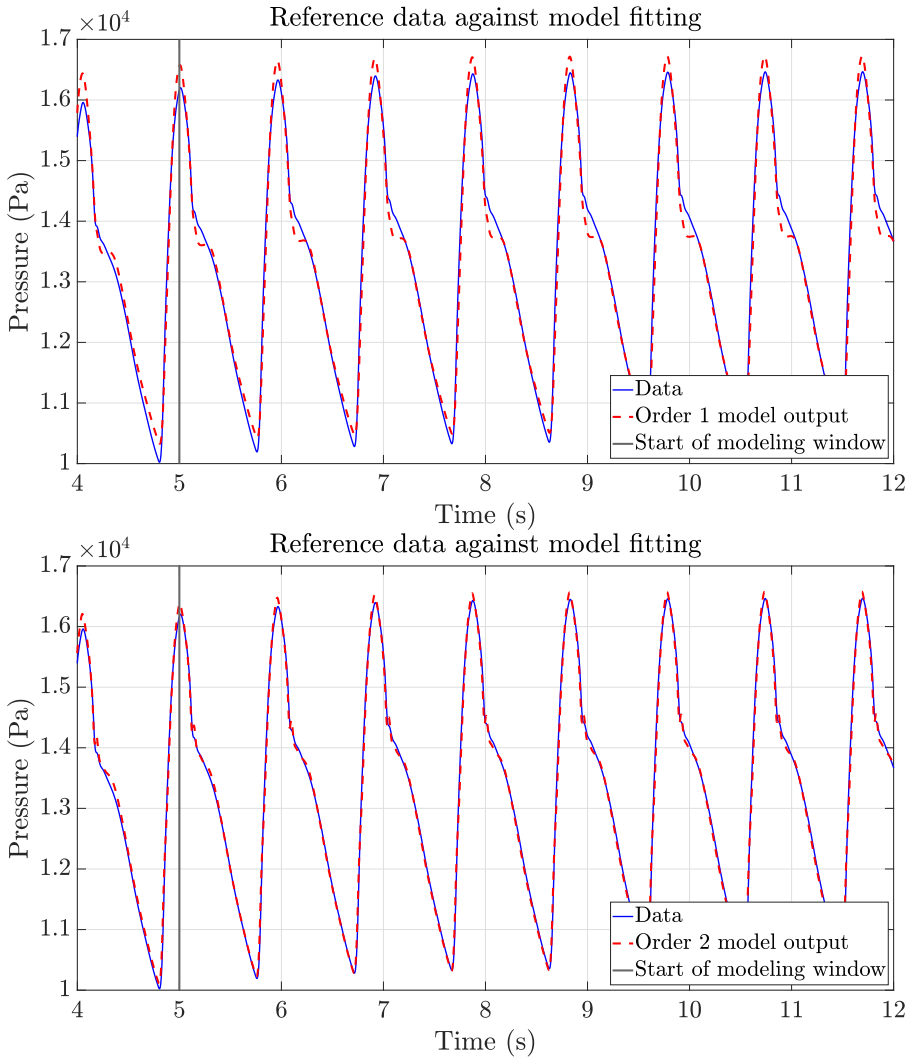

Figure 6.12: RTVF models of the boundary conditions relating pressure and flow at the truncated arterial system outlet. Top panel: $n = 1$. This case is equivalent to the standard RRC windkessel boundary condition. Bottom panel: $n = 2$.

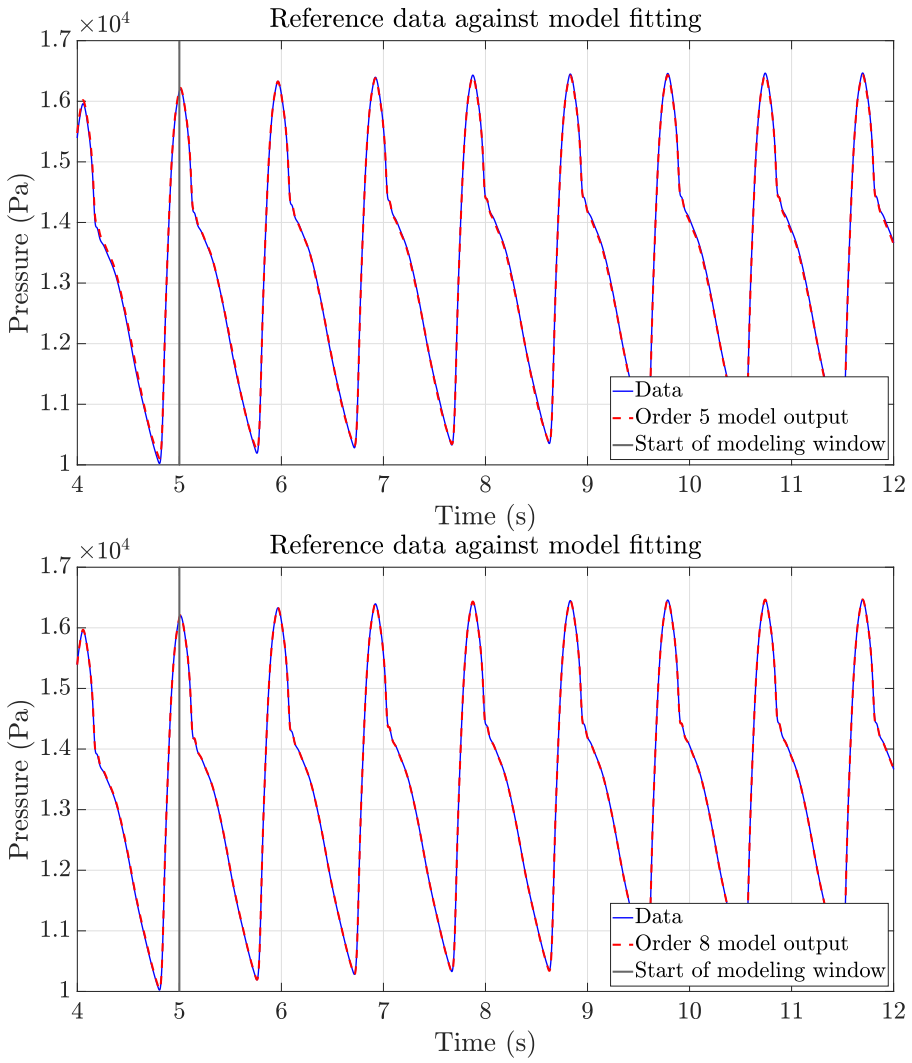

Figure 6.13: RTVF models of the boundary conditions relating pressure and flow at the truncated arterial system outlet. Top panel: $n = 5$. Bottom panel: $n = 8$.

Chapter 7

Discussion

This last chapter discusses the technical contributions proposed in this thesis. The main achievements are summarized and discussed with specific reference to their applicability. A number of relevant open problems are identified, and conclusions are finally drawn.

7.1 Benefits of the proposed approach

This thesis provides novel macromodeling schemes that can be used to generate reduced order surrogates of passive and active components. As experimentally demonstrated, such surrogates enable fast and accurate simulations of the underlying systems, guaranteeing speed-up factors up to two and even three orders of magnitude. The proposed approaches are based on well-established rational fitting schemes that are coupled with numerically manageable constraints, specifically designed to guarantee

- deterministic and robust model generation procedures, depending on a small number of free parameters
- drastic complexity reduction
- provable certificates for important model properties, in particular
    1. uniform passivity for parameterized macromodels of passive components
    2. asymptotic stability for surrogates of nonlinear systems.

The proposed models admit a representation in terms of equivalent netlists that can be integrated in virtually any EDA software, thus enabling significant improvements in terms of design flow efficiency. Additionally, a methodology was proposed to derive reduced order macromodels for system operating in real-time, further extending applicability of the proposed techniques.

7.2 Limitations and open problems

Curse of dimensionality in parameterized macromodeling.

One of the main limiting factors for the practical exploitation of parameterized macromodels is represented by their model complexity in presence of a large number of external parameters. As the dimension of the parameter space increases, the number of basis functions that are involved in the multivariate rational fitting process becomes so high that the model generation procedure becomes inconvenient, both in terms of time and space complexity.

This is particularly true when *structured* parameter-dependent basis functions (such as the multivariate polynomials used in this thesis) are used to define the model parameterization. Some recent research works [116, 113] proposed the usage of radial basis functions in order to overcome the exponential growth of the number of model unknowns in presence of large parameter space dimensions. Although uniform model stability can be enforced easily by exploiting the positivity property of the basis functions proposed in these works, handling the passivity enforcement process in presence of many parameters remains an open problem.

Also, gathering the data describing the structure behavior in large dimensional spaces represents a serious limiting factor for applicability of the available methodologies, due to the non-negligible computational cost required to sample the parameterized frequency response of the reference device on the basis of first-principle descriptions. One possible way to address this problem is to develop suitable adaptive sampling schemes, possibly able to interact with the model generation process, aimed at determining a minimal set of data points able to catch the information required to explain the behavior of interest. The development of such a method is a difficult task, since the lack of apriori information about the frequency response dependence on the parameters makes any adaptive sampling strategy prone to potentially miss certain parameter configurations that could induce large variations in the reference data.

Behavioral models for strongly nonlinear components

Developing reliable behavioral models for strongly nonlinear components starting from data is a challenging task, and represents one of the open macromodeling research fields. As nonlinear dynamics translates into a large variety of admissible qualitatively different behaviors, a general effective and reliable model order reduction scheme is still not available. For an extensive review of the state-of-the-art intrusive MOR techniques for nonlinear systems the reader is referred to [10, 11, 12]. For what concerns more specifically data-driven approaches, classical strategies based e.g. on Volterra series expansions result in highly complex models that quickly become impractical as the degree of nonlinearity of the underlying device increases. In the latest years, methods based on deep learning and recursive neural

networks have been proposed to tackle the problem. Such approaches are numerically accurate and in principle can be applied to a large variety of components, but no formal guarantees about their reliability in scenarios that differs from those described in the training data can be given. Additionally, enforcing the stability of neural networks dynamics (when possible) is a highly complicated process.

An attractive perspective on nonlinear macromodeling is provided by the X parameters, which represent an extension of the standard scattering counterparts to the nonlinear case. X parameters have been successfully exploited to construct behavioral models for RF amplifiers [109], with the inclusion of long-term memory effects [106]. The related research findings suggest that X parameters can be profitably investigated in the future to develop successful nonlinear macromodeling techniques retaining high levels of generality and reliability, at least in the field of RF electronic components.

Handling passivity constraints of large electrical systems.

The passivity enforcement scheme presented in Chapter 4 is suitable only to handle small to medium size modeling problems, and only in case the number of free parameters does not exceed a few units. The reason is that a large number of linear matrix inequalities must be enforced during the model generation in order to reach high levels of accuracy. The size of these constraints and the number of involved variables is determined by the number of ports of the electrical structure under modeling. Therefore, in order to model devices with a large number of electrical ports, some kind of ad-hoc numerical optimization should be employed to reduce the computational burden.

From the theoretical perspective, one viable way to reach the goal could be formulating different strategies to reduce the conservativity of the proposed passivity enforcement scheme. From the numerical standpoint instead, it would be desirable to exploit the structure of the proposed passivity constraints, similarly to what has been proposed in [105], or to rely on optimization solvers aimed at handling extremely large conic problems, as proposed in [81] or in [44]; probably, combining both approaches would lead to appreciable reduction of the computational requirements of the approach.

Extending bias dependent macromodels

The linear parameter varying model structure introduced in Chapter 5 relies on the low-pass filtering operation that provides at each time instant the parameter value that defines the model equations. Performing the parameterization in this way is effective whenever the bias component is slow enough. However, the low-pass filter design is based, at the moment, on heuristic considerations about the bandwidth of the time-varying bias component.

Also, the presented modeling scheme is based on frozen parameter descriptions of the reference device local behaviors. In the LPV identification framework, it is known that models derived from frozen parameter configurations are valid only for slow parameter variations. Alternative schemes, that identify models through time series data in which the parameter changes dynamically have also been proposed [101]. In order to pursue this strategy from the model order reduction point of view, however, expensive time domain transient simulations would be required. Thus, a systematic procedure aimed at minimizing the amount of collected data should be integrated with any model training algorithm.

7.3 Conclusions

Passive macromodeling methods have represented the starting point for the research progress documented in this thesis. As opposed to the univariate macromodeling case, the parameterized setting introduces significant difficulties when the robust enforcement of stability and passivity is required. Before performing the research herein documented, either heuristic procedures or oversimplified strategies were available to generate parameterized macromodels. The former are not able to provide certified passive models, while the latter do so by generating unnecessarily complex models. The strategy proposed in chapter 4 fills this technical gap, by providing a way to generate compact and passive parameterized macromodels following a robust and automated procedure. The practical effectiveness of the workflow has been demonstrated over a number of test cases.

The availability of the solid algorithmic framework provided by combining rational fitting schemes with system theory and convex optimization raised then questions about possible extensions; the main results led to the algorithms discussed in Chapter 5, which concern the local approximation of nonlinear systems. Based on results regarding the small-signal approximation of mildly nonlinear systems with uncertain operating point, the canonical LTI model structure of parameterized models was exploited to generate time varying approximations for non-stationary local behaviors. The mathematical tools used to guarantee the stability in the time invariant setting were inherited by this novel framework, with proper modifications, with the objective of formulating a modeling scheme that preserves the structural stability property of the underlying mildly nonlinear device, while at the same time guaranteeing the accuracy of the model.

Lastly, the classical vector fitting algorithm was modified to handle modeling scenarios in which the standard assumptions on data acquisition characterizing classical macromodeling schemes do not hold. The problem of generating accurate surrogates of actual or simulated complex systems starting from real-time measurements was addressed, thus broadening the number of applications in which this effective algorithm can be successfully employed. The validity of the considered

local approach for solving relevant modeling problems has been confirmed by a large number of practical examples belonging to the domain of electronics, power systems, and even cardiovascular modeling.

Bibliography

[1] Syed M Alam, Donald E Troxel, and Carl V Thompson. "A comprehensive layout methodology and layout-specific circuit analyses for three-dimensional integrated circuits". In: *Proceedings International Symposium on Quality Electronic Design*. IEEE. 2002, pp. 246–251.

[2] Jordi Alastruey, Kim H. Parker, and Spencer J. Sherwin. "Arterial pulse wave haemodynamics". English. In: *11th International Conference on Pressure Surges*. Ed. by S Anderson. Virtual PiE Led t/a BHR Group, Oct. 2012, pp. 401–443. ISBN: 9781855981331.

[3] Farid Alizadeh. "Interior point methods in semidefinite programming with applications to combinatorial optimization". In: *SIAM journal on Optimization* 5.1 (1995), pp. 13–51.

[4] Ziad Alkhoury, Mihály Petreczky, and Guillaume Mercère. "Comparing global input-output behavior of frozen-equivalent LPV state-space models". In: *IFAC-PapersOnLine* 50.1 (2017), pp. 9766–9771.

[5] Brian DO Anderson and Sumeth Vongpanitlerd. *Network analysis and synthesis: a modern systems theory approach*. Dover Publications, 2013.

[6] MOSEK ApS. *MOSEK Optimizer API for C*. 2021. URL: `https://docs.mosek.com/9.3/capi.pdf`.

[7] Narain D Arora et al. "Modeling and extraction of interconnect capacitances for multilayer VLSI circuits". In: *IEEE Transactions on Computer-Aided Design of Integrated Circuits and Systems* 15.1 (1996), pp. 58–67.

[8] T Athay, Robin Podmore, and Sudhir Virmani. "A practical method for the direct analysis of transient stability". In: *IEEE Transactions on Power Apparatus and Systems* 2 (1979), pp. 573–584.

[9] J.S. Bay. *Fundamentals of Linear State Space Systems*. Electrical Engineering Series. WCB/McGraw-Hill, 1999. ISBN: 9780256246391. URL: `https://books.google.it/books?id=vjoZAQAAIAAJ`.

[10] Peter Benner et al. *Model Order Reduction: Volume 1. System-and Data-Driven Methods and Algorithms*. De Gruyter, 2021.

[11] Peter Benner et al. *Model Order Reduction: Volume 2. Snapshot-Based Methods and Algorithms*. 2021.

[12] Peter Benner et al. *Model Order Reduction: Volume 3. Applications*. De Gruyter, 2021.

[13] Jakob Berchtold and Adrian Bowyer. "Robust arithmetic for multivariate Bernstein-form polynomials". In: *Computer-Aided Design* 32.11 (2000), pp. 681–689.

[14] Mario Berljafa and Stefan Guttel. "Generalized rational Krylov decompositions with an application to rational approximation". In: *SIAM Journal on Matrix Analysis and Applications* 36.2 (2015), pp. 894–916.

[15] Franco Blanchini et al. "Stable LPV realization of parametric transfer functions and its application to gain-scheduling control design". In: *IEEE Transactions on Automatic Control* 55.10 (2010), pp. 2271–2281.

[16] Stephen Boyd and Lieven Vandenberghe. *Convex optimization*. Cambridge university press, 2004.

[17] T Bradde et al. "A scalable reduced-order modeling algorithm for the construction of parameterized interconnect macromodels from scattering responses". In: *2018 IEEE Symposium on Electromagnetic Compatibility, Signal Integrity and Power Integrity (EMC, SI & PI)*. IEEE. 2018, pp. 650–655.

[18] T Bradde et al. "Enabling fast power integrity transient analysis through parameterized small-signal macromodels". In: *2019 International Symposium on Electromagnetic Compatibility-EMC EUROPE*. IEEE. 2019, pp. 759–764.

[19] T Bradde et al. "On Dissipativity Conditions for Linearized Models of Locally Active Circuit Blocks". In: *IEEE 29th Conf. on Electrical Performance of Electronic Packaging and Systems*. 2020, pp. 1–3.

[20] Tommaso Bradde, Alessandro Zanco, and Stefano Grivet-Talocia. "Bivariate Macromodeling with Passivity Constraints". In: *2021 IEEE 30th Conference on Electrical Performance of Electronic Packaging and Systems (EPEPS)*. 2021, pp. 1–3. DOI: 10.1109/EPEPS51341.2021.9609137.

[21] Tommaso Bradde et al. "Data-Driven Extraction of Uniformly Stable and Passive Parameterized Macromodels". In: *IEEE Access* 10 (2022), pp. 15786–15804. DOI: 10.1109/ACCESS.2022.3147034.

[22] Tommaso Bradde et al. "Fast Simulation of Analog Circuit Blocks Under Nonstationary Operating Conditions". In: *IEEE Transactions on Components, Packaging and Manufacturing Technology* 11.9 (2021), pp. 1355–1368. DOI: 10.1109/TCPMT.2021.3099215.

[23] Tommaso Bradde et al. "Handling Initial Conditions in Vector Fitting for Real Time Modeling of Power System Dynamics". In: *Energies* 14.9 (2021), p. 2471.

[24] Corentin Briat. *Linear parameter-varying and time-delay systems*. Springer, 2014.

[25] T Buss. *2GHz low noise amplifier with the BFG425W*. Tech. rep. Philips Semiconductors, B.V., Nijmegen, The Netherlands, 1996. URL: http://application-notes.digchip.com/004/4-7999.pdf.

[26] Giuseppe C Calafiore and Laurent El Ghaoui. *Optimization models*. Cambridge university press, 2014.

[27] G. Casinovi and A. Sangiovanni-Vincentelli. "A macromodeling algorithm for analog circuits". In: *IEEE Transactions on Computer-Aided Design of Integrated Circuits and Systems* 10.2 (1991), pp. 150–160. DOI: 10.1109/43.68402.

[28] J. Chai et al. "Measurement-based system reduction using autoregressive model". In: *2016 IEEE/PES Transmission and Distribution Conference and Exposition (T D)*. 2016, pp. 1–5.

[29] Yiran Chen et al. "Model reduction in the time-domain using Laguerre polynomials and Krylov methods". In: *Proceedings 2002 Design, Automation and Test in Europe Conference and Exhibition*. IEEE. 2002, pp. 931–935.

[30] Jan De Caigny et al. "Interpolated modeling of LPV systems". In: *IEEE Transactions on Control Systems Technology* 22.6 (2014), pp. 2232–2246.

[31] D. Deschrijver, L. Knockaert, and T. Dhaene. "A Barycentric Vector Fitting Algorithm for Efficient Macromodeling of Linear Multiport Systems". In: *IEEE Microwave and Wireless Components Letters* 23.2 (Feb. 2013), pp. 60–62. ISSN: 1558-1764. DOI: 10.1109/LMWC.2013.2239282.

[32] Dirk Deschrijver and Tom Dhaene. "Fast passivity enforcement of S-parameter macromodels by pole perturbation". In: *IEEE Transactions on Microwave Theory and Techniques* 57.3 (2009), pp. 620–626.

[33] Dirk Deschrijver, Tom Dhaene, and Daniël De Zutter. "Robust Parametric Macromodeling Using Multivariate Orthonormal Vector Fitting". In: *IEEE Transactions on Microwave Theory and Techniques* 56.7 (2008), pp. 1661–1667. DOI: 10.1109/TMTT.2008.924346.

[34] Dirk Deschrijver, Bart Haegeman, and Tom Dhaene. "Orthonormal vector fitting: A robust macromodeling tool for rational approximation of frequency domain responses". In: *IEEE Transactions on advanced packaging* 30.2 (2007), pp. 216–225.

[35] Dirk Deschrijver et al. "Macromodeling of multiport systems using a fast implementation of the vector fitting method". In: *IEEE Microwave and wireless components letters* 18.6 (2008), pp. 383–385.

[36] Rudy Eid. "Time domain model reduction by moment matching". PhD thesis. Technische Universität München, 2009.

[37] ERCOT. *ERCOT Nodal Operating Guides*. Tech. rep. Austin, TX: ERCOT, Feb. 2018. URL: http://www.ercot.com/content/wcm/libraries/147359/February_1__2018_Nodal_Operating_Guide.pdf.

[38] Gerald Farin. *Curves and surfaces for computer-aided geometric design: a practical guide*. Elsevier, 2014.

[39] Francesco Ferranti, Luc Knockaert, and Tom Dhaene. "Parameterized S-parameter based macromodeling with guaranteed passivity". In: *IEEE Microwave and Wireless Components Letters* 19.10 (2009), pp. 608–610.

[40] Francesco Ferranti, Luc Knockaert, and Tom Dhaene. "Passivity-preserving parametric macromodeling by means of scaled and shifted state-space systems". In: *IEEE Transactions on Microwave Theory and Techniques* 59.10 (2011), pp. 2394–2403.

[41] Francesco Ferranti et al. "Passivity-preserving parametric macromodeling for highly dynamic tabulated data based on Lur'e equations". In: *IEEE Transactions on Microwave Theory and Techniques* 58.12 (2010), pp. 3688–3696.

[42] Luca Formaggia, Alfio Quarteroni, and Allesandro Veneziani. *Cardiovascular Mathematics: Modeling and simulation of the circulatory system*. Vol. 1. Springer Science & Business Media, 2010.

[43] Pascal Gahinet, Pierre Apkarian, and Mahmoud Chilali. "Affine parameter-dependent Lyapunov functions and real parametric uncertainty". In: *IEEE Transactions on Automatic control* 41.3 (1996), pp. 436–442.

[44] Michael Garstka, Mark Cannon, and Paul Goulart. "COSMO: A conic operator splitting method for convex conic problems". In: *Journal of Optimization Theory and Applications* 190.3 (2021), pp. 779–810.

[45] Walton C Gibson. *The method of moments in electromagnetics*. Chapman and Hall/CRC, 2021.

[46] S. Grivet-Talocia. "On driving non-passive macromodels to instability". In: *International Journal of Circuit Theory and Applications* 37.8 (Oct. 2009), pp. 863–886.

[47] S. Grivet-Talocia. "Package Macromodeling via Time-Domain Vector Fitting". In: *IEEE Microwave and Wireless Components Letters* 13.11 (Nov. 2003), pp. 472–474.

[48] S. Grivet-Talocia. "The Time-Domain Vector Fitting Algorithm for Linear Macromodeling". In: *Int. Journal of Electronics and Communications (AEU)* 58 (2004), pp. 293–295.

[49] Stefano Grivet-Talocia. "On driving non-passive macromodels to instability". In: *International Journal of Circuit Theory and Applications* 37.8 (2009), pp. 863–886.

[50] Stefano Grivet-Talocia. "Passivity enforcement via perturbation of Hamiltonian matrices". In: *IEEE Transactions on Circuits and Systems I: Regular Papers* 51.9 (2004), pp. 1755–1769.

[51] Stefano Grivet-Talocia and Bjorn Gustavsen. *Passive macromodeling: Theory and applications*. Vol. 239. John Wiley & Sons, 2015.

[52] Stefano Grivet-Talocia and Riccardo Trinchero. "Behavioral, Parameterized, and Broadband Modeling of Wired Interconnects With Internal Discontinuities". In: *IEEE Transactions on Electromagnetic Compatibility* 60.1 (2018), pp. 77–85.

[53] Stefano Grivet-Talocia and Riccardo Trinchero. "Behavioral, parameterized, and broadband modeling of wired interconnects with internal discontinuities". In: *IEEE Transactions on Electromagnetic Compatibility* 60.1 (2017), pp. 77–85.

[54] Stefano Grivet-Talocia and Andrea Ubolli. "On the generation of large passive macromodels for complex interconnect structures". In: *IEEE transactions on advanced packaging* 29.1 (2006), pp. 39–54.

[55] Stefano Grivet-Talocia et al. "Thermal Noise Compliant Synthesis of Linear Lumped Macromodels". In: *IEEE Transactions on Components, Packaging and Manufacturing Technology* 5.1 (2015), pp. 75–85. DOI: 10.1109/TCPMT.2014.2370096.

[56] Sergei V Gusev and Andrey L Likhtarnikov. "Kalman-Popov-Yakubovich lemma and the S-procedure: A historical essay". In: *Automation and Remote Control* 67.11 (2006), pp. 1768–1810.

[57] B. Gustavsen. "Improving the pole relocating properties of vector fitting". In: *2006 IEEE Power Engineering Society General Meeting*. 2006, 1 pp.-. DOI: 10.1109/PES.2006.1708940.

[58] B. Gustavsen and A. Semlyen. "Rational approximation of frequency domain responses by vector fitting". In: *Power Delivery, IEEE Transactions on* 14.3 (July 1999), pp. 1052–1061. ISSN: 0885-8977. DOI: 10.1109/61.772353.

[59] Bjørn Gustavsen. "Improving the pole relocating properties of vector fitting". In: *IEEE Transactions on Power Delivery* 21.3 (2006), pp. 1587–1592.

[60] Bjørn Gustavsen and Christoph Heitz. "Modal vector fitting: A tool for generating rational models of high accuracy with arbitrary terminal conditions". In: *IEEE Transactions on Advanced Packaging* 31.4 (2008), pp. 664–672.

[61] Bjorn Gustavsen and Adam Semlyen. "Rational approximation of frequency domain responses by vector fitting". In: *IEEE Transactions on power delivery* 14.3 (1999), pp. 1052–1061.

[62] Wouter Hendrickx and Tom Dhaene. "A discussion of" Rational approximation of frequency domain responses by vector fitting"". In: *IEEE Transactions on Power Systems* 21.1 (2006), pp. 441–443.

[63] A. Ionita and A. Antoulas. "Data-Driven Parametrized Model Reduction in the Loewner Framework". In: *SIAM Journal on Scientific Computing* 36.3 (2014), A984–A1007.

[64] Jian-Ming Jin. *The finite element method in electromagnetics*. John Wiley & Sons, 2015.

[65] H.K. Khalil. *Nonlinear Systems*. Pearson Education. Prentice Hall, 2002. ISBN: 9780130673893. URL: https://books.google.it/books?id=t%5C_d1QgAACAAJ.

[66] Georges Klein. "Applications of linear barycentric rational interpolation". PhD thesis. Université de Fribourg, 2012.

[67] Akira Kojima. "A characterization of parameter-dependent LMIs on Bernstein polynomial basis". In: *2018 IEEE Conference on Decision and Control (CDC)*. IEEE. 2018, pp. 4687–4694.

[68] Sanda Lefteriu and Athanasios C Antoulas. "On the convergence of the vector-fitting algorithm". In: *IEEE transactions on microwave theory and techniques* 61.4 (2013), pp. 1435–1443.

[69] Sanda Lefteriu and Athanasios C. Antoulas. "A New Approach to Modeling Multiport Systems From Frequency-Domain Data". In: *IEEE Transactions on Computer-Aided Design of Integrated Circuits and Systems* 29.1 (2010), pp. 14–27. DOI: 10.1109/TCAD.2009.2034500.

[70] EC Levy. "Complex-curve fitting". In: *IRE transactions on automatic control* 1 (1959), pp. 37–43.

[71] Feng Jun Li. "Interpolation and convergence of Bernstein-Bézier coefficients". In: *Acta Mathematica Sinica, English Series* 27.9 (2011), p. 1769.

[72] Lennart Ljung. "System identification". In: *Signal analysis and prediction*. Springer, 1998, pp. 163–173.

[73] J. Löfberg. "YALMIP : A Toolbox for Modeling and Optimization in MATLAB". In: *In Proceedings of the CACSD Conference*. Taipei, Taiwan, 2004.

[74] Tsz Yin Man, Philip KT Mok, and Mansun Chan. "A high slew-rate push–pull output amplifier for low-quiescent current low-dropout regulators with transient-response improvement". In: *IEEE Transactions on Circuits and Systems II: Express Briefs* 54.9 (2007), pp. 755–759.

[75] Robert J Milliken, Jose Silva-Martınez, and Edgar Sánchez-Sinencio. "Full on-chip CMOS low-dropout voltage regulator". In: *IEEE Transactions on Circuits and Systems I: Regular Papers* 54.9 (2007), pp. 1879–1890.

[76] Phan Minh. "Diamond/CNT Film Interface for Heat Dissipation in Electronic Devices". In: *Report of Asian Office of Aerospace Research and Development* (Sept. 2009), p. 10.

[77] S Nagaraj, D Seshachalam, and Sunil Hucharaddi. "Model order reduction of nonlinear circuit using proper orthogonal decomposition and nonlinear autoregressive with eXogenous input (NARX) neural network". In: *2018 16th ACM/IEEE International Conference on Formal Methods and Models for System Design (MEMOCODE)*. IEEE. 2018, pp. 1–4.

[78] Zohreh Naghibi, Sayed Alireza Sadrossadat, and Saeed Safari. "Time-domain modeling of nonlinear circuits using deep recurrent neural network technique". In: *AEU-International Journal of Electronics and Communications* 100 (2019), pp. 66–74.

[79] Yuji Nakatsukasa, Olivier Sète, and Lloyd N Trefethen. "The AAA algorithm for rational approximation". In: *SIAM Journal on Scientific Computing* 40.3 (2018), A1494–A1522.

[80] KG Nichols et al. "Overview of SPICE-like circuit simulation algorithms". In: *IEE Proceedings-Circuits, Devices and Systems* 141.4 (1994), pp. 242–250.

[81] Brendan O'Donoghue et al. "Conic Optimization via Operator Splitting and Homogeneous Self-Dual Embedding". In: *Journal of Optimization Theory and Applications* 169.3 (June 2016), pp. 1042–1068. URL: `http://stanford.edu/~boyd/papers/scs.html`.

[82] Salvatore Bernardo Olivadese et al. "Parameterized and DC-compliant small-signal macromodels of RF circuit blocks". In: *IEEE Transactions on Components, Packaging and Manufacturing Technology* 5.4 (2015), pp. 508–522.

[83] SB Olivadese, P Brenner, and S Grivet-Talocia. "DC-compliant small-signal macromodels of non-linear circuit blocks". In: *2013 17th IEEE Workshop on Signal and Power Integrity*. IEEE. 2013, pp. 1–4.

[84] José C Pedro and Stephen A Maas. "A comparative overview of microwave and wireless power-amplifier behavioral modeling approaches". In: *IEEE transactions on microwave theory and techniques* 53.4 (2005), pp. 1150–1163.

[85] S Pirola et al. "On the choice of outlet boundary conditions for patient-specific analysis of aortic flow using computational fluid dynamics". In: *Journal of biomechanics* 60 (2017), pp. 15–21.

[86] Hartmut Prautzsch and Leif Kobbelt. "Convergence of subdivision and degree elevation". In: *Advances in Computational Mathematics* 2.1 (1994), pp. 143–154.

[87] JB Preibisch et al. "Exploring efficient variability-aware analysis method for high-speed digital link design using PCE". In: *Proc. DesignCon.* 2017, pp. 1–19.

[88] Michal Rewienski and Jacob White. "A trajectory piecewise-linear approach to model order reduction and fast simulation of nonlinear circuits and micromachined devices". In: *IEEE Transactions on computer-aided design of integrated circuits and systems* 22.2 (2003), pp. 155–170.

[89] David E Root et al. "Broad-band poly-harmonic distortion (PHD) behavioral models from fast automated simulations and large-signal vectorial network measurements". In: *IEEE Transactions on Microwave Theory and Techniques* 53.11 (2005), pp. 3656–3664.

[90] Wilson J Rugh and Jeff S Shamma. "Research on gain scheduling". In: *Automatica* 36.10 (2000), pp. 1401–1425.

[91] Elizabeth Rita Samuel et al. "Guaranteed passive parameterized macromodeling by using sylvester state-space realizations". In: *IEEE Transactions on Microwave Theory and Techniques* 61.4 (2013), pp. 1444–1454.

[92] Cok Sanathanan and Judith Koerner. "Transfer function synthesis as a ratio of two complex polynomials". In: *IEEE transactions on automatic control* 8.1 (1963), pp. 56–58.

[93] M Sano and Lianming Sun. "Identification of Hammerstein-Wiener system with application to compensation for nonlinear distortion". In: *41st SICE Annual Conference.* Vol. 3. 2002, pp. 1521–1526.

[94] Carsten Scherer and Siep Weiland. "Linear matrix inequalities in control". In: *Lecture Notes, Dutch Institute for Systems and Control, Delft, The Netherlands* 3.2 (2000).

[95] Jeff S Shamma. "An overview of LPV systems". In: *Control of linear parameter varying systems with applications* (2012), pp. 3–26.

[96] Samira Shamsir et al. "Semiconductor Device Modeling and Simulation for Electronic Circuit Design". In: *Modeling and Simulation in Engineering.* Ed. by Jan Valdman and Leszek Marcinkowski. Rijeka: IntechOpen, 2020. Chap. 11. DOI: 10.5772/intechopen.92037. URL: https://doi.org/10.5772/intechopen.92037.

[97] *Sonnet Software*. www.sonnetsoftware.com. Accessed: 2022-06-15.

[98] I.S. Stievano, I.A. Maio, and F.G. Canavero. "Parametric macromodels of digital I/O ports". In: *IEEE Transactions on Advanced Packaging* 25.2 (2002), pp. 255–264. DOI: 10.1109/TADVP.2002.803260.

[99] Petre Stoica, Randolph L Moses, et al. "Spectral analysis of signals". In: (2005).

[100] Laurent Taylor et al. "Numerical modelling of PCB planar inductors: impact of 3D modelling on high-frequency copper loss evaluation". In: *IET Power Electronics* 10.14 (2017), pp. 1966–1974.

[101] Roland Tóth. *Modeling and identification of linear parameter-varying systems*. Vol. 403. Springer, 2010.

[102] P Triverio, S Grivet-Talocia, and Michel S Nakhla. "An improved fitting algorithm for parametric macromodeling from tabulated data". In: *12th IEEE Workshop on Signal Propagation on Interconnects, 12-15 May 2008, Avignon, France*, pp. 1–4.

[103] Piero Triverio, Stefano Grivet-Talocia, and Michel S Nakhla. "A parameterized macromodeling strategy with uniform stability test". In: *IEEE Transactions on Advanced Packaging* 32.1 (2009), pp. 205–215.

[104] M. Vaiman, R. Quint, et al. "Using Synchrophasors to Improve Bulk Power System Reliability in North America". In: *2018 IEEE Power and Energy Society General Meeting (PESGM)*. 2018, pp. 1–5.

[105] Lieven Vandenberghe et al. "Interior-point algorithms for semidefinite programming problems derived from the KYP lemma". In: *Positive polynomials in control*. Springer, 2005, pp. 195–238.

[106] Jan Verspecht, David Root, and Troels Nielsen. "Dynamic X-parameters*: Behavioral modeling in the presence of long term memory effects". In: *2012 The 7th German Microwave Conference*. 2012, pp. 1–4.

[107] Daniel Vizer et al. "A local approach framework for black-box and gray-box LPV system identification". In: *European Control Conference (ECC)*. 2013, pp. 1916–1921.

[108] John Leonidas Volakis et al. *Finite element method for electromagnetics*. Universities Press, 1998.

[109] Yelin Wang and Torben Larsen. "Applications of X-parameters in behavioral modeling of RF power amplifiers for wireless communications: An overview". In: *2015 17th International Conference on Transparent Optical Networks (ICTON)*. 2015, pp. 1–7. DOI: 10.1109/ICTON.2015.7193444.

[110] M Ronald Wohlers. *Lumped and distributed passive networks*. Academic press, New York, USA, 1969.

[111] Qian Xie, Jun Xu, and Yuan Taur. "Review and Critique of Analytic Models of MOSFET Short-Channel Effects in Subthreshold". In: *IEEE Transactions on Electron Devices* 59.6 (2012), pp. 1569–1579. DOI: 10.1109/TED.2012.2191556.

[112] A Zanco et al. "Multivariate macromodeling with stability and passivity constraints". In: *2018 IEEE 22nd Workshop on Signal and Power Integrity (SPI)*. IEEE. 2018, pp. 1–4.

[113] Alessandro Zanco and Stefano Grivet-Talocia. "Toward Fully Automated High-Dimensional Parameterized Macromodeling". In: *IEEE Transactions on Components, Packaging and Manufacturing Technology* 11.9 (2021), pp. 1402–1416. DOI: 10.1109/TCPMT.2021.3099958.

[114] Alessandro Zanco et al. "Enforcing passivity of parameterized LTI macromodels via Hamiltonian-driven multivariate adaptive sampling". In: *IEEE Transactions on Computer-Aided Design of Integrated Circuits and Systems* 39.1 (2018), pp. 225–238.

[115] Alessandro Zanco et al. "On stabilization of parameterized macromodeling". In: *2019 IEEE 23rd Workshop on Signal and Power Integrity (SPI)*. IEEE. 2019, pp. 1–4.

[116] Alessandro Zanco et al. "Uniformly Stable Parameterized Macromodeling Through Positive Definite Basis Functions". In: *IEEE Transactions on Components, Packaging and Manufacturing Technology* 10.11 (2020), pp. 1782–1794.

[117] Tianhao Zhang, K. Chakrabarty, and R.B. Fair. "Behavioral modeling and performance evaluation of microelectrofluidics-based PCR systems using SystemC". In: *IEEE Transactions on Computer-Aided Design of Integrated Circuits and Systems* 23.6 (2004), pp. 843–858. DOI: 10.1109/TCAD.2004.828115.

[118] Xiping Zhang, Panagiotis Tsiotras, and Carl Knospe. "Stability analysis of LPV time-delayed systems". In: *International journal of control* 75.7 (2002), pp. 538–558.

[119] Bin Zhou. "On asymptotic stability of linear time-varying systems". In: *Automatica* 68 (2016), pp. 266–276.

This Ph.D. thesis has been typeset by means of the TEX-system facilities. The typesetting engine was pdfLATEX. The document class was `toptesi`, by Claudio Beccari, with option `tipotesi=scudo`. This class is available in every up-to-date and complete TEX-system installation.